

The University of Nottingham

UNITED KINGDOM · CHINA · MALAYSIA

School of Chemistry

Synthetic Analogues of the Nickel-Iron Hydrogenase Family of Metalloenzymes

Graham Joseph Jones, MSci.

Thesis submitted to The University of Nottingham
for the degree of Doctor of Philosophy

September 2017

Declaration

Except where specific reference has been made to other sources, the work presented in this thesis is the original work of the author. It has not been submitted, in whole or in part, for any other degree.

Signed: Graham Joseph Jones

Date:

Foreword and Acknowledgements

This thesis bookends a journey I began when I returned to chemistry as an undergraduate many years ago as a mature student. It's never too late to make a change and I have met some wonderful people and friends along the way.

I would like to thank The University of Nottingham and Professor Martin Schröder for the opportunity to join his group and the EPSRC grant through which my PhD was funded. I'd like to mention everyone who made C41 a great place to work in the early days before our unfortunate move to B floor; specifically post-docs Drs Emma Stephen, Carlo Perotto and Joe Dawson who gave me crucial support and advice, as well as entrusting me as the next defender of ancient-yet-critical pieces of one-of-a-kind glassware that I now have the task of passing on. Enormous thanks are extended to Drs Will Lewis and Stephen Davies whose expertise in crystallography and electrochemistry respectively were invaluable at every stage of my studies; I would not be sitting here typing this without them. Special thanks go to Jon McMaster, who took over as my full supervisor after the Schröder group moved to Manchester and who has been a critical part of my success. Thank you also to my fourth year project students Joe Verity-Legg and Alex Kibler who assisted with some of the work in Chapters 2 and 3. I must also thank the close friends who have been on their own journeys alongside me over the past eight years; Sam Quinn, Jack Turner, Jim Furness, Rowena Howie, Nick "it's Jacques" Jacques and James Hickson. Thanks also to the Poliakoff group who graciously found us space in their office in our time of need and became great friends, thanks especially Erica, Johnny, Amy, Ines and Sam.

That brings me to three of the most instrumental people in this whole endeavour, whithout whom I'd have run off into the sunset to run a penguin sanctuary or something; George

Marshall, Gemma Skelton and Jere Tidey. I am not sure there are adequate words to express my gratitude for your help and support from the beginning and all the way through this, so I just say a scarcely adequate “cheers”.

Eternal thanks to my family and friends who have been there for me both emotionally and financially; Dad’s quiet but reassuring presence, Mum’s unwavering help and support, and especially Dr Kathleen Paul, with whom I share a very special connection. My siblings Luke and Lisa, and my excellent cousins Alexandra and Abigail, a source of joy and comfort whenever we get together for games or movies through the year. I thank them all deeply for their great and ceaseless friendship and support. Special thanks to Gemma, and the Rumbold family, who are always there for a chippy tea and the chance to win a bag of quinces or a very-recently ex-pheasant (still warm!) in the village hall quiz.

And of course, my puzzle piece, Jan. Always there for me, and who has put up with entirely too much nonsense over the past few years on the road to the completion of this PhD.

I feel like a quote out of context,
Withholding the rest,
So I can be for you what you want to see.
I got the gesture and sound
Got the timing down
It's uncanny, yeah, you think it was me.
Do you think I should take a class
To lose my southern accent?
Did I make me up, or make the face till it stuck?
*I do the **best** imitation of myself.*

- *Ben Folds*

Table of Contents

	Abstract	x
	Glossary	xii
	Ligand Abbreviations	xiii

Chapter One: Introduction

1.1	Addressing The Need For Alternative Energy	2
1.2	Dihydrogen as a Fuel	2
1.2.1	Production and Storage of Dihydrogen	3
1.3	Introduction to Enzymes and Metalloenzymes	5
1.4	Introduction to Nickel-Iron Hydrogenase Enzymes	7
1.4.1	The Catalytic Cycle of the [NiFe] Hydrogenases	9
1.5	Previous Research	13
1.6	Heterobimetallic analogues that replicate the biologically relevant Ni-(S_2)-M (M = metal) moiety	13
1.7	[NiFe] hydrogenase analogues featuring macrocycles and ligands with pendant arms	19
1.8	Aims of this Work	25
1.9	References	28

Chapter Two: Analogues of the Ni-L State of the [NiFe] Hydrogenase Active Site – Complexes that Access and Exploit the Ni^{I} Oxidation State

	Introduction	
2.1	Introduction and aims	33
	Results and Discussion	
2.2	The synthesis of [Ni(L1)]	38
2.3	The syntheses of [Ni(L1)Fe(R-NC)$_4$](BPh$_4$)$_2$ systems (R = ^{t}Bu, ^{n}Bu, ^{i}Pr, benzyl, cyclohexyl, PhOMe, PhF, 2-naphthyl)	38
2.4	Synthesis of [Ni(L2)Fe(^{t}BuNC)$_4$](BPh$_4$)$_2$	40
2.5	Crystallography – Attempted Crystallisation of Ni(L1)-based complexes.	41
2.6	The X-ray crystal structure of [Ni(L1)Fe(^{t}BuNC)$_4$](BPh$_4$)$_2$	43

2.7 Structures of $[Ni(L1)Fe(R\text{-}NC)_4](BPh_4)_2$, (R = ^{i}Pr, benzyl, cyclohexyl, PhOMe, PhF) 47
2.8 Cyclic Voltammetry of $[Ni(L1)Fe(R\text{-}CN)_4](BPh_4)_2$ (R = ^{t}Bu, ^{n}Bu, ^{i}Pr, cyclohexyl, benzyl, PhOMe) 54
2.9 UV/vis spectroelectrochemistry of $[Ni(L1)Fe(CN\text{-}R)_4](BPh_4)_2$ (R = ^{t}Bu, ^{n}Bu, ^{i}Pr, cyclohexyl, benzyl) 60
2.10 Probing the reduction of $[Ni(L1)Fe(R\text{-}CN)_4](BPh_4)_2$ (R = ^{t}Bu, ^{n}Bu, ^{i}Pr, cyclohexyl, benzyl, PhOMe) by IR Spectroscopy 64
2.11 EPR Spectoscopy of $[Ni(L1)Fe(CN\text{-}R)_4]^{+}$ 67
2.12 DFT calculations of $[Ni(L1)Fe(^{t}BuNC)_4]^{+}$ 71
2.13 Catalytic Studies of $[Ni(L1)Fe(^{t}BuCN)_4](BPh_4)_2$ 76
2.14 Cyclic Voltammetry of $[Ni(L2)Fe(^{t}BuNC)_4](PF_6)_2$ 82
2.15 Conclusions and Future Work 84
2.16 Experimental 85
2.17 References 91

Chapter Three: Analogues of the Ni-C State of the Hydrogenase Active Site – Complexes that Stabilise the Ni^{III} Oxidation State

3.1 Introduction and aims 94
3.2 The synthesis of the $[H_2L3]$ ligand 95
3.3 The synthesis of [Ni(L3)] 97
3.4 The X-ray crystal structure of [Ni(L3)] 97
3.5 The attempted syntheses of $[Ni(L3)](PF_6)$ and $[Ni(L^2N_2S_3)](BF_4)$ 99
3.6 The syntheses of $[Ni(L3)Fe(R\text{-}NC)_4](PF_6)_2$, (R = ^{t}Bu, cyclohexyl, benzyl) 100
3.7.1 The synthesis and X-ray crystal structure of $[Ni(L3)[Fe(CN^{t}Bu)_4](PF_6)_2$ 100
3.7.2 The synthesis of $[Ni(L3)Fe(benzyl\text{-}NC)_4](PF_6)_2$ 103
3.7.3 The attempted Synthesis of $[Ni(L3)Fe(cyclohexyl\text{-}NC)_4](PF_6)_2$ 103
3.8 Electrochemical studies of $[Ni(L3)Fe(R\text{-}NC)_4](PF_6)_2$, R = (^{t}Bu, benzyl) 104
3.8.1 Electrochemical studies of $[Ni(L3)Fe(^{t}BuNC)_4](PF_6)_2$ 104
3.8.2 Electrochemical studies of $[Ni(L3)Fe(benzyl\text{-}NC)_4](PF_6)_2$ 107

3.9.1 Spectroelectrochemistry of $[Ni(L3)Fe(R\text{-}NC)_4](PF_6)_2$ (R = ^{t}Bu, benzyl) 108
3.9.2 IR Spectroelectrochemistry of $[Ni(L3)Fe(R\text{-}NC)_4](PF_6)_2$ (R = ^{t}Bu) and the IR spectrum of $Ni(L3)Fe(R\text{-}NC)_4](PF_6)_2$ (R = benzyl) 111
3.10 EPR spectroscopy of $[Ni(L3)Fe(^tBuNC)_4]^{3+}$ 113
3.11 Electrochemistry of $[Ni(L3)Fe(R\text{-}NC)_4](PF_6)_2$ under hydrogen (R = ^{t}Bu, benzyl) 115
3.12 DFT Calculations 116
3.13 Conclusions and Future Work 126
3.14 Experimental 129
3.15 References 134

Chapter Four: Substitution of Nickel for Other Metals in [NiFe] Enzyme Analogues

4.1 Introduction and aims 137
4.2 Results and discussion
4.2.1 The syntheses of M(L1) (M = Pd, Co and Zn) and the attempted synthesis of Cu(L1) 138
4.2.2 X-ray crystallographic studies of M(L1) (M = Pd, Co and Zn)
4.2.2.1 The X-ray crystal structure of Pd(L1) 140
4.2.2.2 The X-ray crystal structure of Co(L1) 141
4.2.2.3 The X-ray crystal structure of Zn(L1) 142
4.2.2.4 Conclusions from the X-ray crystal structures of M(L1) (M = Pd, Co, Zn) 144
4.2.3 Electrochemical studies of M(L1) (M = Pd, Co and Zn)
4.2.3.1 Electrochemistry of Pd(L1) 145
4.2.3.2 Electrochemistry of Co(L1) 146
4.2.3.3 Electrochemistry of Zn(L1) 147
4.3 The attempted syntheses of $[M(L1)Fe(CN^tBu)_4](BPh_4)_2$ (M = Pd, Co and Zn) 147
4.4 X-ray crystallography of $[Pd(L1)Fe(CN^tBu)_4](BPh_4)_2$ 150
4.5 Infrared spectroscopy of $[Pd(L1)Fe(CN^tBu)_4](BPh_4)_2$ 153
4.6 Electrochemical studies of $[Pd(L1)Fe(CN^tBu)_4](BPh_4)_2$ 154
4.7 DFT Calculations of $[Pd(L1)Fe(CN^tBu)_4]^{2+}$ 155

4.8 X-ray crystallography of $[Co(L1)(CN^tBu)Fe(CN^tBu)_4](BPh_4)_2$ 159
4.9 Electrochemical studies of $[Co(L1)(CN^tBu)Fe(CN^tBu)_4](BPh_4)_2$ 161
4.10 DFT Calculations of $[Co(L1)(CN^tBu)Fe(CN^tBu)_4]^+$ 162
4.11 Conclusions 164
4.12 Experimental 167
4.13 References 171

Chapter Five: Conclusions

5.1 Conclusions 173
5.2 References 177

Appendicies

Appendix 1 General Experimental Procedures and Physical Measurements A1
Appendix 2 X-ray Crystallographic Experimental Details and Structure Solution A2
Appendix 3 Computational Methods A2
Appendix 4 Crystallography Tables A3
Appendicies References A11

Abstract

This thesis describes the syntheses and characterisations of heterobimetallic dithiolate complexes of Ni^{II}, Pd^{II} and Co^{II} with Fe^{II} that derive inspiration from the chemistry and structures of the active sites of the [NiFe] hydrogenase family of metalloenzymes. These studies provide insight into the electronic structures of the Ni-C and Ni-L states of the [NiFe] hydrogenases and the complexes have potential as new catalysts for the production of dihydrogen.

Chapter One outlines the role of dihydrogen as a potential fuel and replacement for energy sources derived from fossil fuel feedstocks. The Chapter describes the roles offered by synthetic analogues of the active sites of the [NiFe] hydrogenases as routes to meet the demand for H_2 production. An introduction to enzymes and the roles of transition metals in biology, together with a description of the structure and function of the [NiFe] hydrogenases, are presented. A proposed catalytic cycle for the [NiFe] hydrogenases and a review of the coordination chemistry relevant to the active site of the [NiFe] hydrogenases is presented. Key questions about the [NiFe] hydrogenases and the aims of the work described in this thesis are summarized.

Chapter Two describes the synthesis and characterisation of a series of bimetallic $[Ni^{II}Fe^{II}]$ complexes that incorporate a four coordinate Ni^{II} centre ligated by the N,N'-diethyl-3,7-diazanonane-1,9-dithiolate $(L1)^{2-}$ ligand bound to a pseudooctahedral Fe^{II} centre to give a Ni-(S_2)-Fe bridging arrangement. The coordination sphere of the Fe^{II} centre is completed by a range of isocyanide ligands, R-NC (R = ^{t}Bu, ^{i}Pr, ^{n}Bu, cyclohexyl, benzyl, 4-methoxyphenyl, 4-fluorophenyl) that act as surrogates for the π-acceptor CO and CN^- found at the active site in the [NiFe] hydrogenases. Electrochemical and EPR studies on these complexes provide insight

into the role of the isonitrile R group on the redox chemistry of the [$Ni^{II}Fe^{II}$] centre. Our electrochemical and spectroscopic studies, supported by DFT calculations, show that these [NiFe] complexes possess a formal $Ni^{II/I}Fe^{II}$ redox couple that is localized around the Ni unit. These complexes are compelling models of the Ni-L state of the [NiFe] hydrogenases and show promise as potential electrocatalysts for proton reduction.

Chapter Three describes the synthesis and characterisation of a pentacoordinate Ni^{II} complex in which Ni^{II} is bound by the 1,1'-(1,4,7-thiadiazonane)bis(2-methylpropane-2-thiol) (H_2L3) ligand. We show that this unit can coordinate to a pseudo-octahedral Fe^{II} centre to generate a bridged Ni-(S_2)-Fe structures in which the coordination sphere of the Fe^{II} centre is completed by four isonitrile ligands. These complexes we show that the heterobinuclear [$Ni^{II}Fe^{II}$] system supports a formal [$Ni^{III/II}Fe^{II}$] redox couple. X-ray crystallographic, and electrochemical and spectroscopic studies, supported by DFT calculations, provide insights into the nature of the [$Ni^{III}Fe^{II}$] species that represents analogues of the Ni-C state of the [NiFe] hydrogenases.

Chapter Four describes the synthesis and characterisation of a range of novel four-coordinate [$M(N_2S_2)$] (M = Pd, Co, Zn) complexes in which the metal centre is bound by N,N'-diethyl-3,7-diazanonane-1,9-dithiolate $(L1)^{2-}$. We describe attempts to coordinate these centres to a $[Fe^{II}(CN^tBu)_4]^{2+}$ fragment to yield the corresponding heterobimetallic [MFe] complexes. We characterize these compounds by X-ray crystallography and investigate their electrochemical properties for direct comparisons with their [NiFe] counterpart described in Chapter Two to provide insight into the effect of substituting Ni^{II} for other transition metal centres.

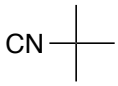
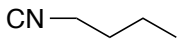
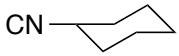
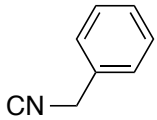
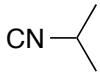
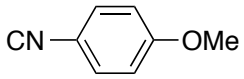
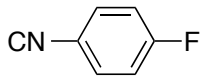
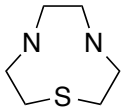
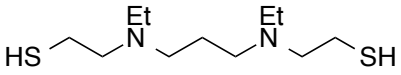
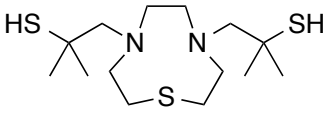
Chapter Five provides a summary of the principal conclusions of the research described in this thesis.

Glossary

(acac)	acetylacetonate
Cp	Cyclopentadienyl ion $(C_5H_5)^-$
Cp*	Pentamethylcyclopentadienyl ion $(C_5Me_5)^-$
CPE	Controlled Potential Electrolysis
CV	Cyclic Voltammetry
d	Doublet (NMR)
DCM	Dichloromethane
DMF	Dimethylformamide
Et_2O	Diethyl ether
EPR	Electron Paramagnetic Resonance
Fc^+/Fc	Ferrocenium ion/Ferrocene
G	Gauss
ICP-OES	Inductively Coupled Plasma Optical Emission Spectroscopy
IR	Infrared Spectroscopy
m	Multiplet (NMR)
MeCN	Acetonitrile
NMR	Nuclear Magnetic Resonance
PhOMe	4-methoxyphenyl
PhF	4-fluorophenyl
pdt	propanedithiol/propanedithiolate
q	quartet (NMR)
s	Singlet (NMR)
sh	Shoulder
SCE	Saturated calomel electrode
SHE	Standard hydrogen electrode
t	Triplet (NMR)
Tf	Triflate
TFA	Trifluoroacetic acid
THF	Tetrahydrofuran
TsCl	*p*-toluenesulfonyl chloride
XRD	X-Ray Diffraction

Ligand Abbreviations

The following abbrevations are used for convenience throughout this body of work.

Abbreviation	Name	Structure
^{t}BuNC	*tert*-butyl isocyanide	
^{n}BuNC	N-butyl isocyanide	
cyclohexyl-NC	cyclohexyl isocyanide	
benzyl-NC	benzyl isocyanide	
^{i}Pr-NC	isopropyl isocyanide	
PhOMe-NC	4-methoxyphenyl isocyanide	
PhF-NC	4-fluorophenyl isocyanide	
[N_2S]	1,4,7-thiadiazonane	
[H_2L1]	N,N'-diethyl-3,7-diazanonane-1,9-dithiol (dithiolate in metal complexes)	
[H_2L3]	1,1'-(1,4,7-thiadiazonane)bis(2-methylpropane-2-thiol) (dithiolate in metal complexes)	

Chapter One

Introduction

1.1 Addressing The Need For Alternative Energy

The human race consumes a vast amount of energy, the majority of which is primarily non-renewable hydrocarbons from fossil sources, and the global demand is forecast to increase from 2012 levels by almost 50% by 2040.[1] This increase in demand is ultimately unsustainable unless we diversify the sources of energy we employ. One of the most significant challenges facing our move toward more sustainable sources are fuels for transportation that are currently overwhelmingly supplied through liquid fossil sources such as oil and natural gas.[2] There are significant research and engineering hurdles that must be overcome before these sources of energy become practical and economically viable.[3]

1.2 Dihydrogen as a Fuel

With an increasingly pressing need to reduce our dependence on fossil fuels, significant effort has been directed into finding alternative energy sources that are sustainable and non-damaging to the environment.[4] Dihydrogen has the potential to be a solution to that need, though significant hurdles must be overcome before it can serve as an economically feasible or practical replacement on a large scale.[5, 6]

Hydrogen fuel cells that exploit the reaction of dihydrogen and dioxygen to generate electrical power have been in use for many years and have been in development since the early 1930s.[7] For example, between 1968 and 1974, the Apollo Command and Service Module derived its primary electrical power (and as a useful by-product, potable drinking water) for supporting manned spaceflight missions from three alkaline H_2/O_2 fuel cells generating up to 1.4 kW at 27-31 volts in compact, low-mass modules manufactured by General Electric (Figure 1.2.1).[8, 9] This demonstrates that effective power generation using dihydrogen as a fuel source for small vehicles is possible, albeit expensive, and has been for some time. As of 2016, several

automotive manufacturers have demonstrated practical replacements for traditional internal combustion engines in the form of dihydrogen fuel cell systems of similar size and power output to a commercial and consumer internal combustion engines to power consumer vehicles and which have lowered the costs of purchase and ownership significantly.[10] Static installations designed to replace on-site diesel backup generators are already an established commercial enterprise,[11] alongside a development programme to replace diesel units as the prime mover in railway applications where non-electrified track is common.[12] These development vehicles and large-scale building installations, however, demonstrate the two primary obstacles to the more widespread use of fuel cells: the production of dihydrogen and its subsequent transportation and storage in an efficient and cost effective manner. These are significant problems that must be overcome, although it is clear that there is a nascent demand and that this demand is continuing to grow.[3]

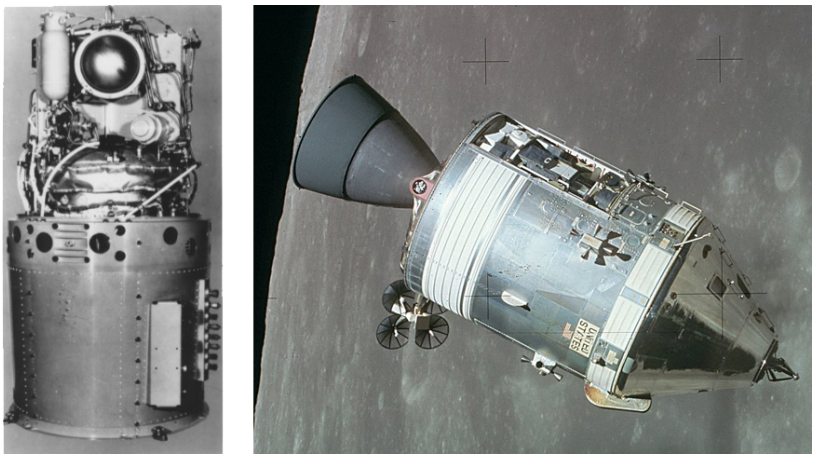


Figure 1.2.1: General Electric 1.4 kW alkaline fuel cell (left), and Apollo 15 CSM 'Endeavour' (right) in lunar orbit, August 1971.[13, 14]

1.2.1 Production and Storage of Dihydrogen

The current methods for the production of dihydrogen are energy intensive and primarily rely on the combustion of fossil fuels.[15] The most common industrial production method is the steam reformation of methane over a platinum catalyst, which requires high temperatures (700-

1200 ºC) and access to a hydrocarbon feedstock.[16] Alternative methods that rely on renewable resources such as the electrolysis of water or basic aqueous solutions are more expensive than steam reforming due to their use of corrosive electrolyte solutions, a high maintenance requirement of the equipment and a dependence on electricity costs.[3] The development of more efficient and safer reactors for the production of dihydrogen *via* water splitting are ongoing, but are not currently in the commercial phase of development.[17] Smaller-scale methods using biomass as a feedstock are also available, but are more suited to small-scale production and are also costly to run.[3, 16] The use of enzymes bound to electrode surfaces present another possible route, but this method poses challenges in scale up from laboratory systems as well as the potential sensitivity of the enzymes to dioxygen.[18]

The transportation and storage of dihydrogen also represents a challenge. The fuel cells used during the Apollo programme were fed with dihydrogen and dioxygen gas generated from liquid dihydrogen and dioxygen stored as cryogens,[8] but this is an impractical solution for widespread consumer adoption due to the high energy cost of liquefying dihydrogen and the hazards associated with the storage and transportation of cryogenic liquids.[19] Currently vehicles powered by dihydrogen fuel cell typically use tanks that store dihydrogen as a compressed gas at a working pressure around 700 bar; despite the significant complexities and increased weight compared to those associated with a standard liquid fuel tank. With current technologies it is possible to store sufficient quantities of dihydrogen (approximately 5 kg) for a driving range comparable to that of a petrol or diesel-powered car without compromising safety.[20] For comparison, the Apollo CSM launched with approximately 13 kg of dihydrogen to support operations for two weeks.[8] These improvements in tank design and materials from a flight-hardened cryogenic dewar approximately the size of small propane barbeque tank to a H_2 gas storage tank that fits unobtrusively under the floor of a car chassis have made safe and

practical vehicles a realistic target for the consumer. In addition, hydrogen-powered vehicles can be quickly refuelled given the right infrastructure, unlike purely battery powered cars and trucks.[10,21, 22]

Even with these challenges met, and with commercial H_2 vehicles currently available for sale to the public, if hydrogen fuel cells are to attain widespread adoption as an alternative to fossil fuels a cost effective and sustainable route to the production of dihydrogen is required. Catalytic dihydrogen production inspired by the chemistry of biological systems could provide one of the solutions to this problem.

1.3 Introduction to Enzymes and Metalloenzymes

Enzymes are extremely important proteins that catalyse a broad range of reactions in nature that would otherwise be impossible under physiological chemical conditions.[23] They are essential for nearly all life on Earth and their study can offer insights into novel approaches to catalysis.[24-26]

An enzyme works by lowering the Gibbs free energy of activation ($\Delta G^{\ddagger}$) for a reaction to a point where the reaction can occur under physiological conditions (Figure 1.3.1).[27] One example is the fixation of dinitrogen into ammonia by bacteria that compares to the energy-intensive Haber process. The N_2 triple bond is strong (*ca*. 945 $kJmol^{-1}$)[28] and N_2 does not react readily under biological conditions. However, the nitrogenases found in, for example, *Rhodopseudomonas palustris*[29] catalyse the production of ammonia from dinitrogen under physiological conditions in contrast to the harsh conditions employed in the Haber process.[30]

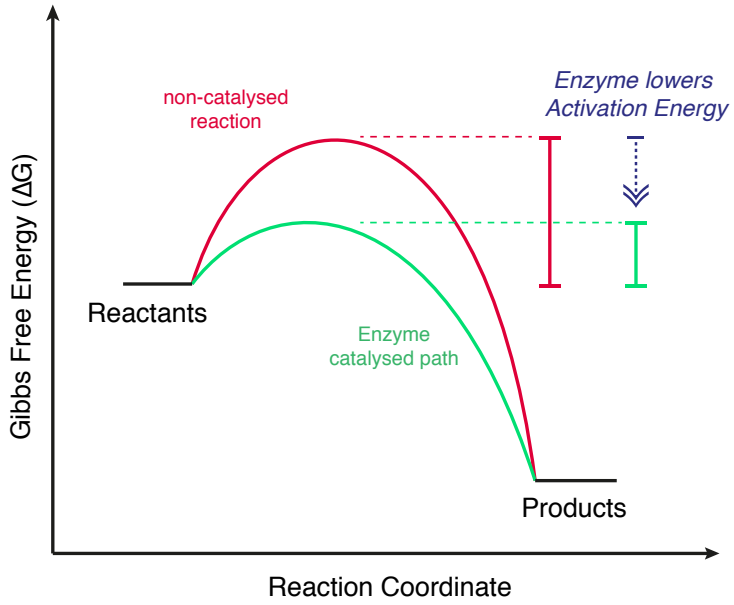


Figure 1.3.1: Schematic representation of a hypothetical enzyme-catalysed reaction pathway.

The active site of an enzyme usually possesses a specific geometry and electronic structure that binds at least one of the substrate molecules in a reaction in a particular conformation and electronic state to reduce the activation energy for the reaction.[27] Thus, enzymes are usually highly specific, catalysing one or two reactions only rather than acting on any substrate. For this reason, there is no universal enzyme and thus a vast range of different enzyme families exist to catalyse the wide range of reactions that facilitate life on earth.[23, 27]

Due to their specific nature, enzymes have a wide variety of structures and some incorporate metal centres as critical components at their active site. These enzymes are known as metalloenzymes.[27] Metalloenzymes that incorporate transition metal centres at their active sites exploit the varying oxidation states associated with these centres to catalyse redox reactions.[31] Transition metal centres can also support ligand exchange due to the ability of these complexes to adopt varying geometries; many of these complexes possess conformational flexibility in 4, 5 and 6 coordinate systems.[32]

1.4 Introduction to Nickel-Iron Hydrogenase Enzymes

The hydrogenase family are a group of enzymes that catalyse the reversible two-electron reduction of protons to dihydrogen (Equation 1.4.1).[33]

Equation 1.4.1: $2H^+ + 2e^- \leftrightharpoons H_2$

There are four classes of hydrogenases that have been recognized: (i) the [NiFe] hydrogenases, which contain Ni and Fe and are the most numerous, (ii) the [NiFeSe] hydrogenases that are similar to the [NiFe] hydrogenases but contain one selenocysteine residue as a ligand for Ni (iii) the [FeFe] and (iv) the Fe-only enzymes.[7] The latter two enzyme classes do not contain Ni and differ due to the presence of one (Fe-only) or two ([FeFe]) iron atoms located at the active site.[34, 35]

The first X-ray crystallographic determination of the structure of a [NiFe] hydrogenase was published in 1995 for the [NiFe] hydrogenase from *Desulfovibrio gigas* (Figure 1.4.1) at 2.85 Å resolution.[36] The enzyme is heterodimeric with one sub-unit (shown in purple, Figure 1.4.1) containing the heterobimetallic [NiFe] active site and a second, smaller subunit (shown in green, Figure 1.4.1) that contains three Fe–S clusters: two [Fe_4S_4] and one [Fe_3S_4] cluster. The proximal [Fe_4S_4] cluster is 13 Å from the [NiFe] containing active site, the distal [Fe_4S_4] is close to the surface of the protein and [Fe_3S_4] cluster is located between the [Fe_4S_4] centres. These Fe–S clusters form a pathway for electron transfer between the surface of the protein connecting the active site to the surface, where electron exchange with a protein redox partner (cytochrome c_3) can occur.[34, 37]

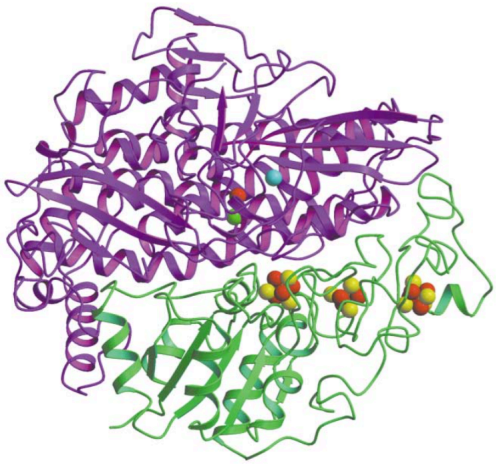


Figure 1.4.1: Polypeptide fold of the [NiFe] Hydrogenase found in D. gigas. The large (purple) and small (green) subunit are depicted here, with the approximate locations of FeS clusters (yellow and red spheres) and the active site location in the heart of the protein (nickel atom; green sphere, iron atom; red sphere).[37]

The heterobinuclear [NiFe] active site (Figure 1.4.2) is contained in a larger 60 kDa subunit approximately 30 Å from the surface of the protein at the bottom of a hydrophobic pocket through which dihydrogen can diffuse.[36]

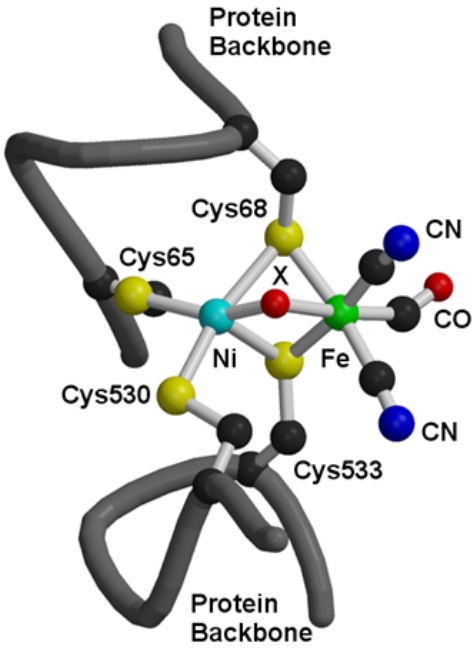


Figure 1.4.2: solid state structure of the active site of the [NiFe] hydrogenase from Desulfovibrias gigas.[38]

The Ni centre at the active site is ligated by four cysteine residues via sulfur atoms. Two of these sulfurs are terminally bound while the other two bridge between the Ni and an adjacent Fe centre.[36, 38] Three, small non-protein ligands also coordinate to the Fe centre and these have been unambiguously identified as two CN^- and one CO ligands by FTIR and chemical analysis on the [NiFe] hydrogenase from *Chromatium vinosum*.[39, 40] The CO ligand lies in a hydrophobic pocket, whereas the CN^- ligands interact with the protein through hydrogen bonds to serine and arginine residues.[41] In addition to the bridging thiolates between the Ni and Fe centres, a third bridging species has been identified in a number of different states of the enzyme. These species, not conclusively identified in the original diffraction experiments, have been assigned as either a hydride (predominantly), a peroxide or a hydroxide ligand during subsequent spectroscopic studies, depending on the enzyme state.[42] In addition the Ni-Fe distance varies with the oxidation level of the active site. Thus, in the reduced states of the enzyme the Ni-Fe distance is approximately 2.5 to 2.6 Å, while in the oxidised form this lengthens to 2.9 Å.[36, 40, 43]

1.4.1 The Catalytic Cycle of the [NiFe] Hydrogenases

The enzymes of the [NiFe] hydrogenase family can catalyse the reaction shown in Equation 1.4.1 at *ca.* 9000 turnovers per second depending on the particular enzyme; electrochemical studies have demonstrated that this cycle operates near the thermodynamic potential for the reaction (-0.3 V vs SCE, 30 ºC, pH 7, 0.1 bar H_2).[44] Of the known hydrogenases, most can catalyse the reaction shown in Equation 1.4.1 in both directions depending on the redox conditions and reagents available to the enzyme.[45] For example, in the presence of dihydrogen and an electron acceptor species, the [NiFe] hydrogenases will catalyse the reverse reaction and act as a dihydrogen uptake enzyme. In contrast, in the presence of an electron donor and water, the forward reaction can be catalysed, with the enzyme using the protons from water, or

other acidic media, as an electron acceptor and thus releasing dihydrogen.[33] The [NiFe] hydrogenases exploit this ability to function reversibly to perform a range of physiological functions; for example, (i) energy management (respiration, NAD(P)H formation) where the production of protons or electrons is desired, (ii) as a sink for excess reducing potential via the production of dihydrogen through re-oxidation of electron carriers or reduced pyridine nucleotides[5] or (iii) for methanogenesis.[33]

The active site exists in several different states depending on the local physiological environment, external factors and the current step of the catalytic cycle (Figure 1.4.3, Table 1.4.1). These states are labelled Ni-A, Ni-B, Ni-C, Ni-L, Ni-SI and Ni-R.[46, 47] The Ni-A, Ni-B, Ni-C and Ni-L states are paramagnetic and have been probed via EPR spectroscopy, with the A and B states exhibiting the highest oxidation states. The EPR spectroscopic results demonstrate that the redox chemistry predominantly centred on the Ni centre that involves $Ni^{II/I}$ or $Ni^{III/II}$ redox couples, rather than a radical-based system centred on a ligand. The Fe centre remains as a low-spin Fe^{II} centre in all of the observed states of the [NiFe] hydrogenases.[48] The Ni-C and Ni-L forms possess rhombic EPR spectroscopic signatures (Ni-C; *g*-values: 2.20, 2.14, 2.02), (Ni-L; *g*-values: 2.28, 2.11, 2.05) that are consistent with a primarily metal-based S = ½ configuration.[49-52] The Ni-SI and Ni-R states are EPR-silent and Ni^{II} and Fe^{II} centres with the Ni-R state identified as the fully reduced form.[53] The nature of the catalytic cycle of the [NiFe] hydrogenases is still being debated. The current proposed cycle (Figure 1.4.3) involves the active site cycling between the Ni-C, Ni-R and Ni-SI states during turnover.[39, 49, 54]

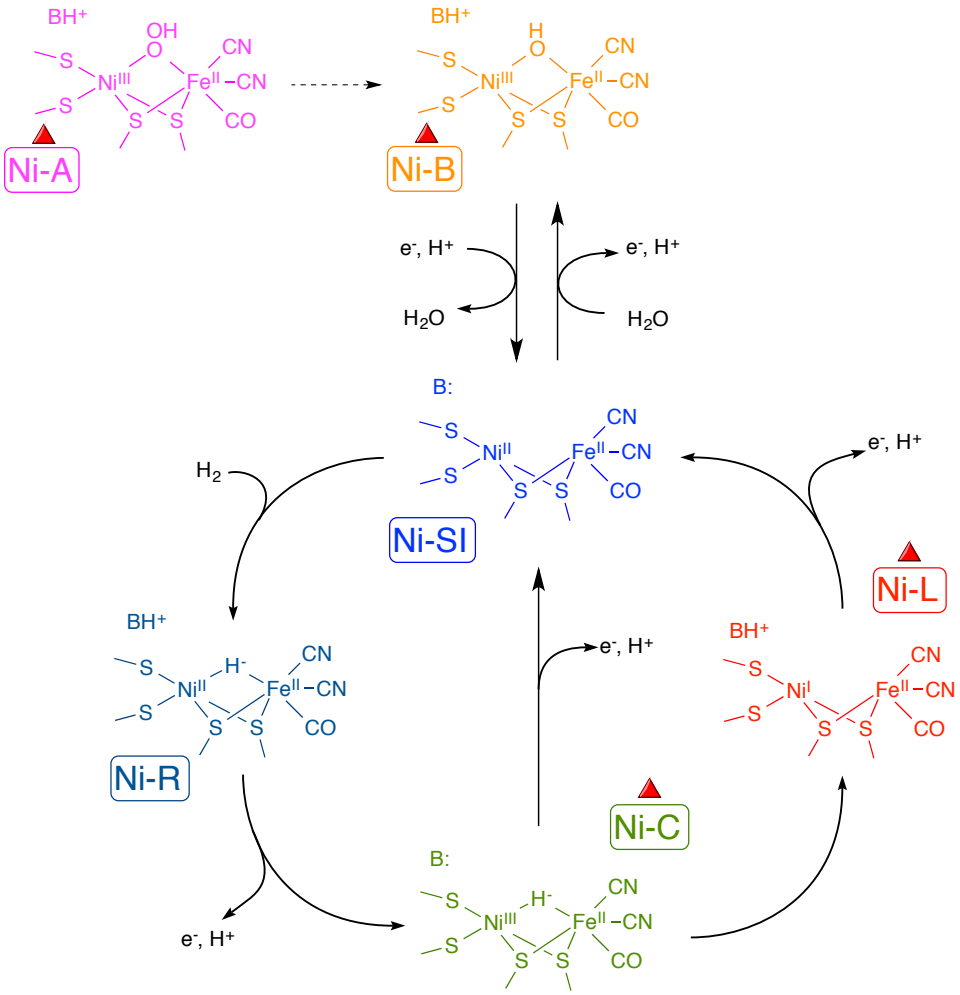


Figure 1.4.3: Schematic diagram showing the most commonly observed key states of the active site of the [NiFe] hydrogenase enzyme family. Paramagnetic states are indicated by a red triangle.[47, 55, 56]

Table 1.4.1: A summary of the states of the active site of the [NiFe] hydrogenases.

Name	Oxidation States		Part of Catalytic Cycle?
Ni-A	Ni (III)	Fe (II)	No – "unready"
Ni-B	Ni (III)	Fe (II)	No – "ready"
Ni-C	Ni (III)	Fe (II)	Yes
Ni-SI	Ni (II)	Fe (II)	Yes
Ni-R	Ni (II)	Fe (II)	Yes
Ni-L	Ni (I)	Fe (II)	Yes – secondary pathway[55]

The Ni-A and Ni-B states are non-active and are atypical for the enzyme but can occur in the presence of oxygen or other physiological conditions, and can be converted back to one of the

active states that participate in the catalytic cycle through reduction by proximal FeS clusters or through other means.[57]

The catalytic cycle proposed by Fontecilla-Camps *et al.* starts with the Ni-SIa state which features a vacant Ni-Fe bridging site (Figure 1.4.3).[37, 49] Dihydrogen binds to the Ni centre where it is heterolytically cleaved into H^- and a proton. The hydride ligand in Ni-R is located in a bridging position between Ni and Fe while the proton can be transferred to either a terminal thiolate residue or a neighboring Glu residue (BH). After electron transfer to the proximal [Fe_4S_4] cluster the paramagnetic Ni-C state is generated. The cycle is finally closed by the transfer of one electron and one proton which regenerates the Ni-SIa state.[9] Recent research has identified a second pathway involving the Ni-L state that may also be a key biologically relevant intermediate in the cycle.[55, 58, 59] Previously, Ni-L had not been viewed as being catalytically relevant given the conditions required for its formation. However, recent *in situ* IR spectroelectrochemical studies have demonstrated that Ni-L may be generated reversibly in the dark under turnover conditions.[55] Therefore, the regeneration of the Ni-SI state could occur either directly from the Ni-C state, via the concerted transfer of an electron and a proton, or by oxidation of the Ni-L state. These studies, together with previous DFT calculations,[60] open up the possibility that separate proton and electron transfer events may be associated with the regeneration of the Ni-SI state from Ni-C, and that these steps may involve the Ni-L state (Figure 1.4.3).

Unlike other more robust enzymes and organisms that have been exploited for human use, for example, bread yeasts, brewing yeasts or antibiotic synthesis,[61, 62] the [NiFe] hydrogenases are typically highly oxygen sensitive.[63] Thus research and development has moved towards using the chemistry exhibited by the active sites of the [NiFe] hydrogenases as

inspiration for synthetic structural or functional analogues that may serve as new catalysts for the production of dihydrogen.

1.5 Previous Research

The nature of the active site of the [NiFe] hydrogenases has inspired a range of novel coordination chemistry.[47, 64-69] Many of the syntheses of these complexes seek to replicate the heterobimetallic core of the active site by using Ni and Fe or by using other transition metals including Co, Ru, Pd and Pt among others.[64, 70, 71] Other reports have focused on the syntheses of mononuclear complexes as catalysts for the production of dihydrogen that incorporate Ni, Fe or other transition metals.[72] The synthesis of an efficient catalyst that incorporates only Ni and/or Fe as the core metal components, or that is restricted to the 3*d* metals, is a desirable and highly active area of research because of the high abundance and low cost of these metals when compared to the Pt group metals.

1.6 Heterobimetallic analogues that replicate the biologically relevant Ni-(S_2)-M (M = metal) moiety

There have been several reported functional analogues of the active site of the [NiFe] hydrogenases that feature transition metals at their cores and which have also demonstrated potential as proton reduction/hydrogen evolution catalysts. These complexes attempt to reproduce a four-coordinate Ni species bound to at least two sulfur atoms and which is paired with an organometallic iron moiety to generate a Ni-(S_2)-Fe system.[46, 60, 64, 73] The first complex to be structurally characterised with a Ni-(S)-Fe thiolate bridge, [Ni(BME-DACO)$Fe(CO)_4$] [BME-DACO = (1,5-bis(mercaptoethyl)-1,5-diazacyclooctane)], was reported by Darensbourg *et al*. (Figure 1.6.1).[74] [Ni(BME-DACO)$Fe(CO)_4$] was synthesised from the four coordinate Ni complex [Ni(BME-DACO) that was combined with [$Fe_2(CO)_9$]. [Ni(BME-

DACO)Fe(CO)$_4$] contains a single Ni-S-Fe thiolate bridge and a Ni-Fe distance of 3.76 Å. This distance is too long for any significant metal-metal interaction, however, the isolation of [Ni(BME-DACO)Fe(CO)$_4$] demonstrated the potential of this synthetic route. As a result this self assembly approach, the combination of a monomeric Ni complex with an iron species has proven to be a rich avenue for the syntheses of complexes containing Ni and Fe centres.[46, 64]

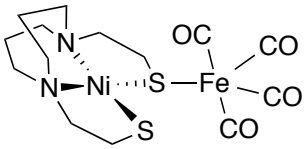


Figure 1.6.1: The first structurally characterised [NiFe] analogue demonstrating a thiolate bridged structure.[74]

While a range of complexes incorporating a Ni-(S_2)-Fe centre have been prepared (Figure 1.6.2) they do not show evidence as catalysts for the evolution of H_2.[46, 75, 76]

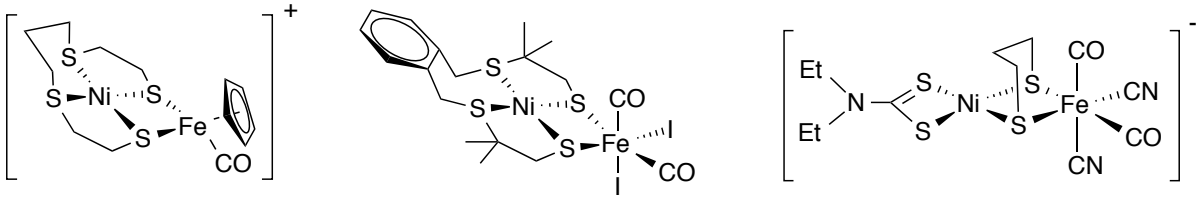


Figure 1.6.2: Selected early examples of [NiFe] hydrogenase structural analogues that replicate the Ni-(μS_2)-Fe moiety found in the enzyme active site.[46, 76, 77]

The first published [NiFe]-inspired mimic to demonstrate catalytic activity with respect to hydrogen production was published by Schröder *et al* (Figure 1.6.3),[78] and while the system was stable for at least 45 minutes in acidic conditions, the catalytic activity was low. It also deviates from the idealised Ni-(S_2)-Fe system that these mimics seek to replicate, featuring a trinuclear [$NiFe_2$] centre.

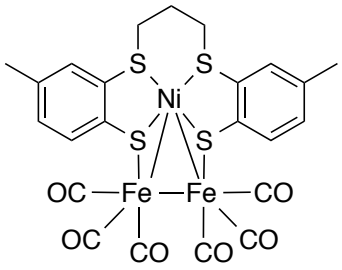


Figure 1.6.3: The first published [NiFe] hydrogenase mimic that demonstrates catalytic activity with respect to hydrogen.[78]

More recent systems improve on earlier bimetallic analogues that retain the Ni-(μS_2)-Fe core moiety while also demonstrating potential as electrocatalysts and the ability to stabilise a bridging hydride intermediate species. The complex [(dppe)Ni(μ-pdt)Fe$(CO)_3$], reported by Rauchfuss *et al.*[65] and Schröder *et al.*[38], can be protonated to form a bridged hydride intermediate [(dppe)Ni(μ-pdt)(μ-H)Fe$(CO)_3]^+$ using HBF_4 (Figure 1.6.4, **a**) (pdt = propanedithiolato). These systems have also been prepared with different ligands such as triphenylphosphine and triphenylphosphite around the iron centre to yield [(dppe)Ni(μ-pdt)(μ-H)Fe$(PPh_3)(CO)_2]^+$ and [(dppe)Ni(μ-pdt)(μ-H)Fe$(P(OPh)_3)(CO)_2]^+$ respectively (Figure 1.6.4, **b** and **c**).[65, 79] These complexes are capable electrocatalysts for H_2 production in DCM with TFA (trifluoroacetic acid) acting as a proton source at approximately 1 V overpotential.[80] Complexes (1.6.4 **b** and **c**) are also able to turn over H_2 at lower overpotentials (0.26 to 0.43 V) in acetonitrile solution, however their stability is limited when compared to their solutions in DCM.[65]

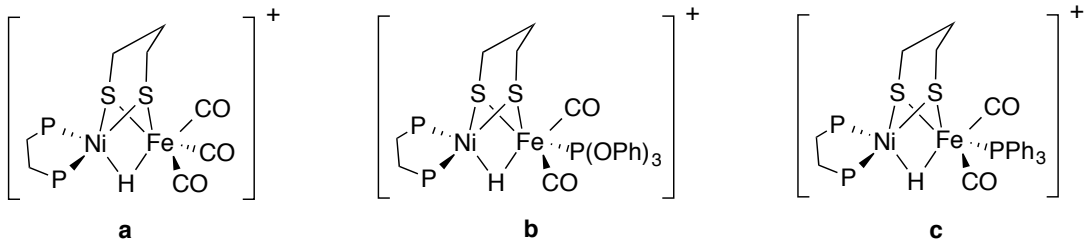


Figure 1.6.4: Functional analogues of the active sites of the [NiFe] hydrogenases based on a [(dppe)Ni(μ-pdt)Fe] core capable of forming bridging hydride intermediate species (dppe = 1,2-Bis(diphenylphosphino)ethane).

The overpotentials can be lowered through the substitution of the Fe atom in these systems for

Ru, and a large family of these [NiRu] analogues have been reported, some of which are capable electrocatalysts with respect to hydrogen production.[64] These systems incorporate a [Ni(xbsms)] core unit (xbsms = 1,2-bis(4-mercapto-3,3- dimethyl-2-thiabutyl)benzene) bound to a Ru centre with CO ligands that act as reporters for the electronic structure through spectroscopic study of the υ_{CO} stretch (Figure 1.6.5). These studies show that more electron-rich metal centres correlate with improved catalyst performance with up to a 200 mV improvement in overpotential and improved turnover rate overall.[81-83] Heterobimetallic [NiRu] complexes have also been reported by Ogo *et al*, using aromatic ligands bound to ruthenium to facilitate electron rich metal centres that can support a bridging hydride and that show potential as electrocatalysts (Figure 1.6.6).[84, 85] $[(Ni^{II}L)(H_2O)(\mu\text{-}H)Ru^{II}(\eta^6\text{-}C_6Me_6)](NO_3)$, where L = N,N′-dimethyl-N,N′- bis(2-mercaptoethyl)-1,3-propanediamine, is formed through the heterolytic cleavage of H_2 in aqueous solution under ambient conditions by the precursor $[(Ni^{II}L)Ru^{II}(H_2O)(\eta^6\text{-}C_6Me_6)](NO_3)$, demonstrating the robustness of this family of complexes.[85] $[(Ni^{II}L)Ru^{II}(H_2O)(\eta^6\text{-}C_6Me_6)](NO_3)$ has also demonstrated the ability to catalytically decompose formic acid to liberate H_2 and CO_2 gas.[86]

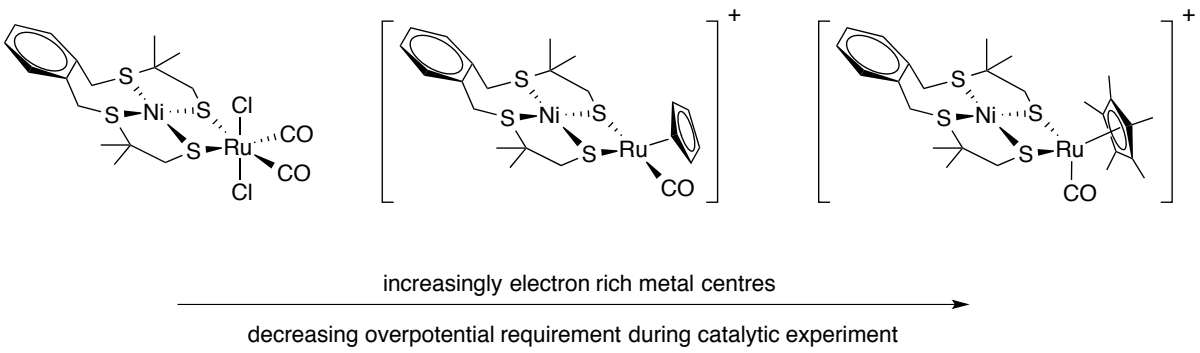


Figure 1.6.5: Successive [NiRu] systems synthesised by Artero et al demonstrating increasing electron density around the metal correlating with improved catalyst performance.[64, 83]

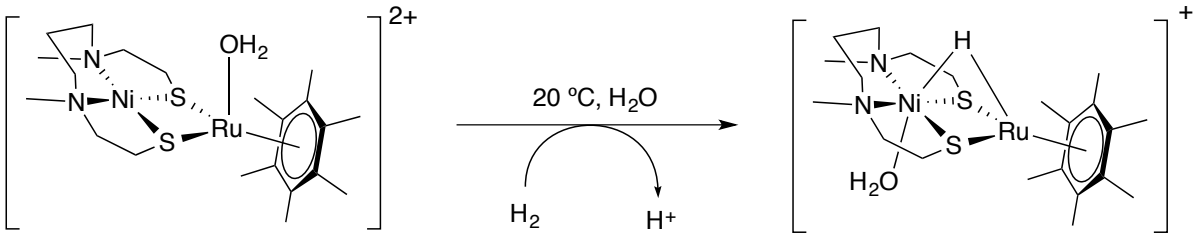


Figure 1.6.6: A [NiRu] complex reported by Ogo et. al. with high affinity for stabilising a bridging hydride moiety under mild aqueous conditions.[85]

In 2013 Ogo and coworkers published a [NiFe] analogue based around the Ni-(μS_2)-Fe bridged thiolate core featuring an Ni unit bound by the ligand N,N'-diethyl-3,7-diazanonane-1,9-dithiol (N_2S_2) bound to an Fe centre that completes its coordination sphere with four triethylphosphite ligands. However, on reduction of the system with $NaBH_4$ and precipitation with $NaBPh_4$ from acetonitrile solution, the compound $[Ni(N_2S_2)Fe(MeCN)(P(OEt)_3)_3](BPh_4)_2$ was isolated with a highly labile MeCN ligand terminally bound to the iron centre (Figure 1.6.7, **a**).[87]

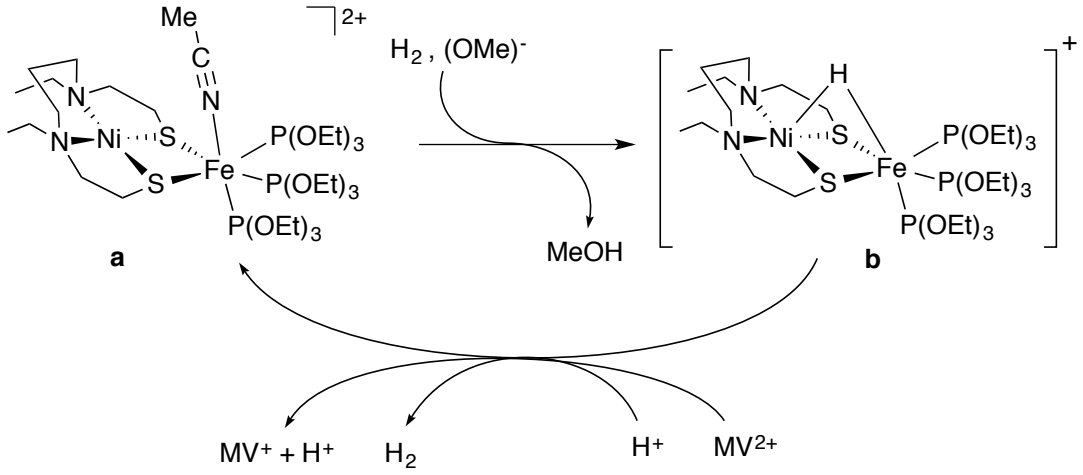
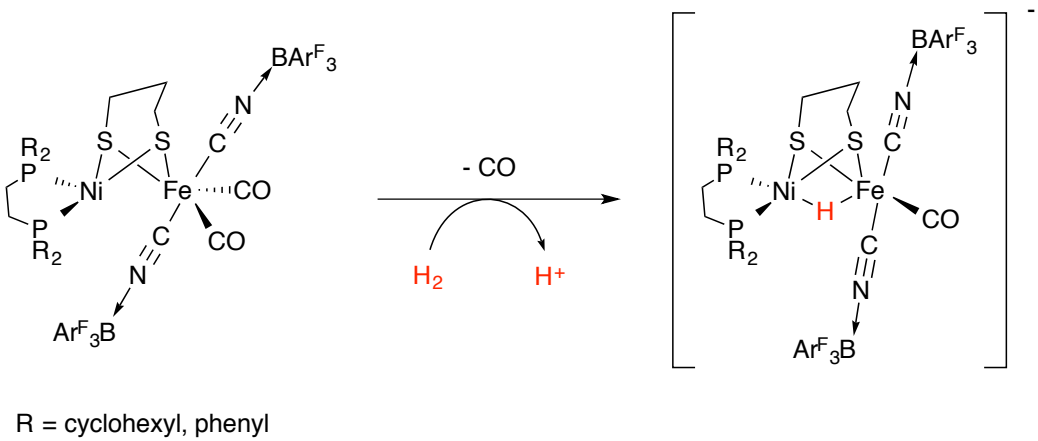


*Figure 1.6.7: Heterolytic activation of H_2 in basic conditions by $[Ni(N_2S_2)Fe(MeCN)(P(OEt)_3)_3]^{2+}$ (**a**) to yield the reducing hydride bridged system $[Ni(N_2S_2)Fe(H)(P(OEt)_3)_3]^{+}$ (**b**) that can reduce various substrates (shown here, methyl viologen, MV), or reduce protons to liberate H_2 and regenerate (**a**).*[87]

$[Ni(N_2S_2)Fe(MeCN)(P(OEt)_3)_3](BPh_4)_2$ may be being converted to a bridged hydride structure $[Ni(N_2S_2)Fe(H)(P(OEt)_3)_3]^{+}$ under an atmosphere of H_2 in basic solution (Figure 1.6.7, **b**) to

yield a complex demonstrating potent reducing power of various substrates through electron or hydride transfer. It also decomposes back to the $[Ni(N_2S_2)Fe(MeCN)(P(OEt)_3)_3]^{2+}$ complex in acidic conditions, liberating hydrogen gas.[87] While $[Ni(N_2S_2)Fe(MeCN)(P(OEt)_3)_3]^{2+}$ is a compelling model for that of the active site of the [NiFe] hydrogenases and does show potential as an electrocatalyst for proton reduction, the solid state structure and other spectroscopic measurements of this system indicate that the hydride, and the redox chemistry, is primarily iron-based with the Fe-H distance (1.57(5) Å) being significantly shorter than the Ni-H distance (2.16(4) Å).[87, 88]

Rauchfuss and coworkers reported two complexes containing a Ni-(μS_2)-Fe motif based on a $[Ni(P_2S_2)]$ unit complexed with an Fe centre featuring mixed cyanide and carbon monoxide ligands.[89] These neutral compounds, $[(P_2R_2)Ni(pdt)Fe(CN)_2(CO)_2]$, ($P_2R_2$ = dppe (1,2-bis(diphenylphosphino)ethane), dcpe = (1,2-bis(dicyclohexylphosphino)ethane)), (pdt = propanedithiolato) contain Ni^{II} and Fe^{II} centres. To supress the basicity of the CN^- ligands,[90] and thus improve the stability of the complexes in acidic media while retaining their anionic nature, they were protected through the use of the bulky organoborane $B(C_6F_5)_3$, commonly abbreviated as (BAr^F_3), to effectively create a 'masked cyanide' that retains the desirable features, such as the potent π acceptor and donator properties, while limiting some of the disadvantages. $[(P_2R_2)Ni(pdt)Fe(CN\text{-}BAr^F_3)_2(CO)_2]$ (Figure 1.6.8), reacts with H_2 after decarbonylation to yield the Ni-(H)-Fe hydrido derivatives and subsequently release H_2 upon treatment with strong acids.



R = cyclohexyl, phenyl

Figure 1.6.8: Novel structural [NiFe] hydrogenase analogues capable of activating hydrogen featuring oganoborane-masked cyanides (BAr^F_3 = $B(C_6F_5)_3$), (R = cyclohexyl, phenyl) reported by Rauchfuss et al.[89]

The use of these protected cyanide groups in this family of complexes could offer a route to modulating the electron density around the metal centres through the use of other functionalised CN ligands. For example, the isocyanide (also known as isonitrile) functional group (R-NC) is effectively a masked cyanide, acting as a π-donor and π-acceptor ligand in organometallic chemistry with comparable properties to the CN^- ligand group, while also possessing a functionality that may be employed to tune the nature of the metal-ligand interaction through the variation of the R group bound to the N atom within the ligand. The variation of R may affect the strength of the CN bond and the subsequent orbital interaction with the metal centre.[31] This effect can be investigated spectroscopically through FTIR techniques in a range of solvents; the υ_{CN} stretch may be observed around 2000-2200 cm^{-1} in acetonitrile.[91]

1.7 [NiFe] hydrogenase analogues featuring macrocycles and ligands with pendant arms

While the active site of the [NiFe] hydrogenases contains a heterobimetallic core that features a pseudo-octahedral Fe centre and a four coordinate Ni centre, it is also surrounded in close proximity by various protein residues that supplement the coordination environment. These residues can act as ligand donors and acceptors or as a sink or source for electrons as required.

For example, a proton channel near the Ni centre may serve as a temporary proton store[41] and the nearby [Fe-S] clusters provide a route for electron transfer to and from the active site.[47] These supporting components demonstrate that the active site does not function alone, being afforded stability during turnover by the wider structural features of the enzyme. These aspects have been considered in the syntheses of analogues, for example, through the incorporation of pendant arms that can act as a base, or as a temporary ligand to complete the coordination sphere of a metal centre.[72, 92, 93] These features can serve to confer stability for unusual geometries and oxidation states, and potentially to facilitate catalytic behaviour.

Tanase *et al* have synthesised a range of $[Ni^{II}Rh^{III}]$ complexes incorporating the functionalised macrocycle [RTACN-S_2] (RTACN = 1,4-bis(2-mercaptoethyl)-7-R-1,4,7-triazacyclononane (R = ^{i}Pr, Ts) of the type $[Ni(RTACN\text{-}S_2)RhCp^*Cl]^+$ (Figure 1.7.1, **a**).[93] These complexes are able to heterolytically activate H_2 in aqueous media to form bridged hydrido complexes, supporting a geometry change through a considerable contraction of the Ni-Rh distance (by approximately 0.5 Å) and through the increased coordination of the pendant amine to the Ni centre (Figure 1.7.1, **b**). The functionalisation of the pendant amine had a marked effect on the stability of the resulting hydrido complexes through a modulation of the Ni-NR distance. The substitution of the R group from tosyl to ^{i}Pr, for example, decreases the Ni-N distance from 2.188(3) to 2.056(2) Å and results in a complex that is stable enough in aqueous solution to reduce benzaldehyde.

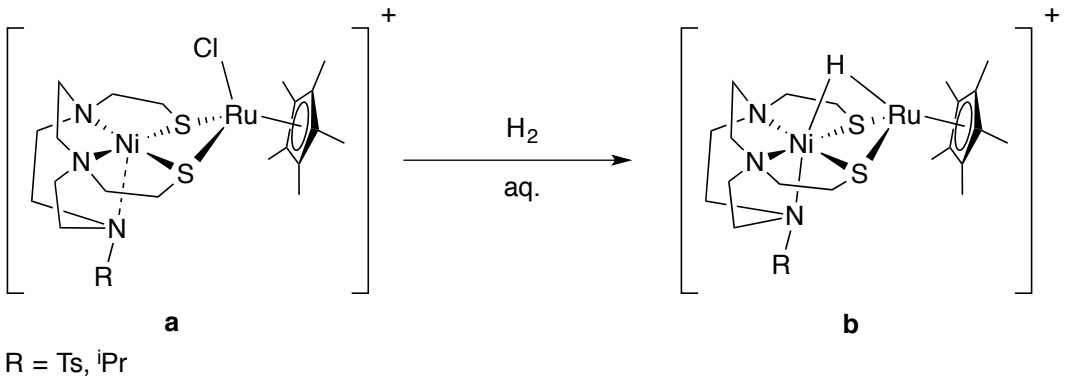
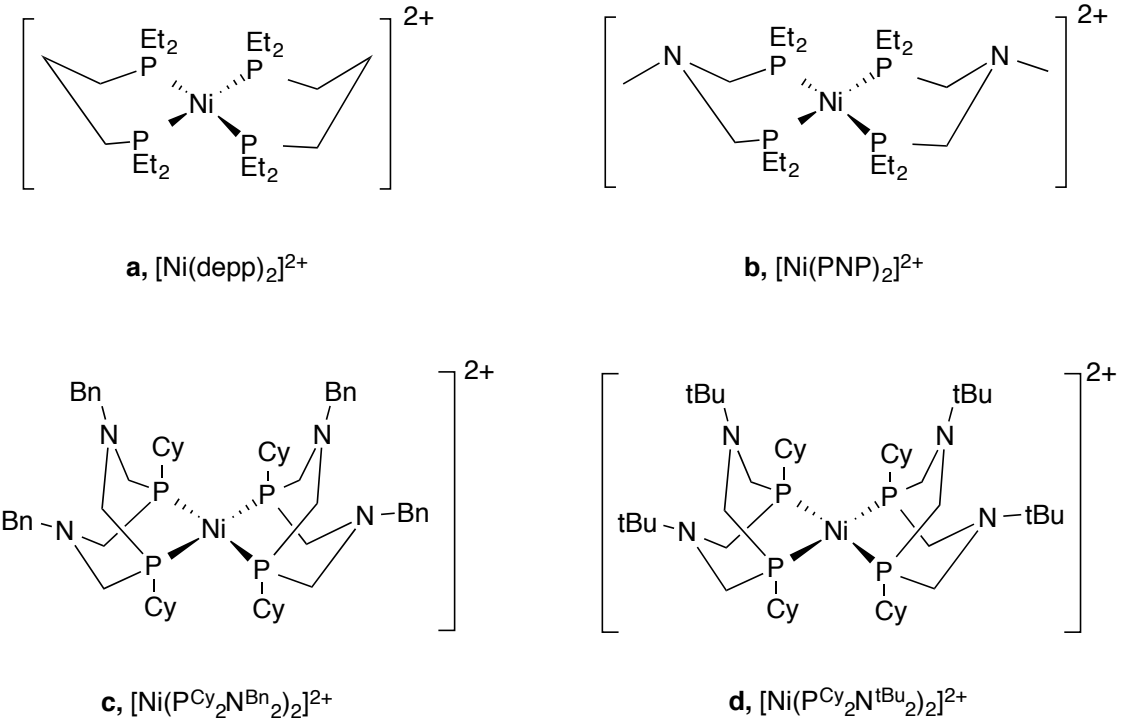


Figure 1.7.1: Hydride-bridged macrocylic [NiRh] complexes stabilised by a functionalised pendant amine reported by Tanase et al.[93]

Dubois and coworkers have published a series of mononuclear electrocatalysts with a [Ni(P_4)] coordination sphere that demonstrate the effect of pendant amines on catalytic performance.[94] The root system, $[Ni(depp)_2]^{2+}$, (depp = 1,3-bis(diethylphosphino)propane), (Figure 1.7.2, **a**) with no pendant amines is an electrocatalyst for H_2 oxidation under basic conditions (with NEt_3), but the reaction rate is slow (< 0.2 turnover per second).[94] However, the complex $[Ni(PNP)_2]^{2+}$ (PNP = $Et_2PCH_2N(Me)CH_2PEt_2$) (Figure 1.7.2, **b**) that incorporates a tertiary amine into the carbon backbone, is a more effective catalyst; while the turnover number was unchanged, electrocatalytic oxidation of H_2 occurs at a potential that is approximately 0.6 V lower than that observed for $[Ni(depp)_2]^{2+}$, approaching that of the $Ni^{II/I}$ couple in this solvent.[94, 95] In systems that position the pendant nitrogen with favourable geometry with respect to the metal centre,[96] and through tuning the basicity of the amine through the choice of attached functional group, it is possible to further improve the performance of these catalysts. For example, $[Ni(P^{Cy}_2N^{Bn}_2)_2]^{2+}$ ($P^{Cy}_2N^{Bn}_2$ = 1,5-dibenzyl-3,7- dicyclohexyl-1,5,3,7-diazadiphosphocane) and $[Ni(P^{Cy}_2N^{tBu}_2)_2]^{2+}$ ($P^{Cy}_2N^{tBu}_2$ = 1,5-di-t-butyl-3,7-dicyclohexyl-1,5,3,7-diazadiphosphocane) (Figure 1.7.2, **c**,**d**), exhibit turnover numbers of 10 and 50 TON s^{-1}, respectively.[95]

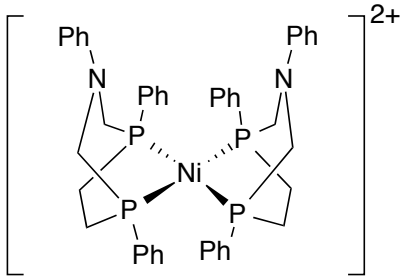


a, $[Ni(depp)_2]^{2+}$ **b,** $[Ni(PNP)_2]^{2+}$

c, $[Ni(P^{Cy}_2N^{Bn}_2)_2]^{2+}$ **d,** $[Ni(P^{Cy}_2N^{tBu}_2)_2]^{2+}$

Figure 1.7.2: Mononuclear Ni complexes with and without pendant bases that moderate their performance as H_2 electrocatalysts.[94]

This approach was refined by DuBois *et al* to synthesise an extremely potent H_2 electrocatalyst, $[Ni(P^{Ph}_2N^{Ph})2]^{2+}$ ($P^{Ph}_2N^{Ph}$ = 1,3,6-triphenyl-1-aza-3,6-diphosphacycloheptane) that exhibits a turnover frequency of over 33,000 TON s^{-1} in dry MeCN solution and up to 106,000 TON s^{-1} in the presence of 1.2 M of water at -1.13 V vs Fc^+/Fc (Figure 1.7.3).[97]



$[Ni(P^{Ph}_2N^{Ph})_2]^{2+}$

Figure 1.7.3 Macrocyclic Ni electrocatalyst $[Ni(P^{Ph}_2N^{Ph})2]^{2+}$ demonstrating high performance as an H_2 electrocatalyst.[97]

Bullock *et al* proposed a mononuclear Fe complex ligated by a macrocyclic diphosphine ligand and a functionalised Cp ring, $[Cp^{C6F5}Fe(P^{tBu}{}_2N^{Bn}{}_2)H]$ (Bn = benzyl), that uses a pendant base to facilitate heterolytic H_2 activation to generate an Fe-hydrido species (Figure 1.7.4, **d**). This process is catalytic, with the hydride undergoing intramolecular proton transfer to the pendant base upon oxidation. This is followed by the loss of the proton to a base in solution to regenerate the coordinatively unsaturated complex (Figure 1.7.4, **a**).[54, 72] This behaviour is similar to that proposed for the turnover of the [NiFe] hydrogenases where promixal basic residues may accept and donate protons as required by the active site.[48]

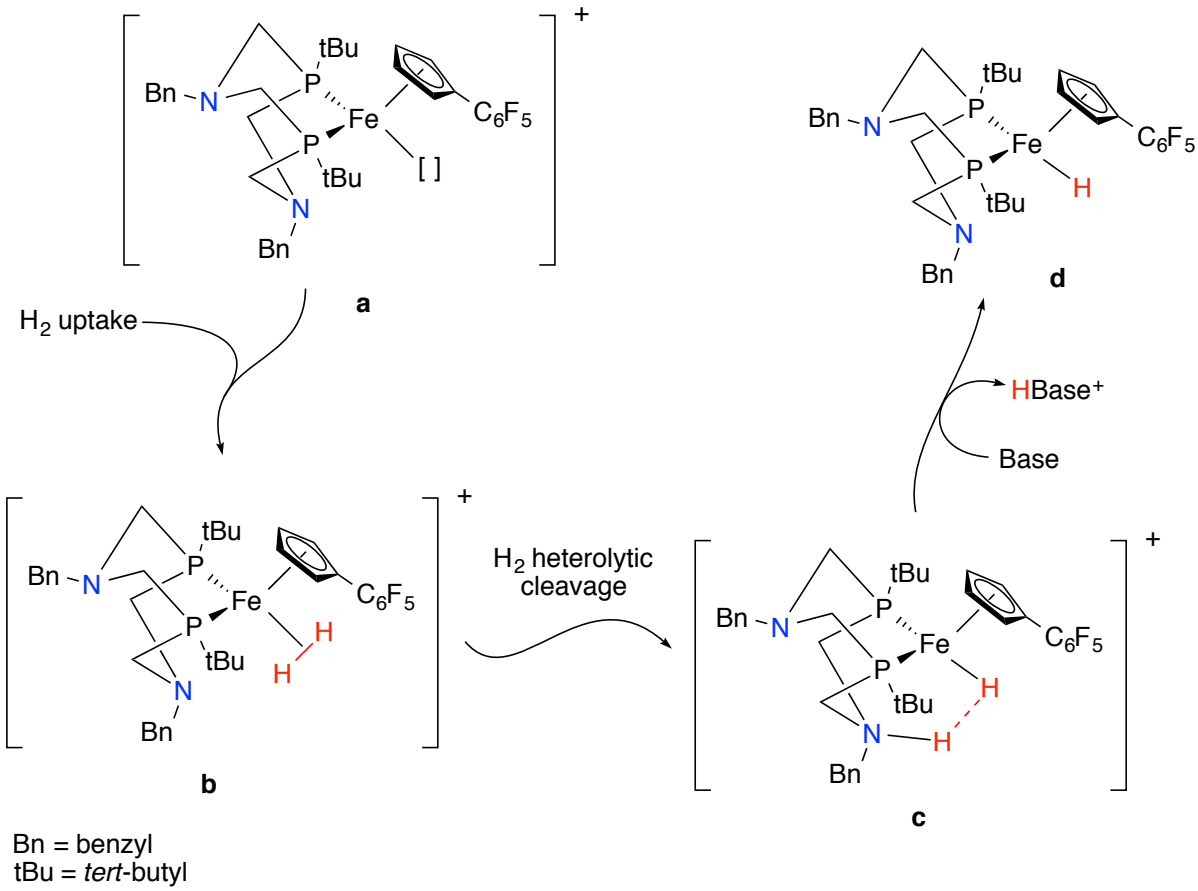


Figure 1.7.4: Ligation and subsequent heterolytic activation of H_2 by a macrocyclic mononuclear iron complex facilitated by a proximal pendant amine.[72]

Macrocyclic ligands have also been used to stabilise the unusual oxidation states of transition metals. For example, the macrocycles [9]aneS_3, (1,4,7-trithiacyclononane), [9]aneNS_2-CH_3, (N- methyl-1-aza-4,7-dithiacyclononane) and [9]aneNS_2-C_2H_4, (1,2-bis-(1-aza-4,7-dithiacyclononylethane) have been used to prepare the corresponding Ni^{II} complexes $[Ni([9]aneS_3)]^{2+}$, $[Ni([9]aneNS_2\text{-}CH_3)]^{2+}$ and $[Ni([9]aneNS_2\text{-}C_2H_4)]^{2+}$, which have been electrochemically oxidised to yield stable Ni^{III} species (Figure 1.7.5). These Ni^{III} complexes have been isolated and characterised by XRD and EPR studies.[98] The isolation of these pseudo-octahedral systems demonstrate a potential approach to accessing and stabilising the Ni^{I} and Ni^{III} states that have been proposed in the catalytic cycle of the [NiFe] hydrogenases (Figure 1.4.3).[35, 48] The structural characterisation of these macrocyclic complexes also demonstrate that these ligands possess conformational flexibility and thus can react to changes in oxidation state of the metal centre. For example, the axial Ni-S bond distances in $[Ni([9]aneNS_2\text{-}C_2H_2)]^{2+}$ are longer (2.435(8) Å) than the oxidised form $[Ni([9]aneNS_2\text{-}C_2H_2)]^{3+}$, (2.3982(2) Å) due to the reduced electron density of the Ni^{III} centre,[98] in spite of the expected axial lengthening that might be expected from the Jahn-Teller effect.[31]

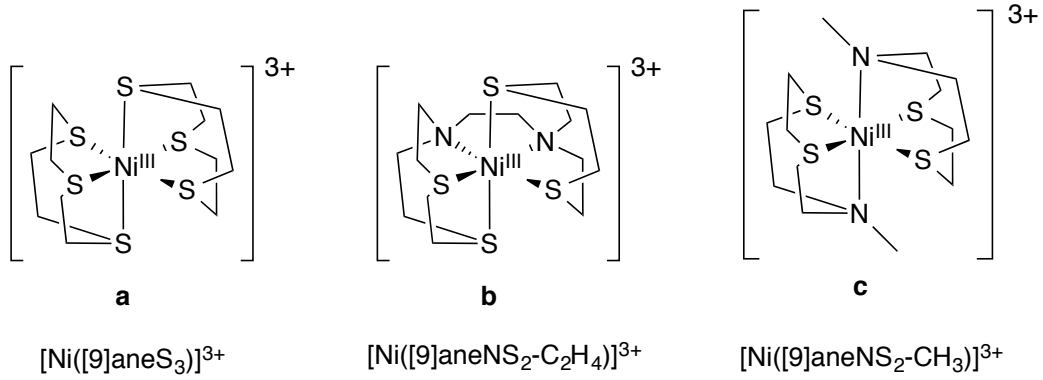


Figure 1.7.5: Macrocyclic complexes featuring thioether and amine functional groups affording a stable Ni^{III} oxidation state published by Schröder et al.[98]

This weaker thioether coordination at the apical position is also observed in other coordinatively unsaturated systems,[99] for example, in the five-coordinate [Ni(DSP)I_2] complex (DSP = bis(*o*-methylthiophenyl)phenylphosphine) (Figure 1.7.6), which adopts a square-based pyramidal geometry with a virtually square planar Ni[I_2SP] base and an axial thioether with a considerably longer Ni-S distance (2.789 Å) than that found for the equatorial Ni-S bond (2.189 Å).[100]

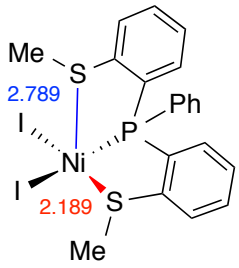


Figure 1.7.6: Five coordinate square-based pyramidal nickel complex [Ni(DSP)I_2] demonstrating conformational flexibility of thioether donors in otherwise symmetrical tridentate DSP ligand (Measurements in Å, from XRD structure).[100]

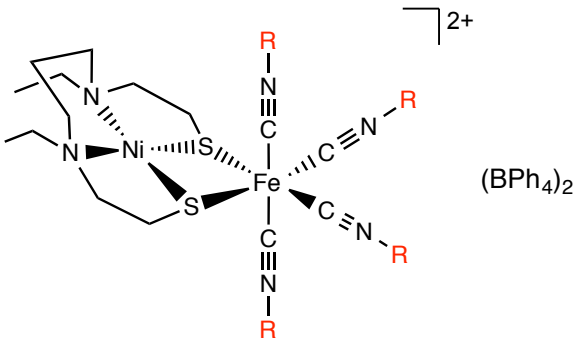
These examples demonstrate the potential for the use of functionalised macrocyclic ligands to participate in the completion of a metal coordination sphere, affording a captive, labile ligand under redox conditions that may allow for the ability to access particular oxidation states or to stabilise the often unusual geometry of unstable intermediate states.

1.8 Aims of this Work

Inspite of the recent advances in the syntheses and characterization of small molecule analogues of the active sites of the [NiFe] hydrogenases, key aspects of the nature of the [NiFe] hydrogenases have not been replicated. In particular, complexes possessing a [$Ni^{III}Fe^{II}$] electronic configuration, characteristic of the Ni-C, Ni-SI, Ni-A and Ni-B states[56, 101] and [$Ni^{I}Fe^{II}$], characteristic of the Ni-L state[55] have proven difficult to realize. The principal aim of

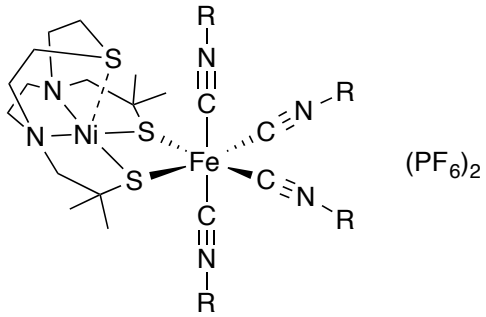
the work described in this thesis was therefore to attempt to synthesise and characterise $[Ni^{II}Fe^{II}]$ complexes as precursors to complexes exhibiting these unusual oxidation states. Particular emphasis has been placed on the influence of the variation of the coordination at the Fe centre on the electronic properties of the [NiFe] complexes where the use of isocyanide ligands with varying electronic and steric requirements have been used to modulate the electronic structure.

Chapter Two focusses on the synthesis and characterization of $[Ni(N_2S_2)Fe(R)_4]^{2+}$ complexes (R = varying isocyanides) (Figure 1.8.1). A key aspect of this study is the potential of $[Ni(N_2S_2)Fe(R)_4]^{2+}$ to support a reversible reduction process to yield $[Ni(N_2S_2)Fe(R)_4]^{+}$ as analogues of the Ni-L state of the [NiFe] hydrogenases.[102] Chapter Three focusses on the syntheses of $[Ni(N_2S_3)Fe(R)_4]^{2+}$ (R = ^{t}BuNC, benzyl-NC) (Figure 1.8.2) that contain a Ni centre coordinated by a macrocyclic N_2S_3 ligand system as a route to support a formal $Ni^{III/II}$ couple and as a framework to develop analogues of the Ni-C, Ni-SI, Ni-A and Ni-B states of the [NiFe] hydrogenases. We also report in Chapter Four a series of novel $[M(N_2S_2)]$ (M = Co, Pd, Zn) precursors and their reactions with $[Fe(CN^{t}Bu)_4]^{2+}$ to yield $[M^{II}Fe^{II}]$ (M = Co, Pd) heterobimetallic complexes with a view to the investigation of the impact of the substitution of the Ni centre in $[Ni(N_2S_2)Fe(R)_4]^{2+}$ on the electrochemistry of the complexes.



$[Ni(L1)Fe(CN\text{-}R)_4](BPh_4)_2$

Figure 1.8.1: General structure for complexes featured in Chapter Two. R = ^{t}Bu, ^{i}Pr, ^{n}Bu, cyclohexyl, benzyl, PhOMe, PhF.



$[Ni(L3)Fe(CN\text{-}R)_4](PF_6)_2$

Figure 1.8.2: General structure for complexes featured in Chapter Three. R = ^{t}Bu, benzyl.

A bio-mimetic approach may provide an opportunity to develop new catalysts for the uptake and/or evolution of dihydrogen that may offer alternatives to those incorporating Pt. A number of synthetic $NiFe_2$ and Ni-only catalysts have been found to catalyze the reduction of protons to H_2, however, catalysis supported by synthetic heterodinuclear [NiFe] complexes has been little explored. Thus, assessments of the catalytic competencies of the complexes synthesised in Chapters Two and Three are also presented.

1.9 References

1. J. Conti, P. Holtberg and J. Diefenderfer, ed. U. D. o. Energy, Washington DC, 2016.
2. International Energy Agency, *Fossil Fuel Energy Consumption*, OECD, 2014.
3. International Energy Agency, *Prospects for hydrogen and fuel cells*, IEA Publications, Paris, France, 2005.
4. U.S. Energy Information Administration, US Department of Energy, Washington DC, USA, 2016.
5. R. Cammack, M. Frey, R. Robson, R. Cammack, M. Frey and R. Robson, *Hydrogen as a Fuel : Learning from Nature*, Taylor & Francis, London; New York, 2001.
6. M. K. Debe, *Nature*, 2012, **486**, 43-51.
7. B. Schumm, in *Encyclopedia Britannica*, Encyclopedia Britannica, inc, Chicago, IL, 2010.
8. NASA, *Apollo Operations Handbook, Block II Spacecraft, SM2A-03-Block II-(1), SID 66-1508*, NASA, 1969.
9. B. J. Crowe, *Fuel Cells: A Survey*, Technology Utilization Office, NASA, Washington DC, 1973.
10. U. Eberle, B. Müller and R. von Helmolt, *Energy & Environmental Science*, 2012, **5**, 8780.
11. Ballard Power Systems Inc., Bend, Oregon, USA, 2017.
12. Alstom SA, Saint-Ouen, Cedex France, 2016.
13. G. Sandstede, E. J. Cairns, V. S. Bagotsky and K. Wiesener, in *Handbook of Fuel Cells*, 2010.
14. NASA Image Library, ed. AS15-88-11963, NASA, 1971.
15. J. D. Holladay, J. Hu, D. L. King and Y. Wang, *Catal. Today*, 2009, **139**, 244-260.
16. G. W. Crabtree, M. S. Dresselhaus and M. V. Buchanan, *Physics Today*, 2004, **57**, 39.
17. B. Rausch, M. D. Symes, G. Chisholm and L. Cronin, *Science*, 2014, **345**, 1326-1330.
18. J. A. Cracknell, K. A. Vincent and F. A. Armstrong, *Chem. Rev. (Washington, DC, U. S.)*, 2008, **108**, 2439-2461.
19. F. J. Edeskuty and W. F. Stewart, *Safety in the Handling of Cryogenic Fluids*, Plenum Press, New York, 1996.
20. Toyota Motor Corporation, 2017.
21. H. A. Bonges and A. C. Lusk, *Transportation Research Part A: Policy and Practice*, 2016, **83**, 63-73.
22. A. Mahmoudzadeh Andwari, A. Pesiridis, S. Rajoo, R. Martinez-Botas and V. Esfahanian, *Renewable and Sustainable Energy Reviews*, 2017, **78**, 414-430.
23. J. M. Berg, J. L. Tymoczko and L. Stryer, *Biochemistry*, 7th edn., W H Freeman, New York, 2011.
24. T. R. Ward, *Bio-inspired Catalysts*, Springer-Verlag Berlin Heidelberg, 2009.
25. J. C. Lewis, *ACS Catalysis*, 2013, **3**, 2954-2975.
26. L. Que, Jr. and W. B. Tolman, *Nature*, 2008, **455**, 333-340.
27. T. Bugg, *An introduction to enzyme and coenzyme chemistry*, Blackwell Science, Oxford, 1996.
28. D. R. Lide, *Handbook of Chemistry and Physics*, 81 edn., CRC Press, Boca Raton, Florida, 2000.
29. F. W. Larimer, P. Chain, L. Hauser, J. Lamerdin, S. Malfatti, L. Do, M. L. Land, D. A. Pelletier, J. T. Beatty, A. S. Lang, F. R. Tabita, J. L. Gibson, T. E. Hanson, C. Bobst, J. L. Torres, C. Peres, F. H. Harrison, J. Gibson and C. S. Harwood, *Nat. Biotechnol.*, 2004, **22**, 55-61.

30. F. Ullmann, W. Gerhartz and B. Elvers, *Ullmann's encyclopedia of industrial chemistry*, 5th completely rev. ed. / executive editor Wolfgang Gerhartz. Vol. A1-. edn., VCH, Weinheim, 1985.
31. P. W. Atkins, T. Overton, J. Rourke, M. Weller and F. A. Armstrong, *Shriver & Atkins' Inorganic Chemistry*, Oxford University Press, Oxford; New York, 2010.
32. J. Reglinski, S. Morris and D. E. Stevenson, *Polyhedron*, 2002, **21**, 2175-2182.
33. P. M. Vignais and B. Billoud, *Chem. Rev. (Washington, DC, U. S.)*, 2007, **107**, 4206-4272.
34. W. Lubitz, E. Reijerse and M. van Gastel, *Chem. Rev. (Washington, DC, U. S.)*, 2007, **107**, 4331-4365.
35. J. C. Fontecilla-Camps, A. Volbeda, C. Cavazza and Y. Nicolet, *Chem. Rev. (Washington, DC, U. S.)*, 2007, **107**, 4273-4303.
36. A. Volbeda, M. H. Charon, C. Piras, E. C. Hatchikian, M. Frey and J. C. Fontecilla-Camps, *Nature*, 1995, **373**, 580-587.
37. A. Volbeda and J. C. Fontecilla-Camps, *Dalton Trans.*, 2003, 4030-4038.
38. W. Zhu, A. C. Marr, Q. Wang, F. Neese, D. J. E. Spencer, A. J. Blake, P. A. Cooke, C. Wilson and M. Schröder, *Proc. Natl. Acad. Sci. U. S. A.*, 2005, **102**, 18280-18285.
39. D. M. Heinekey, *J. Organomet. Chem.*, 2009, **694**, 2671-2680.
40. A. Volbeda, E. Garcin, C. Piras, A. L. de Lacey, V. M. Fernandez, E. C. Hatchikian, M. Frey and J. C. Fontecilla-Camps, *J. Am. Chem. Soc.*, 1996, **118**, 12989-12996.
41. J. Fritsch, P. Scheerer, S. Frielingsdorf, S. Kroschinsky, B. Friedrich, O. Lenz and C. M. Spahn, *Nature*, 2011, **479**, 249-252.
42. S. Foerster, M. van Gastel, M. Brecht and W. Lubitz, *J. Biol. Inorg. Chem.*, 2005, **10**, 51-62.
43. Y. Nicolet, C. Piras, P. Legrand, C. E. Hatchikian and J. C. Fontecilla-Camps, *Structure*, 1999, **7**, 13-23.
44. H. R. Pershad, J. L. C. Duff, H. A. Heering, E. C. Duin, S. P. J. Albracht and F. A. Armstrong, *Biochemistry*, 1999, **38**, 8992-8999.
45. P. M. Vignais, B. Billoud and J. Meyer, *FEMS Microbiol. Rev.*, 2001, **25**, 455-501.
46. S. Canaguier, V. Artero and M. Fontecave, *Dalton Trans.*, 2008, 315.
47. W. Lubitz, H. Ogata, O. Rudiger and E. Reijerse, *Chem. Rev. (Washington, DC, U. S.)*, 2014, **114**, 4081-4148.
48. F. Dole, A. Fournel, V. Magro, E. C. Hatchikian, P. Bertrand and B. Guigliarelli, *Biochemistry*, 1997, **36**, 7847-7854.
49. J. C. Fontecilla-Camps, M. Frey, C. E. Hatchikian, A. Volbeda, E. Garcin and Y. Montet, *Pure Appl. Chem.*, 1998, **70**, 25-31.
50. S. Foerster, M. Stein, M. Brecht, H. Ogata, Y. Higuchi and W. Lubitz, *J. Am. Chem. Soc.*, 2003, **125**, 83-93.
51. S. P. J. Albracht, E. G. Graf and R. K. Thauer, *FEBS Lett.*, 1982, **140**, 311-313.
52. M. Teixeira, I. Moura, A. V. Xavier, B. H. Huynh, D. V. DerVartanian, H. D. Peck, J. LeGall and J. J. Moura, *J. Biol. Chem.*, 1985, **260**, 8942-8950.
53. Y. Higuchi, H. Ogata, K. Miki, N. Yasuoka and T. Yagi, *Structure*, 1999, **7**, 549-556.
54. T. R. Simmons and V. Artero, *Angew. Chemiw Intl. Ed.*, 2013, **52**, 6143-6145.
55. R. Hidalgo, P. A. Ash, A. J. Healy and K. A. Vincent, *Angew. Chemiw Intl. Ed.*, 2015, **54**, 7110-7113.
56. H. Ogata, W. Lubitz and Y. Higuchi, *Dalton Trans.*, 2009, 7577-7587.
57. V. Radu, S. Frielingsdorf, O. Lenz and L. J. Jeuken, *Chem Commun (Camb)*, 2016, **52**, 2632-2635.
58. P. A. Ash, Dalton 2016 Joint Interests Group Meeting, Warwick University, UK, 2016.

59. H. Tai, K. Nishikawa, M. Suzuki, Y. Higuchi and S. Hirota, *Angew. Chemiw Intl. Ed.*, 2014, **53**, 13817-13820.
60. O. A. Ulloa, M. T. Huynh, C. P. Richers, J. A. Bertke, M. J. Nilges, S. Hammes-Schiffer and T. B. Rauchfuss, *J. Am. Chem. Soc.*, 2016, **138**, 9234-9245.
61. M. T. Madigan, J. M. Martinko and T. D. Brock, *Brock Biology of Microorganisms*, Pearson Prentice Hall, Upper Saddle River, NJ, 2006.
62. M. Schallmey, A. Singh and O. P. Ward, *Can. J. Microbiol.*, 2004, **50**, 1-17.
63. Y. Shomura, K. S. Yoon, H. Nishihara and Y. Higuchi, *Nature*, 2011, **479**, 253-256.
64. T. R. Simmons, G. Berggren, M. Bacchi, M. Fontecave and V. Artero, *Coord. Chem. Rev.*, 2014, **270-271**, 127-150.
65. B. E. Barton and T. B. Rauchfuss, *J. Am. Chem. Soc.*, 2010, **132**, 14877-14885.
66. H. Ahmad, S. K. Kamarudin, L. J. Minggu and M. Kassim, *Renewable and Sustainable Energy Reviews*, 2015, **43**, 599-610.
67. S. Ogo, *Chem. Commun. (Cambridge, U. K.)*, 2009, 3317-3325.
68. L. Gan, T. L. Groy, P. Tarakeshwar, S. K. Mazinani, J. Shearer, V. Mujica and A. K. Jones, *J. Am. Chem. Soc.*, 2015, **137**, 1109-1115.
69. A. Jablonskyte, J. A. Wright, S. A. Fairhurst, J. N. Peck, S. K. Ibrahim, V. S. Oganesyan and C. J. Pickett, *J. Am. Chem. Soc.*, 2011, **133**, 18606-18609.
70. N. Kaeffer, M. Chavarot-Kerlidou and V. Artero, *Acc. Chem. Res.*, 2015, **48**, 1286-1295.
71. D. L. DuBois, *Inorg. Chem.*, 2014, **53**, 3935-3960.
72. T. Liu, D. L. Dubois and R. M. Bullock, *Nature Chem.*, 2013, **5**, 228-233.
73. D. Brazzolotto, M. Gennari, N. Queyriaux, T. R. Simmons, J. Pecaut, S. Demeshko, F. Meyer, M. Orio, V. Artero and C. Duboc, *Nature Chem.*, 2016, **8**, 1054-1060.
74. C.-H. Lai, J. H. Reibenspies and M. Y. Darensbourg, *Angew. Chemiw Intl. Ed.*, 1996, **35**, 2390-2393.
75. M. Ito, M. Kotera, Y. Song, T. Matsumoto and K. Tatsumi, *Inorg. Chem.*, 2009, **48**, 1250-1256.
76. C. Tard and C. J. Pickett, *Chem. Rev. (Washington, DC, U. S.)*, 2009, **109**, 2245-2274.
77. Z. Li, Y. Ohki and K. Tatsumi, *J. Am. Chem. Soc.*, 2005, **127**, 8950-8951.
78. A. Perra, E. S. Davies, J. R. Hyde, Q. Wang, J. McMaster and M. Schroder, *Chem. Commun. (Cambridge, U. K.)*, 2006, 1103-1105.
79. B. E. Barton, C. M. Whaley, T. B. Rauchfuss and D. L. Gray, *J. Am. Chem. Soc.*, 2009, **131**, 6942-6943.
80. S. Canaguier, M. Field, Y. Oudart, J. Pecaut, M. Fontecave and V. Artero, *Chem Commun (Camb)*, 2010, **46**, 5876-5878.
81. J. A. W. Verhagen, D. D. Ellis, M. Lutz, A. L. Spek and E. Bouwman, *Dalton Trans.*, 2002, 1275-1280.
82. S. Canaguier, M. Fontecave and V. Artero, *Eur. J. Inorg. Chem.*, 2011, **2011**, 1094-1099.
83. Y. Oudart, V. Artero, J. Pecaut and M. Fontecave, *Inorg. Chem.*, 2006, **45**, 4334-4336.
84. T. Matsumoto, B. Kure and S. Ogo, *Chem. Lett.*, 2008, **37**, 970-971.
85. S. Ogo, R. Kabe, K. Uehara, B. Kure, T. Nishimura, S. C. Menon, R. Harada, S. Fukuzumi, Y. Higuchi, T. Ohhara, T. Tamada and R. Kuroki, *Science*, 2007, **316**, 585-587.
86. N. T. Nguyen, Y. Mori, T. Matsumoto, T. Yatabe, R. Kabe, H. Nakai, K. S. Yoon and S. Ogo, *Chem. Commun. (Cambridge, U. K.)*, 2014, **50**, 13385-13387.
87. S. Ogo, K. Ichikawa, T. Kishima, T. Matsumoto, H. Nakai, K. Kusaka and T. Ohhara, *Science*, 2013, **339**, 682-684.

88. C. R. Groom, I. J. Bruno, M. P. Lightfoot and S. C. Ward, *Acta Crystallogr. B*, 2016, **72**, 171-179.
89. B. C. Manor and T. B. Rauchfuss, *J. Am. Chem. Soc.*, 2013, **135**, 11895-11900.
90. A. Jablonskyte, J. A. Wright and C. J. Pickett, *Dalton Trans.*, 2010, **39**, 3026-3034.
91. A. Vogler, *Isonitrile Chemistry*, Academic Press, New York, 1971.
92. A. D. Wilson, R. H. Newell, M. J. McNevin, J. T. Muckerman, M. Rakowski DuBois and D. L. DuBois, *J. Am. Chem. Soc.*, 2006, **128**, 358-366.
93. B. Kure, A. Taniguchi, T. Nakajima and T. Tanase, *Organometallics*, 2012, **31**, 4791-4800.
94. C. J. Curtis, A. Miedaner, R. Ciancanelli, W. W. Ellis, B. C. Noll, M. Rakowski DuBois and D. L. DuBois, *Inorg. Chem.*, 2003, **42**, 216-227.
95. D. L. DuBois and R. M. Bullock, *Eur. J. Inorg. Chem.*, 2011, **2011**, 1017-1027.
96. Y. Nicolet, A. L. de Lacey, X. Vernède, V. M. Fernandez, E. C. Hatchikian and J. C. Fontecilla-Camps, *J. Am. Chem. Soc.*, 2001, **123**, 1596-1601.
97. M. L. Helm, M. P. Stewart, R. M. Bullock, M. R. DuBois and D. L. DuBois, *Science*, 2011, **333**, 863-866.
98. E. Stephen, D. Huang, J. L. Shaw, A. J. Blake, D. Collison, E. S. Davies, R. Edge, J. A. Howard, E. J. McInnes, C. Wilson, J. Wolowska, J. McMaster and M. Schroder, *Chem.--Eur. J.*, 2011, **17**, 10246-10258.
99. S. G. Murray and F. R. Hartley, *Chem. Rev. (Washington, DC, U. S.)*, 1981, **81**, 365-414.
100. D. W. Meek and J. A. Ibers, *Inorg. Chem.*, 1969, **8**, 1915-1920.
101. H. Ogata, K. Nishikawa and W. Lubitz, *Nature*, 2015, **520**, 571-574.
102. C. U. Perotto, G. Marshall, G. J. Jones, E. Stephen Davies, W. Lewis, J. McMaster and M. Schroder, *Chem. Commun. (Cambridge, U. K.)*, 2015, **51**, 16988-16991.

Chapter Two

Analogues of the Ni-L State of the [NiFe] Hydrogenase Active Site – Complexes that Access and Exploit the Ni^{I} Oxidation State

2.1 Introduction and aims

Three key states have been identified in a catalytic cycle of the [NiFe] hydrogenases (Figure 2.1.1): Ni-SI, Ni-R and Ni-C. [1, 2] Thus, H_2 reacts with Ni-SI and undergoes heterolytic cleavage to form Ni-R which contains a bridging H^- ligand. A co-ordinated Cys ligand may act as an initial proton acceptor for the accompanying proton before its transfer to other bases (B) about the active site. The removal of an electron generates the EPR active S = ½ Ni-C state, which can be converted to an EPR-active S = ½ $Ni^{I}Fe^{II}$ state (Ni-L) following the photolysis at low temperatures. Previously, Ni-L had not been viewed as being catalytically relevant given the conditions required for its formation. However, recent *in situ* IR spectroelectrochemical studies have demonstrated that the light-sensitive Ni-L state may be generated reversibly in the dark under turnover conditions. Therefore, the regeneration of the Ni-SI state could occur either directly from the Ni-C state, *via* the concerted transfer of an electron and a proton, or by oxidation of the Ni-L state.[3, 4] These studies open up the possibility that separate proton and electron transfer events may be associated with the regeneration of the Ni-SI state from Ni-C, and that these steps may involve the Ni-L state (Figure 2.1.1).

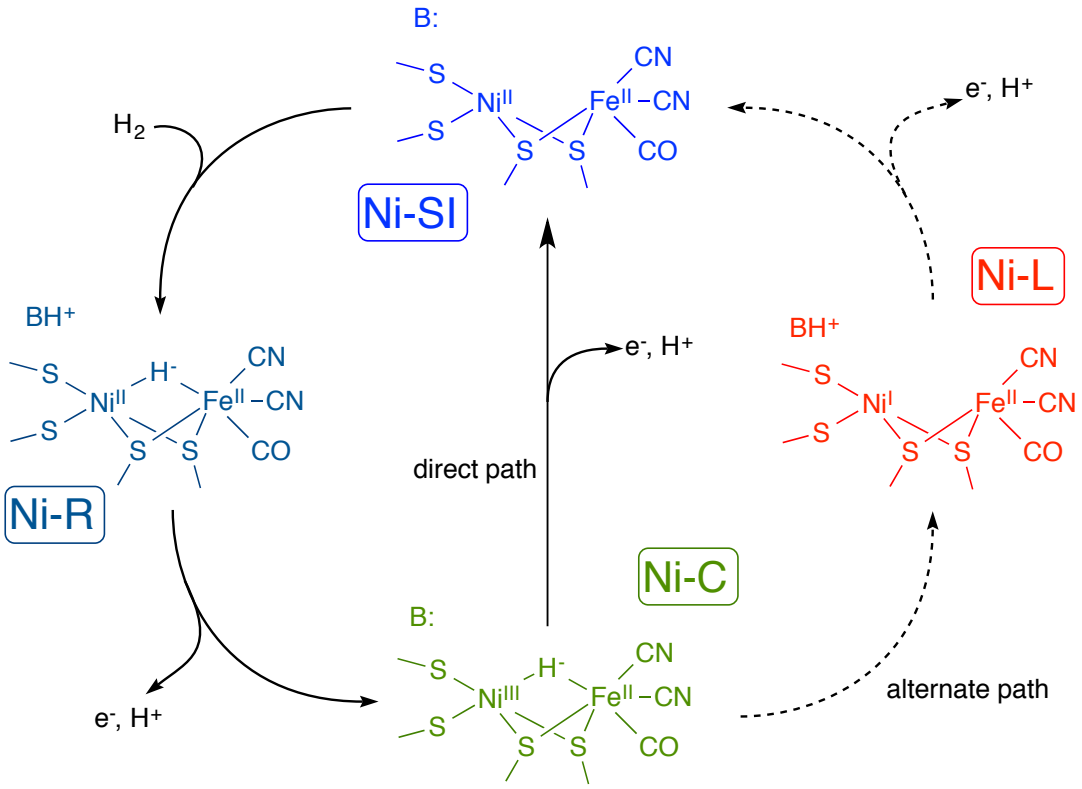


Figure 2.1.1: [NiFe] Hydrogenase active site configurations during cycle turnover featuring direct and alternate path involving Ni-L state, adapted from Hidalgo et al.[4]

Despite the large number of diamagnetic $Ni^{II}Fe^{II}$ complexes that have been prepared as analogues of the [NiFe] hydrogenases, the syntheses of complexes reproducing the $Ni^{I}Fe^{II}$ electronic configuration proposed for the Ni-L form of the [NiFe] hydrogenases has proven to be difficult. This chapter sets out to synthesise a range of [NiFe] structural analogues, based on a four-coordinate Ni moiety and a pseudo-octahedral iron centre bridged by two thiolate donors. The Ni precursor, [Ni(L1)] (Figure 2.1.2), possesses an $[N_2S_2]$ coordination sphere featuring two amine and two thiolato donors and our use of this precursor is inspired by previous work on similar complexes reported in the literature including $[Ni(N_2S_2)Fe(MeCN)(P(OEt)_3)_3](BPh_4)_2$ (Figure 2.1.3) and $[Ni(N_2S_2)_2]Ni$.[5-8]

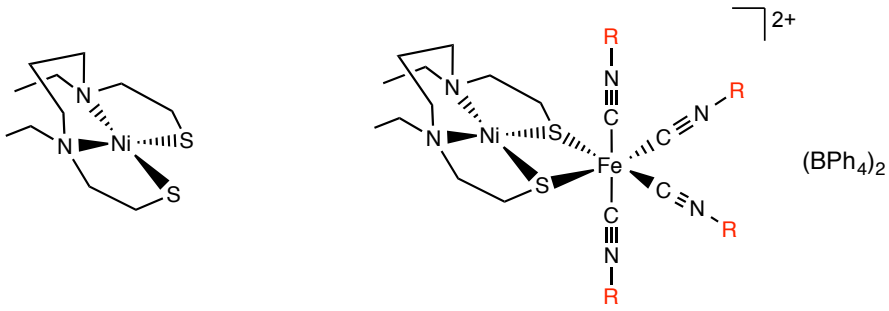


Figure 2.1.2:[Ni(L1)] precursor and [Ni(L^{1}N$_2$S$_2$)Fe(CN-R)$_4$](BPh$_4$)$_2$ general structure that forms the basis of the work in this chapter. R = ^{t}Bu, ^{i}Pr, ^{n}Bu, benzyl, cyclohexyl, 4-fluorophenyl, 4-methoxypehnyl.

An analogue of the active site of the [NiFe] hydrogenases that incorporates the [Ni(L1)] precursor [Ni(L1)Fe(MeCN)(P(OEt)$_3$)$_3$]$^{2+}$ has been reported as a proton reduction catalyst (Figure 2.1.3), however, the reduction of [Ni(L1)Fe(MeCN)(P(OEt)$_3$)$_3$]$^{2+}$ has been shown to be primarily Fe-based rather than centred on the Ni unit.[6] However, this complex has demonstrated the ability to replace the MeCN ligand with H$^-$ upon reduction to form a bridging structure between the Ni and Fe centres in solution and which has been verified in the solid state by X-ray crystallography.[6]

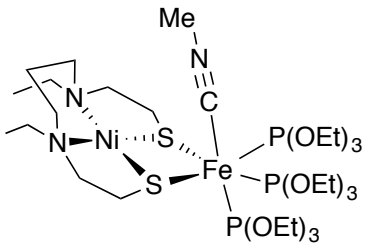


Figure 2.1.3: A Ni(L1)-based structural mimic of the [NiFe] hydrogenase enzyme that has shown promise as a proton reduction catalyst.[6]

The [Ni(L1)] unit has also been incorporated into binuclear complexes containing 4*d* transition metals that show promise for proton reduction (Figure 2.1.4). The complex

[(dppe)Ni(μ-pdt)Ru(cymene)] has been characterized as a $Ni^{I}Ru^{II}$ centre that shows a formal Ni^{I} centre can be isolated in a heterobimetallic complex.[9]

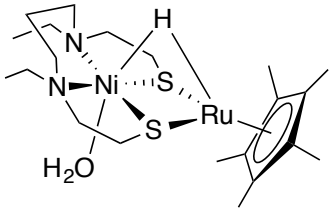


Figure 2.1.4: A novel [NiRu] complex that incorporates the [Ni(L1)] unit.[9]

Our proposed system features [Ni(L1)] bound to a $[Fe(CN\text{-}R)_4]^{2+}$ (R = ^{t}Bu, ^{i}Pr, ^{n}Bu, cyclohexyl, benzyl, 4-fluorophenyl, 4-methoxyphenyl) unit (Figure 2.1.2), which contains a similar Ni-(S_2)-Fe core that is found at the active sites of the [NiFe] hydrogenases. The Fe centre is co-ordinated by isocyanide ligands that provide a convenient spectroscopic handle and which serve as analogues of the CO and CN^- ligands bound to the Fe centre at the active site of the enzyme.[2] The isocyanides selected feature a range of terminal functional groups with the aim of tuning the electronic properties of the resulting [NiFe] complexes (Table 2.1.1) to modulate their catalytic activity.

A number of commercially-available isocyanides were selected as ligands, which were chosen for their varying steric and electronic properties (Table 2.1.1) and ease of handling. Most of these isocyanides are available as liquids, while the larger molecular weight reagents are viscous gels or solids and were used as solutions in MeCN.

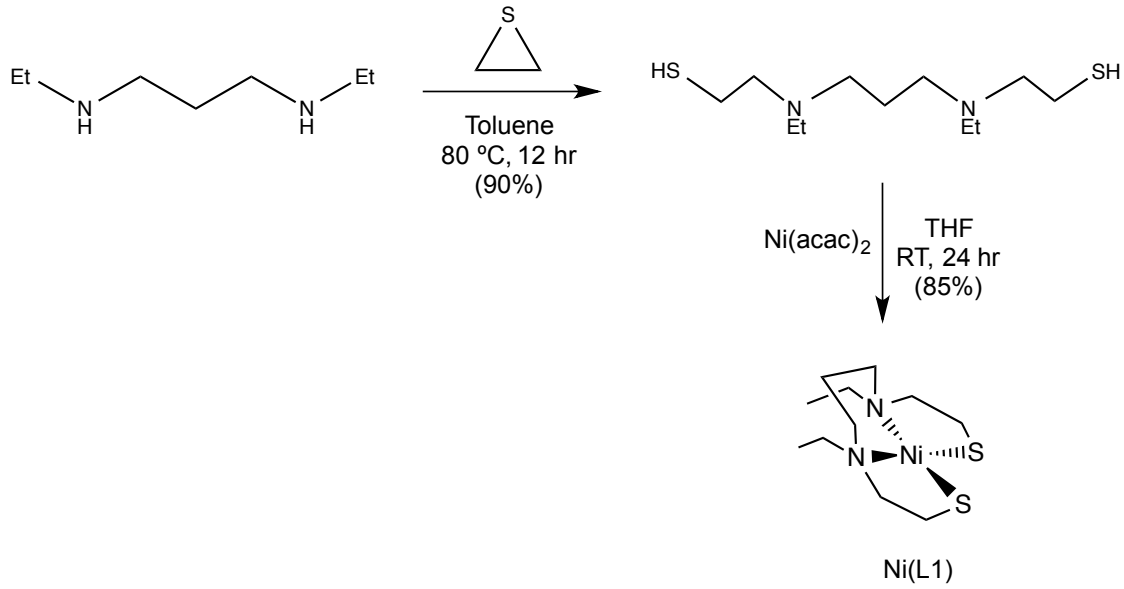
Table 2.1.1: Selected isocyanide ligands used in this chapter.

Isocyanide	**Label**
tert-butyl isocyanide	^{t}BuNC
n-butyl isocyanide	^{n}BuNC
cyclohexyl isocyanide	cyclohexyl-NC
benzyl isocyanide	benzyl-NC
isopropyl isocyanide	^{i}Pr-NC
4-methoxyphenyl isocyanide	PhOMe-NC
4-fluorophenyl isocyanide	PhF-NC
2-napthyl isocyanide	napthyl-NC

Results and Discussion

2.2 The synthesis of [Ni(L1)]

The ligand N,N'-diethyl-3,7-diazanonane-1,9-dithiol (H_2L1) was synthesised using a modified literature preparation[10] from the reaction of N,N-diethylpropane-1,3-diamine and ethylene sufide in toluene at 110 ºC for 12 hours. The resulting oil was reacted with $Ni(acac)_2$ in THF to yield [Ni(L1)] as a purple solid (Scheme 1).

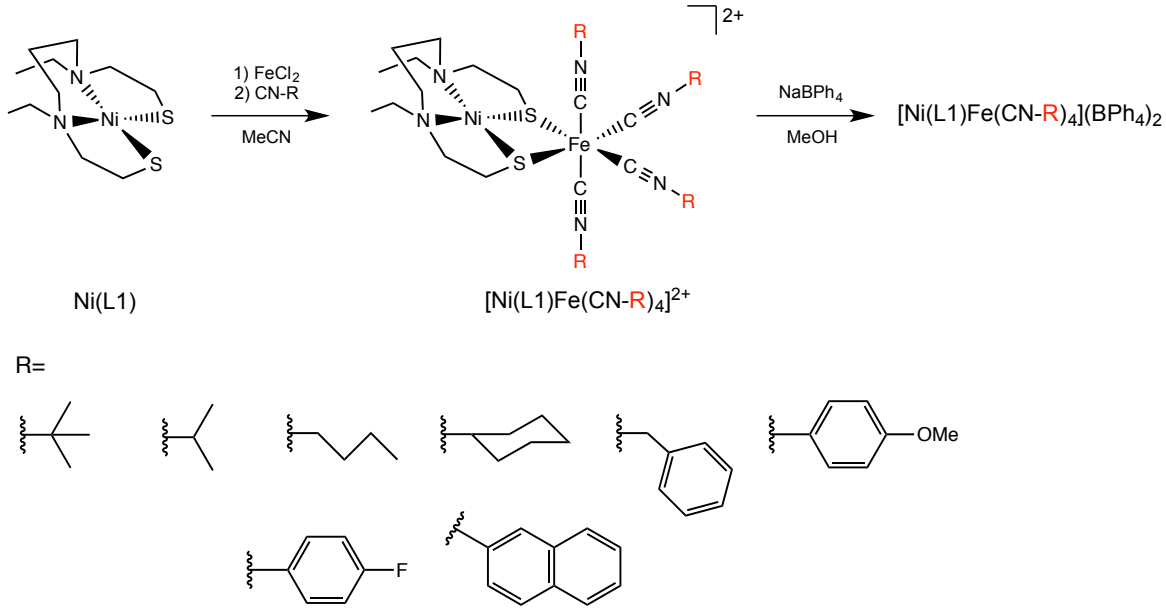


Scheme 1: Synthesis of the [Ni(L1)] precursor.

2.3 The syntheses of $[Ni(L1)Fe(R\text{-}NC)_4](BPh_4)_2$ systems (R = ^{t}Bu, ^{n}Bu, ^{i}Pr, benzyl, cyclohexyl, PhOMe, PhF, 2-naphthyl)

The synthetic approach for the syntheses of $[Ni(\mathbf{L1})Fe(R\text{-}NC)_4](BPh_4)_2$ was inspired by those employed for the preparation of $[Ni(N_2S_2)(MeCN)Fe(P(OEt)_3)_3]^{2+}$ and $[Fe(S_2C_6H_4)(CN)_2(CO)_2]^{2+}$ through the treatment of a precursor complex with an iron species and through complexation of these iron adducts with cyanide-type ligands.[6, 11] [Ni(**L1**)] reacts with $FeCl_2$ giving rise to an intermediate that is not isolated but reacts with four equivalents of the chosen isocyanide. The formation of the resulting complex is confirmed via mass

spectrometry (the mass spectrum of $[Ni(\mathbf{L1})Fe(^{t}BuNC)_4]^{2+}$ is shown in Figure 2.3.1) and is subsequently isolated as the $[BPh_4]^-$ salt by precipitation from a solution of the complex in methanol (Scheme 2) following the addition of four equivalents of $NaBPh_4$.



*Scheme 2: Synthesis of [Ni(**L1**)Fe(R-NC)$_4$](BPh$_4$)$_2$ complexes, R = tBu, iPr, nBu, cyclohexyl, benzyl, PhOMe, PhF, naphthyl.*

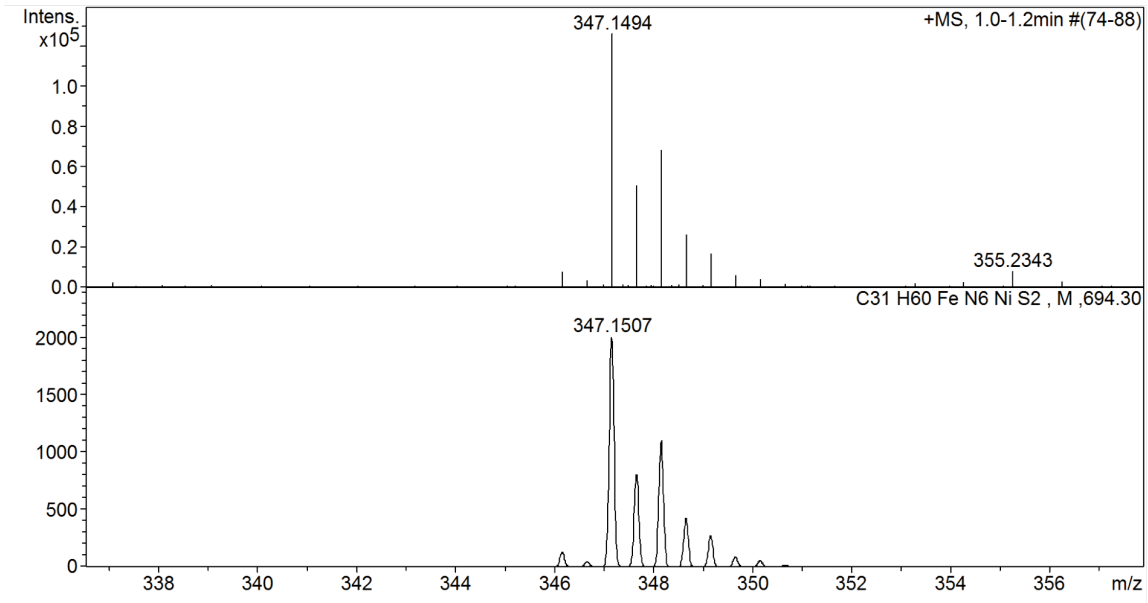


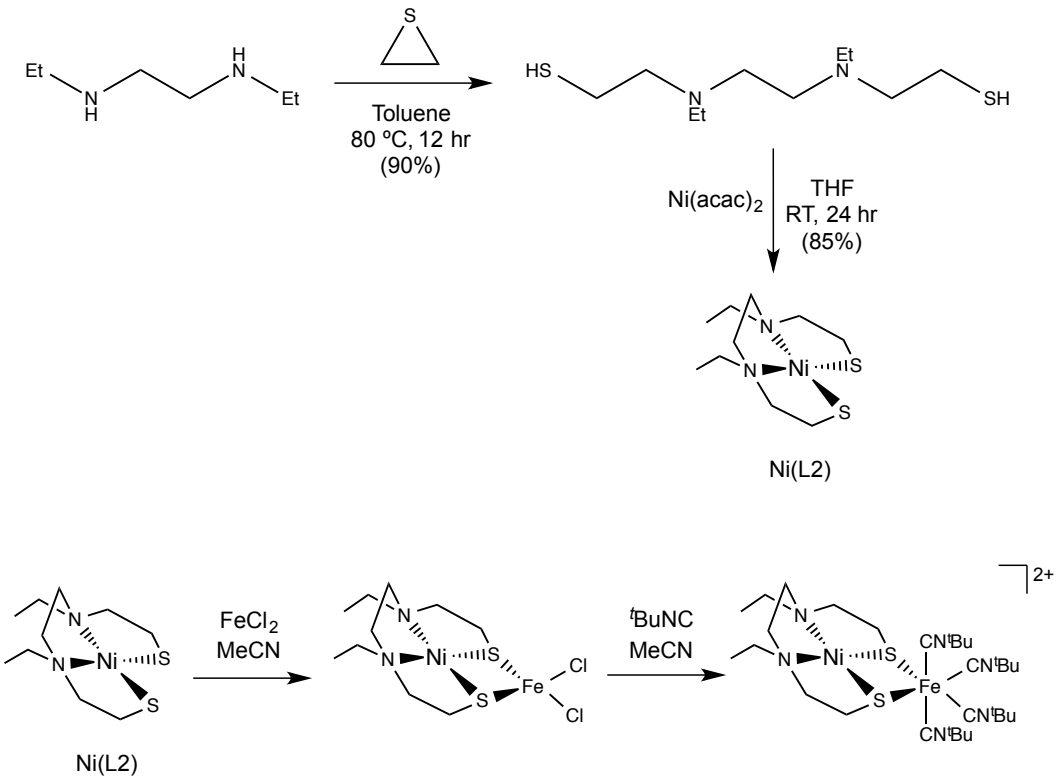
*Figure 2.3.1: Mass spectrometry (ESI-MS+) recorded isotope pattern (top) and simulated pattern (bottom) for [Ni(**L1**)Fe(^{t}BuNC)$_4$]$^{2+}$ confirming ligation of four equivalents of ^{t}BuNC to the [NiFe] intermediate in solution.*

These syntheses were successful for [Ni(**L1**)Fe(CN-R)$_4$](BPh$_4$)$_2$ for R = ^{t}Bu, ^{n}Bu, ^{i}Pr, benzyl, cyclohexyl, PhOMe, PhF. For R = 2-naphthyl, the isocyanide did not appear to react with the [NiFe] precursor. No evidence of the desired product was detected by mass spectrometry even after extended reaction times. This suggests that the 2-napththyl isocyanide ligand is too sterically demanding to form a stable [NiFe] complex. For R = PhF, [Ni(**L1**)Fe(CNPhF)$_4$](BPh$_4$)$_2$ was recovered in low yield (< 0.5 %) in sufficient quantities to determine the solid state structure through XRD experiments but not for further analyses.

2.4 Synthesis of [Ni(L2)Fe(^{t}BuNC)$_4$](BPh$_4$)$_2$

An alternative nickel precursor, [Ni(L2)][12] ([H$_2$L2] = 2,2'-(ethane-1,2-diylbis(ethylazanediyl))bis(ethane-1-thiol) that possesses an ethyl bridge between the ligating amine groups in place of the propyl bridge present in (H$_2$L1) was also synthesised to probe the effect of this change on the chemical behaviour. The reduction in the number of C atoms in the backbone of the chelating ligand affects the bite angle (S-Ni-S = 81.612(5) º and 85.14(3) º for [Ni(Lx), x = 1 and 2, respectively], which has the potential to affect the chemistry of the resulting [NiFe] complexes.[13] [Ni(L2)Fe(^{t}BuNC)$_4$](BPh$_4$)$_2$ was synthesised with this precursor (Scheme 3) for direct comparison with [Ni(L1)Fe(CN-R)$_4$](BPh$_4$)$_2$ (R = ^{t}Bu, ^{n}Bu, ^{i}Pr, benzyl, cyclohexyl, PhOMe, PhF).

Following the results of preliminary electrochemical studies on [Ni(L2)Fe(^{t}BuNC)$_4$](BPh$_4$)$_2$ that demonstrated no electrochemically reversible processes (*vide infra*), this avenue of study was not continued with the [Ni(L2)] precursor, and instead focussed solely on the more promising [Ni(L1)] systems.



Scheme 3: The syntheses of [Ni(L3)] and [Ni(L3)Fe(CN^{t}Bu)$_4$](BPh$_4$)$_2$.

2.5 Crystallography – Attempted Crystallisation of Ni(L1)-based complexes.

Attempts were made to grow crystals suitable for X-ray diffraction studies of [Ni(L1)Fe(R-NC)$_4$](BPh$_4$)$_2$ by vapour diffusion, liquid diffusion and evaporation techniques. However, the presence of a recurring decomposition product and its subsequent facile crystallisation complicated attempts to isolate crystals of [Ni(L1)Fe(R-NC)$_4$](BPh$_4$)$_2$. X-ray crystallography shows that the decomposition product, (Ni[Ni(L1)]$_2$)(BPh$_4$)$_2$, features two [Ni(L1)] subunits bridged via the thiolate donors to a third Ni atom. The decomposition and crystallization processes are facile in the presence of Fe in MeCN and DCM solutions and occur overnight yielding large brown crystals that crystallise in the *P*-1 space group. The decomposition process does not occur for pure solutions of [Ni(L1)] in MeCN or DCM that are left to stand overnight. (Ni[Ni(L1)])$^{2+}$ has been isolated as both the [BPh$_4$]$^-$ and [PF$_6$]$^-$ salts after attempts were made to substitute the anion as a potential route to discourage the formation

of $(Ni[Ni(L1)])^{2+}$. The structure of $(Ni[Ni(L1)])(BPh_4)_2$ is shown in Figure 2.5.1. An analysis of the crystals by ESI-MS confirms that the structure of $(Ni[Ni(L1)]_2)(BPh_4)_2$ contains three Ni atoms rather than a bridging Fe atom with the mass spectrum exhibiting a characteristic peak at *m/z* 336.0476 $[M^{2+}]$ with a confirmed isotope pattern. In this respect the formation of $(Ni[Ni(L1)])(BPh_4)_2$ is similar to the trinuclear Ni complexes synthesised by Tatsumi *et al.* upon treatment of [Ni(L1)] with $NiBr_2$.[8] Thus, it appears that Fe^{II} in solution may facilitate the formation of $(Ni[Ni(L1)])(BPh_4)_2$ through transmetellation of some [Ni(L1)] to [Fe(L1)], enabling subsequent free Ni^{2+} ions to combine with two units of [Ni(L1)] form the tri-nuclear complex.

The solid-state structure of the analogous $(Ni[Ni(L2)]_2)(PF_6)_2$ compound is shown in Figure 2.5.2. $[Ni(L2)Fe(^tBuNC)_4](PF_6)_2$ also decomposes readily to form crystals of $(Ni[Ni(L2)]_2)(PF_6)_2$ that crystallise in the $P2_1/n$ space group.

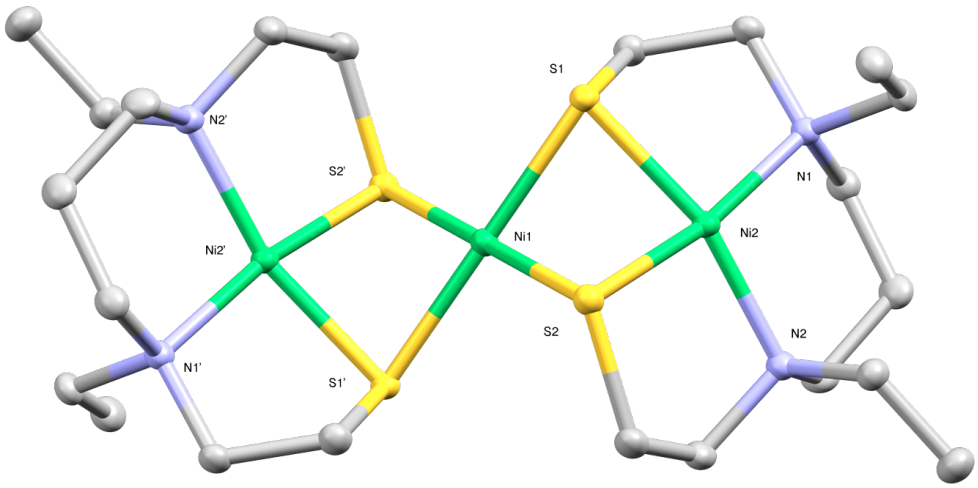


Figure 2.5.1: The X-ray crystal structure of the $(Ni[Ni(L1)]_2)^{2+}$ decomposition product with elipsoids at 50% probability. H atoms and $[BPh_4]^-$ anions omitted for clarity.

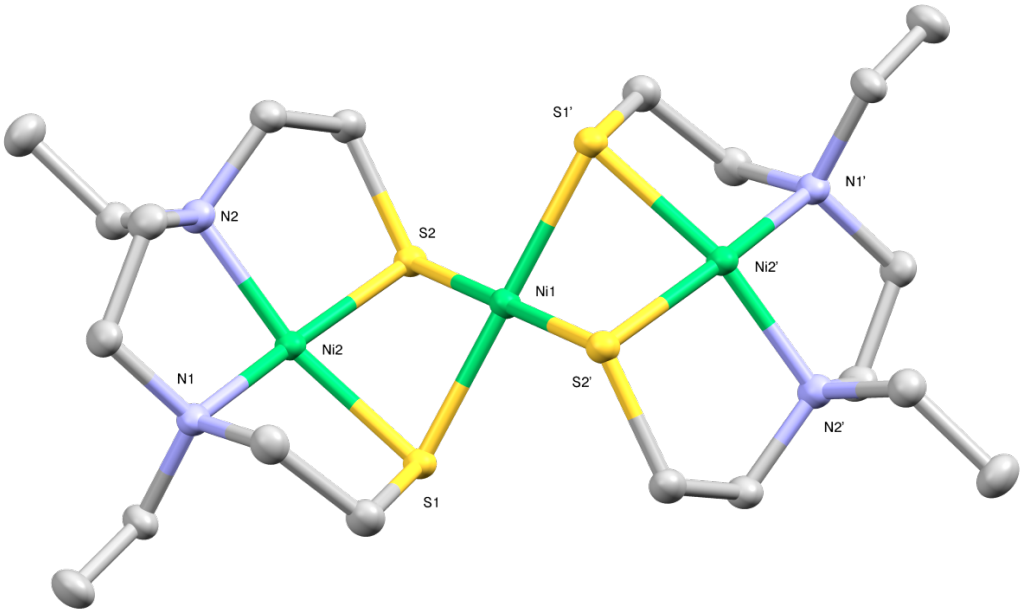


Figure 2.5.2: X-ray crystal structure of the $(Ni[Ni(L2)]_2)^{2+}$ decomposition product with elipsoids at 50% probability. H atoms and $[PF_6]^-$ anions omitted for clarity.

The S(1)-Ni(1)-S(2) bite angle and S(1)-S(2) distance is greater for the $[Ni(L2)Fe(^tBuNC)_4](PF_6)_2$ complex, (85.14(3) º and 2.9257(8) Å respectively) compared to $[[Ni(L1)]_2Ni]^{2+}$ (81.612(5) º and 2.82777(14) Å), reflecting the shorter carbon backbone acting to pinch the geometry around the Ni centre like a clothespin[13] that is also reflected in the respective Ni-N (ca. 1.95 Å vs ca. 2.0 Å) and Ni-S (ca. 2.16 Å vs ca. 2.2 Å) distances for Ni[Lx] x = 2, 1 respectively.

2.6 The X-ray crystal structure of $[Ni(L1)Fe(^tBuNC)_4](BPh_4)_2$

Crystals suitable for X-ray diffraction of $[Ni(L1)Fe(^tBuNC)_4](BPh4)_2$ were grown from a solution in MeCN layered with MeOH and crystallise in the triclinic *P*-1 space group. Selected bond lengths and angles are shown in Table 2.6.1 and the structure of $[Ni(L1)Fe(^tBuNC)_4]^{2+}$ is shown in Figure 2.6.1.

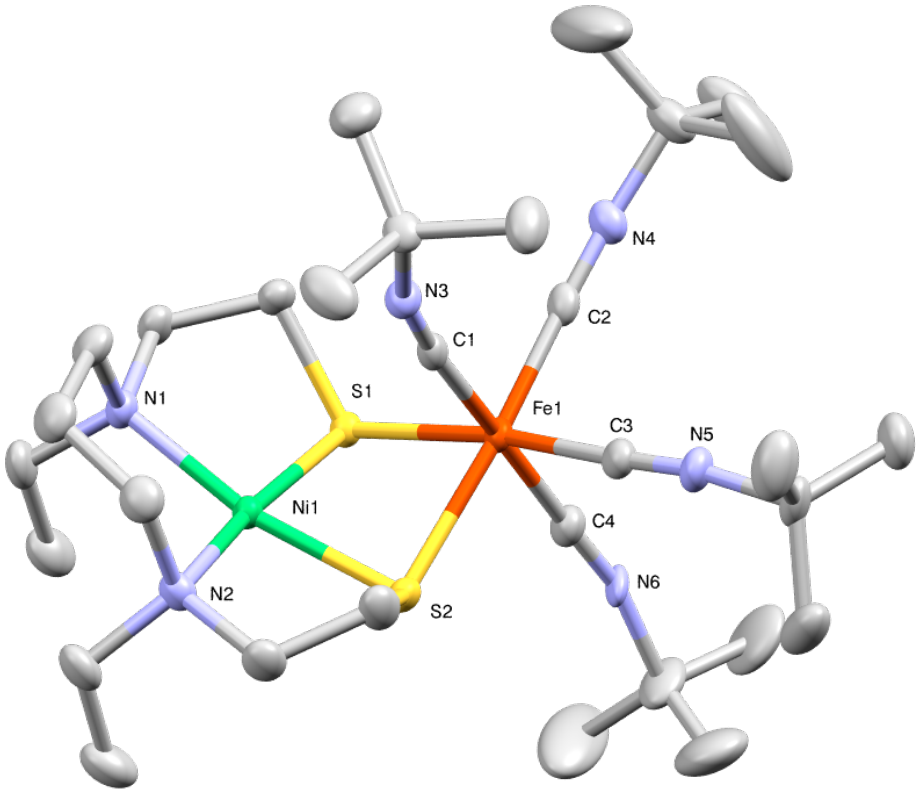


Figure 2.6.1: X-ray crystal structure of [Ni(L1)Fe(^{t}BuNC)$_4$](BPh$_4$)$_2$ with ellipsoids at 50% probability. H atoms and [BPh$_4$]$^-$ anions omitted for clarity.

Table 2.6.1: Selected bond lengths and angles for [Ni(L1)Fe(^{t}BuNC)$_4$](BPh$_4$)$_2$.

Bond	**Length /Å**	**Atoms**	**Angle /º**	**Atoms**	**Angle /º**
Ni(1)-N(1)	2.016(1)	N(1)-Ni(1)-N(2)	98.51(6)	S(1)-Fe(1)-S(2)	77.36(2)
Ni(1)-N(2)	2.034(1)	S(1)-Ni(1)-S(2)	83.17(2)	C(1)-Fe(1)-C(4)	174.77(7)
Ni(1)-S(1)	2.1722(5)	N(2)-Ni(1)-S(2)	88.76(4)	S(2)-Fe(1)-C(2)	175.19(5)
Ni(1)-S(2)	2.1684(5)	N(1)-Ni(1)-S(2)	88.69(4)	C(2)-Fe(1)-C(3)	89.36(7)
Fe(1)-S(1)	2.2958(6)	N(1)-Ni(1)-S(2)	168.75(4)	C(1)-N(3)-C(^{t}Bu)	162.38(15)
Fe(1)-S(2)	2.3140(5)	N(2)-Ni(1)-S(1)	170.24(4)		
Fe(1)-C(1)	1.888(1)	Ni(1)-S(1)-Fe(1)	90.28(2)	**Torsion**	**Angle /º**
Fe(1)-C(2)	1.857(2)	S(1)-Fe(1)-C(1)	94.79(5)	Ni(1)-S(1)-S(2)-Fe(1)	135.48(2)
Fe(1)-C(3)	1.858(2)	S(1)-Fe(1)-C(2)	97.87(5)		
Fe(1)-C(4)	1.889(1)	S(1)-Fe(1)-C(3)	172.55(6)		
Ni(1)-Fe(1)	3.1682(5)	S(1)-Fe(1)-C(4)	88.89(6)		

The Ni centre in [Ni(L1)Fe(^{t}BuNC)$_4$]$^{2+}$ adopts an approximate square-planar N_2S_2 co-ordination geometry with the Fe centre possessing a pseudo-octahedral co-ordination sphere comprised of four ^{t}BuNC ligands and two S donors derived from [Ni(L1)]. The Ni[N_2S_2]

fragment retains the structural features of the [Ni(L1)] precursor,[7] the most significant difference being a smaller S(1)-Ni(1)-S(2) angle [81.76(2)°] in [Ni(L1)] relative to that in $[Ni(L1)Fe(^{t}BuNC)_4]^{2+}$ [83.17(2)°]. This difference may reflect the steric demands of the co-ordinated $[Fe(CN^{t}Bu)_4]^{2+}$ fragment in $[Ni(L1)Fe(^{t}BuNC)_4]^{2+}$. The equatorial ^{t}BuNC ligands defined by C(2) and C(3) bind to Fe(1) in an essentially linear mode with C-N-C^{tBu} angles of 171.17(17) ° and 169.78(17) °, respectively. In contrast the axial ^{t}BuNC ligands, defined by C(1) and C(4), co-ordinate in a bent geometry with C-N-C^{tBu} angles of 162.38(15) º and 164.3(15) °, respectively. The Ni(1)-C(1) and Ni(1)-C(4) distances [3.1927(15) and 4.1379(16) Å, respectively] are significantly greater than the Fe(1)-C(1) and Fe(1)-C(4) distances [1.8875(15) and 1.8892(17) Å, respectively]. Thus, the axial ^{t}BuNC ligands do not appear to adopt bridging modes between the Ni and Fe centres in $[Ni(L1)Fe(^{t}BuNC)_4]^{2+}$. The Ni(1)-Fe(1) distance is 3.1682(5) Å which is slightly longer than the 2.9 Å distance between the metal centres found in the oxidised form of the enzyme observed in *D. gigas*.[14]

The X-ray crystal structure of $[Ni(L1)Fe(^{t}BuNC)_4]^{2+}$ provides a rationalization of the characteristic signals observed in the ^{1}H NMR of $[Ni(L1)Fe(^{t}BuNC)_4](BPh_4)_2$ for the methyl groups of the ^{t}Bu moieties, which provide a useful quantitative assay of the complex after purification. Using the ethyl groups attached to N(1) and N(2) as a reference, the terminal methyl protons result in a triplet that is assigned as 6 protons. The ^{t}Bu groups attached to nitrogen atoms labelled N(4), N(5) and N(6) give rise to a singlet in the ^{1}H spectrum at 1.49 ppm that integrates to 27 protons, while the ^{t}Bu group attached to N(3) generates a singlet at 1.81 ppm that integrates to 9 protons. This difference in chemical shift can be attributed to the axial position defined by N(3) being sterically crowded by the nearby [Ni(L1)] unit, which is not found at the other axial or the equatorial positions occupied by the other three isocyanide ligands about the Fe centre (Figure 2.6.2). The differing environments of the isocyanide ligands

is also reflected in the C-N-C^{tBu} angles (where C^{tBu} is the central carbon of the ^{t}Bu group) of the isocyanide ligand. For the equatorial isocyanide ligands defined by N(5) and N(6) C-N-C^{tBu} is essentially linear (C-N-C^{tBu} = 169.78(17) to 171.17(17) º) whereas for the isocyanide defined by atom N(3) C(1)-N(3)-C^{tBu} = 162.4(2) º. The other axial isocyanide (N(4)) demonstrates a slightly wider angle than the face crowded ligand (164.3(15) º, but still appears to be magnetically equivalent to the equatorial pair, suggesting that a through-space interaction may be partly responsible for the separation of the NMR signals of these four groups. Using this rationale it is also possible to assign the ^{1}H NMR spectra of $[Ni(L1)Fe(R\text{-}CN)_4](BPh_4)_2$ (R = ^{i}Pr, ^{n}Bu, cyclohexyl, benzyl, PhOMe) that exhibit analogous behaviour with three of the isocyanide ligands appearing chemically equivalent with the fourth demonstrating a downfield shift with the protons integrating in a 3:1 ratio.

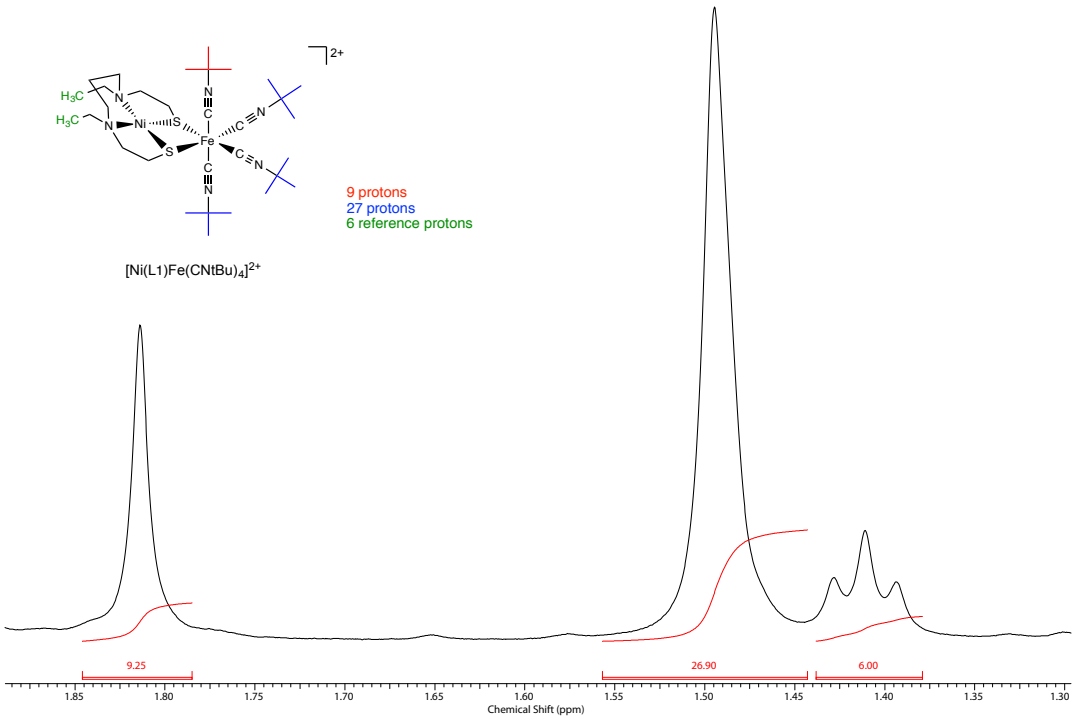


Figure 2.6.2: Detail of 400 MHz ^{1}H NMR spectrum in CD_3CN at 298 K demonstrating the characteristic singlets corresponding to the ^{t}Bu groups from the isocyanide ligands in $[Ni(L1)Fe(^{t}BuNC)_4](BPh4)_2$ and the terminal methyl triplet from the [Ni(L1)] ligand used as an integration reference.

2.7 Structures of [Ni(L1)Fe(R-NC)$_4$](BPh$_4$)$_2$, (R = ^{i}Pr, benzyl, cyclohexyl, PhOMe, PhF)

Crystals suitable for X-ray diffraction experiments were obtained for [Ni(L1)Fe(R-NC)$_4$](BPh$_4$)$_2$, (R = ^{i}Pr, benzyl, cyclohexyl, PhOMe, PhF) either by slow evaporation from MeOH solutions or via solution layering with MeOH on top of a solution of the complex in MeCN or MeNO$_2$. The structures of [Ni(L1)Fe(R-NC)$_4$](BPh$_4$)$_2$, (R = ^{i}Pr, benzyl, cyclohexyl, PhOMe, PhF) along with corresponding selected bond lengths and angles are shown in Figures 2.7.1 to 2.7.5 and Tables 2.7.1 to 2.7.5 .

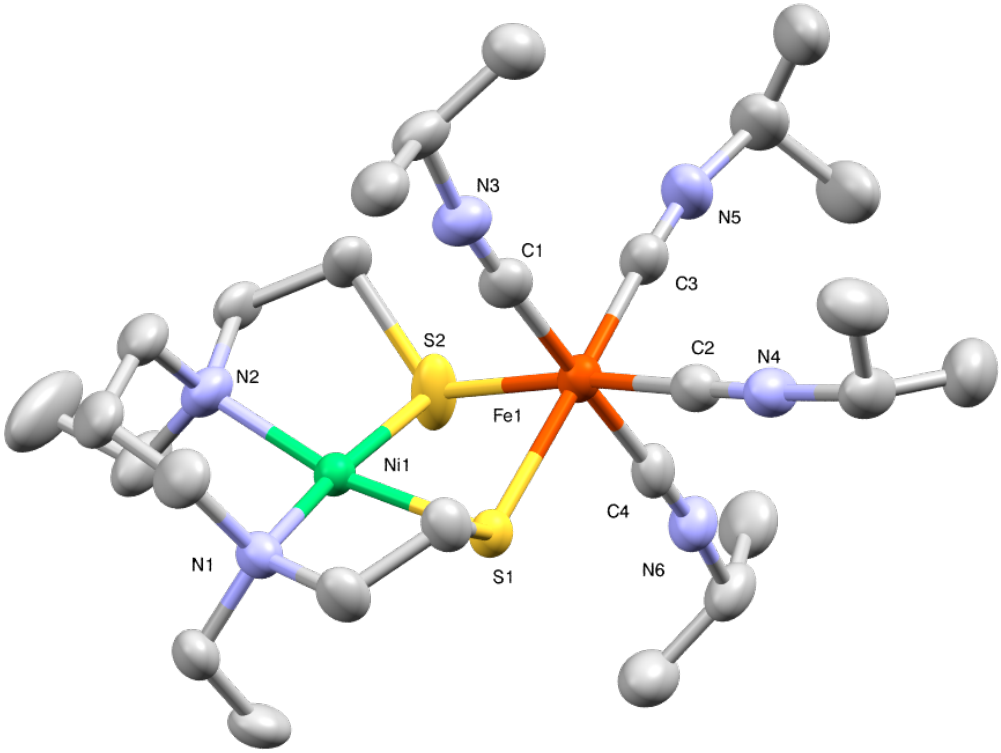


Figure 2.7.1: X-ray crystal structure of [Ni(L1)Fe(^{i}PrNC)$_4$](BPh$_4$)$_2$ with ellipsoids at 50% probability. H atoms and [BPh$_4$]$^-$ anions omitted for clarity.

[Ni(L1)Fe(^{i}PrNC)$_4$](BPh$_4$)$_2$ crystallises in *P*-1.

Table 2.7.1: Selected bond lengths and angles for [Ni(L1)Fe(^{i}PrNC)$_4$](BPh$_4$)$_2$

Bond	**Length /Å**	**Atoms**	**Angle /º**	**Atoms**	**Angle /º**
Ni(1)-N(1)	2.028(3)	N(1)-Ni(1)-N(2)	99.5(2)	S(1)-Fe(1)-C(4)	87.0(1)
Ni(1)-N(2)	2.008(4)	S(1)-Ni(1)-S(2)	83.71(5)	C(1)-Fe(1)-C(4)	179.0(2)
Ni(1)-S(1)	2.167(1)	N(1)-Ni(1)-S(1)	88.6(1)	C(1)-N(3)-C(13)	172.3(5)
Ni(1)-S(2)	2.163(1)	N(2)-Ni(1)-S(2)	87.7(1)		
Fe(1)-S(1)	2.307(1)	N(1)-Ni(1)-S(2)	171.9(1)	**Torsion**	**Angle /º**
Fe(1)-S(2)	2.302(1)	S(1)-Ni(1)-N(2)	168.5(1)	Ni(1)-S(1)-S(2)-Fe(1)	141.46(6)
Fe(1)-C(1)	1.879(5)	Ni(1)-S(1)-Fe(1)	91.93(4)		
Fe(1)-C(2)	1.859(4)	S(1)-Fe(1)-S(2)	77.62(4)		
Fe(1)-C(3)	1.881(5)	S(1)-Fe(1)-C(1)	93.9(1)		
Fe(1)-C(4)	1.890(4)	S(1)-Fe(1)-C(2)	94.9(1)		
Ni(1)-Fe(1)	3.2179(7)	S(1)-Fe(1)-C(3)	172.1(1)		

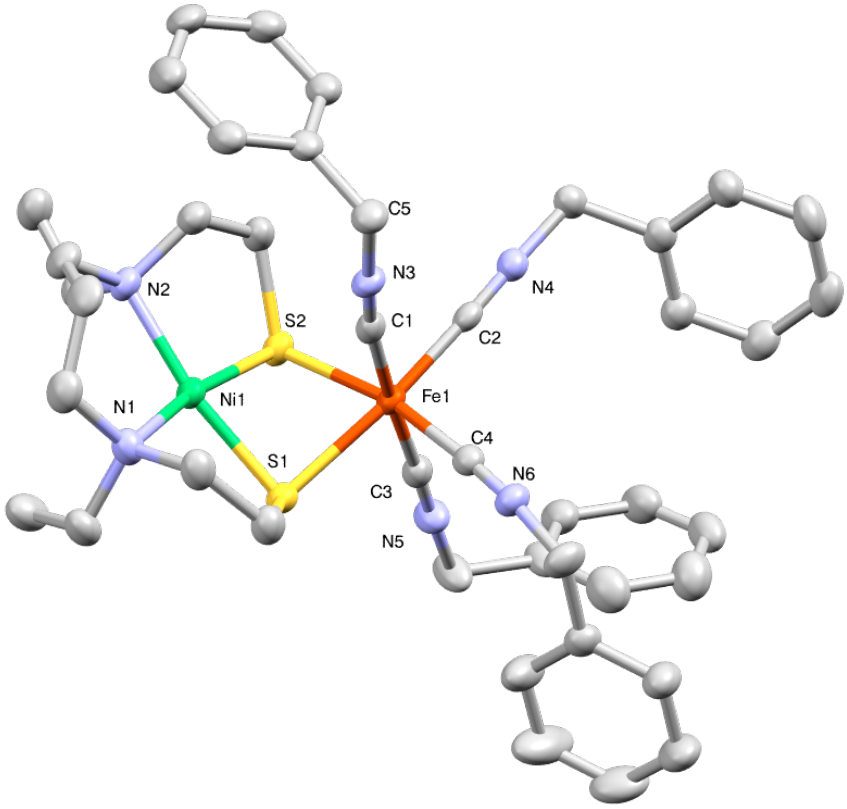


Figure 2.7.2: X-ray crystal structure of [Ni(L1)Fe(benzyl-NC)$_4$](BPh$_4$)$_2$ with ellipsoids at 50% probability. H atoms and [BPh$_4$]$^-$ anions omitted for clarity.

[Ni(L1)Fe(benzyl-NC)$_4$](BPh$_4$)$_2$ crystallises in $P2_1/n$.

Table 2.7.2: Selected bond lengths and angles for [Ni(L1)Fe(benzyl-NC)$_4$](BPh$_4$)$_2$.

Bond	**Length /Å**	**Atoms**	**Angle /º**	**Atoms**	**Angle /º**
Ni(1)-N(1)	2.003(3)	N(1)-Ni(1)-N(2)	101.7(1)	C(1)-Fe(1)-C(3)	176.8(1)
Ni(1)-N(2)	2.001(3)	S(1)-Ni(1)-S(2)	82.98(4)	S(1)-Fe(1)-C(2)	170.3(1)
Ni(1)-S(1)	2.1756(9)	N(1)-Ni(1)-S(1)	87.30(9)	C(1)-N(3)-C(5)	173.6(3)
Ni(1)-S(2)	2.179(1)	N(2)-Ni(1)-S(2)	87.63(9)		
Fe(1)-S(1)	2.330(1)	N(1)-Ni(1)-S(2)	169.6(1)	**Torsion**	**Angle /º**
Fe(1)-S(2)	2.316(1)	S(1)-Ni(1)-N(2)	169.53(9)	Ni(1)-S(1)-S(2)-Fe(1)	130.80(5)
Fe(1)-C(1)	1.901(4)	Ni(1)-S(1)-Fe(1)	88.27(4)		
Fe(1)-C(2)	1.881(3)	S(1)-Fe(1)-C(1)	96.9(1)		
Fe(1)-C(3)	1.905(4)	S(1)-Fe(1)-C(2)	170.3(1)		
Fe(1)-C(4)	1.861(3)	S(1)-Fe(1)-C(3)	85.3(1)		
Ni(1)-Fe(1)	3.140(1)	S(1)-Fe(1)-C(4)	91.9(1)		

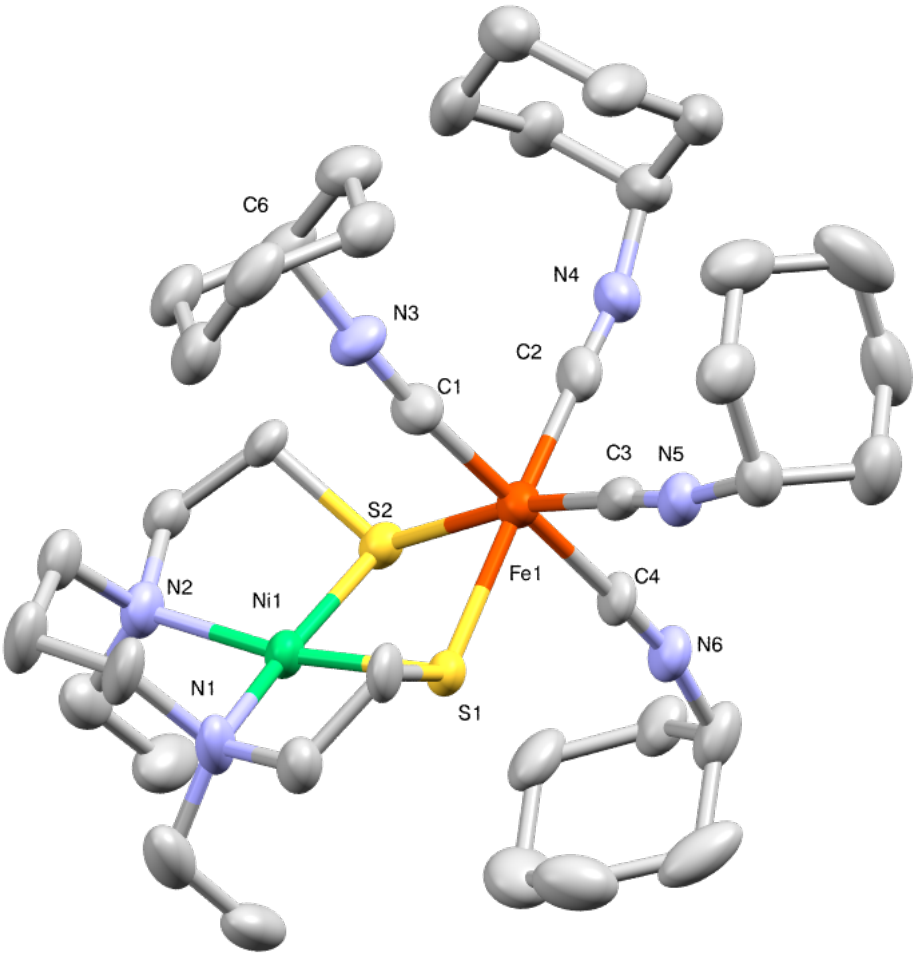


Figure 2.7.3: X-ray crystal structure of [Ni(L1)Fe(cyclohexyl-NC)$_4$](BPh$_4$)$_2$ with ellipsoids at 25% probability. H atoms and [BPh$_4$]$^-$ anions omitted for clarity.

[Ni(L1)Fe(cyclohexyl-NC)$_4$](BPh$_4$)$_2$ crystallises in $P2_1/c$.

Table 2.7.3: Selected bond lengths and angles for [Ni(L1)Fe(cyclohexyl-NC)$_4$](BPh$_4$)$_2$.

Bond	**Length /Å**	**Atoms**	**Angle /º**	**Atoms**	**Angle /º**
Ni(1)-N(1)	2.021(8)	N(1)-Ni(1)-N(2)	99.6(3)	C(1)-Fe(1)-C(2)	176.5(4)
Ni(1)-N(2)	2.013(7)	S(1)-Ni(1)-S(2)	83.12(9)	S(1)-Fe(1)-C(2)	171.9(3)
Ni(1)-S(1)	2.154(3)	N(1)-Ni(1)-S(1)	87.4(2)	C(1)-N(3)-C(6)	172(1)
Ni(1)-S(2)	2.163(3)	N(2)-Ni(1)-S(2)	89.2(2)		
Fe(1)-S(1)	2.269(2)	N(1)-Ni(1)-S(2)	168.8(2)	**Torsion**	**Angle /º**
Fe(1)-S(2)	2.328(3)	S(1)-Ni(1)-N(2)	170.5(2)	Ni(1)-S(1)-S(2)-Fe(1)	147.4(1)
Fe(1)-C(1)	1.89(1)	Ni(1)-S(1)-Fe(1)	95.55(9)		
Fe(1)-C(2)	1.88(1)	S(1)-Fe(1)-C(1)	97.3(3)		
Fe(1)-C(3)	1.87(1)	S(1)-Fe(1)-C(2)	171.9(3)		
Fe(1)-C(4)	1.910(8)	S(1)-Fe(1)-C(3)	91.8(3)		
Ni(1)-Fe(1)	3.276(2)	S(1)-Fe(1)-C(4)	83.9(3)		

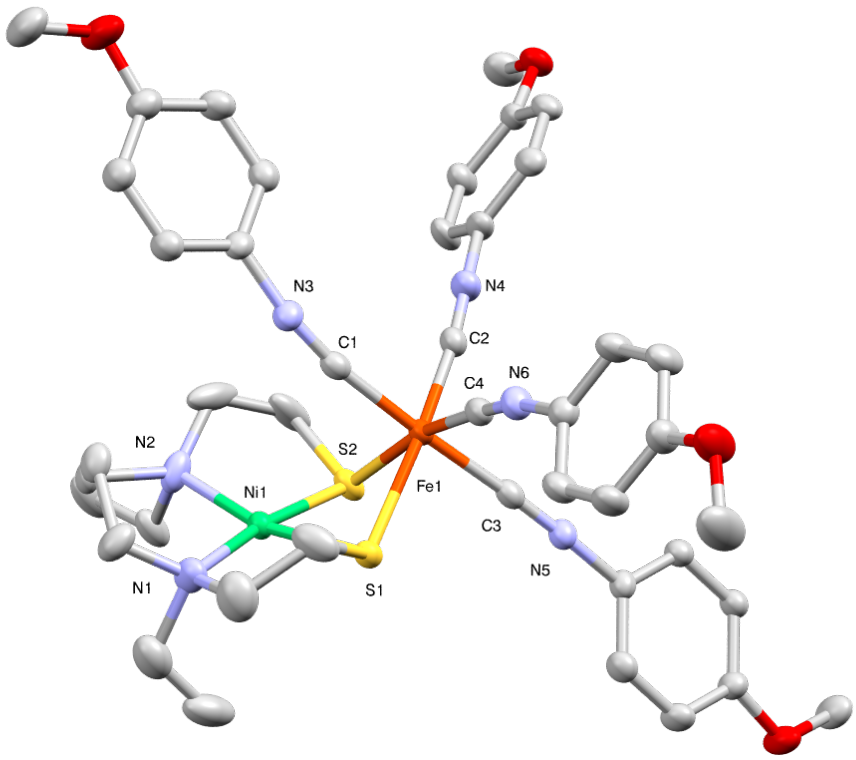


Figure 2.7.4: X-ray crystal structure of [Ni(L1)Fe(PhOMe-NC)$_4$](BPh$_4$)$_2$ with ellipsoids at 50% probability. H atoms and [BPh$_4$]$^-$ anions omitted for clarity.

[Ni(L1)Fe(PhOMe-NC)$_4$](BPh$_4$)$_2$ crystallises in *P*-1.

Table 2.7.4: Selected bond lengths and angles for [Ni(L1)Fe(PhOMe-NC)$_4$](BPh$_4$)$_2$.

Bond	**Length /Å**	**Atoms**	**Angle /º**	**Atoms**	**Angle /º**
Ni(1)-N(1)	2.003(2)	N(1)-Ni(1)-N(2)	100.42(8)	C(1)-Fe(1)-C(3)	177.21(9)
Ni(1)-N(2)	1.988(2)	S(1)-Ni(1)-S(2)	82.70(2)	C(1)-N(3)-C(12)	165.6(2)
Ni(1)-S(1)	2.1672(5)	N(1)-Ni(1)-S(1)	89.20(6)		
Ni(1)-S(2)	2.1670(7)	N(2)-Ni(1)-S(2)	88.29(6)	**Torsion**	**Angle /º**
Fe(1)-S(1)	2.3109(7)	N(1)-Ni(1)-S(2)	171.00(6)	Ni(1)-S(1)-S(2)-Fe(1)	125.22(3)
Fe(1)-S(2)	2.3463(5)	S(1)-Ni(1)-N(2)	165.46(6)		
Fe(1)-C(1)	1.873(2)	Ni(1)-S(1)-Fe(1)	86.73(2)		
Fe(1)-C(2)	1.855(2)	S(1)-Fe(1)-C(1)	96.30(6)		
Fe(1)-C(3)	1.895(2)	S(1)-Fe(1)-C(2)	167.69(7)		
Fe(1)-C(4)	1.848(2)	S(1)-Fe(1)-C(3)	86.47(6)		
Ni(1)-Fe(1)	3.0765(6)	S(1)-Fe(1)-C(4)	93.32(7)		

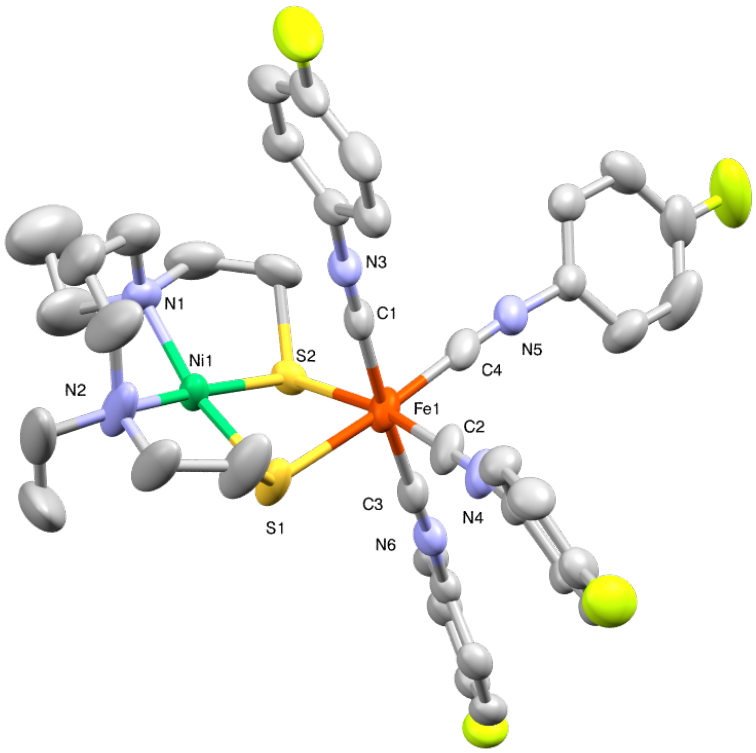


Figure 2.7.5: X-ray crystal structure of [Ni(L1)Fe(PhF-NC)$_4$](BPh$_4$)$_2$ with ellipsoids at 50% probability. H atoms and [BPh$_4$]$^-$ anions omitted for clarity.

[Ni(L1)Fe(PhF-NC)$_4$](BPh$_4$)$_2$ crystallises in $P2_1/c$.

Table 2.7.5: Selected bond lengths and angles for [Ni(L1)Fe(PhF-NC)$_4$](BPh$_4$)$_2$

Bond	**Length /Å**	**Atoms**	**Angle /º**	**Atoms**	**Angle /º**
Ni(1)-N(1)	2.007(3)	N(1)-Ni(1)-N(2)	98.4(2)	C(1)-Fe(1)-C(3)	175.1(2)
Ni(1)-N(2)	1.999(4)	S(1)-Ni(1)-S(2)	82.26(4)	S(1)-Fe(1)-C(4)	169.5(1)
Ni(1)-S(1)	2.156(1)	N(1)-Ni(1)-S(2)	88.6(1)	C(1)-N(3)-C(34)	173.0(5)
Ni(1)-S(2)	2.1564(9)	S(1)-Ni(1)-N(2)	89.8(1)		
Fe(1)-S(1)	2.300(1)	N(1)-Ni(1)-S(1)	167.9(1)	**Torsion**	**Angle /º**
Fe(1)-S(2)	2.3092(9)	N(2)-Ni(1)-S(2)	170.2(1)	Ni(1)-S(1)-S(2)-Fe(1)	137.21(4)
Fe(1)-C(1)	1.915(7)	Ni(1)-S(1)-Fe(1)	91.89(4)		
Fe(1)-C(2)	1.857(4)	S(1)-Fe(1)-C(1)	94.1(2)		
Fe(1)-C(3)	1.903(4)	S(1)-Fe(1)-C(2)	93.2(1)		
Fe(1)-C(4)	1.851(4)	S(1)-Fe(1)-C(3)	90.1(1)		
Ni(1)-Fe(1)	3.2043(6)	S(1)-Fe(1)-C(4)	169.5(1)		

The solid state structures of [Ni(L1)Fe(R-NC)$_4$](BPh$_4$)$_2$ (R = ^{t}Bu, ^{i}Pr, benzyl, cyclohexyl, PhOMe, PhF) share significant similarities. All of the complexes adopt a Ni(1)-(S$_2$)-Fe(1) core incorporating a pseudo-octahedral Fe centre and an essentially square planar

[[Ni(L1)] unit. The Ni...Fe distance is uniformly longer than that observed in the oxidised form of the [NiFe] hydrogenase enzyme active site (2.9 Å),[15] ranging from 3.0765(6) Å to 3.27(2) Å. This Ni…Fe distance is correlated with the Ni(1)-S(1)-S(2)-Fe(1) torsion angle (defined as the angle between the planes S(1)-Ni(1)-S(2) and S(1)-Fe(1)-S(2)), with a more obtuse dihedral angle reflecting a longer distance between the Ni and Fe atoms. This ranges from 125.22(3) º at its most narrow for the R = PhOMe structure to 147.4(1) º for R = cyclohexyl). A range of *ca* 22 º that affects the Ni…Fe distance by *ca* 0.2 Å.

The dihedral angle between the planes defined by Ni(1)-S(1)-S(2) and Fe(1)-S(1)-S(2) also appears to show a general correlation with the C(1)-N(3)-C(R) angle that is associated with the face-crowded isocyanide ligand in which smaller dihedral angles tend to be associated with a smaller C(1)-N(3)-C(R) angle (Table 2.7.6). However, it should be noted that this trend is not universal and is also likely to be modulated by the steric demands of each R group in the isocyanide ligand.

Table 2.7.6: Selected properties of $[Ni(L1)Fe(R\text{-}NC)_4](BPh4)_2$ complexes. R = L1-6

$[Ni(L1)Fe(R\text{-}NC)_4](BPh_4)_2$ R =	**S(1)-Ni(1)-S(2) bite angle /º**	**Ni(1)-S(1)-S(2)-Fe(1) torsion /º**	**Face-crowded CN-R bend /º**
^{t}Bu	83.17(2)	135.48(2)	162.4(2)
^{i}Pr	83.71(5)	141.46(6)	172.3(5)
benzyl	82.98(4)	130.80(5)	173.6(3)
cyclohexyl	83.12(9)	147.4(1)	172(1)
4-methoxyphenyl	82.70(2)	125.22(3)	165.6(2)
4-fluorophenyl	82.26(4)	137.21(4)	173.0(5)

The S(1)-Ni(1)-S(2) angle varies from 82.26(4) to 83.71(5) º in $[Ni(L1)Fe(R\text{-}NC)_4](BPh_4)_2$, (R = ^{t}Bu ^{i}Pr, benzyl, cyclohexyl, PhOMe, PhF) and each is smaller than that for the [Ni(L1)] precursor [S(1)-Ni(1)-S(2) = 84.20(2) º].[16] The similarity of the S(1)-Ni(1)-S(2) angle in

$[Ni(L1)Fe(R\text{-}NC)_4](BPh_4)_2$, (R = ^{i}Pr, benzyl, cyclohexyl, PhOMe, PhF) demonstrates that the [Ni(L1)] unit can accommodate a range of $[Fe(CN\text{-}R)_4]^{2+}$ fragments.

2.8 Cyclic Voltammetry of $[Ni(L1)Fe(R\text{-}CN)_4](BPh_4)_2$ (R = ^{t}Bu, ^{n}Bu, ^{i}Pr, cyclohexyl, benzyl, PhOMe)

The cyclic voltammograms of $[Ni(L1)Fe(R\text{-}CN)_4](BPh_4)_2$ (R = ^{t}Bu, ^{n}Bu, ^{i}Pr, cyclohexyl, benzyl, PhOMe) recorded at 298 K as 1 mM solutions in MeCN with 0.2 M $[N^{n}Bu_4][BF_4]$ as supporting electrolyte are shown in Figures 2.8.1 to 2.8.6 and an overlay of the cyclic voltammograms at a scan rate of 100 mVs^{-1} for $[Ni(L1)Fe(R\text{-}CN)_4](BPh_4)_2$ is shown in Figure 2.8.7. Each complex exhibits one reduction process between -1.18 and -1.40 V *vs* Fc^{+}/Fc that shifts as the nature of R is varied (Table 2.8.1). There are no other redox process observed between -0.9 and 1.7 V *vs* Fc^{+}/Fc except for the irreversible oxidation of the BPh_4^{-} anion that occurs at 0.441 V *vs* Fc^{+}/Fc.[17] Values for ip^{a}/ip^{c} are approximately 1 for all complexes.

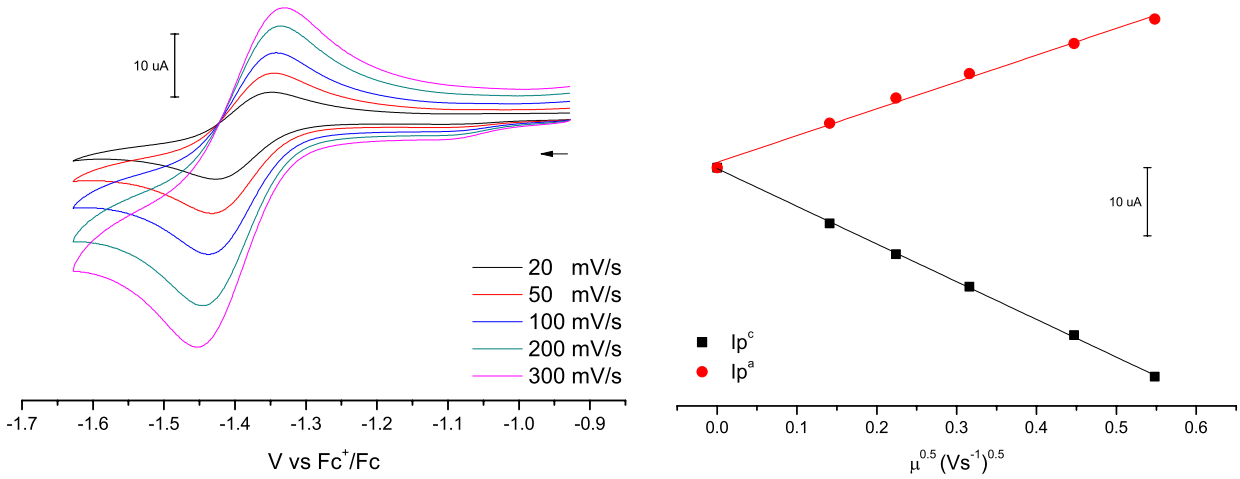


Figure 2.8.1: Cyclic voltammogram of 1 mM $[Ni(L1)Fe(^{t}BuNC)_4](BPh4)_2$ in MeCN with 0.2 M $[N^{n}Bu_4][BF_4]$ as supporting electrolyte between 20-300 mVs^{-1} and plot of $\mu^{0.5}$ vs i (right).

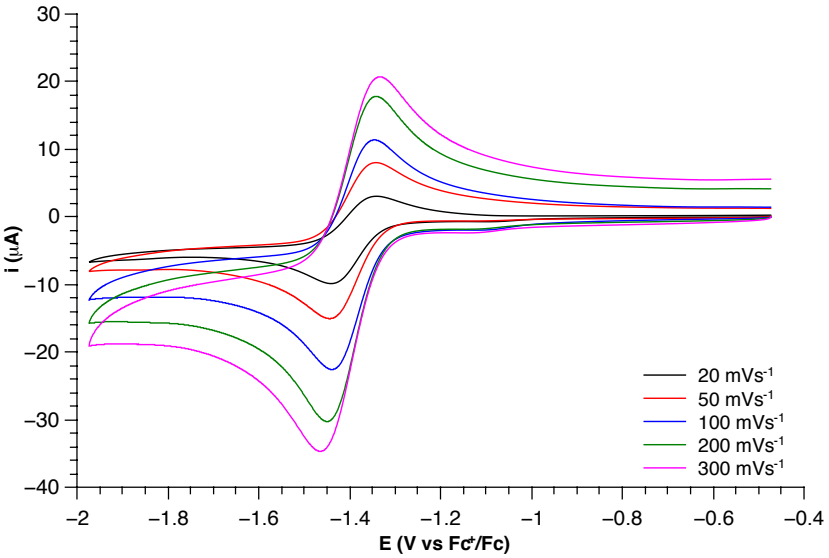


Figure 2.8.2: Cyclic voltammograms of 1 mM solutions of [Ni(L1)Fe(^{n}Bu-NC)$_4$](BPh$_4$)$_2$ at 100 mVs^{-1} in MeCN with 0.2 M [N^{n}Bu4][BF$_4$] as supporting electrolyte.

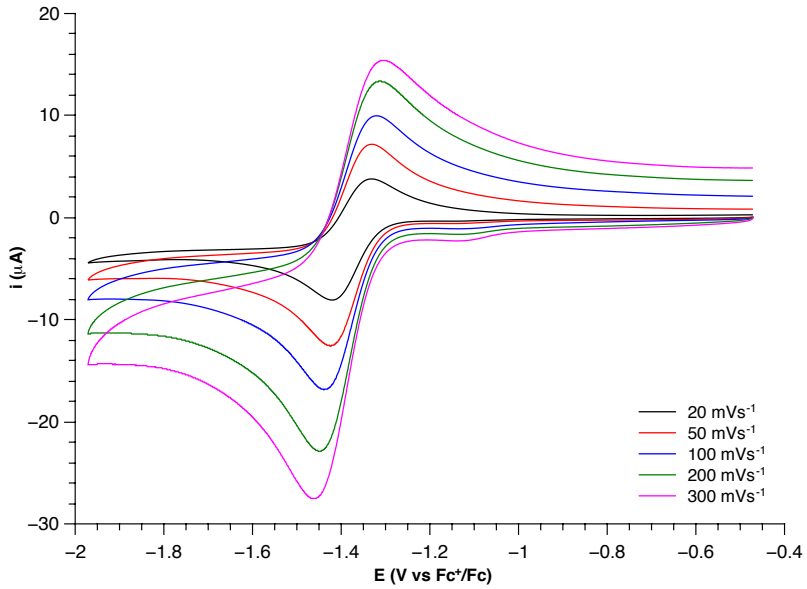


Figure 2.8.3: Cyclic voltammograms of 1 mM solutions of [Ni(L1)Fe(cyclohexyl-CN)$_4$](BPh$_4$)$_2$ at 100 mVs^{-1} in MeCN with 0.2 M [N^{n}Bu4][BF$_4$] as supporting electrolyte.

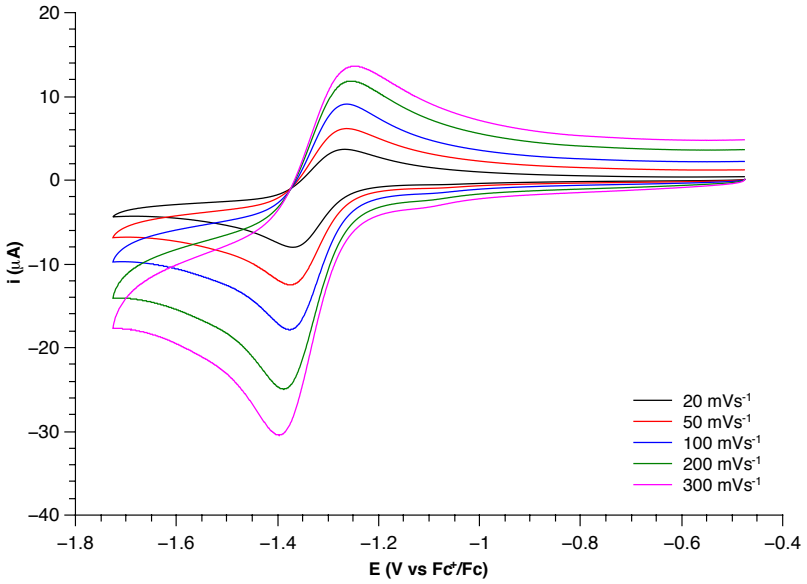


Figure 2.8.4: Cyclic voltammograms of 1 mM solutions of [Ni(L1)Fe(benzyl-CN)$_4$](BPh$_4$)$_2$ at 100 mVs^{-1} in MeCN with 0.2 M [N^{n}Bu4][BF$_4$] as supporting electrolyte.

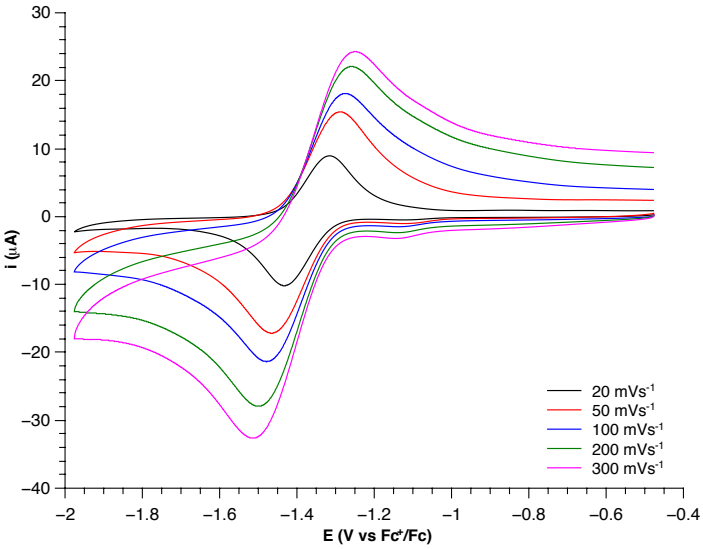


Figure 2.8.5: Cyclic voltammograms of 1 mM solutions of [Ni(L1)Fe(^{i}Pr-NC)$_4$](BPh$_4$)$_2$ at 100 mVs^{-1} in MeCN with 0.2 M [N^{n}Bu4][BF$_4$] as supporting electrolyte.

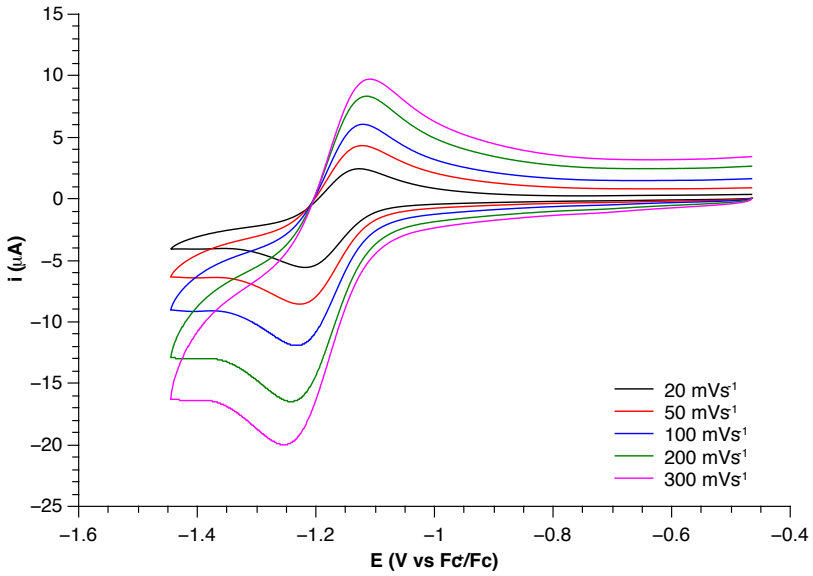
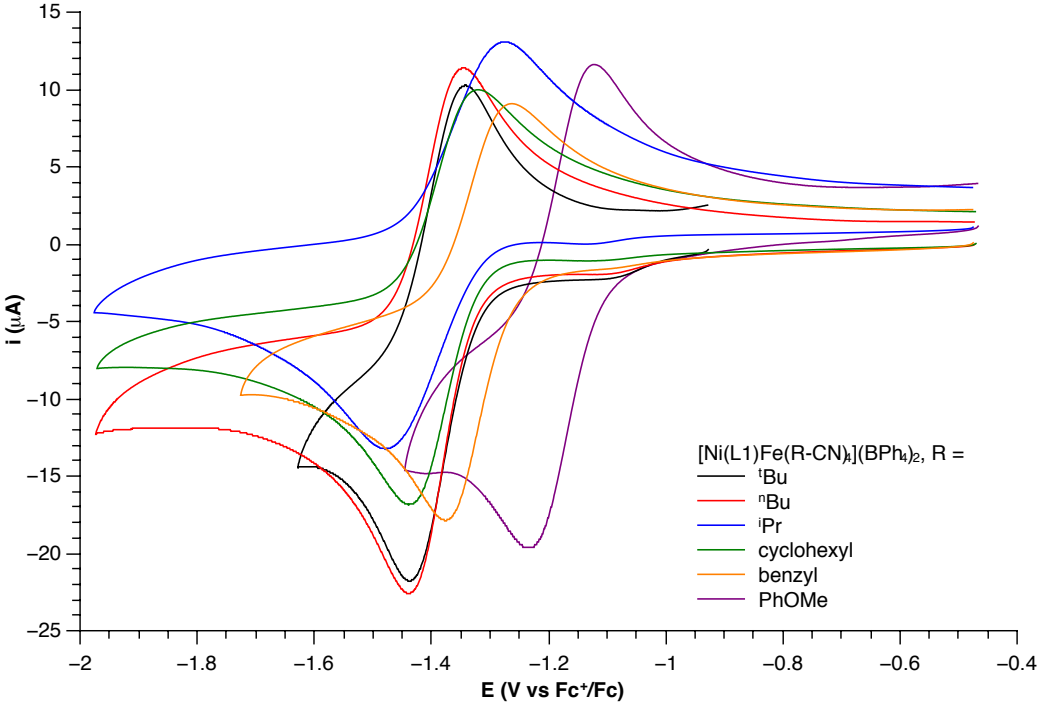


Figure 2.8.6: Cyclic voltammograms of 1 mM solutions of $[Ni(L1)Fe(PhOMe\text{-}CN)_4](BPh_4)_2$ at 100 mVs^{-1} in MeCN with 0.2 M $[N^nBu_4][BF_4]$ as supporting electrolyte.



F*igure 2.8.7: Overlay of cyclic voltammograms of 1 mM solutions of $[Ni(L1)Fe(R\text{-}CN)](BPh_4)_2$ at 100 mVs^{-1} in MeCN with 0.2 M $[N^nBu4][BF_4]$ as supporting electrolyte.*

Table 2.8.1: $E_{1/2}$ values for 1 mM $[Ni(L1)Fe(R\text{-}NC)_4](BPh_4)_2$ complexes in MeCN with 0.2 M $[N^nBu][BF4]$ as supporting electrolyte recorded at 100 mVs^{-1} scan rate.

$[Ni(L1)Fe(R\text{-}NC)_4](BPh_4)_2$, R=	**$E_{1/2}$ (V vs Fc+/Fc)**
^{t}Bu	-1.39
^{n}Bu	-1.33
cyclohexyl	-1.38
benzyl	-1.40
^{i}Pr	-1.37
PhOMe	-1.18

An examination of the plots of the cathodic and anodic currents *vs* $\mu^{0.5}$, ip_c/ip_a and ΔE (approximately 75-80 mV for each sample and for Fc^+/Fc) suggest that each reduction process tend to reversible and subsequent controlled potential electrolysis of $[Ni(L1)Fe(R\text{-}NC)_4](BPh_4)_2$, (Figures 2.8.8, 2.8.9) is consistent with a one electron reduction process for each complex.

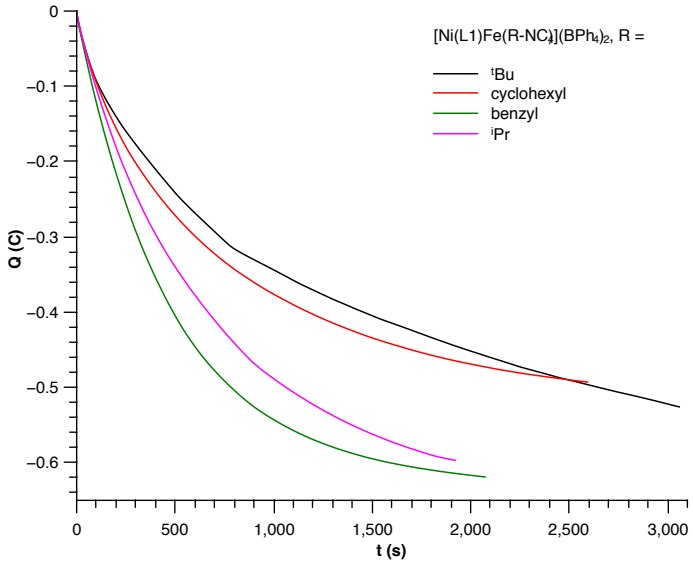


Figure 2.8.8: Plots of Q vs t for $[Ni(L1)Fe(R\text{-}NC)_4](BPh_4)_2$ as 1 mM solutions in with 0.2 M $[N^nBu4][BF_4]$ as supporting electrolyte.

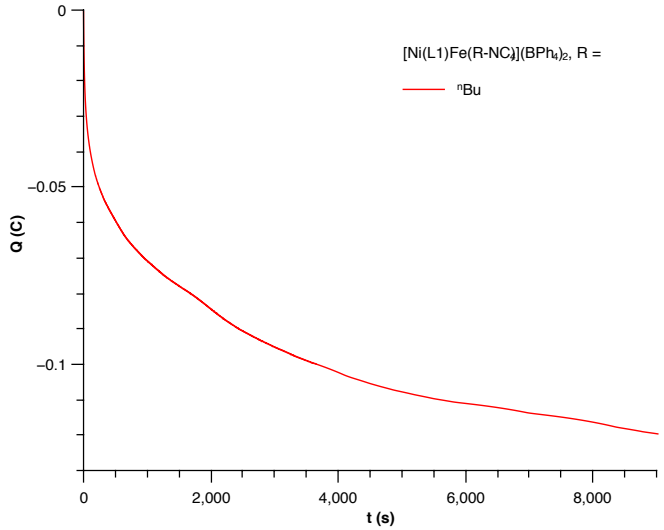


Figure 2.8.9: Plots of Q vs t for [Ni(L1)Fe(^{n}Bu-NC)$_4$](BPh$_4$)$_2$ as 1 mM solution in with 0.2 M [N^{n}Bu4][BF$_4$] as supporting electrolyte.

The cyclic voltammogram of [Ni(L1)] recorded under the same conditions reveals a reduction process at E_p^c = -2.35 V *vs* Fc^+/Fc,[10] assigned to the reduction of [Ni(L1)] to the formal Ni^I state on the basis of comparisons with previously reported Ni[N_2S_2] complexes possessing similar co-ordination spheres. The shift of *ca.* +1 V for the reduction of [Ni(L1)Fe(R-NC)$_4$](BPh$_4$)$_2$ relative to that of [Ni(L1)] is consistent with the formation of a Lewis base Lewis acid adduct between [Ni(L1)] and [Fe(CN-R)$_4$]$^{2+}$; *ca.* +0.5 V shifts in potential have been observed previously for (Ni[N_2S_2])W(CO)$_4$ relative to their parent Ni[N_2S_2] complexes.[18] The potentials of the reduction process for [Ni(L1)Fe(CN-R)$_4$](BPh$_4$)$_2$ (R = ^{t}Bu, ^{n}Bu, ^{i}Pr, cyclohexyl, benzyl, PhOMe) (Table 2.8.1) show that as the R substituents become more electron donating the reduction potential becomes more cathodic. This general trend may be rationalised through an increase in electron density at the Ni centre, communicated through the bridging thiolate S-donors.

2.9 UV/vis spectroelectrochemistry of $[Ni(L1)Fe(CN\text{-}R)_4](BPh_4)_2$ (R = ^{t}Bu, ^{n}Bu, ^{i}Pr, cyclohexyl, benzyl)

The electrochemically reversible processes of $[Ni(L1)Fe(R\text{-}CN)_4](BPh_4)_2$ were examined by spectroelectrochemistry to determine whether these processes were chemically reversibile. A 1 mM solution of each complex in MeCN with 0.2 M $[N^nBu_4][BF_4]$ as supporting electrolyte was reduced at 258 K by controlled potential electrolysis in a custom quartz cuvette cell and examined *in situ* via UV/vis spectroscopy with scans from 1100 to 250 nm taken every 2 minutes. Upon full reduction, indicated by no further change in the spectra, the potential was reversed and the complex oxidised to return to the starting state. Spectra for $[Ni(L1)Fe(R\text{-}CN)_4](BPh_4)_2$ are shown in Figures 2.9.1 to 2.9.5 and changes in the spectrum of each $[Ni(L1)Fe(R\text{-}NC)_4](BPh_4)_2$ are summarized in Table 2.9.1.

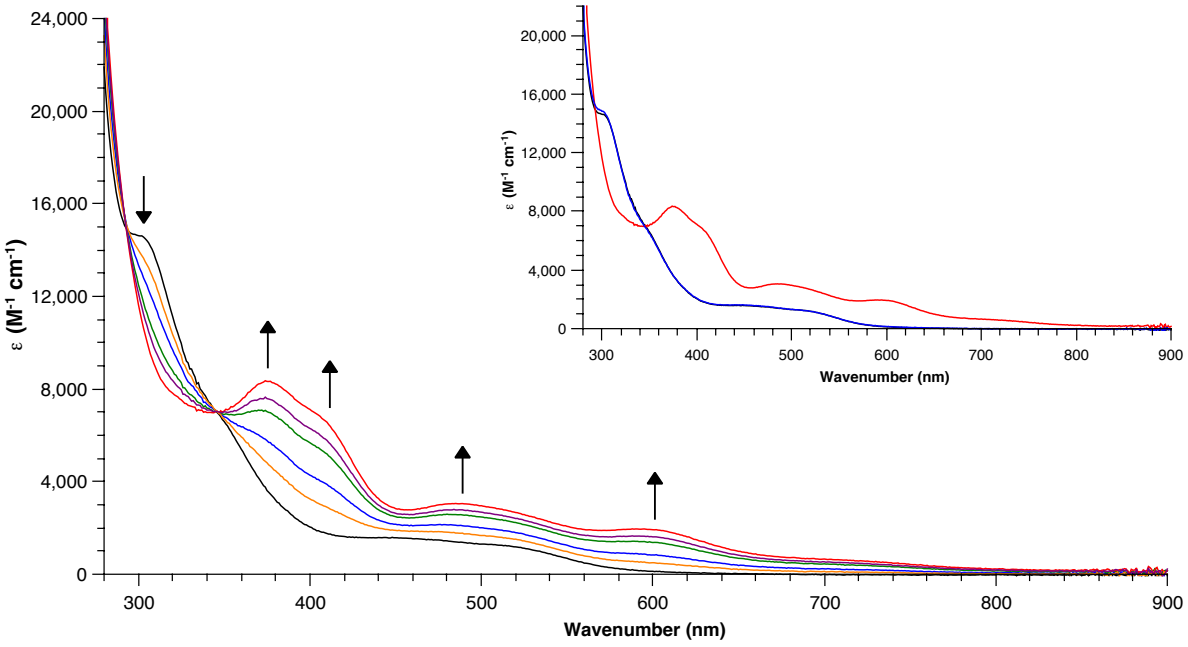


Figure 2.9.1: Spectroelectrochemistry of $[Ni(L1)Fe(^tBuNC)_4](BPh_4)_2$ at -1.39 V vs Fc^+/Fc at -20 ºC in MeCN with 0.2 M $[N^nBu_4][BF_4]$ as supporting electrolyte over repeat scans from oxidised (black) to reduced (red), and (inset); oxidised (black), reduced (red) and re-oxidised (blue).

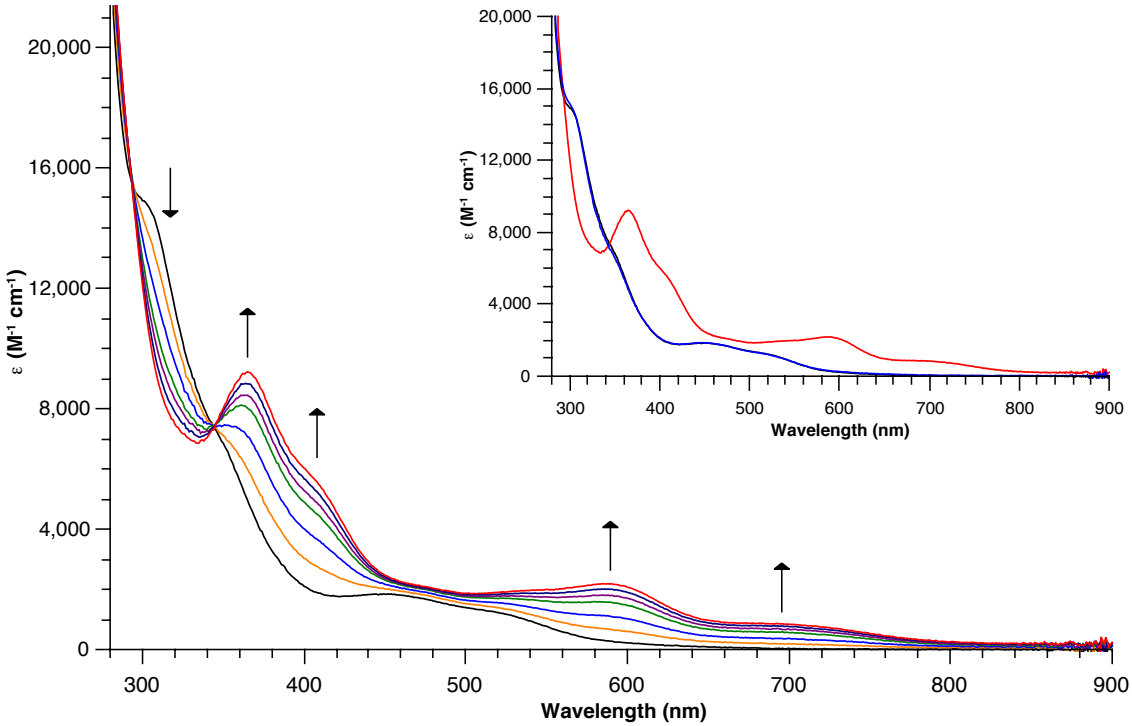


Figure 2.9.2: Spectroelectrochemistry of [Ni(L1)Fe(^{n}BuNC)$_4$](BPh$_4$)$_2$ process at -1.33 V vs Fc$^+$/Fc at -20 ºC in MeCN with 0.2 M [N^{n}Bu$_4$][BF$_4$] as supporting electrolyte over repeat scans from oxidised (black) to reduced (red), and (inset); oxidised (black), reduced (red) and re-oxidised (blue).

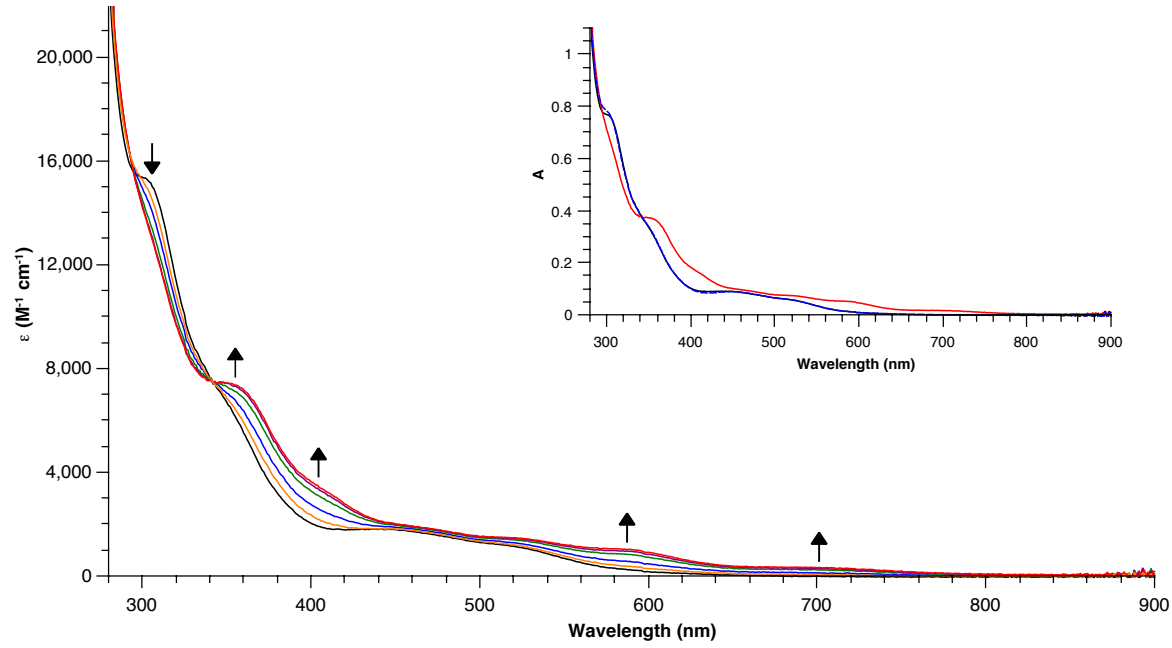


Figure 2.9.3: Spectroelectrochemistry of [Ni(L1)Fe(cyclohexyl-NC)$_4$](BPh$_4$)$_2$ process at -1.38 V vs Fc$^+$/Fc at -20 ºC in MeCN with 0.2 M [N^{n}Bu$_4$][BF$_4$] as supporting electrolyte over repeat scans from oxidised (black) to reduced (red), and (inset); oxidised (black), reduced (red) and re-oxidised (blue).

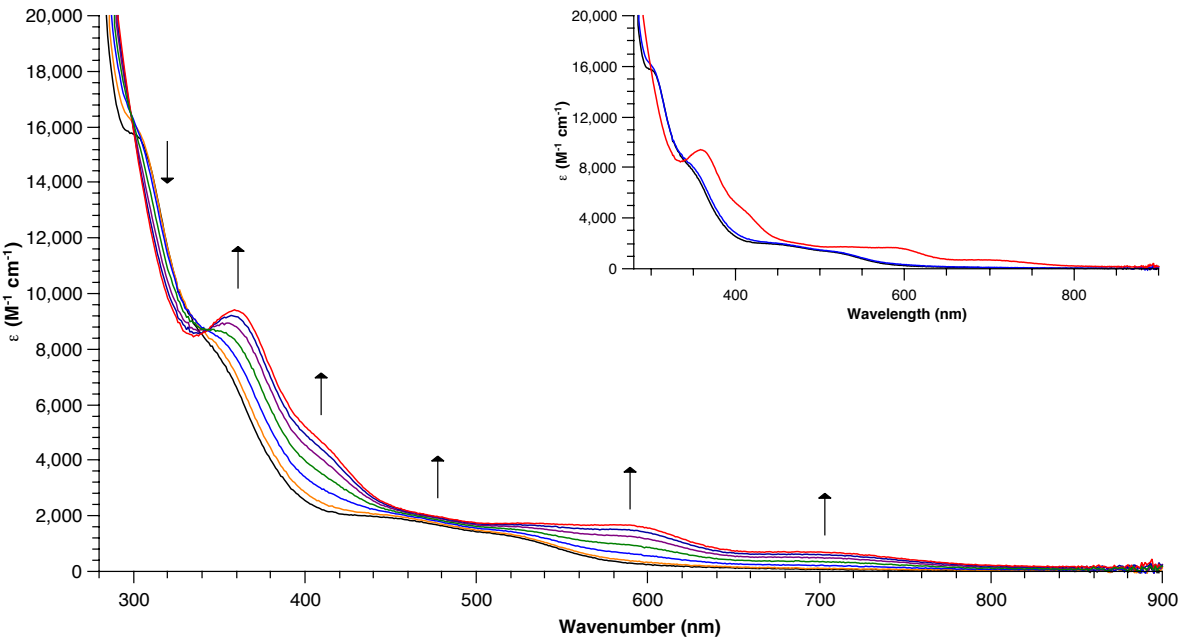


Figure 2.9.4: Spectroelectrochemistry of [Ni(L1)Fe(benzyl-NC)$_4$](BPh$_4$)$_2$ process at -1.40 V vs Fc$^+$/Fc at -20 ºC in MeCN with 0.2 M [N^{n}Bu$_4$][BF$_4$] as supporting electrolyte over repeat scans from oxidised (black) to reduced (red), and (inset); oxidised (black), reduced (red) and re-oxidised (blue).

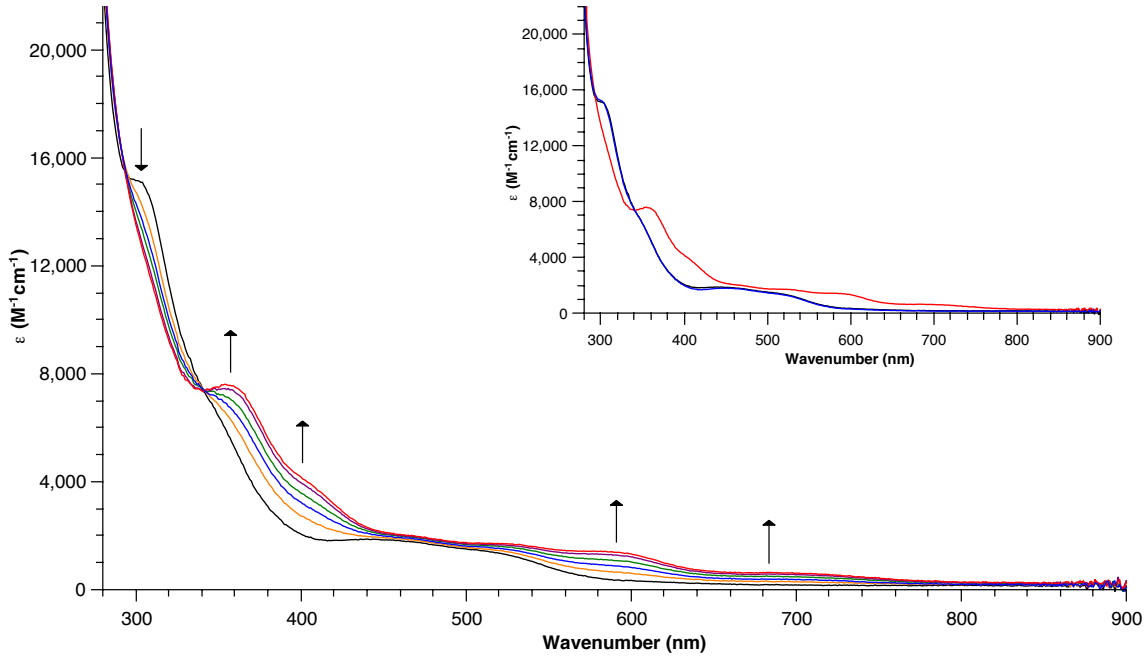


Figure 2.9.5: Spectroelectrochemistry of [Ni(L1)Fe(^{i}Pr-NC)$_4$](BPh$_4$)$_2$ process at -1.37 V vs Fc$^+$/Fc at -20 ºC in MeCN with 0.2 M [N^{n}Bu$_4$][BF$_4$] as supporting electrolyte over repeat scans from oxidised (black) to reduced (red), and (inset); oxidised (black), reduced (red) and re-oxidised (blue).

Table 2.9.1: Summary of the UV/vis spectra of $[Ni(L1)Fe(R\text{-}NC)_4]^{1+/2+}$

Complex	**λ_{max} (nm)**	**ε (mol^{-1} dm^3 cm^{-1})**	**Isosbestic point (nm)**
$[Ni(L1)Fe(^tBuNC)_4]^{2+}$	300, 447, 513	14680, 1680, 1232	
$[Ni(L1)Fe(^tBuNC)_4]^{1+}$	375, 410, 489, 600, 710	8410, 6590, 3054, 1982, 640	345
$[Ni(L1)Fe(^nBuNC)_4]^{2+}$	302, 457, 523	14834, 1866, 1262	
$[Ni(L1)Fe(^nBuNC)_4]^{1+}$	365, 407, 588, 697	9234, 5752, 2220, 908	344
$[Ni(L1)Fe(cyclohexyl\text{-}NC)_4]^{2+}$	302, 449, 519	15340, 1826, 1234	
$[Ni(L1)Fe(cyclohexyl\text{-}NC)_4]^{1+}$	352, 406, 587, 700	7400, 3452, 1036, 340	342
$[Ni(L1)Fe(benzyl\text{-}NC)_4]^{2+}$	297, 453, 521	15758, 1964, 1340	
$[Ni(L1)Fe(benzyl\text{-}NC)_4]^{1+}$	360, 407, 589, 706	9464, 4822, 1742, 714	340
$[Ni(L1)Fe(^iPr\text{-}NC)_4]^{2+}$	302, 449, 521	15156, 1884, 1424	
$[Ni(L1)Fe(^iPr\text{-}NC)_4]^{1+}$	355, 404, 590, 699	7578, 3996, 1378, 644	341

Each series of spectra recorded for the reduction of $[Ni(L1)Fe(R\text{-}NC)_4](BPh_4)_2$ possess isosbestic points that indicates that each reduction proceeds directly without of the involvement of any detectable intermediates over the timescale of the experiment. The close correspondence of the UV/vis spectra of $[Ni(L1)Fe(R\text{-}NC)_4](BPh_4)_2$ before reduction and after the reoxidation of $[Ni(L1)Fe(R\text{-}NC)_4]^+$ show that the reduction process of $[Ni(L1)Fe(R\text{-}NC)_4](BPh_4)_2$ is chemically reversible on the timescale of the experiment. Each $[Ni(L1)Fe(R\text{-}NC)_4](BPh_4)_2$ possesses a similar UV/vis spectrum that shows similar changes as each complex is reduced to $[Ni(L1)Fe(R\text{-}NC)_4]^+$. The reduction process is associated with the growth of a low energy band at *ca.* 700 nm that may be associated with charge transfer between the two metal centres as well as higher energy MLCT bands at *ca.* 350-370 nm assigned into the π* orbitals of the bound isocyanide ligands.[19] These spectra suggest that the IR spectrum of the reduced species could be a useful technique to probe the system, since the UV-Vis spectra demonstrate that electron density changes at the nickel have the potential to perturb the CN bonds. Upon re-oxidation back to the starting solution the spectra are idential to the pre-reduction spectra recorded, indicating a chemically reversible $Ni^{I/II}$ redox couple. The presence of isosbestic points in the

spectra indicate that the transition between the I/II oxidation state proceeds without the presence of long lived intermediate states.

2.10 Probing the reduction of $[Ni(L1)Fe(R\text{-}CN)_4](BPh_4)_2$ (R = ^{t}Bu, ^{n}Bu, ^{i}Pr, cyclohexyl, benzyl, PhOMe) by IR Spectroscopy

The changes in the IR spectra of the each $[Ni(L1)Fe(CN\text{-}R)_4](BPh_4)_2$ (R = ^{t}Bu, ^{n}Bu, ^{i}Pr, cyclohexyl, benzyl, PhOMe) were recorded following the treatment of a 1 mM solution of $[Ni(L1)Fe(CN\text{-}R)_4](BPh_4)_2$ in MeCN (4 mL) with $Co(Cp^*)_2$ ($E_{½}$ = -1.91 V vs Fc^+/Fc in MeCN)[20] at 243 K under an argon atmosphere. The IR spectra of $[Ni(L1)Fe(CN^tBu)_4]^{2+}$ and $[Ni(L1)Fe(CN^tBu)_4]^+$ in the isonitrile C-N stretching region are shown in Figure 2.10.1. The IR spectra of $[Ni(L1)Fe(CN\text{-}R)_4]^+$ are compared in Figure 2.10.4, and the changes in the isonitrile stretching frequencies are presented in Table 2.10.1.

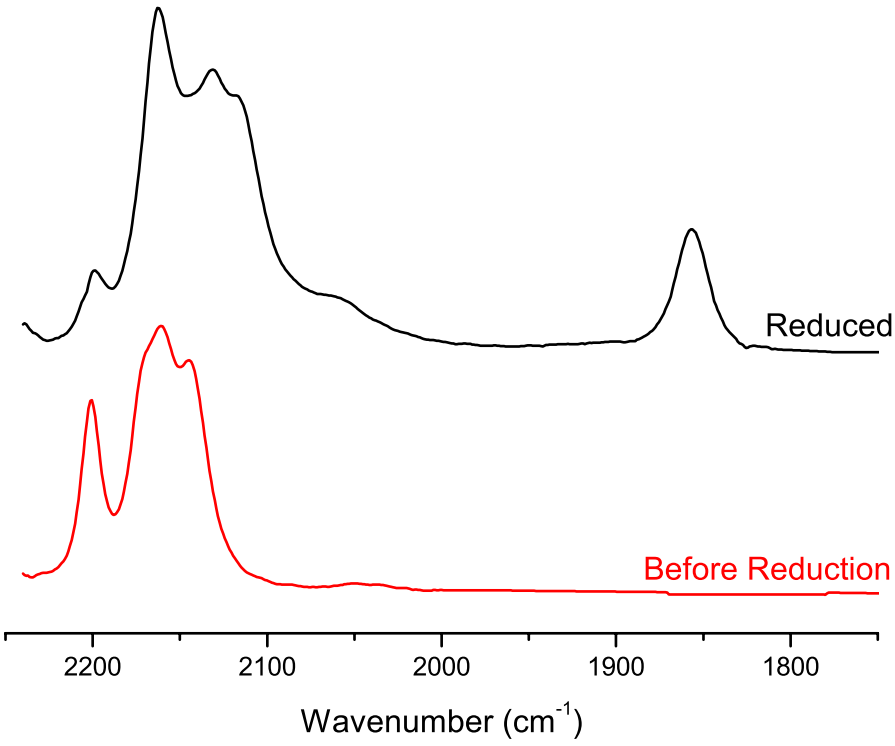


Figure 2.10.1: IR spectra of 1 mM $[Ni(L1)Fe(^tBuNC)_4](BPh4)_2$ at -30 ºC in MeCN before reduction and after reduction with $Co(Cp^*)_2$

Table 2.10.1: IR bands for $[Ni(L1)Fe(R\text{-}CN)_4](BPh_4)_2$ recorded in MeCN at 293 K.

$[Ni(L1)Fe(R\text{-}CN)_4](BPh_4)_2$, R =	**Wavenumber (cm^{-1})**
^{t}Bu	2201, 2170sh, 2160, 2145
^{n}Bu	2218, 2188sh, 2173, 2154
cyclohexyl	2206, 2174sh, 2160
benzyl	2219, 2190sh, 2174, 2155sh
^{i}Pr	2208, 2191sh, 2167, 2160
PhOMe	2192, 2163sh, 2151, 2141sh

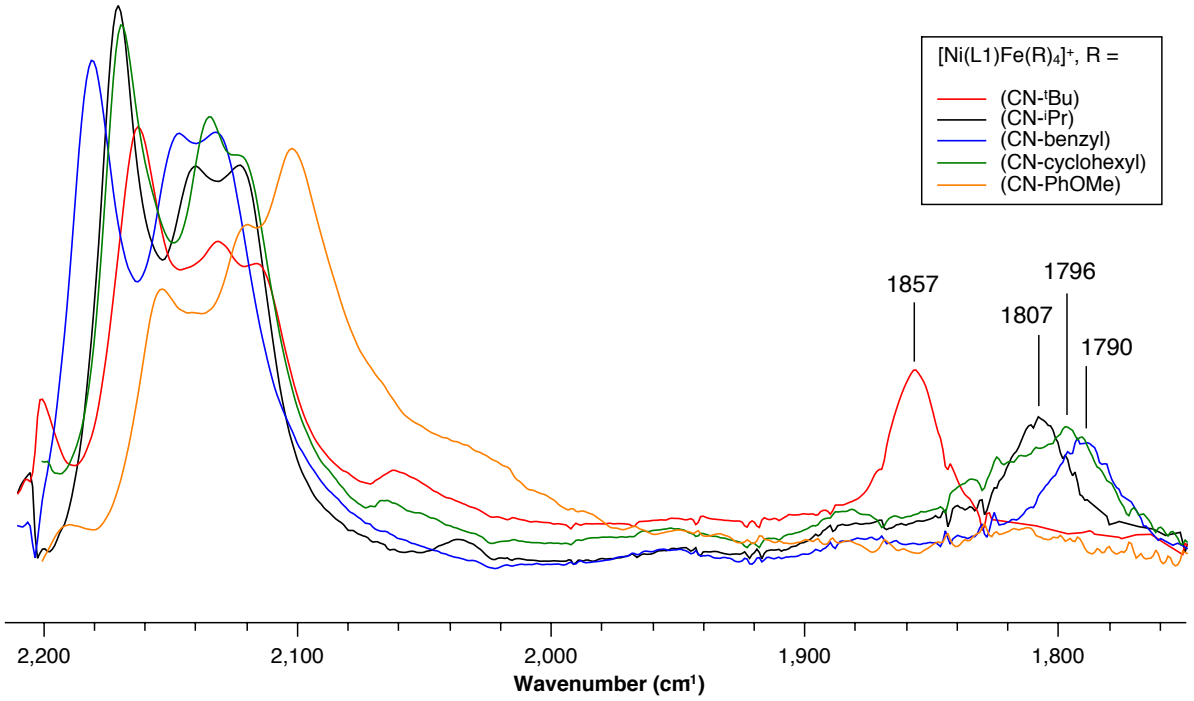


Figure 2.10.4: IR spectra of 1 mM $[Ni(L1)Fe(R\text{-}NC)_4]^+$ at -30 ºC in MeCN after reduction via CPE demonstrating terminal CN stretches (left) and the emergence of a bridging band (right) for most complexes. R = ^{t}Bu, ^{i}Pr, benzyl, cyclohexyl, PhOMe.

$[Ni(L1)Fe(R\text{-}CN)_4](BPh_4)_2$, (R = ^{t}Bu, ^{n}Bu, ^{i}Pr, cyclohexyl, benzyl, PhOMe) exhibit four frequencies between 2219 and 2141 cm^{-1} that are typical of isonitrile ligands bound in a terminal mode to transition metal centres.[21] For R = (^{t}Bu, ^{n}Bu, ^{i}Pr, cyclohexyl, benzyl) these appear at similar frequencies. In contrast $[Ni(L1)Fe(PhOMe\text{-}CN)_4](BPh_4)_2$ possesses bands at 2192, 2163, 2151 and 2141 cm^{-1} that are shifted down in frequency by an average of 7-9 cm^{-1} when compared to their R = alkyl counterparts (Table 2.10.1). This is consistent with the

increased electron donating character of the MeO substituent that either directly donates electron density into the π* orbitals of the isonitrile C-N bond[19] or promotes the back-donation of electron density from the Fe centre into the π* orbitals of the isonitrile ligands. The overall shift of the bands to lower frequencies following the reduction of $[Ni(L1)Fe(R\text{-}CN)_4]^{2+}$ to $[Ni(L1)Fe(R\text{-}CN)_4]^{+}$ (Figure 2.10.4) is consistent with an increase in the electron density about the Ni-Fe core and a corresponding increase in π-back-donation into the isonitrile ligands. All of the spectra of $[Ni(L1)Fe(R\text{-}CN)_4]^{+}$ (R = alkyl) possess one low frequency band in the range of 1790 to 1857 cm^{-1} in MeCN solution that suggests that one terminal, apical R-NC ligand moves to a bridging mode between the Ni and Fe centres following the reduction of $[Ni(L1)Fe(R\text{-}CN)_4]^{2+}$; a similar bridging mode is found in $[Fe_2(pdt)(MeNC)_7](PF_6)_2$ (pdt = propanedithiolate) where one MeNC ligand bridges between the two Fe centres.[21, 22]

It is likely that the isonitrile ligand at the face-crowded axial position adopts a bridging geometry between the Fe and Ni centres (Figure 2.10.3) with a consequent reduction of the C-N bond order considerably and a shift to lower vibrational frequencies.

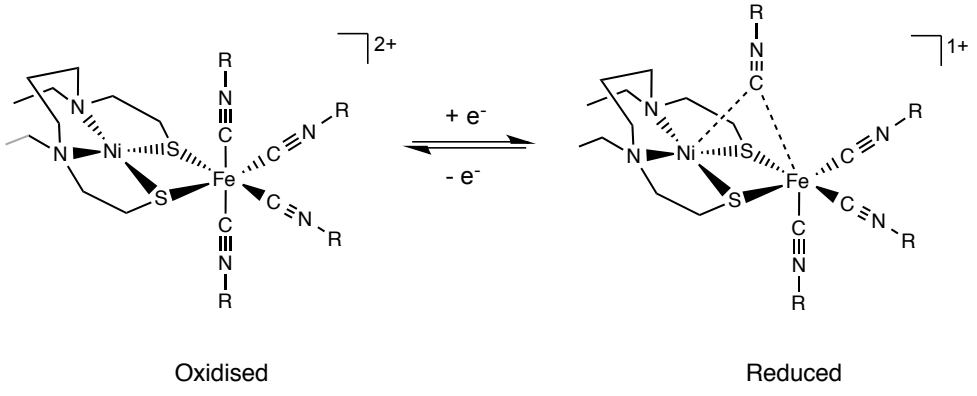


Figure 2.10.3: Geometry change via formation of bridging isocyanide upon reduction from $[Ni(L1)Fe(R\text{-}NC)_4]^{2+}$ to $[Ni(L1)Fe(R\text{-}NC)_4]^{+}$.

There is no apparent trend that links reduction potential of the $[Ni(L1)Fe(R\text{-}NC)_4]^{2+/+}$ couple to the energy of the C-N stretching frequency assigned to a bridging isonitrile ligand.

However R = ^{t}Bu and PhOMe appear to stand apart from R = (^{n}Bu, ^{i}Pr, cyclohexyl, benzyl), which all possess a similar stretching frequency between 1790-1807 cm^{-1}. For R = ^{t}Bu the C-N stretch appears at 1857 cm^{-1} and suggests that ^{t}Bu-NC adopts only a partial bridging mode when compared to R = (^{n}Bu, ^{i}Pr, cyclohexyl, benzyl) that may be associated with the greater steric demands of the R = ^{t}Bu group.

$[Ni(L1)Fe(PhOMe\text{-}NC)_4]^+$ does not appear to possess a low frequency band associated with a bridging isonitrile ligand. Back donation into the π^* orbitals of the C-N bond is associated with a shift from a linear CN-R bonding mode, which tends to promote bridging bonding modes.[23] Thus, the sp^2 hybridized *ipso* C atom of the phenyl ring in CN-PhOMe may preclude this ligand from being able to easily adopt the bridging mode.

2.11 EPR Spectoscopy of $[Ni(L1)Fe(CN\text{-}R)_4]^+$ (R = ^{t}Bu, ^{n}Bu, ^{i}Pr, cyclohexyl, benzyl)

1 mM solutions of $[Ni(L1)Fe(CN\text{-}R)_4](BPh_4)_2$ (R = ^{t}Bu, ^{n}Bu, ^{i}Pr, cyclohexyl, benzyl) in MeCN with $[N^{n}Bu_4][BF_4]$ as supporting electrolyte were reduced by controlled potential electrolysis to generate $[Ni(L1)Fe(CN\text{-}R)_4]^+$ that were examined via X-band EPR spectroscopy. Fluid solution measurements of $[Ni(L1)Fe(CN\text{-}^{t}Bu)_4]^+$ reveal a paramagnetic species with an isotropic *g* value of 2.1225 (Figure 2.11.1) that is consistent with spin-orbit coupling of an unpaired electron about a metal centre, rather than a radical-based system with an unpaired electron localized principally on the ligand for which $g_{iso} \approx g_e$.[24]

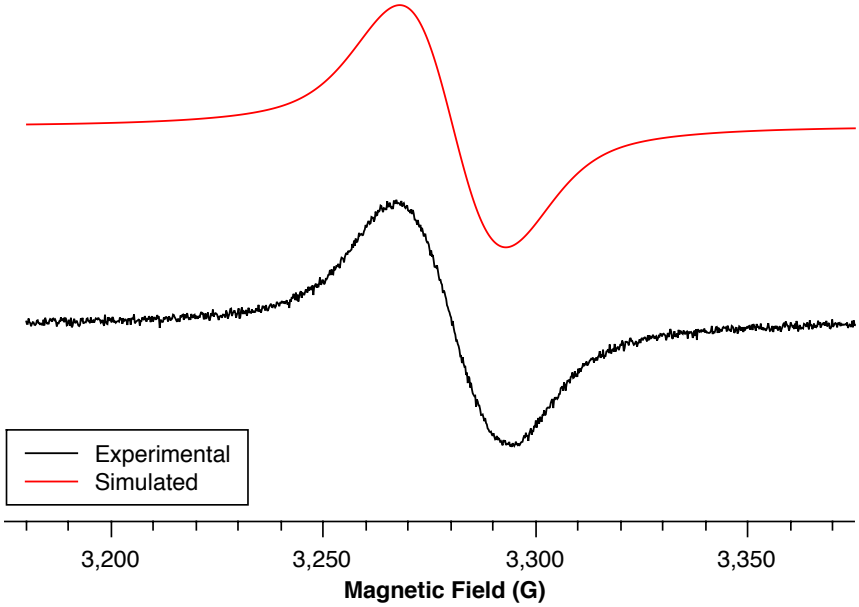


Figure 2.11.2: X-band EPR solution spectrum of electrochemically generated [Ni(L1)Fe(^{t}BuNC)$_4$]$^+$ in MeCN with 0.2 M [N^{n}Bu$_4$][BF$_4$] as supporting electrolyte (black) and simulated fluid spectrum (red) at 293 K. Spin Hamiltonion paramaters for simulation: g_{iso} = 2.1225, Gaussian linewidth W_{iso} = 25 G, Lorentzian/Gaussian line shape = 0.2.

The X-band frozen spectra of [Ni(L1)Fe(R-NC)$_4$]$^+$ are essentially axial ($g_{zz} > g_{xx} \approx g_{yy}$) (Figures 2.11.2 – 2.11.6, Table 2.11.1) and are similar in character to previously reported Ni^I systems bound to two amine N and two thiolate S donors.[25] Crucially, the spectra are substantially different to those of Fe^I centres including [Fe(CO)$_3$(PPh$_3$)$_2$]$^+$ (g_{xx} = 2.053, g_{yy} = 2.090, g_{zz} = 2.001)[26] and [(dppe)Ni(μ-pdt)Fe(CO)$_3$]$^+$ (g_{xx} = 2.052, g_{yy} = 2.050, g_{zz} = 2.005 for one isomer).[27] Thus, the EPR spectroscopic data are consistent with a formal Ni^{I}Fe^{II} unit in [Ni(L1)Fe(R-NC)$_4$]$^+$ where the Ni^I centre adopts a d^9, S = ½ configuration in which the unpaired electron resides in d-orbital orientated in the equatorial plane of the Ni^IN_2S_2 unit with associated spin Hamiltonian parameters $g_{zz} > g_{xx} \approx g_{yy} > g_e$.[28, 29]

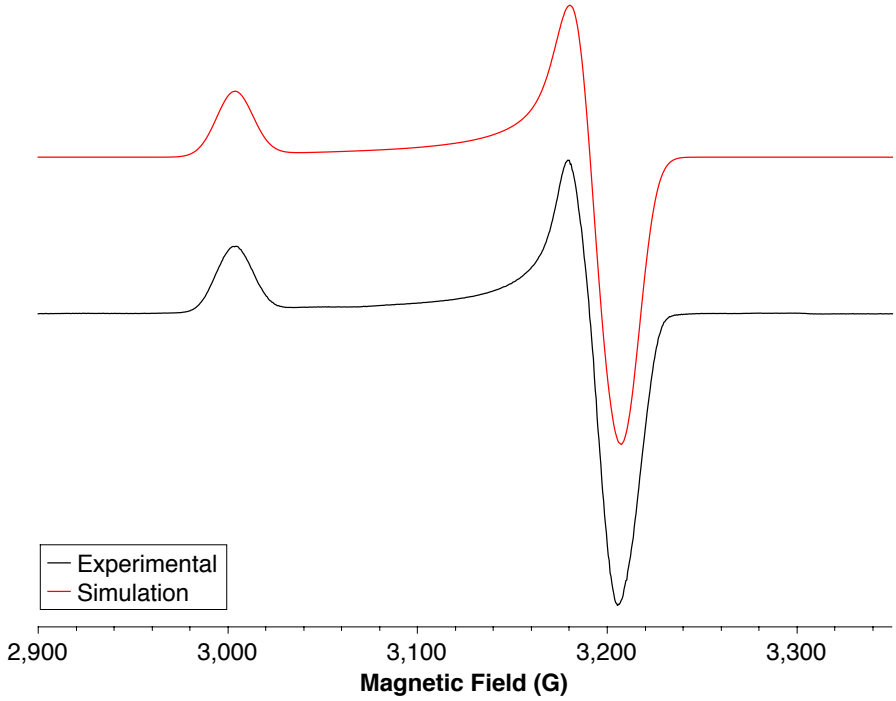


Figure 2.11.2: Frozen X-band EPR spectrum of electrochemically generated [Ni(L1)Fe(^{t}BuNC)$_4$]$^+$ in MeCN at 77 K (black) and simulated spectrum (red).

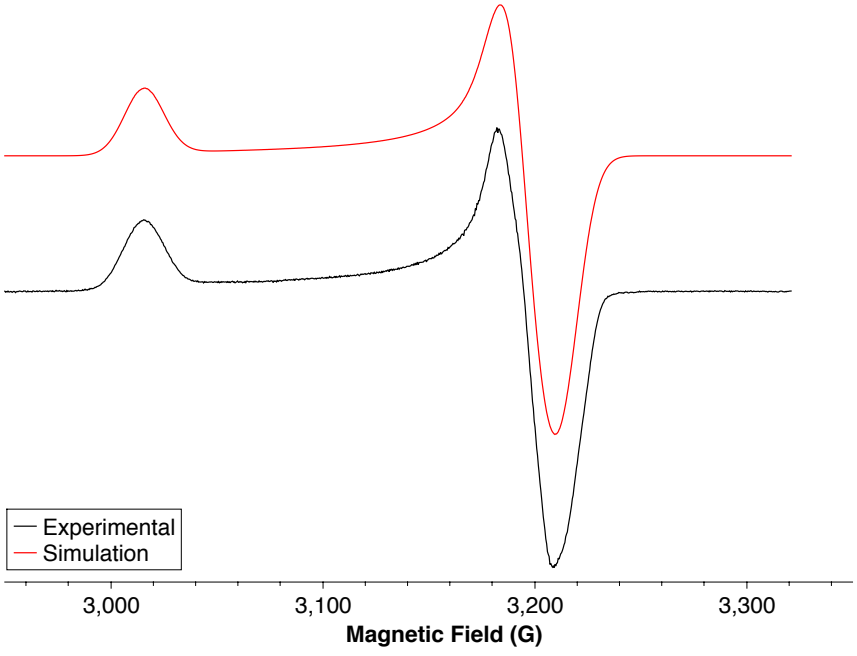


Figure 2.11.3: Frozen X-band EPR spectrum of electrochemically generated [Ni(L1)Fe(^{i}PrNC)$_4$]$^+$ in MeCN at 77 K (black) and simulated spectrum (red).

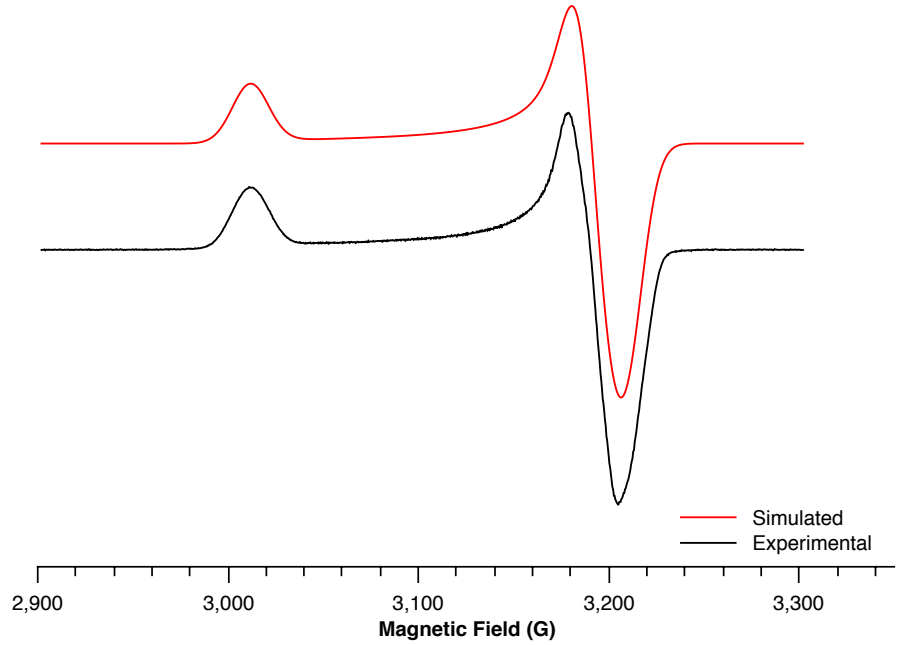


Figure 2.11.4: Frozen X-band EPR spectrum of electrochemically generated [Ni(L1)Fe(^{n}BuNC)$_4$]$^+$ in MeCN at 77 K (black) and simulated spectrum (red).

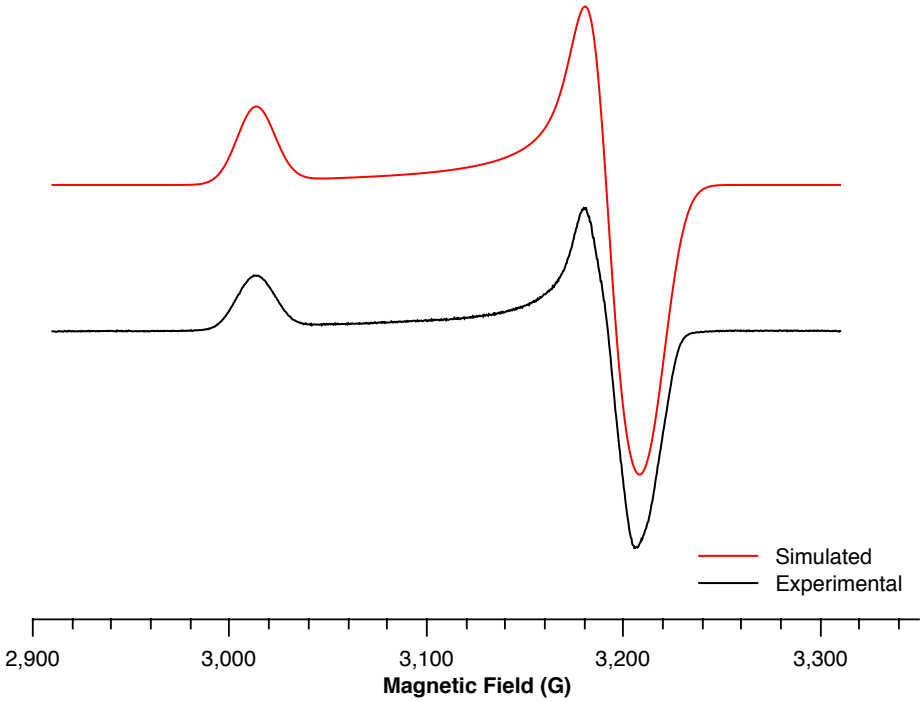


Figure 2.11.5: Frozen X-band EPR spectrum of electrochemically generated [Ni(L1)Fe(cyclohexyl-NC)$_4$]$^+$ in MeCN at 77 K (black) and simulated spectrum (red).

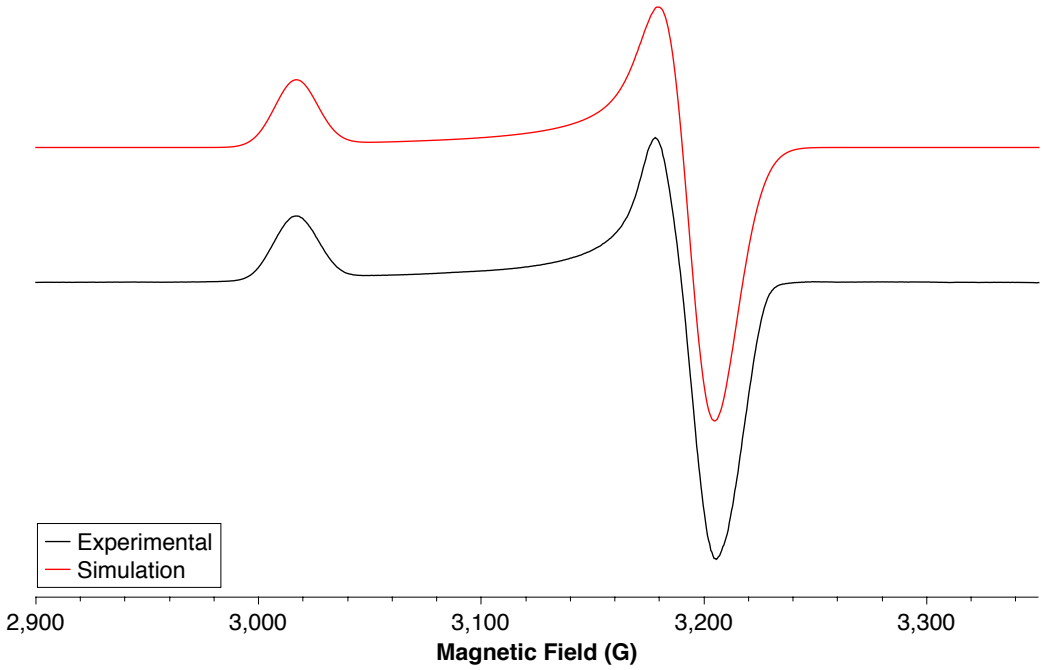


Figure 2.11.6: Frozen X-band EPR spectrum of electrochemically generated [Ni(L1)Fe(benzyl-NC)$_4$]$^+$ in MeCN at 77 K (black) and simulated spectrum (red).

Table 2.11.1: Spin Hamiltonian paramaters used for similation of EPR spectra of [Ni(L1)Fe (R-NC)$_4$]$^+$

Complex, R =	**g_{11}**	**g_{22}**	**g_{33}**	**W_1 /G**	**W_2 /G**	**W_3 /G**
^{t}Bu	2.2089	2.0795	2.067	19	17	17
^{n}Bu	2.2027	2.0790	2.067	19	17	18
cyclohexyl	2.2020	2.0790	2.065	19	17	20
benzyl	2.1990	2.0770	2.070	19	19.5	24.5
^{i}Pr	2.2020	2.0750	2.081	20	18	25

2.12 DFT calculations of [Ni(L1)Fe(^{t}BuNC)$_4$]$^+$

In order to support the proposed assignment of [Ni(L1)Fe(CN-R)$_4$]$^+$ to a formal Ni^{I}Fe^{II} centre and investigate the changes in geometric and electronic structure that occurs on the reduction of [Ni(L1)Fe(CN-R)$_4$]$^{2+}$ we undertook DFT calculations on [Ni(L1)Fe(CN-R)$_4$]$^{2+}$ (S = 0) and [Ni(L1)Fe(CN-R)$_4$]$^+$ (S = ½). We used the solid state structure of [Ni(L1)Fe(^{t}BuNC)$_4$](BPh$_4$)$_2$ derived from X-ray crystallography as a starting geometry. The DFT calculations were performed using ADF 2012 software[30] and employed the BP86 functional and a TZP basis

set.[30, 31] Selected metrical parameters for the geometry optimized structures are presented in Table 2.12.1 and the calculated structures of $[Ni(L1)Fe(CN\text{-}R)_4]^{2+}$ and $[Ni(L1)Fe(CN\text{-}R)_4]^{+}$ are shown in Figures 2.12.1 and 2.12.2, respectively. The calculated IR spectra of $[Ni(L1)Fe(CN\text{-}R)_4]^{2+}$ and $[Ni(L1)Fe(CN\text{-}R)_4]^{+}$ in the isonitrile stretching region are shown in Figure 2.12.3.

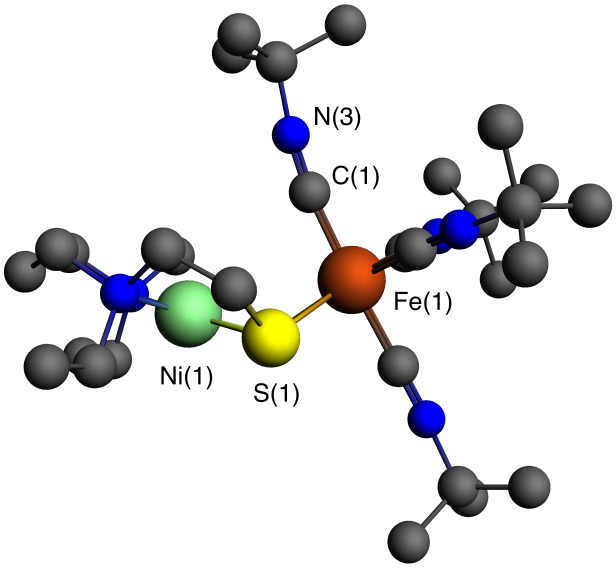


Figure 2.12.1: The gas phase geometry optimised structure of $[Ni(L1)Fe(^tBuNC)_4]^{2+}$.

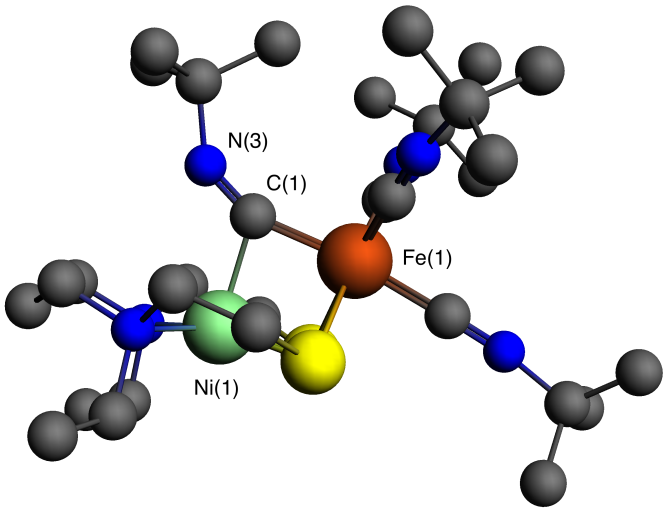


Figure 2.12.2: Gas phase geometry optimised structure of $[Ni(L1)Fe(^tBuNC)_4]^{+}$.

Table 2.12.1: Selected bond lengths and angles of the solid state structure of $[Ni(L1)Fe(^tBuNC)_4]2^+$ and the gas phase geometry optimised DFT calculation of $[Ni(L1)Fe(^tBuNC)_4]^{2+}$and $[Ni(L1)Fe(^tBuNC)_4]^+$.

Bond /Å	**XRD**	***[Ni(L1)Fe(tBuNC)4]2+***	***[Ni(L1)Fe(tBuNC)4]+***
Ni(1)-Fe(1)	3.1683(3)	3.2463	2.6399
Ni(1)-S(1)	2.1723(4)	2.2039	2.3365
Ni(1)-S(2)	2.1682(4)	2.2039	2.3343
Fe(1)-S(1)	2.2957(4)	2.4101	2.4533
Fe(1)-S(2)	2.3140(4)	2.4108	2.4533
Fe(1)-C(1)	1.8567(17)	1.8973	1.9527
Ni(1)-C(1)	3.1927(15)	3.3467	2.0332
Fe(1)-C(2)	1.8580(17)	1.8681	1.8406
Fe(1)-C(3)	1.8875(16)	1.868	1.8398
Fe(1)-C(4)	1.8893(17)	1.9097	1.8969

Angle /º	**XRD**	***[Ni(L1)Fe(tBuNC)4]2+***	***[Ni(L1)Fe(tBuNC)4]+***
C(1)-N(3)-C(5)	162.38(15)	172.82	141.62
C(2)-N(4)-C(6)	169.78(17)	177.28	173.42
C(3)-N(6)-C(7)	171.17(17)	177.43	172.65
C(4)-N(5)-C(8)	164.3(13)	177.42	171.7
Ni(1)-S(1)-Fe(1)	90.281(16)	89.31	66.84
Fe(1)-C(1)-N(3)	172.53(15)	172.53	156.73
Fe(1)-C(2)-N(4)	172.31(14)	178.65	178.29
Fe(1)-C(2)-N(5)	177.08(15)	177.99	178.49
Fe(1)-C(4)-N-(6)	171.3(8)	179.37	178.45

Torsion /º	**XRD**	***[Ni(L1)Fe(tBuNC)4]2+***	***[Ni(L1)Fe(tBuNC)4]+***
Ni(1)-S(1)-S(2)-Fe(1)	135.48(2)	129.27	95.43

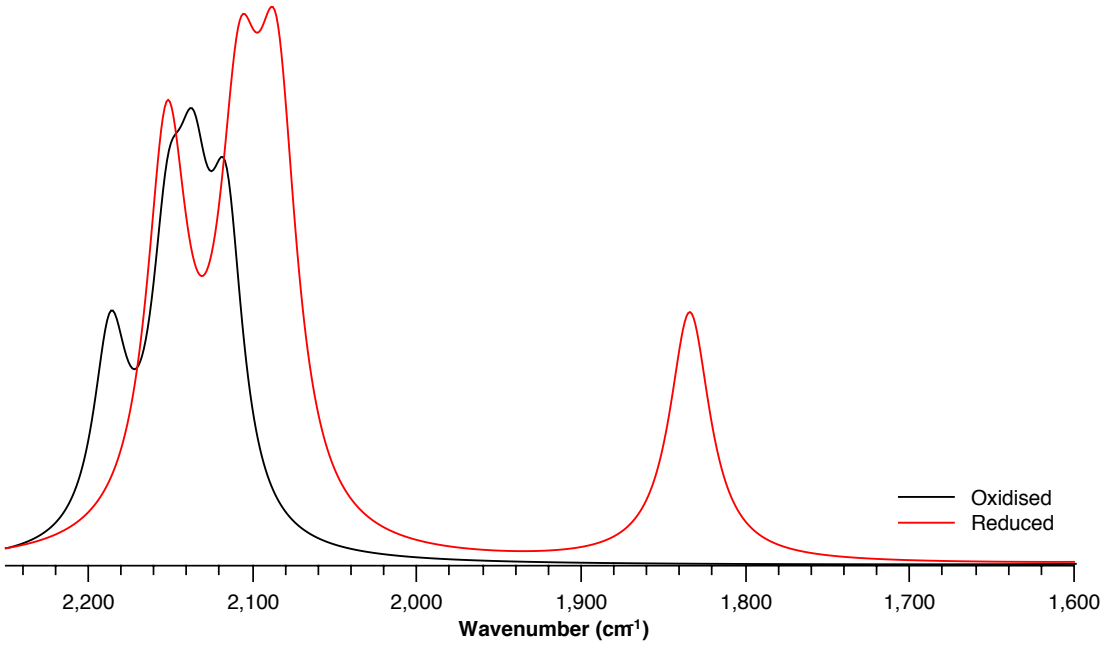


Figure 2.12.3: Simulated gas-phase IR spectra for [Ni(L1)Fe(^{t}BuNC)$_4$]$^{2+}$ (black) and [Ni(L1)Fe(^{t}BuNC)$_4$]$^+$ (red).

The calculated structure of [Ni(L1)Fe(^{t}BuNC)$_4$]$^{2+}$ reproduces the principal features of the experimentally determined structure (Section 2.7); the average Fe-C distances are *ca.* 0.01 Å longer and the Ni-S and Fe-S distances *ca.* 0.03 Å longer in the calculated structure of [Ni(L1)Fe(^{t}BuNC)$_4$]$^{2+}$ (Table 2.12.1). The principal differences between the calculated and experimental structures are (i) a relaxation of the dihedral angle defined by the S(1)-Ni(1)-S(2) and S(1)-Fe(1)-S(2) planes [129.27 º and 135.48(2) º in the calculated and experimental structures, respectively], (ii) an increase in the Ni(1)-Fe(1) distance of *ca* 0.085 Å in the calculated relative to the experimental structure of [Ni(L1)Fe(^{t}BuNC)$_4$]$^{2+}$ [Ni(1)-Fe(1) = 3.2463 Å and 3.1683(3) Å for the calculated and experimental structures, respectively, (Table 2.12.1), and (iii) an increase in the of the C-Fe(1)-C and Fe(1)-C-N angles for the axial ^{t}BuNC ligands defined by C(1) and C(4) (Table 2.12.1). The calculated IR spectrum of [Ni(L^{1}N$_2$S$_2$)Fe(^{t}BuNC)$_4$]$^{2+}$ possesses four bands in the C-N stretching region at 2186, 2149, 2138 and 2120 cm^{-1} that compare well with the experimental stretching frequencies (Table

2.10.1). Thus, the close correspondence between the calculated and experimental structures, and IR spectra suggest that the DFT calculations provide a reasonable description of the geometric and electronic structure of $[Ni(L1)Fe(^tBuNC)_4]^{2+}$.

The calculated structure of $[Ni(L1)Fe(^tBuNC)_4]^{+}$ suggests that significant changes in geometry about the Ni(1) and Fe(1) centres accompany the reduction of $[Ni(L1)Fe(^tBuNC)_4]^{+}$ [Figures 2.12.1 and 2.12.2, Table 2.12.1]. These include a marked decrease in the dihedral angle between the S(1)-Ni(1)-S(2) and S(1)-Fe(1)-S(2) planes (95.43 ° and 129.27 °, for $[Ni(L1)Fe(^tBuNC)_4]^{+}$ and $[Ni(L1)Fe(^tBuNC)_4]^{2+}$, respectively) and a shortening of the Ni(1)-Fe(1) distance [Ni(1)-Fe(1) = 2.6399 Å and 3.2463 Å for $[Ni(L1)Fe(^tBuNC)_4]^{+}$ and $[Ni(L1)Fe(^tBuNC)_4]^{2+}$, respectively. On the reduction of $[Ni(L1)Fe(^tBuNC)_4]^{2+}$ one axial ^{t}BuNC ligand, defined by C(1), moves to a bridging mode between the Fe(1) and Ni(1) centres with Fe(1)-C(1) and Ni(1)-C(1) distances of 1.9527 Å and 2.0332 Å, respectively. The adoption of a bridging mode for this ligand is accompanied by a significant bend in the backbone of the ligand [C(1)-N(3)-C(^{t}Bu) = 141.62 °], which is commonly observed for bridging isocyanides.[21] The calculated IR spectrum for $[Ni(L1)Fe(^tBuNC)_4]^{+}$ shows three intense C-N stretches at 2151, 2105 and 2088 cm^{-1} for the terminal isocyanides and a single band at 1834 cm^{-1} for the C-N stretching mode of the bridging ^{t}BuNC ligand. This calculated spectrum shows close correspondence to the experimental IR spectrum of $[Ni(L1)Fe(^tBuNC)_4]^{+}$ (Figure 2.10.1) and strongly supports a structural rearrangement in which a terminal ^{t}BuNC ligand moves to a bridging mode on the reduction of $[Ni(L1)Fe(^tBuNC)_4]^{2+}$.

The calculated SOMO of $[Ni(L1)Fe(^tBuNC)_4]^{+}$ (Figure 2.12.4) is consistent with the unpaired electron residing essentially on the [Ni(L1)] unit in the equatorial plane in a molecular orbital composed principally of the Ni $d_{x^2-y^2}$ orbital (45%) and the sulfur 3*p* orbitals (22%) and

nitrogen 2*p* orbitals (10%). This is consistent with the experimental EPR spectrum recorded for $[Ni(L1)Fe(^tBuNC)_4]^+$ (Section 2.44) and confirms the assignment of $[Ni(L1)Fe(^tBuNC)_4]^+$ to a formal Ni^IFe^{II} centre with the Ni centre adopting a d^9, S =1/2 electronic configuration.

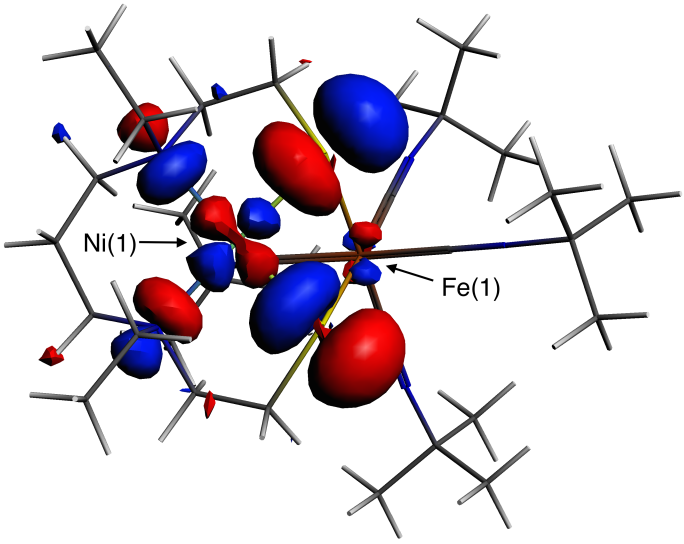


Figure 2.12.4: DFT calculated SOMO of $[Ni(L1)Fe(^tBuNC)_4]^+$ plotted with an isosurface value of 0.03 eÅ^{-3} showing unpaired electron in an equitorial molecular orbital of Ni^I.

2.13 Catalytic Studies of $[Ni(L1)Fe(^tBuCN)_4](BPh_4)_2$

Based on the data observed in the electrochemistry and IR reduction experiments and the evidence for reactivity toward small molecules, $[Ni(L1)Fe(^tBuCN)_4](BPh_4)_2$ was examined for potential catalytic behaviour with respect to protons. The experiment was carried out in a sealed three-electrode cell under argon by cyclic voltammetry under varying concentrations of TFA and at varying scan rate according to a method described by Nicholson *et al.*,[32, 33] modified and used previously in the group.[34]

Upon addition of a proton source the characteristic reversible voltammogram adopts a new shape, in the case of a reduction process, a large increase in cathodic current followed by a loss of the anodic return wave with an increasing response at higher acid concentration at a fixed

scan rate (Figure 2.13.1), reflecting a system that is giving up electrons to the H^+ in the solution (and being reoxidised in the process) and then being subsequently reduced again at the electrode. This regeneration of the species in the diffusion layer manifests in a large increase in current response from the potentiostat. No mechanism is proposed for the formation of H_2 itself; it is presumed that the reduced protons combine via some unknown mechanism to form H_2 gas.

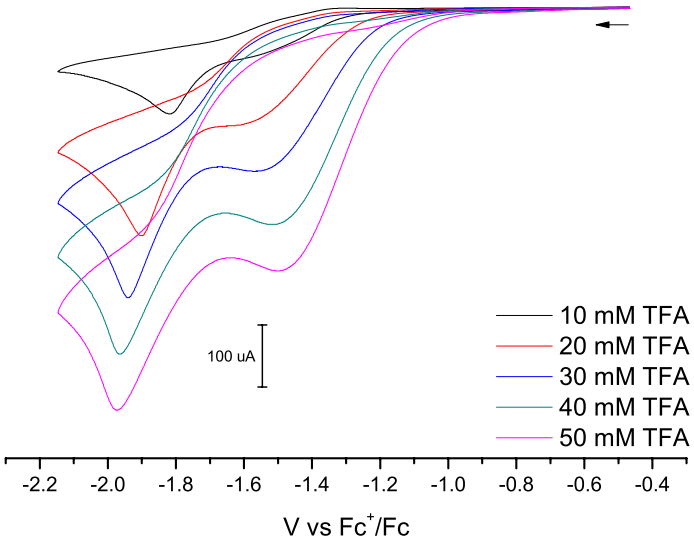


Figure 2.13.1: Cyclic voltammogram reduction process at -1.39 V of 1 mM $[Ni(L1)Fe(^tBuCN)_4](BPh_4)_2$ in MeCN with 0.2 M $[N^nBu_4][BF_4]$ as supporting electrolyte under increasing TFA concentration at 100 mVs^{-1}.

This increase in current response at the reduction potential is proportional to the scan rate at fixed TFA concentration indicating that the system has not reached a steady state under the experimental conditions. The anodic current at a fixed potential in the first reduction wave (-1.5 V vs Fc^+/Fc) plotted against the scan rate is shown in Figure 2.13.2.

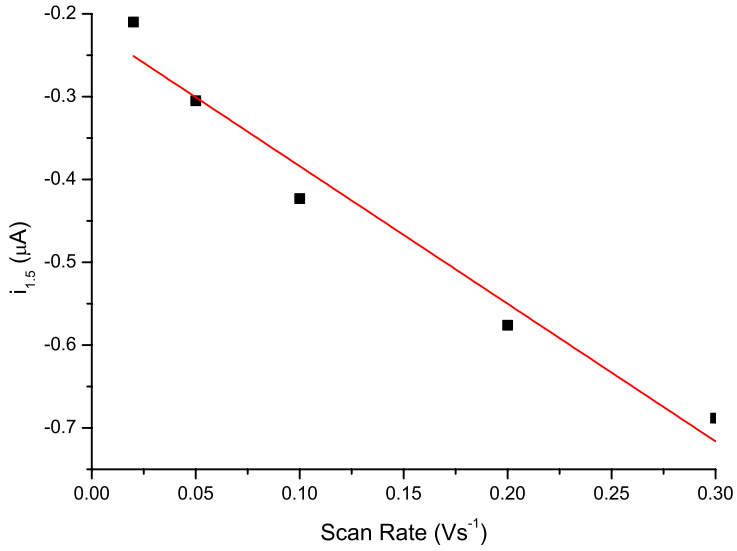


Figure 2.13.2: Plot of i at -1.5 V vs Fc^{+}/Fc vs μ for 1 mM [Ni(L1)Fe(^{t}BuCN)$_4$](BPh$_4$)$_2$ in MeCN with 0.2 M [$N^{n}Bu_4$][BF_4] at 50 mM TFA concentration demonstrating that system has not reached steady state conditions. R^2= 0.99.

Since the experiment is carried out at increasing scan rates, time is still a variable in any resulting plot. To examine the effect of the catalytic behaviour of the complex alone a plot of the current over $\mu^{0.5}$ vs μ demonstrates the potential electrocatalytic activity of [Ni(L1)Fe(^{t}BuCN)$_4$](BPh$_4$)$_2$ towards the reduction of protons (Figure 2.13.3).[32, 34]

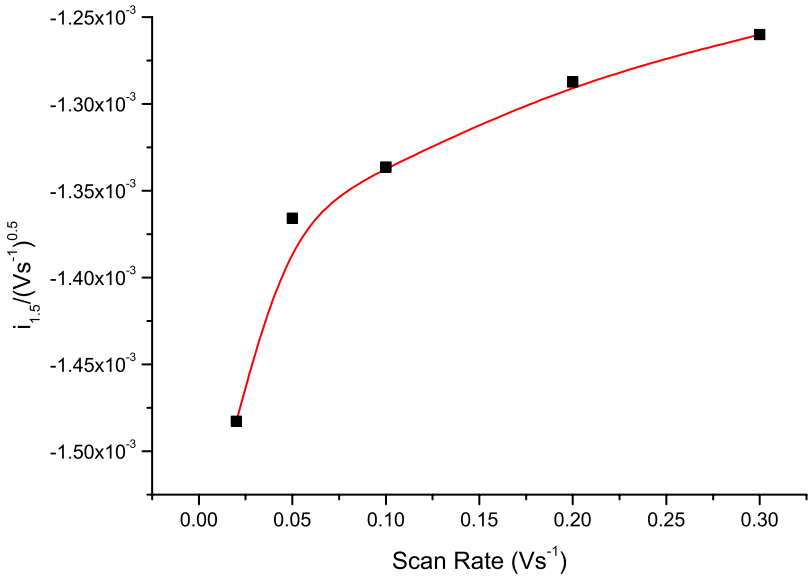


Figure 2.13.3: Plot of $i_{-1.5}/\mu^{0.5}$ vs μ for 1 mM [Ni(L1)Fe(^{t}BuCN)$_4$](BPh$_4$)$_2$ demonstrating catalytic response curve at varying scan rates with 50 mM TFA as a proton source.[34]

This catalytic response is common to the $[Ni(L1)Fe(R\text{-}CN)_4](BPh_4)_2$ complexes with an aliphatic carbon alpha to the nitrogen (R = ^{t}Bu, ^{i}Pr (Figure 2.15.4), ^{n}Bu (Figure 2.13.5) cyclohexyl, benzyl (Figure 2.13.6)), but is not observed for $[Ni(L1)Fe(PhOMe\text{-}CN)_4](BPh_4)_2$, featuring the directly attached aromatic group (Figure 2.13.7). This complex was also the only member of this group to not demonstrate evidence of a bridging band in the IR spectrum upon reduction, suggesting that this geometry change could be a key requirement for catalytic behaviour.

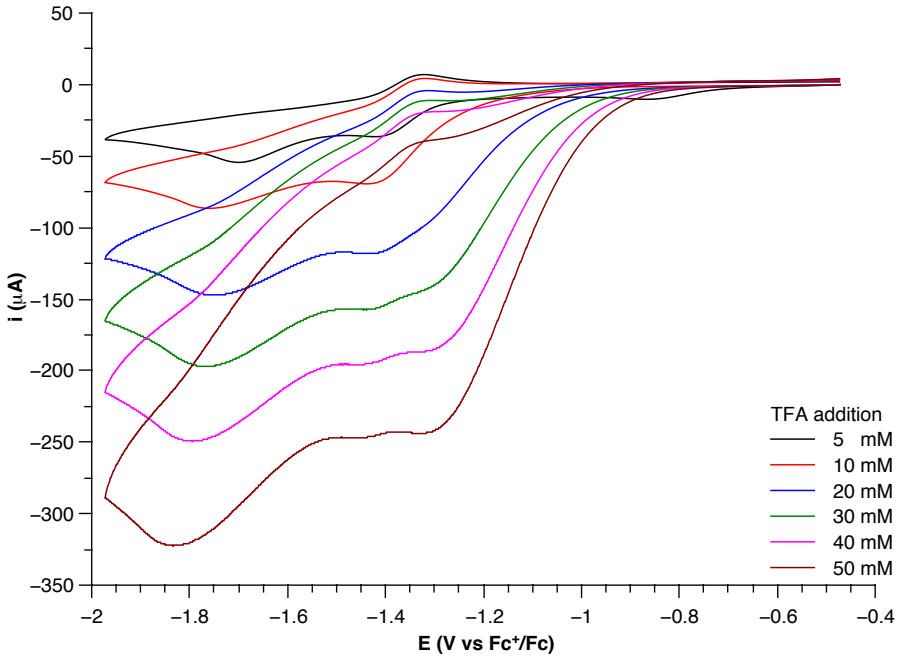


Figure 2.13.4: Cyclic voltammogram reduction process at -1.37 V of 1 mM $[Ni(L1)Fe(^{i}PrCN)_4](BPh_4)_2$ in MeCN with 0.2 M $[N^{n}Bu_4][BF_4]$ as supporting electrolyte under increasing TFA concentration at 100 mVs^{-1}.

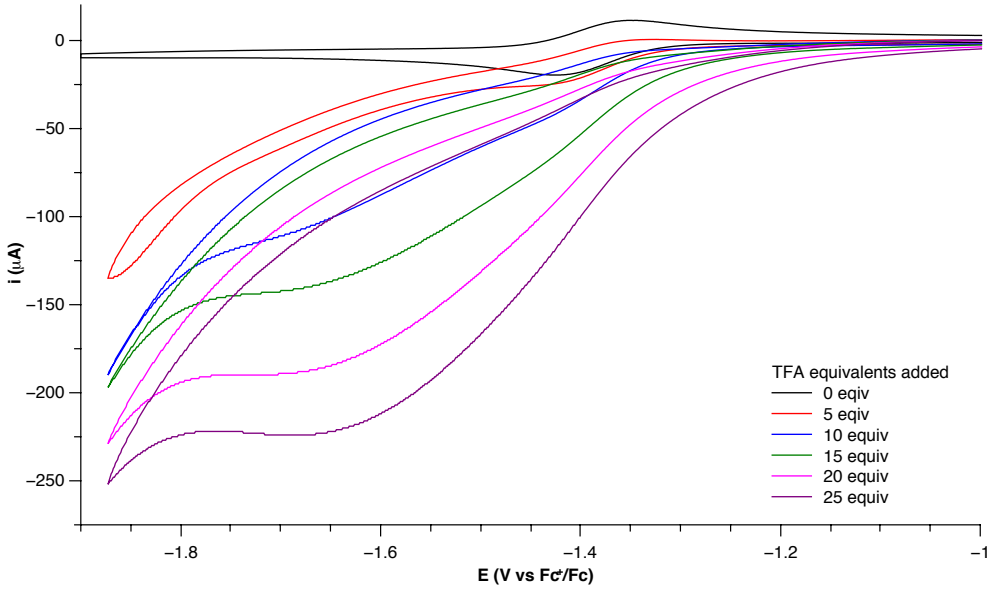


Figure 2.13.5: Cyclic voltammogram reduction process at -1.33 V of 1 mM [Ni(L1)Fe(^{n}BuCN)$_4$](BPh$_4$)$_2$ in MeCN with 0.2 M [N^{n}Bu$_4$][BF$_4$] as supporting electrolyte under increasing TFA concentration at 100 mVs^{-1}.

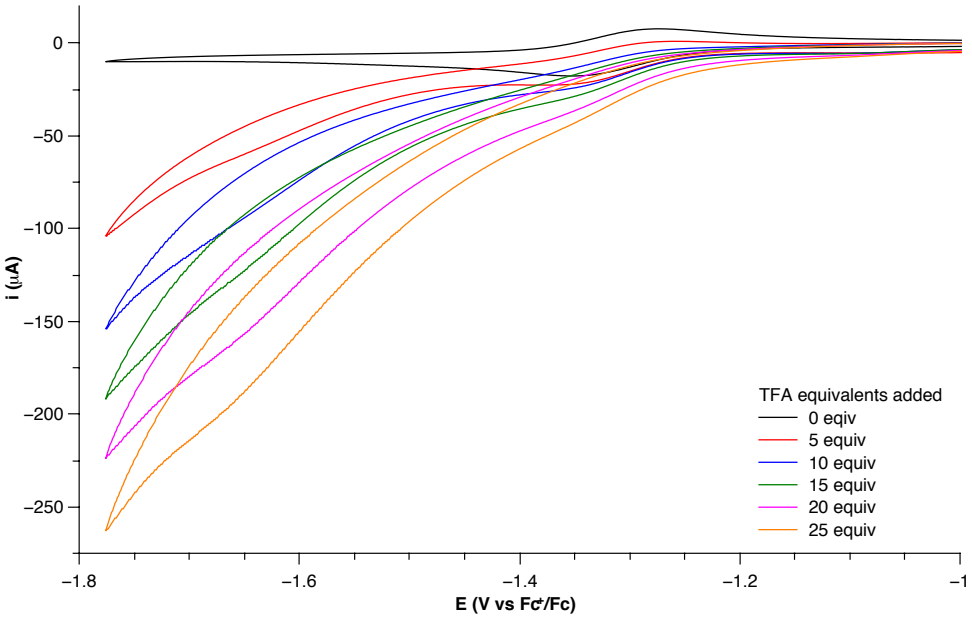


Figure 2.13.6: Cyclic voltammogram reduction process at -1.40 V of 1 mM [Ni(L1)Fe(benzyl-CN)$_4$](BPh$_4$)$_2$ in MeCN with 0.2 M [N^{n}Bu$_4$][BF$_4$] as supporting electrolyte under increasing TFA concentration at 100 mVs^{-1}

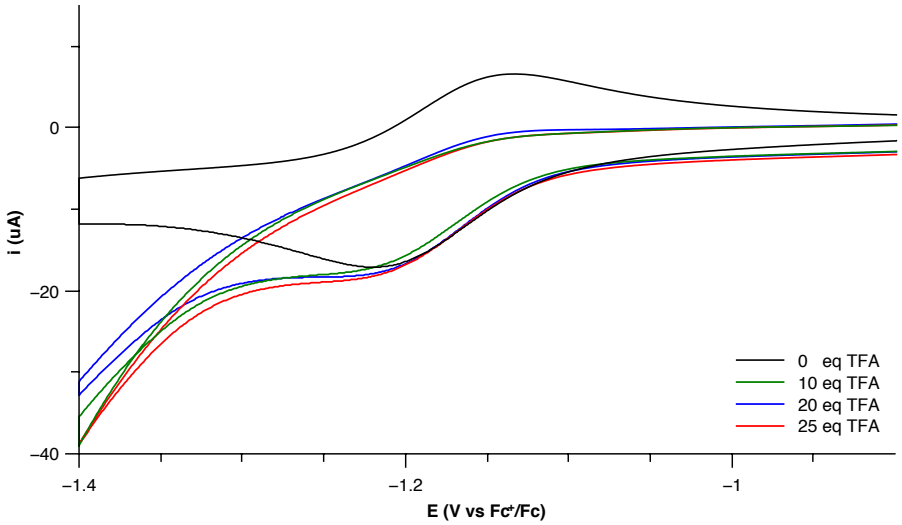


Figure 2.13.7: Cyclic voltammogram reduction process at -1.18 V of 1 mM [Ni(L1)Fe(PhOMe-CN)$_4$](BPh$_4$)$_2$ in MeCN with 0.2 M [N^{n}Bu$_4$][BF$_4$] as supporting electrolyte under increasing TFA concentration at 100 mVs^{-1} demonstrating no increasing current response.

These experiments demonstrate that [Ni(L1)Fe(R-CN)$_4$](BPh$_4$)$_2$, where (R = ^{t}Bu, ^{n}Bu, ^{i}Pr, cyclohexyl, benzyl) have the potential to act as proton reduction catalysts under the conditions of this experiment, however, further studies are required to more fully characterise this behavior. The quantification of the production of dihydrogen by gas chromatography, for example, will allow the determination of turnover number and repeated measurements will establish the stability of [Ni(L1)Fe(R-CN)$_4$](BPh$_4$)$_2$ under these conditions over the long term.

After neutralisation of the TFA by the addition of triethylamine after 45 minutes, the original cyclic voltammogram of [Ni(L1)Fe(CN-R)$_4$](BPh$_4$)$_2$ returns, indicating the stability of these complexes to acidic conditions over the timescale of the experiment (Figure 2.13.8).

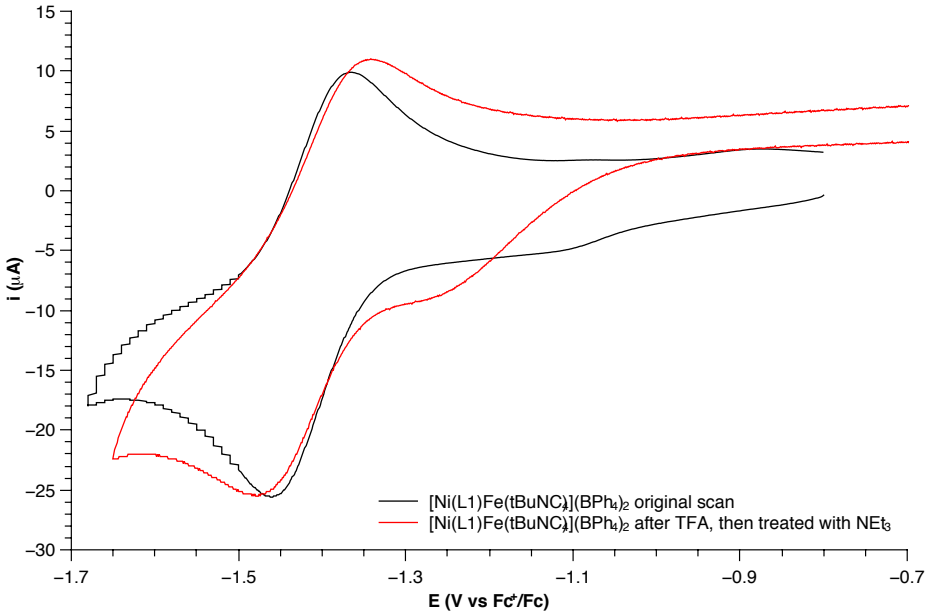


Figure 2.13.8: Recovery of the original cyclic voltammogram of [Ni(L1)Fe(^{t}BuCN)$_4$](BPh$_4$)$_2$ after 45 minutes in acidic conditions upon neutralisation of the solution with triethylamine.

2.14 Cyclic Voltammetry of [Ni(L2)Fe(^{t}BuNC)$_4$](PF$_6$)$_2$

In contrast to the complexes based on the Ni(L1) precursor that feature a propyl bridge between the amine N donors, Ni(L2) complexes with an ethyl bridge in this position, for example, [Ni(L2)Fe(^{t}BuNC)$_4$](PF$_6$)$_2$ (Figure 2.14.1), exhibit an irreversible reduction process at ca. -1.39 V vs Fc$^+$/Fc (Figure 2.14.2).

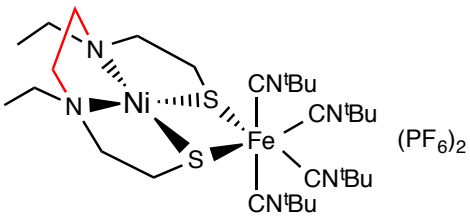


Figure 2.14.1: [Ni(L2)Fe(^{t}BuNC)$_4$](PF$_6$)$_2$ featuring ethyl backbone (red) between the amine donors in the ($L^3N_2S_2$) ligand fragment, in contrast to the propyl bridge featured in most of the complexes in this chapter.

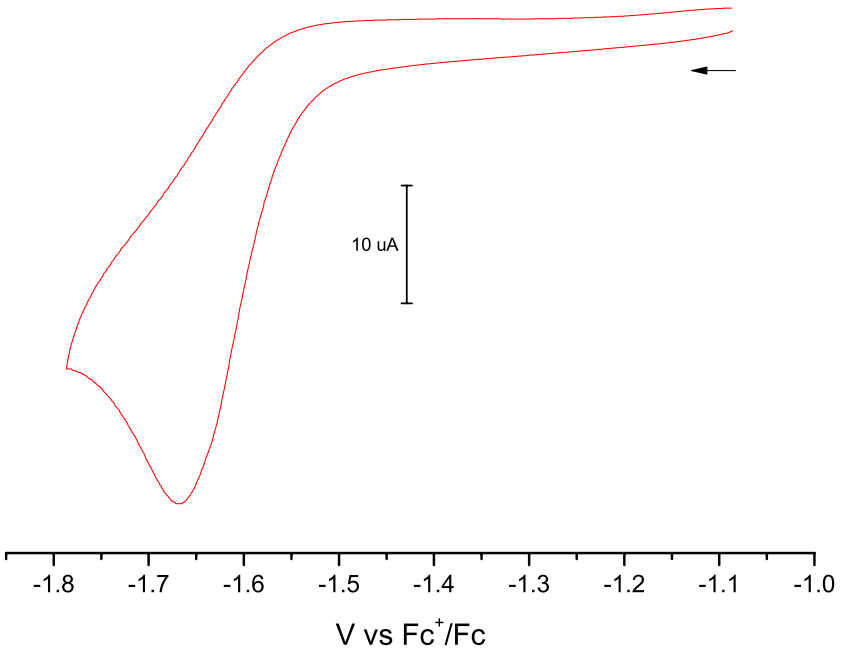


Figure 2.14.2: Cyclic voltammogram of 1 mM [Ni(L2)Fe(^{t}BuNC)$_4$](PF$_6$)$_2$ in MeCN with 0.2 M [N^{n}Bu$_4$][BF$_4$] as supporting electrolyte at 100 mVs^{-1} showing irreversible reduction process at ca. -1.6 V vs Fc$^+$/Fc.

This result suggests that the geometry around the nickel centre is a key factor in controlling the reversible behavior of the $Ni^{II/I}$ redox couple with a small perturbation in the geometry of the N_2S_2 ligand backbone having a large effect on the properties of the resulting complex. The S(1)-Ni(1)-S(2) bite angle, that is a function of the number of carbons in the backbone between N(1) and N(2) may be responsible for this difference.[13]

Attempts to grow crystals of [Ni(L2)Fe(^{t}BuNC)$_4$](PF$_6$)$_2$ for direct comparison with the coordination sphere around the Ni centre to the structure of the analogous [Ni(L1)Fe(^{t}BuNC)$_4$](BF$_4$)$_2$ were unsuccessful. With the absence of a reversible $Ni^{II/I}$ redox couple for [Ni(L2)Fe(^{t}BuNC)$_4$](PF$_6$)$_2$, no further [Ni(L2)Fe(CN-R)$_4$](PF$_6$)$_2$ were investigated.

2.15 Conclusions and Future Work

We have synthesised a range of novel [NiFe] complexes that possess a reversible $Ni^{II/I}$ reduction process couple at –1.18 to –1.40 V vs Fc^{+}/Fc. X-ray crystallographic studies demonstrate that $[Ni(L1)Fe(CN\text{-}R)_4]^{2+}$ reproduce the principal structural features of the Ni-SI form of the [NiFe] hydrogenases,[14, 15] namely the key Ni-(S_2)-Fe core. Electrochemical, UV/vis, IR and EPR spectroscopic measurements, supported by DFT calculations, demonstrate that the reduction of $[Ni(L1)Fe(CN\text{-}R)_4]^{2+}$ to $[Ni(L1)Fe(R\text{-}CN)_4]^{+}$ (R = ^{t}Bu, ^{n}Bu, ^{i}Pr, cyclohexyl, benzyl) is reversible and is associated with a structural rearrangement involving the emergence of a bridging isocyanide ligand between the Ni and Fe centres. Our studies show that the reduction is localized at the $[Ni(N_2S_2)]$ centre such that $[Ni(L1)Fe(CN\text{-}R)_4]^{+}$ may be formulated as a formal $Ni^{I}Fe^{II}$ centre. Our studies have extended the range of synthetic analogues that model the $[Ni^{I}Fe^{II}]$ electronic configuration, found in the Ni-L state of the hydrogenase enzyme.[28, 35]

Synthesis of the $[Ni(L1)Fe(^{t}BuCN)_4](BPh_4)_2$ complex using the ^{61}Ni isotope (I = 3/2)[36] to enable the study of the hyperfine structure of the EPR spectrum of the electrochemically reduced species will be carried out to enable a more detailed exploration of the electronic structure of the Ni^{I} centre of these complexes. In addition, while the the results of the catalytic experiments show some promise, the ability for $[Ni(L1)Fe(CN\text{-}R)_4](BPh_4)_2$ to produce hydrogen has yet to be proven conclusively and requires further study.

2.16 Experimental

Synthesis of N,N'-diethyl-3,7-diazanonane-1,9-dithiol (H_2L1) (**1**)

Using a modified literature procedure[10], N,N-diethylpropane 1,3-diamine (7.95 ml, 50 mmol) and ethylene sufide (6.55 ml, 60.12 mmol, 10% excess) in toluene (15 ml) was heated at 110 ºC in a pressure tube for 12 hours. The solution was cooled to room temperature and filtered to remove an insoluble white precipitate then the solvent removed *in vacuo* to leave a colourless oil which was used without further purification. (9.81 g, 94%). MS (ESI+, m/z): 250.149 (M+), ^{1}H NMR (400 MHz, $CDCl_3$) ∂ ppm, 2.64 - 2.79 (m, 2H), 2.16 - 2.63 (m, 16H), 1.59 - 1.80 (m, 2H), 1.38 - 1.59 (m, 2H), 0.85 - 1.02 (m, 6H). ^{13}C NMR (101 MHz, CD_3CN) ∂ ppm, 56.2 (CH_2), 51.0 (CH_2), 47.2 (CH_2), 24.9 (CH_2), 22.6 (CH_2), 11.7 (CH_3).

Synthesis of N,N'-diethyl-3,7-diazanonane-1,9-dithiol nickel II, Ni(L1) (**2**)

Using a modified literature procedure[10], **1** (9.80 g, 39.0 mmol) was added to a solution of $Ni(acac)_2$ (10.02 g, 39.0 mmol) in THF (60 ml) at room temperature. The solution changed colour from green to brown immediately, then additional THF (150 ml) was added and the mixture was stirred overnight. The solution was filtered to recover a purple crystalline solid that was washed with THF (3x 10 ml) and dried *in vacuo*. (8.20 g, 68%). MS (ESI+, m/z): 307.079 (M+H), 329.060 (M+Na). ^{1}H NMR (400 MHz, CD_3CN) ∂ 3.31 - 3.43 (m, 2H), 3.04 - 3.16 (m, 2H), 2.42 - 2.64 (m, 2H), 2.15 - 2.39 (m, 6H), 1.68 (dt, J = 2.45, 5 Hz, 2H), 1.37 - 1.56 (m, 2H), 1.15 - 1.30 (m, 2H), 0.64 (t, J = 7 Hz, 6H).

Synthesis of $[Ni(L1)Fe(^tBuNC)_4](BPh_4)_2$ (**3**)

Based on a modified literature procedure[11], a solution of **2** (0.1g, 0.326 mmol) in MeCN (10 ml) was added dropwise to $FeCl_2$ (0.041 g, 0.326 mmol) in MeCN (12 ml) and stirred for 3 h. The deep red solution was filtered then *tert*-butyl isocyanide (0.15 ml, 1.30 mmol) was added

dropwise and the mixture was stirred for 2 h. The solvent was removed *in vacuo* to leave a red solid residue which was dissolved in MeOH (15 ml) and an excess of $NaBPh_4$ (0.34 g, 1.0 mmol) was added to precipitate the product as a red crystalline solid which was collected by filtration then washed with MeOH (2x 5 ml) and Et_2O (2x 5 ml) and dried *in vacuo*. MS (ESI+, m/z): 347.149 (M2+, [-2(BPh_4)]), 1013.469 (M+ [-BPh_4]). ^{1}H NMR (400 MHz, CD_3CN) ∂ ppm 7.27 (br. s., 16H), 7.00 (t, J = 7 Hz, 16H), 6.76 - 6.91 (m, 8H), 2.91 - 3.06 (m, 8H), 2.80 - 2.90 (m, 4H), 2.61 - 2.77 (m, 6H), 1.81 (s, 9H), 1.49 (br. s., 27H), 1.41 (t, J = 7 Hz, 6H). ^{13}C NMR (101 MHz, CD_3CN) ∂ ppm 164.0 (C), 163.0 (C), 135.8 (CH), 125.6 (CH), 121.8 (CH), 59.4 (CH2), 56.0 (CH2), 51.0 (CH2), 31.3, 31.1, 30.9, 30.3 (CH2), 9.3 (CH3). Anal. Calcd. (%) for $C_{79}H_{100}B_2FeN_6NiS_2$: C, 71.13; H, 7.56; N, 6.30; Found: C, 70.72; H, 7.58; N, 6.21.

Synthesis of [Ni(L1)Fe(^{t}BuNC)$_4$](PF$_6$)$_2$ (3b)

Published synthesis as (**3**) except with NH_4PF_6 in place of $NaBPh_4$[28]. ^{1}H NMR (400 MHz, CD_3CN) ∂ 2.91 - 3.06 (m, 8H), 2.80 - 2.90 (m, 4H), 2.61 - 2.77 (m, 6H), 1.81 (s, 9H), 1.49 (br. s., 27H), 1.41 (t, J = 7 Hz, 6H). ^{13}C NMR (101 MHz, CD_3CN) ∂ ppm 164.0 (C), 163.0 (C), 60.0 (CH2), 56.0 (CH2), 52.0 (CH2), 31.3, 31.1, 30.9, 30.3 (CH2), 9.3 (CH3). Anal. Calcd. (%) for $C_{31}H_{60}F_{12}FeN_6NiP_2S_2$: C, 37.78; H, 6.14; N, 8.53; Found: C, 38.52; H, 6.22; N, 8.44.

Synthesis of [Ni(L1)Fe(^{n}BuNC)$_4$](BPh$_4$)$_2$ (4)

Procedure as (**3**) using *n*-butyl isocyanide (0.15 ml, 1.302 mmol) in place of *tert*-butyl isocyanide. Product is a red solid. MS (ESI+, m/z): 347.149 (M2+, [-2(BPh_4)]), 1013.47 (M+ [-BPh_4]). ^{1}H NMR (400 MHz, CD_3CN) ∂ ppm 0.96 (td, *J*=7.3, 2.1 Hz, 10H), 1.07 (t, *J*=7.4 Hz, 4H), 1.38 (t, *J*=7.1 Hz, 6H), 1.41 - 1.50 (m, 6H), 1.57 - 1.72 (m, 8H), 2.47 (d, *J*=3.5 Hz, 2H), 2.62 - 2.82 (m, 6H), 2.89 - 3.07 (m, 6H), 3.68 (t, *J*=6.4 Hz, 6H), 4.19 (t, *J*=6.6 Hz, 4H), 6.79 - 6.92 (m, 8H), 7.00 (t, *J*=7.4 Hz, 16H), 7.28 (br. s., 16H). ^{13}C NMR (101 MHz, CD_3CN) ∂ ppm

143.0 (C), 137.1 (CH), 127.0 (CH), 123.1 (CH), 63.6 (CH2), 57.1 (CH2), 52.2 (CH2), 32.5 (CH2), 32.2 (CH2), 27.8 (CH2), 20.6 (CH2), 20.5 (CH2), 13.9 (CH2), 9.8, (CH3). Anal. Calcd. (%) for $C_{79}H_{100}B_2FeN_6NiS_2$: C, 71.13; H, 7.56; N, 6.30; Found: C, 70.93; H, 7.63; N, 6.44.

Synthesis of [Ni(L1)Fe(cyclohexyl-NC)$_4$](BPh$_4$)$_2$ (5)

Procedure as (**3**) using cyclohexyl isocyanide (0.14 ml, 1.302 mmol) in place of tert-butyl isocyanide. Product is a red solid. MS (ESI+, m/z): 399.180 (M2+ [-2(BPh_4)]). ^{1}H NMR (400 MHz, CD_3CN) ∂ ppm 1.39 (t, *J*=7.1 Hz, 6 H) 1.43 - 1.54 (m, 12 H) 1.56 - 1.76 (m, 16 H) 1.77 - 1.89 (m, 10 H) 2.01 - 2.25 (m, 8 H) 2.38 - 2.49 (m, 2 H) 2.62 - 2.72 (m, 4 H) 2.77 (br. s., 2 H) 2.95 (dt, *J*=16.7, 6.9 Hz, 4 H) 6.81 - 6.90 (m, 8 H) 7.01 (t, *J*=7.5 Hz, 16 H) 7.28 (br. s, 16 H). ^{13}C NMR (101 MHz, CD_3CN) ∂ ppm 165.4 (C), 164.4 (C), 137.1 (CH), 127.0 (CH), 126.9 (CH), 123.2 (CH), 63.8 (CH2), 57.1 (CH2), 52.3 (CH2), 33.4 (CH2), 33.2 (CH2), 28.2 (CH2), 25.9 (CH2), 23.5 (CH2), 10.0 (CH3). Anal. Calcd. (%) for $C_{87}H_{108}B_2FeN_6NiS_2$: C, 72.66; H, 7.57; N, 5.84; Found: C, 71.52; H, 7.65; N, 5.87.

Synthesis of [Ni(L1)Fe(benzyl-NC)$_4$](BPh$_4$)$_2$ (6)

A solution of **2** (0.1g, 0.326 mmol) in MeCN (10 ml) was added dropwise to $FeCl_2$ (0.041 g, 0.326 mmol) in MeCN (12 ml) and the mixture was stirred for 3 h. The deep red solution was filtered and then benzyl isocyanide (0.14 ml, 1.302 mmol) was added dropwise and the mixture was stirred for 12 h. The solvent was removed *in vacuo* to leave a red solid residue, which was dissolved in MeOH (15 ml) and an excess of $NaBPh_4$ added to yield a red solid which was collected by filtration, washed with MeOH (2x 5 ml) and Et_2O (2x 5 ml) and dried *in vacuo*. The product was purified by chromatography on basic alumina (Eluent: DCM/MeOH, 99:1). The compound fraction was reduced in volume to 1-2 ml and this solution was added dropwise to a large excess of rapidly stirred Et_2O to precipitate the product as a red crystalline powder.

MS (ESI+, m/z): 415.116 (M2+ [-2(BPh_4)]). Anal. Calcd. (%) for $C_{91}H_{92}B_2FeN_6NiS_2$: C, 74.35; H, 6.31; N, 5.72; Found: C, 73.31; H, 6.08; N, 5.60.

Synthesis of [Ni(L1)Fe(^{i}Pr-NC)$_4$](BPh$_4$)$_2$ (7)

Procedure as (**3**) using isopropyl isocyanide (0.12 ml, 1.302 mmol) in place of tert-butyl isocyanide. Product is a bright red solid. MS (ESI+, m/z): 319.117 (M2+ [-2(BPh_4)]). ^{1}H NMR (400 MHz, CD_3CN) δ ppm 1.26 - 1.50 (m, 24 H) 1.70 (d, *J*=6.5 Hz, 6 H) 2.05 - 2.13 (m, 2 H) 2.47 (dd, *J*=13.7, 3.3 Hz, 2 H) 2.63 - 2.84 (m, 6 H) 2.98 (td, *J*=14.2, 6.9 Hz, 4 H) 4.00 - 4.17 (m, 3 H) 4.55 - 4.67 (m, 1 H) 6.77 - 6.91 (m, 8 H) 7.00 (t, *J*=7.4 Hz, 16 H) 7.27 (br. s., 16 H). ^{13}C NMR (101 MHz, CD_3CN) δ 164.4 (C), 137.1 (CH), 127.0 (CH), 123.1 (CH), 63.7 (CH2), 57.0 (CH2), 52.2 (CH2), 28.0 (CH2), 24.4 (CH3), 24.1 (CH2), 23.9 (CH3), 9.9 (CH3). Anal. Calcd. (%) for $C_{75}H_{92}B_2FeN_6NiS_2$: C, 70.49; H, 7.26; N, 6.58; Found: C, 69.82; H, 7.30; N, 6.53.

Synthesis of [Ni(L1)Fe(PhOMe-NC)$_4$](BPh$_4$)$_2$ (8)

Procedure as (**6**) using 4-methoxyphenyl isocyanide (0.173 g, 1.302 mmol) in MeCN (10 ml) in place of benzyl isocyanide. The product was isolated as a dark brown solid. Crystals suitable for X-ray diffraction experiments were grown from a solution of the product in nitromethane layered with MeOH. MS (ESI+, m/z): 447.106 (M2+ [-2(BPh_4)]), 1213.383 (M+ [-BPh_4]). ^{1}H NMR (300 MHz, CD_3CN) δ ppm 7.80 - 7.90 (m, 2 H) 7.63 - 7.72 (m, 1 H) 7.39 - 7.60 (m, 7 H) 7.21 - 7.33 (m, 21 H) 7.05 - 7.22 (m, 4 H) 6.93 - 7.05 (m, 28 H) 6.89 - 6.93 (m, 1 H) 6.78 - 6.88 (m, 11 H) 3.89 (s, 3 H) 3.83 (s, 3 H) 3.82 (s, 6 H) 3.13 (td, *J*=14.4, 7.4 Hz, 10 H) 2.74 - 3.00 (m, 10 H) 2.45 (br. s., 7 H) 1.35 (t, *J*=7.1 Hz, 6 H). Anal. Calcd. for $C_{87}H_{84}B_2FeN_6NiO_4S_2$: C, 71.25; H, 6.04; N, 5.48. Found: C, 70.95; H, 6.12; N, 5.49.

Synthesis of [Ni(L1)Fe(PhF-NC$_4$)](BPh$_4$)$_2$ (9)

Procedure as (**6**) using 4-fluorophenyl isocyanide (0.157 g, 1.302 mmol) in MeCN (10 ml) in place of benzyl isocyanide. Crystals suitable for X-ray diffraction experiments were recovered from the reaction flask, however no bulk product was isolated. MS (ESI+, m/z): 423.070 (M2+ [-2(BPh$_4$)]).

Attempted Synthesis of [Ni(L1)Fe(naphthyl-NC$_4$)](BPh$_4$)$_2$ (10)

Procedure as (**6**) using 2-naphthyl isocyanide (0.199 g, 1.302 mmol) in MeCN (10 ml) in place of benzyl isocyanide. No desired product was formed, with ESI-MS indicating only starting material in the solution.

Synthesis of 2,2'-(ethane-1,2-diylbis(ethylazanediyl))bis(ethane-1-thiol) (H$_2$L2) (10)

Using a modified literature procedure[10], a mixture of N,N-diethylethylenediamine (2.32 g, 20 mmol) and ethylene sufide (2.62 ml, 44 mmol, 10% excess) in toluene (15 ml) was heated at 110 ºC in a pressure tube for 12 hours. The solution was cooled to room temperature and filtered to remove any insoluble material then the solvent removed *in vacuo* to leave a very pale yellow oil (4.15 g, 88%). MS (ESI+, m/z): 237.140 (M+H)

Synthesis of Ni(L2) (11)

10 (4.15 g, 17.5 mmol) was added to a solution of Ni(acac)$_2$ (4.50 g, 17.5 mmol) in dry THF (80 ml) to effect an immediate colour change from green to brown. The solution was stirred for 12 h to precipitate a purple crystalline solid that was recovered by filtration and washed with THF (3x 5 ml) and dried in vacuo (4.30 g, 84%). MS (ESI+, m/z): 293.071 [M+H], 315.047 (M+Na)

Synthesis of [Ni(L2)Fe(^{t}BuNC)$_4$](PF$_6$)$_2$ (12)

Based on a modified literature procedure[11], a solution of **11** (0.1g, 0.326 mmol) in MeCN (10 ml) was added dropwise to $FeCl_2$ (0.041 g, 0.326 mmol) in MeCN (12 ml) and the mixture was stirred for 3 h. The deep red solution was filtered and then tert-butyl isocyanide (0.15 ml, 1.304 mmol) was added dropwise and the mixture was stirred overnight. The solvent was removed *in vacuo* to leave a red solid residue which was dissolved in MeOH (15 ml) and an excess of NH_4PF_6 was added to precipitate the product as a red crystalline solid which was collected by filtration then washed with MeOH (2x 5 ml) and Et_2O (2x 5 ml) and dried *in vacuo*. MS (ESI+, m/z): 340.141 (M2+ [-2PF$_6$]), 825.258 (M+ [-PF$_6$]).

2.17 References

1. H. Ogata, W. Lubitz and Y. Higuchi, *Dalton Trans.*, 2009, 7577-7587.
2. J. C. Fontecilla-Camps, A. Volbeda, C. Cavazza and Y. Nicolet, *Chem. Rev. (Washington, DC, U. S.)*, 2007, **107**, 4273-4303.
3. L. A. Flanagan and A. Parkin, *Biochem. Soc. Trans.*, 2016, **44**, 315-328.
4. R. Hidalgo, P. A. Ash, A. J. Healy and K. A. Vincent, *Angew. Chemiw Intl. Ed.*, 2015, **54**, 7110-7113.
5. B. E. Barton, C. M. Whaley, T. B. Rauchfuss and D. L. Gray, *J. Am. Chem. Soc.*, 2009, **131**, 6942-6943.
6. S. Ogo, K. Ichikawa, T. Kishima, T. Matsumoto, H. Nakai, K. Kusaka and T. Ohhara, *Science*, 2013, **339**, 682-684.
7. C. Perotto, University of Nottingham, 2012.
8. M. Ito, M. Kotera, Y. Song, T. Matsumoto and K. Tatsumi, *Inorg. Chem.*, 2009, **48**, 1250-1256.
9. S. Ogo, R. Kabe, K. Uehara, B. Kure, T. Nishimura, S. C. Menon, R. Harada, S. Fukuzumi, Y. Higuchi, T. Ohhara, T. Tamada and R. Kuroki, *Science*, 2007, **316**, 585-587.
10. F. Osterloh, W. Saak and S. Pohl, *J. Am. Chem. Soc.*, 1997, **119**, 5648-5656.
11. T. B. Rauchfuss, S. M. Contakes, S. C. N. Hsu, M. A. Reynolds and S. R. Wilson, *J. Am. Chem. Soc.*, 2001, **123**, 6933-6934.
12. C.-H. Lai, J. H. Reibenspies and M. Y. Darensbourg, *Angew. Chemiw Intl. Ed.*, 1996, **35**, 2390-2393.
13. J. A. Denny and M. Y. Darensbourg, *Chem Rev*, 2015, **115**, 5248-5273.
14. A. Volbeda, M. H. Charon, C. Piras, E. C. Hatchikian, M. Frey and J. C. Fontecilla-Camps, *Nature*, 1995, **373**, 580-587.
15. A. Volbeda, E. Garcin, C. Piras, A. L. de Lacey, V. M. Fernandez, E. C. Hatchikian, M. Frey and J. C. Fontecilla-Camps, *J. Am. Chem. Soc.*, 1996, **118**, 12989-12996.
16. J. Schneider, R. Hauptmann, F. Osterloh and G. Henkel, *Acta Crystallographica Section C Crystal Structure Communications*, 1999, **55**, 328-330.
17. P. K. Pal, S. Chowdhury, M. G. B. Drew and D. Datta, *New J. Chem.*, 2002, **26**, 367-371.
18. M. V. Rampersad, S. P. Jeffery, M. L. Golden, J. Lee, J. H. Reibenspies, D. J. Darensbourg and M. Y. Darensbourg, *J. Am. Chem. Soc.*, 2005, **127**, 17323-17334.
19. G. L. Geoggroy and M. S. Wrighton, *Organometallic Photochemistry*, Academic Press, USA, 1979.
20. N. G. Connelly and W. E. Geiger, *Chem. Rev. (Washington, DC, U. S.)*, 1996, **96**, 877-910.
21. A. Vogler, *Isonitrile Chemistry*, Academic Press, New York, 1971.
22. J. M. Basset, R. Psaro, D. Roberto and R. Ugo, *Modern Surface Organometallic Chemistry*, Wiley, 2009.
23. F. P. Pruchnik, *Organometallic Chemistry of the Transition Elements*, Springer US, New York, 1990.
24. P. W. Atkins, T. Overton, J. Rourke, M. Weller and F. A. Armstrong, *Shriver & Atkins' Inorganic Chemistry*, Oxford University Press, Oxford; New York, 2010.
25. P. J. Farmer, J. H. Reibenspies, P. A. Lindahl and M. Y. Darensbourg, *J. Am. Chem. Soc.*, 1993, **115**, 4665-4674.
26. D. Schilter, M. J. Nilges, M. Chakrabarti, P. A. Lindahl, T. B. Rauchfuss and M. Stein, *Inorg. Chem.*, 2012, **51**, 2338-2348.

27. J. H. MacNeil, A. C. Chiverton, S. Fortier, M. C. Baird, R. C. Hynes, A. J. Williams, K. F. Preston and T. Ziegler, *J. Am. Chem. Soc.*, 1991, **113**, 9834-9842.
28. C. U. Perotto, G. Marshall, G. J. Jones, E. Stephen Davies, W. Lewis, J. McMaster and M. Schroder, *Chem. Commun. (Cambridge, U. K.)*, 2015, **51**, 16988-16991.
29. A. G. Lappin and A. McAuley, *Adv. Inorg. Chem.*, 1988, **32**, 241-295.
30. G. te Velde, F. M. Bickelhaupt, E. J. Baerends, C. Fonseca Guerra, S. J. A. van Gisbergen, J. G. Snijders and T. Ziegler, *J. Comput. Chem.*, 2001, **22**, 931-967.
31. E. Van Lenthe and E. J. Baerends, *J. Comput. Chem.*, 2003, **24**, 1142-1156.
32. R. S. Nicholson, *Anal. Chem.*, 1966, **38**, 1406-1406.
33. R. S. Nicholson and I. Shain, *Anal. Chem.*, 1964, **36**, 706-723.
34. A. Perra, E. S. Davies, J. R. Hyde, Q. Wang, J. McMaster and M. Schroder, *Chem. Commun. (Cambridge, U. K.)*, 2006, 1103-1105.
35. H. Tai, K. Nishikawa, S. Inoue, Y. Higuchi and S. Hirota, *J. Phys. Chem. B*, 2015.
36. I. Mills, T. Cvitas, K. Homann, N. Kallay and K. Kuchitsu, *Quantities, Units and Symbols in Physical Chemistry*, Blackwell Scientific Publications, Oxford, UK, 1988.

Chapter Three

Analogues of the Ni-C State of the Hydrogenase Active Site – Complexes that Stabilise the Ni^{III} Oxidation State

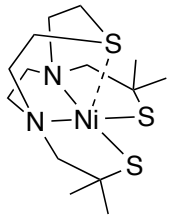
3.1 Introduction and aims

At least ten different states of the [NiFe] hydrogenases have been identified (see Chapter 1) with formulations that vary with the oxidation state of the Ni centre (i.e. Ni^{III}, Ni^{II} and Ni^{I}). The importance of each state in the catalytic cycle continues to be debated, however, it is widely accepted that catalytic turnover is associated with changes of the formal oxidation state of the Ni center while the Fe center remains as low spin Fe^{II}. A key feature of the [NiFe] hydrogenases is an accessible Ni^{III} state [$E_{½}$ ($Ni^{III/II}$) = -150.5 to -435.5 mV *vs.* SHE for *D. vulgaris* Miyazaki F][1, 2] that plays a crucial role in the catalytic activation of H_2.

A range of analogues of the active site of the [NiFe] hydrogenases have been synthesized and characterized in attempts to replicate the principal structural and functional features of the active sites of the [NiFe] hydrogenases (see Chapter 1).[3-5] There has been considerable success in reproducing key aspects of the proposed catalytic cycle for the [NiFe] hydrogenases and in the development of complexes containing a [$Ni^{II}Fe^{II}$] centre.[5] However, the syntheses of relevant paramagnetic analogues have proven more challenging; typically the redox events in these complexes are associated principally with the Fe center rather than the Ni unit.[6] In particular, complexes possessing a [$Ni^{III}Fe^{II}$] electronic configuration, characteristic of the Ni-C, Ni-SI, Ni-A and Ni-B states,[7-9] have proven more difficult to realize and the aim of this Chapter is to synthesise and characterise [NiFe] complexes that support oxidation processes that are localized at the Ni-centre. Our principal aim is to reproduce the proposed redox changes associated with the formation of the Ni-C state of the hydrogenases.[10]

Our approach employs 1,1'-(1,4,7-thiadiazonane)bis(2-methylpropane-2-thiolato)nickel(II)**,** [Ni(L3)] (Figure 3.1.1) as the Ni-containing unit. Our group has shown previously that [Ni(L3)] can support an electrochemically reversible oxidation process at -0.597 V *vs* Fc^{+}/Fc,[11, 12] which

may be assigned to a formal $Ni^{III/II}$ couple. In this chapter we explore the combination of [Ni(L3)] with $[Fe(R\text{-}NC)_4]^{2+}$ (R = ^{t}Bu, cyclohexyl, benzyl) fragments to develop new [NiFe] complexes that may have the potential to support a Ni-based oxidation process, relevant to the Ni-C state of the [NiFe] hydrogenases.

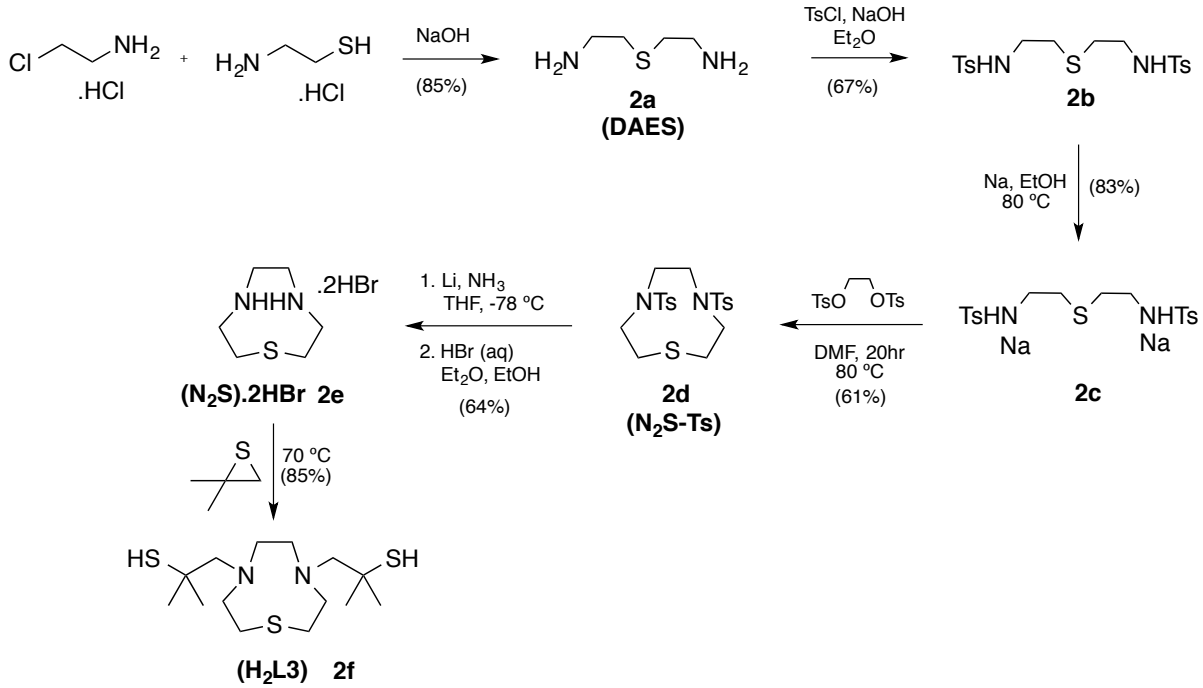


[Ni(L3)]

Figure 3.1.1: 1,1'-(1,4,7-thiadiazonane)bis(2-methylpropane-2-thiolato)nickel(II), [Ni(L3)]

3.2 The synthesis of the [H_2L3] ligand

$[L3]^{2-}$ has been reported previously and shown to co-ordinate Fe^{II} and Ni^{II}.[13, 14] In this work we have optimized and improved the synthesis (Scheme 3.2.1) of [H_2L3] and [Ni(L3)] to improve the yield of these compounds.



Scheme 3.2.1: A modified scheme for synthesis of (H_2L3) ligand.

Diaminoethylene sulfide (DAES) (**2a**) was prepared according to literature procedures.[15] A basic aqueous solution of DAES oil was added to tosyl chloride in Et_2O at 0 ºC to yield [DAES-Ts] (**2b**) as a precipitate. **2b** was converted to the disodium salt (**2c**) by the reaction of **2b** in EtOH at 80 ºC with sodium metal. **2c** was isolated as a sticky white paste that dries to a chalky solid after being placed under vacuum. **2c** was then treated with ethylenedi(*p*-toluenesulfonate) in DMF at 80 ºC under high dilution conditions over 20 hours. After reducing the volume of DMF the macrocycle [N_2S-Ts] (**2d**) was isolated as a cream coloured solid following the pouring of the reaction mixture into a large volume of ice water. Recrystallisation of the crude product from DCM/MeOH gave **2d** as a fine white powder in excellent yield (61 %). The conditions for this step were optimised to improve the overall yield of the reaction considerably, especially for the macrocyclic product (*ca.* 35-40% improvement over previous synthesis within the group).

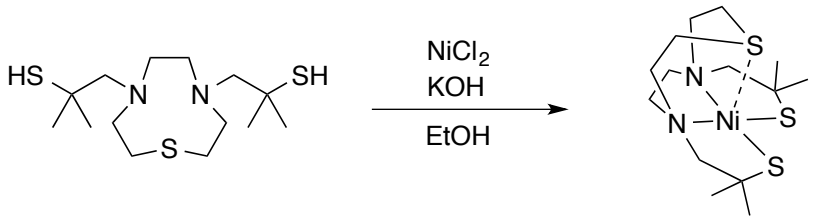
The published method for the removal of the tosyl protecting groups in **2d** involves the boiling of **2d** in glacial acetic acid for several days.[14] We have developed a more effective and time-efficient method that employs a modified Birch reduction[16, 17] followed by an aqueous work up to yield unprotected macrocycle as the HBr salt (**2e**). The deprotection is complete after 12 h. Lithium metal was added in portions to a solution of **2d** in THF and liquid ammonia with a catalytic quantity of EtOH at -78 ºC over 30 minutes. The reaction mixture was then warmed to room temperature overnight over which period the ammonia evaporated to leave a THF solution. Following work up and the addition of HBr (36% w/v) **2e** was isolated as a white crystalline solid.

In a modification to the literature procedure,[13] **2e** was reacted with neat isobutylene sulfide, prepared according to literature procedures,[18] without solvent in a pressure tube at 70 ºC for 2

hours. These conditions were sufficient to yield the [H_2L3] dithiol product, **2f**, as a colourless oil after removal of excess isobutylene sulfide *in vacuo*. The shorter reaction time associated with our modified procedure eliminates the formation of insoluble by-products and yields a product that was suitable for use without further purification.

3.3 The synthesis of [Ni(L3)]

[Ni(L3)] was synthesised by the dropwise addition of a solution of (H_2L3), **2f**, in dry EtOH with anhydrous $NiCl_2$ and KOH in EtOH (Scheme 3.3.1). The solution turned brown almost immediately and KCl precipitated.



(H_2L3) 2f **[Ni(L3)] 2g**

Scheme 3.3.1: Synthesis of [Ni(L3)]

The solution was filtered then the solvent removed *in vacuo* to leave a brown solid that was extracted in DCM and subsequently in MeCN to yield the product as a dark brown/purple solid, [Ni(L3)]. The formulation of [Ni(L3)] was confirmed by mass spectrometry and by elemental analysis.

3.4 The X-ray crystal structure of [Ni(L3)]

Crystals of [Ni(L3)] suitable for X-ray diffraction were grown from vapour of diffusion Et_2O into a solution of [Ni(L3)] in a MeCN. Crystals of [Ni(L3)] are dark green in colour and crystallise in the $P2_1/n$ space group. The colour of the crystals contrasts with the dark

purple/brown colour of [Ni(L3)] in its powder form. The molecular structure of [Ni(L3)] is shown in Figure 3.4.1, and selected bond lengths and angles are shown in Table 3.4.1.

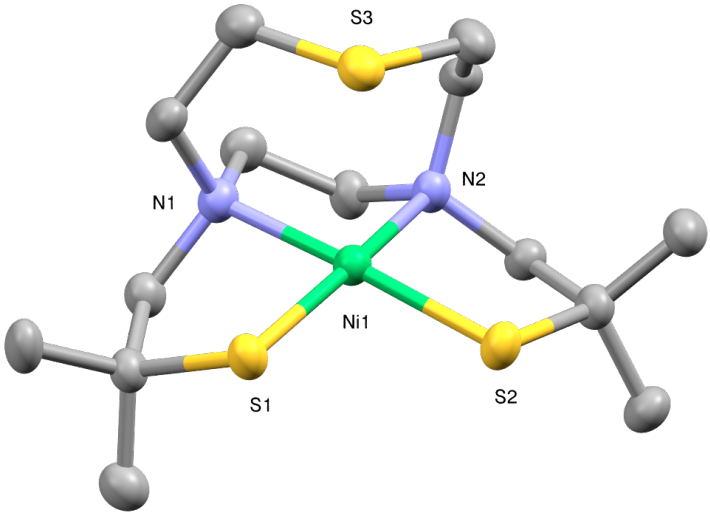


Figure 3.4.1: X-ray crystal structure of [Ni(L3)] with thermal ellipsoids at 50%. Hydrogen atoms omitted for clarity.

Table 3.4.1: Selected bond lengths and angles for [Ni(L3)]

Bond	**Length /Å**	**Atoms**	**Angle /º**	**Atoms**	**Angle /º**
Ni(1)-N(1)	1.983(4)	N(1)-Ni(1)-N(2)	87.1(2)	S(1)-Ni(1)-N(2)	171.1(1)
Ni(1)-N(2)	1.970(4)	S(1)-Ni(1)-S(2)	94.87(6)	N(1)-Ni(1)-S(3)	83.0(1)
Ni(1)-S(1)	2.188(1)	N(1)-Ni(1)-S(1)	87.2(1)	S(1)-Ni(1)-S(3)	98.72(5)
Ni(1)-S(2)	2.175(2)	N(2)-Ni(1)-S(2)	90.1(1)		
Ni(1)-S(3)	2.820(2)	N1(1)-Ni(1)-S(2)	173.7(1)	$\tau = 0.04$	

The Ni^{II} centre adopts an approximately square pyramidal geometry through the coordination of the two amine [N(1) and N(2)] and two thiolate [S(1) and S(2)] donors, with a weakly coordinating thioether moiety S(3) above the plane. The degree of distortion within pentacoordinate structures from an ideal square pyramidal towards a trigonal bipyramidal geometry may be assessed quantitatively by considering the structural index parameter $\tau = (\beta-\alpha)/60$ where β is the largest basal angle, N(1)-Ni(1)-S(2) and α = S(1)-Ni(1)-N(2) for [Ni(L3)].[19] For regular square pyramidal and trigonal bipyramidal geometries $\tau = 0$ and 1, respectively. For [Ni(L3)] $\tau = 0.04$ confirming an essentially square pyramidal geometry for

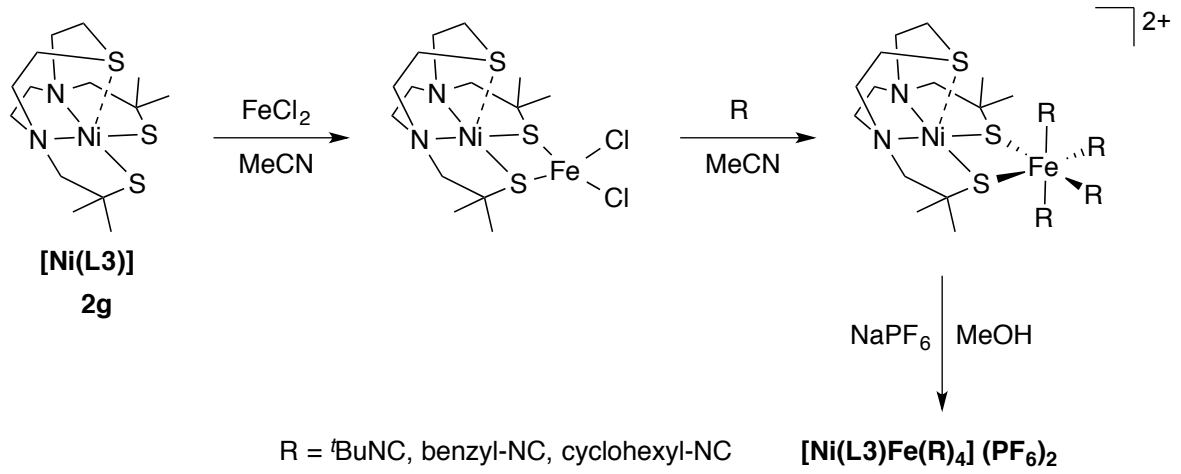
[Ni(L3)]. The structure of [Ni(L3)] agrees well with a previously reported structure of [Ni(L3)] reported by Grapperhaus *et al.*[20] with bond distances and angles showing no significant differences between one another in the two structures.

3.5 The attempted syntheses of [Ni(L3)](PF_6) and [Ni(L3)](BF_4)

We attempted to prepare, crystallize and determine the X-ray crystal structures of [Ni(L3)](PF_6) and [Ni(L3)](BF_4) for direct comparison with that of [Ni(L3)] (Section 3.4). An MeCN solution of [Ni(L3)] was treated with ferrocinium hexafluorophosphate ($FcPF_6$) at -20 ºC.[21] The brown solution turned deep blue on the addition of $FcPF_6$, which then gradually changed to green over approximately 15 minutes. The solvent was removed *in vacuo* to leave a dark solid that was washed with ice cold Et_2O, which turned orange as the ferrocene by-product was removed. Attempts to recrystallize the solid residue by the vapour diffusion of Et_2O into a solution of the crude product in MeCN, the layering of Et_2O onto a solution of the crude product in MeCN and the evaporation of MeCN from a solution of the crude product were made but no crystals suitable for X-ray diffraction were isolated. Crystallisation of the complex directly from the reaction mixture by layering with Et_2O and storage at -15 ºC without removing the ferrocene by-product was also attempted without success. We also attempted to oxidise [Ni(L3)] with $AgBF_4$ in DCM[21] at -20 ºC. This reaction yielded a brown precipitate that was dissolved in MeCN and layered with Et_2O, however, no crystals suitable for X-ray diffraction were obtained.

3.6 The syntheses of $[Ni(L3)Fe(R\text{-}NC)_4](PF_6)_2$, (R = tBu, cyclohexyl, benzyl)

$[Ni(L3)Fe(R\text{-}NC)_4](PF_6)_2$ was synthesised by the dropwise addition of $FeCl_2$ in MeCN to [Ni(L3)] in MeCN followed by dropwise addition of the selected isocyanide either as a neat liquid or in MeCN solution. (Scheme 3.6.1).



Scheme 3.6.1: General synthesis of $[Ni(L3)Fe(R\text{-}NC)_4](PF_6)_2$ complexes

Each reaction mixture was left to stir for 12 hours before the solvent was removed *in vacuo*, the solid dissolved in MeOH then the $[Ni(L3)Fe(R\text{-}NC)_4](PF_6)_2$ precipitated by the addition of $NaPF_6$. The product was purified variously by crystallisation directly from MeOH solution or by chromatography on basic alumina (eluent 99:1 DCM/MeOH) under anerobic conditions. The formulation of each $[Ni(L3)Fe(R\text{-}NC)_4](PF_6)_2$ was established by mass spectrometry and by elemental analysis.

3.7.1 The synthesis and X-ray crystal structure of $[Ni(L3)[Fe(CN^tBu)_4](PF_6)_2$

$[Ni(L3)[Fe(^tBuNC)_4](PF_6)_2$ was synthesised via Scheme 3.6.1 above, using *tert*-butyl isocyanide as the ligand about the Fe centre. The complex was isolated as a red crystalline solid via preciptation from MeOH. Crystals suitable for X-ray diffraction studies were grown via slow evaporation from a MeOH solution over 96 hours. $[Ni(L3)[Fe(^tBuNC)_4](PF_6)_2$ crystallises

in the $P2_1/c$ space group. The structure of the $[Ni(L3)[Fe(^tBuNC)_4]^{2+}$ cation is shown in Figure 3.7.1 and selected bond lengths and angles are shown in Table 3.7.1.

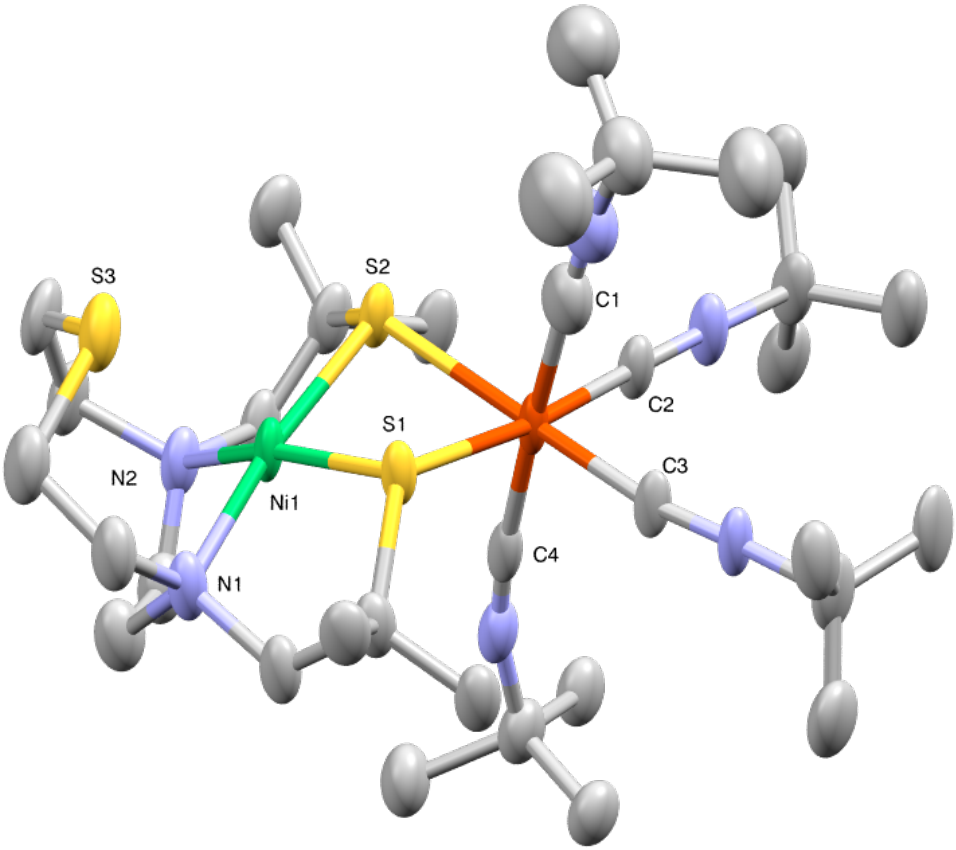


Figure 3.7.1: The X-ray crystal structure of $[Ni(L3)[Fe(^tBuNC)_4](PF_6)_2$ with thermal ellipsoids at 50%. Hydrogen atoms and $(PF_6)^-$ anions omitted for clarity.

Table 3.7.1: Selected bond lengths and angles for $[Ni(L3)[Fe(^tBuNC)_4](PF_6)_2$.

Bond	**Length /Å**	**Bond Angle**	**Angle /º**	**Bond Angle**	**Angle /º**
Ni(1)-N(1)	1.97(1)	N(1)-Ni(1)-N(2)	88.7(6)	S(1)-Fe(1)-C(2)	173.2(5)
Ni(1)-N(2)	1.97(1)	S(1)-Ni(1)-S(2)	87.5(1)	C(1)-Fe(1)-C(4)	177.6(7)
Ni(1)-S(1)	2.183(3)	S(1)-Ni(1)-N(1)	89.7(4)		
Ni(1)-S(2)	2.179(4)	S(2)-Ni(1)-N(2)	91.8(4)	$\tau = 0.15$	
Ni(1)-S(3)	2.615(5)	S(1)-Ni(1)-N(2)	162.9(4)		
Fe(1)-S(1)	2.356(3)	S(2)-Ni(1)-N(1)	172.1(4)		
Fe(1)-S(2)	2.338(4)	S(1)-Ni(1)-S(3)	108.4(2)		
Fe(1)-C(1)	1.85(2)	N(1)-Ni(1)-S(3)	85.7(4)		
Fe(1)-C(2)	1.83(1)	S(1)-Fe(1)-C(1)	86.0(6)		
Fe(1)-C(3)	1.87(1)	S(2)-Fe(1)-C(1)	85.5(6)		
Fe(1)-C(4)	1.88(2)	S(1)-Fe(1)-C(3)	93.7(4)		
Ni(1)-Fe(1)	3.111(3)	S(2)-Fe(1)-C(2)	96.7(5)		

$[Ni(L3)Fe(CN^tBu)_4](PF_6)_2$ adopts a similar solid state structure to the analogous $[Ni(L1)Fe(CN^tBu)_4](BF_4)_2$ compound discussed in Chapter 2 and reported by us previously.[22]

The Ni centre in $[Ni(L3)Fe(^tBuNC)_4]^{2+}$ possesses an approximate square pyramidal geometry and is coordinated by five heteroatoms derived from the pentadentate ligand, $(L3)^{2-}$. The $Ni(N_2S_3)$ fragment retains the structural features of the precursor [Ni(L3)] with Ni(1)-S(1) and Ni(1)-S(2) distances [2.183(3) and 2.179(4) Å] that are similar to Ni-S bond lengths observed in other four coordinate Ni^{II} complexes.[23-25] The most significant differences in the geometry of the $Ni(N_2S_3)$ fragment in [Ni(L3)] and $[Ni(L3)Fe(^tBuNC)_4]^{2+}$ are a smaller S(1)-Ni(1)-S(2) angle of [87.5(1)º *vs* 94.87(6)º for the free [Ni(L3)] precursor] and a shorter Ni(1)-S(3) distance [2.615(5) *vs* 2.820(2) Å for the free [Ni(L3)] precursor] induced by the coordination of the $[Fe(^tBuNC)_4]^{2+}$ fragment. The structural index parameter (τ = 0.15, Table 3.7.1) for the $Ni(N_2S_3)$ unit in $[Ni(L3)Fe(^tBuNC)_4]^{2+}$ is greater than that for the [Ni(L3)] precursor (τ = 0.04, Table 3.4.1) that reveals a small distortion towards a trigonal pyramidal geometry on the coordination of the $[Fe(^tBuNC)_4]^{2+}$ fragment to [Ni(L3)]. The Fe atom in $[Ni(L3)Fe(^tBuNC)_4]^{2+}$ occupies a pseudo-octahedral environment where [Ni(L3)] acts as a bidentate ligand through the two bridging thiolate donors S(1) and S(2) and in which four ^{t}BuNC ligands complete the coordination sphere. The Fe-C distances for the isocyanides are not significantly different from one another and range from 1.83 to 1.88 Å, and compare well with other Fe-C distances for previously published Fe-isocyanide complexes that range from 1.82 to 1.99 Å.[26-28] The Fe-C-N bond angles are essentially linear, ranging from 171.2(13) º to 177(2) º. The Ni(1)-C(4) distance [3.24(1) Å] is considerably longer than the Fe(1)-C(4) distance [1.88(2) Å] and, therefore, excludes a bridging mode for the ^{t}BuNC ligand defined by atom C(4). The Ni-(S_2)-Fe moiety approximates the core structure of the active site of the

[NiFe] hydrogenase from *Desulfovibrio gigas* in the Ni-SI state, the Fe(1) and Ni(1) centres in $[Ni(L3)Fe(^{t}BuNC)_4]^{2+}$ are separated by 3.111(3) Å, which is longer than the Ni-Fe distances (2.9 Å) for the Ni-SI state of the [NiFe] hydrogenase from *D. gigas*.[29]

3.7.2 The synthesis of $[Ni(L3)Fe(benzyl\text{-}NC)_4](PF_6)_2$

$[Ni(L3)[Fe(benzyl\text{-}NC)_4](PF_6)_2$ was synthesised using the methods shown in Scheme 3.6.1, using benzyl isocyanide as the ligand about the Fe centre. The complex was isolated as a dark solid by preciptation from MeOH and subsequent purification via anaerobic column chromatography (99:1 DCM/MeOH). The solvent was removed *in vacuo* to leave the product as a deep red oil. This oil was dissolved in a minimum volume of DCM (2 ml) and the product was preciptated by the addition of this solution dropwise to rapidly swirling Et_2O (60 ml). The product was recovered as a fine brown powder. Attempts to grow crystals suitable for X-ray diffraction were made by the slow evaporation from a MeOH solution of $[Ni(L3)[Fe(benzyl\text{-}NC)_4](PF_6)_2$, by Et_2O vapour diffusion into MeCN solution of $[Ni(L3)[Fe(benzyl\text{-}NC)_4](PF_6)_2$ and by the layering of Et_2O onto a solution of $[Ni(L3)[Fe(benzyl\text{-}NC)_4](PF_6)_2$ in MeCN. However, no crystals suitable for analysis were recovered. Crystalline samples of $[Ni(L3)[Fe(benzyl\text{-}NC)_4](PF_6)_2$ were taken to the Diamond Light Source in Oxford, however, these samples also exhibited poor diffraction.

3.7.3 The attempted synthesis of $[Ni(L3)Fe(cyclohexyl\text{-}NC)_4](PF_6)_2$

Attempts to isolate $[Ni(L3)[Fe(cyclohexyl\text{-}NC)_4](PF_6)_2$ using the method outlined in Scheme 3.6.1 were made, using cyclohexyl isocyanide as the ligand about the Fe centre. Although the desired product was detected by mass spectroscopy in solution and a crude red solid was obtained by the precipitation of the crude product from a MeOH solution, no pure sample was

isolated. Attempts to purify the product via anaerobic column chromatography (eluent 99:1, DCM/MeOH) were unsuccessful.

3.8 Electrochemical studies of [Ni(L3)Fe(R-NC)$_4$](PF$_6$)$_2$, R = (^{t}Bu, benzyl)

3.8.1 Electrochemical studies of [Ni(L3)Fe(^{t}BuNC)$_4$](PF$_6$)$_2$

[Ni(L3)Fe(^{t}BuNC)$_4$](PF$_6$)$_2$ demonstrates an electrochemically reversible process at $E_{½}$ = 0.15 V *vs* Fc^+/Fc (Figure 3.8.1) in MeCN solution with 0.2 M [N^nBu_4][BF_4] as supporting electrolyte.

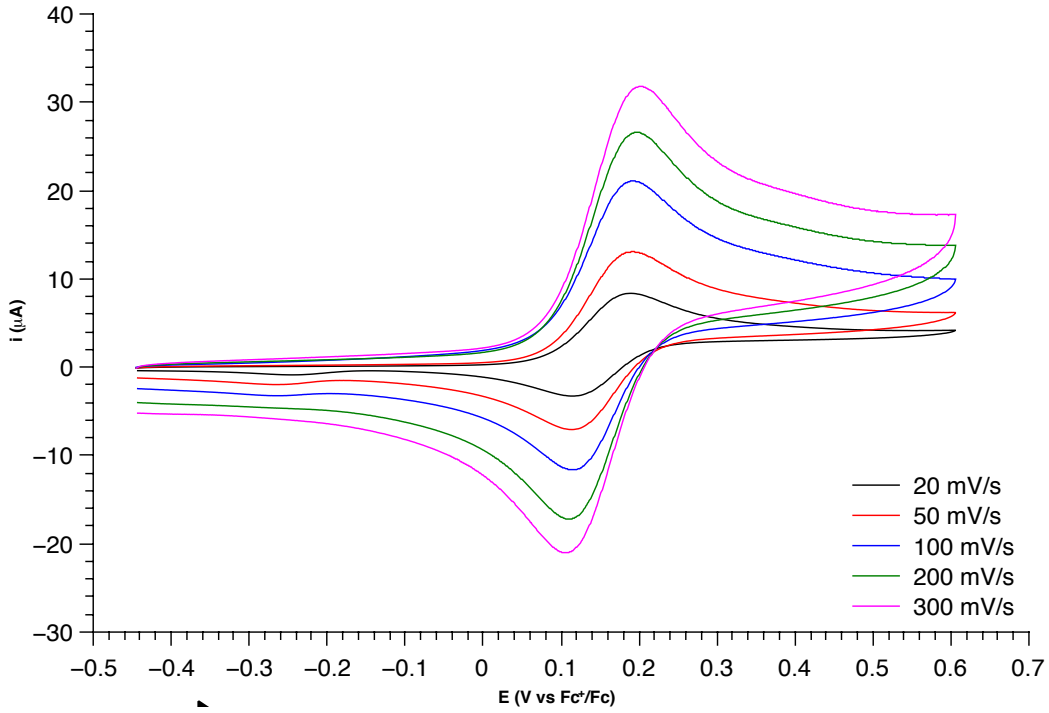


Figure 3.8.1: Cyclic voltammogram of 1 mM [Ni(L3)Fe(^{t}BuNC)$_4$] (PF$_6$)$_2$ in MeCN with 0.2 M [N^nBu_4][BF_4] as supporting electrolyte recorded at scan rates of 20-300 mVs^{-1}

This process exhibits a linear relationship between current and the square root of the scan rate (Figure 3.8.2) and i_{pc}/i_{pa} of *ca.* 0.8 across these scan rates, satisfying the conditions for an electrochemically reversible process under the conditions of the experiment.[30] The value of $(E_{pc}-E_{pa})/n$ is 77 mV and is essentially identical to that for decamethylferrocene recorded in this experiment (76 mV) and is consistent with the transfer of a single electron associated with

the $[Ni(L3)Fe(^{t}BuNC)_4]^{3+/2+}$ process, also confirmed via Coulometry measurements (Figure 3.8.3). A reversible redox process is also observed for [Ni(L3)] at -0.60 V *vs* Fc^{+}/Fc that is assigned to the Ni^{III}/Ni^{II} couple on the basis of the EPR spectroscopic results for $[Ni(L3)]^{+}$.[11] This, together with the EPR spectroscopic results for $[Ni(L3)Fe(^{t}BuNC)_4]^{3+}$, and through comparisons with other Ni^{II} complexes that may be oxidized to their Ni^{III} counterparts,[31] suggests that the $[Ni(L3)Fe(^{t}BuNC)_4]^{3+/2+}$ redox process may also be largely Ni-based and may be assigned as a formal $Ni^{III}Fe^{II}/Ni^{II}Fe^{II}$ couple.

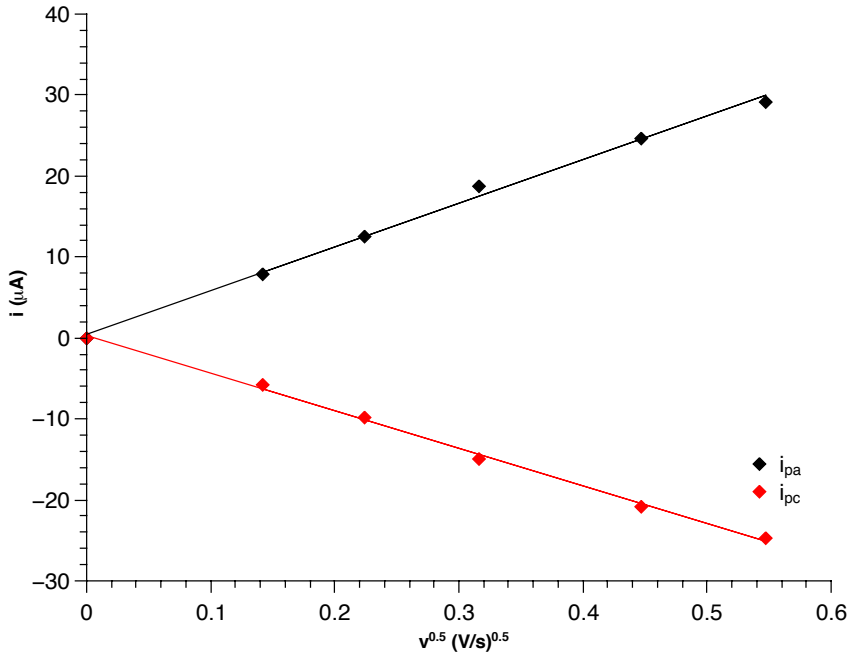


Figure 3.8.2: Plot of i (μA) vs $v^{0.5}$ $(V/s)^{0.5}$ for $[Ni(L3)Fe(^{t}BuNC)_4](PF_6)_2$ process at $E_{½}$ = 0.15 V vs Fc^{+}/Fc.

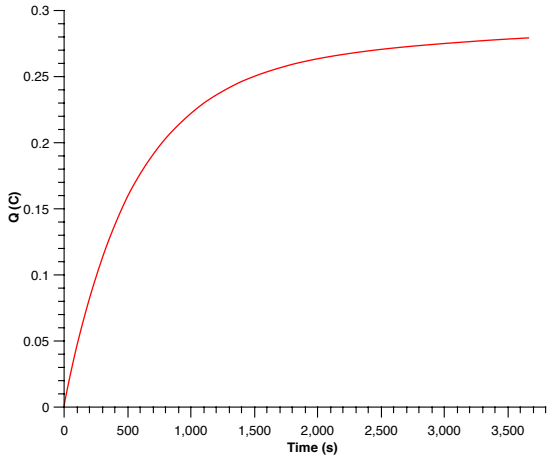


Figure 3.8.3: Coulometry trace of 0.03215 mM of [Ni(L3)Fe(^{t}BuNC)$_4$]$^{2+/3+}$ oxidation at +0.9 V overpotential (vs SHE) in MeCN with with 0.2 M [N^{n}Bu$_4$][BF$_4$] as supporting electrolyte.

The [Ni(L3)Fe(^{t}BuNC)$_4$]$^{3+/2+}$ process ($E_{½}$ = 0.15 V *vs* Fc^+/Fc) occurs at a significantly more positive potential compared to the [Ni(L3)]$^{+/0}$ process ($E_{½}$ = -0.60 V *vs* Fc^+/Fc) of the precursor complex (Figure 3.8.4).[11, 12] This suggests that the Ni centre [Ni(L3)Fe(^{t}BuNC)$_4$]$^{2+}$ possesses less electron density than the Ni centre in [Ni(L3)]. This is consistent with the coordination of the [Ni(L3)] unit to a [Fe(^{t}Bu-CN)$_4$]$^{2+}$ fragment in [Ni(L3)Fe(^{t}BuNC)$_4$]$^{2+}$ that withdraws electron density away from the Ni centre.

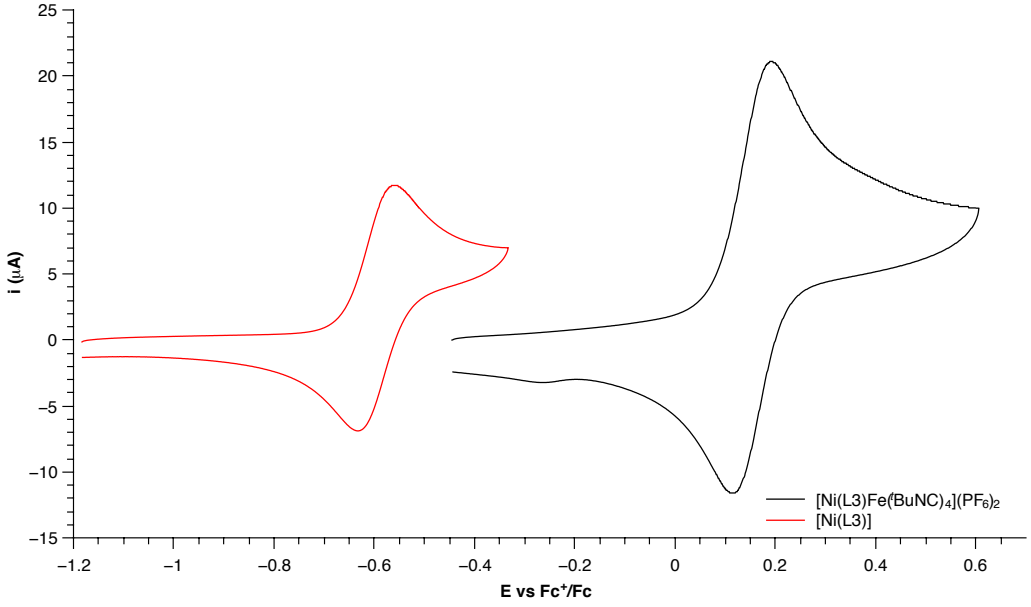


Figure 3.8.4: Cyclic voltammogram of 1 mM [Ni(L3)Fe(^{t}BuNC)$_4$](PF$_6$)$_2$ (black) and 1 mM [Ni(L3)] (red) in MeCN with 0.2 M [N^{n}Bu$_4$][BF$_4$] as supporting electrolyte at 100 mVs^{-1}.

The potential of the $[Ni(L3)Fe(^tBuNC)_4]^{3+/2+}$ couple occurs at markedly more positive potentials than the catalytically-relevant $Ni^{III/II}$ redox couples observed in the [NiFe] hydrogenases involving the Ni-R and Ni-C states (-1.028 to -1.059 V vs Fc^+/Fc) and the Ni-C and Ni-SIa states (-0.998 V vs Fc^+/Fc).[32] This suggests that $[Ni(L3)Fe(^tBuNC)_4](PF_6)_2$ may be unsuitable as a proton reduction or H_2 oxidation catalyst.

3.8.2 Electrochemical studies of $[Ni(L3)Fe(benzyl\text{-}NC)_4](PF_6)_2$

$[Ni(L3)Fe(benzyl\text{-}NC)_4](PF_6)_2$ demonstrates an electrochemically quasireversible process at $E_{1/2}$ = 0.21 V *vs* Fc^+/Fc (Figure 3.8.4). This potential is more positive than that of $[Ni(L3)Fe(^tBuNC)_4](PF_6)_2$ ($E_{1/2}$ = 0.15 V vs Fc^+/Fc), and the voltammogram exhibits a less symmetrical shape (Figure 3.8.5). The use of the empirical fitting published by Nicholson[33] demonstrates that i_{pc}/i_{pa} is approximately 0.7, and the value for $(E_{pc}\text{-}E_{pa})$ = 85 mV, which is greater than the 77 mV recorded for $[Ni(L3)Fe(^tBuNC)_4](PF_6)_2$ and for decamethylferrocene ($Me_{10}Fc$) recorded in this experiment but consistent with a single electron process. A plot of i (A) vs the square root of scan rate $(V/s)^{0.5}$ is linear (Figure 3.8.6).

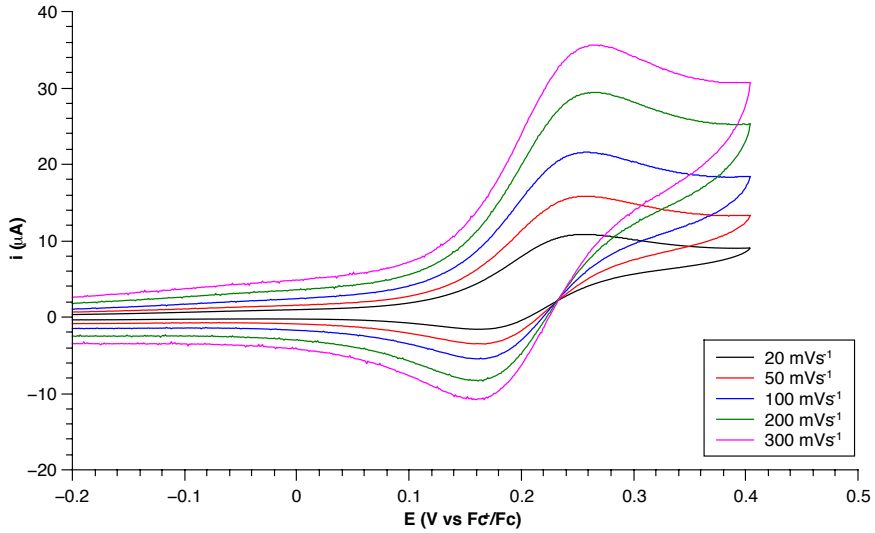


Figure 3.8.4: Cyclic voltammograms of 1 mM $[Ni(L3)Fe(benzyl\text{-}NC)_4](PF_6)_2$ in MeCN with 0.2 M $[N^nBu_4][BF_4]$ as supporting electrolyte recorded at scan rates of 20-300 mVs^{-1}.

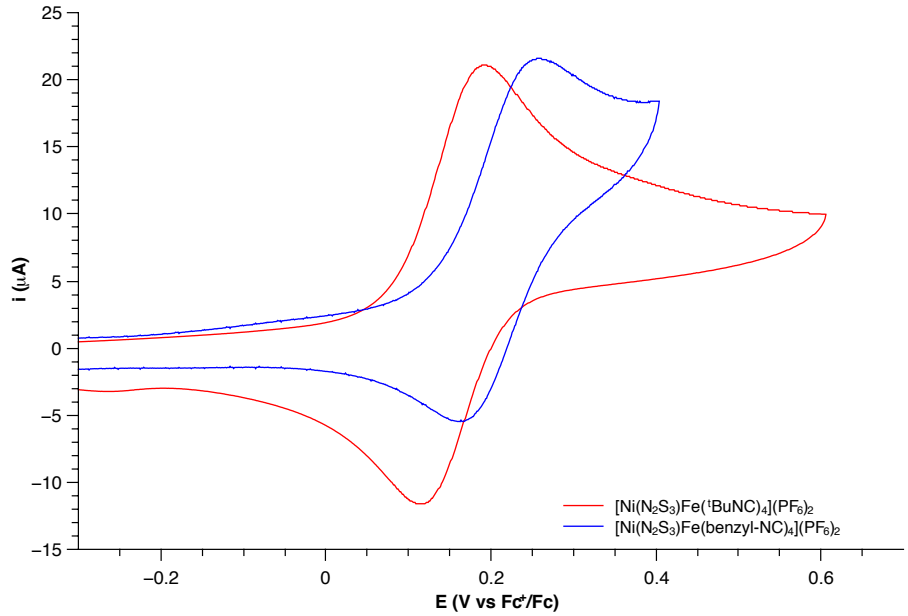


Figure 3.8.5: Cyclic voltammograms of 1 mm [Ni(L3)Fe(R-NC)$_4$](PF$_6$)$_2$ (R = ^{t}Bu, red), (R = benzyl, blue) in MeCN with 0.2 M [N^{n}Bu$_4$][BF$_4$] as supporting electrolyte at 100 mVs^{-1}.

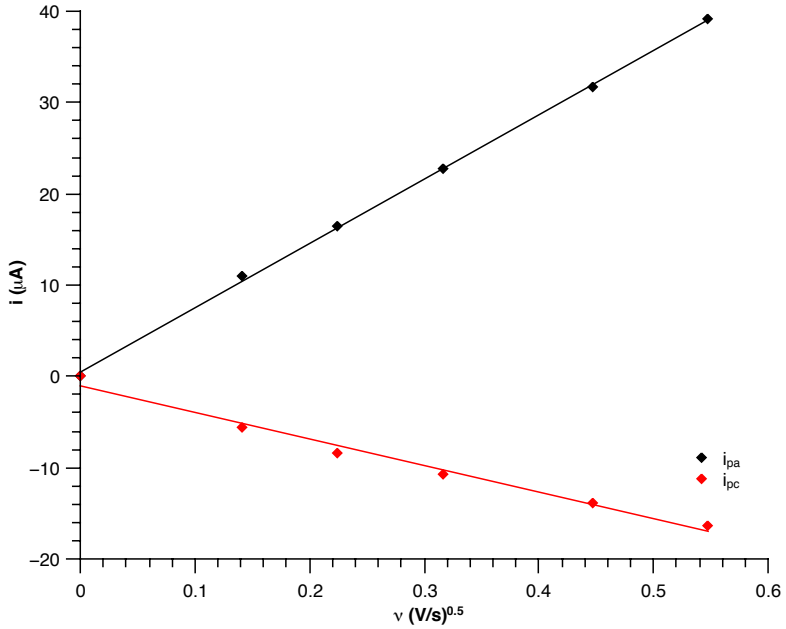


*Figure 3.8.6 Plot of i (µA) vs $\nu^{0.5}$ (V/s)$^{0.5}$ for [Ni(L3)Fe(*benzyl-NC*)$_4$](PF$_6$)$_2$ process at E$_{½}$ = 0.21 V vs Fc$^+$/Fc.*

3.9.1 Spectroelectrochemistry of [Ni(L3)Fe(R-NC)$_4$](PF$_6$)$_2$ (R = ^{t}Bu, benzyl)

The chemical reversibility of the [Ni(L3)Fe(R-NC)$_4$]$^{3+/2+}$ process at E$_{½}$ = 0.15 V vs Fc$^+$/Fc (R = ^{t}Bu) and E$_{½}$ = 0.21 V vs Fc$^+$/Fc (R = benzyl) was examined by UV/Vis

spectroelectrochemistry at -20 ºC in MeCN solution with 0.2 M [$N^{n}Bu_4$][BF_4] as supporting electrolyte (Figures 3.9.1 and 3.9.2). The changes in the UV/vis spectrum associated with the [Ni(L3)Fe(R-NC)$_4$]$^{3+/2+}$ process are shown in Table 3.9.1.

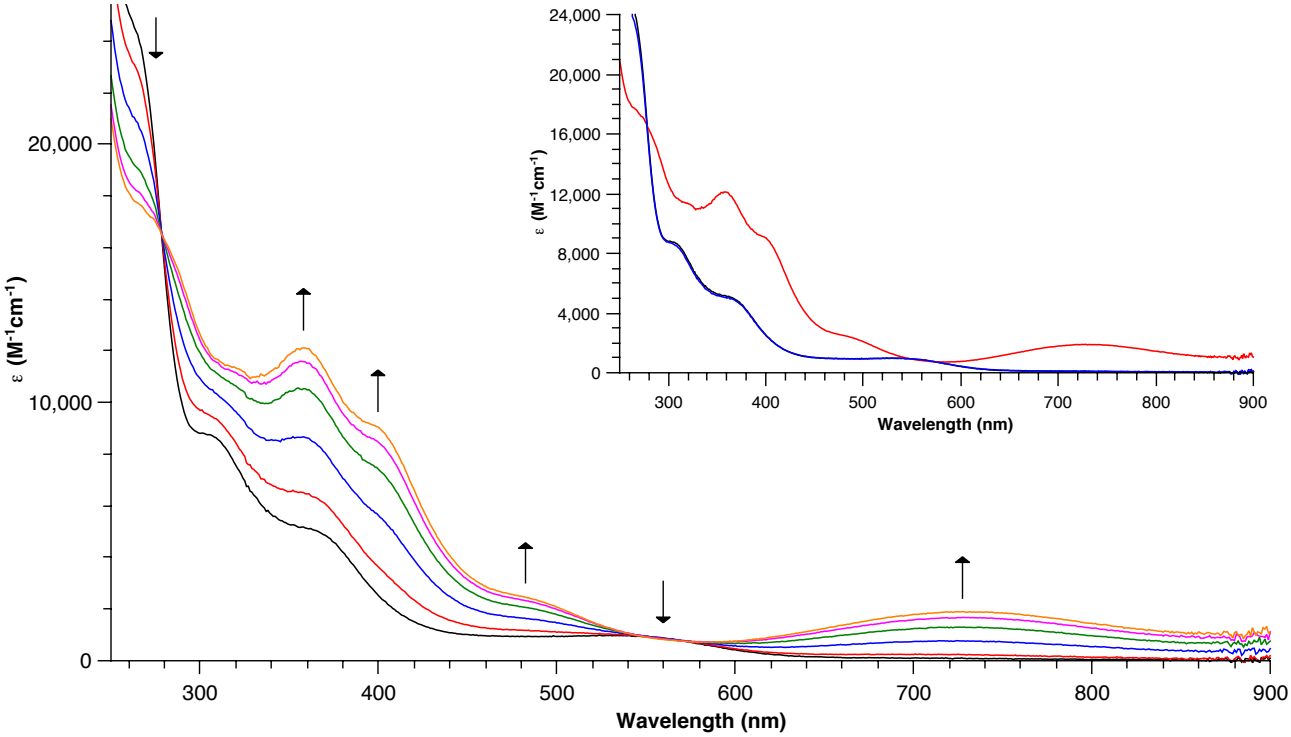


Figure 3.9.1: Spectroelectrochemistry of [Ni(L3)Fe(^{t}BuNC)$_4$](PF$_6$)$_2$ redox process at 0.15 V vs Fc+/Fc at -20 ºC in MeCN with 0.2 M [$N^{n}Bu_4$][BF_4] as supporting electrolyte over repeat scans from reduced (black) to oxidised (orange), and (inset); reduced (black), oxidised (red) and re-reduced (blue).

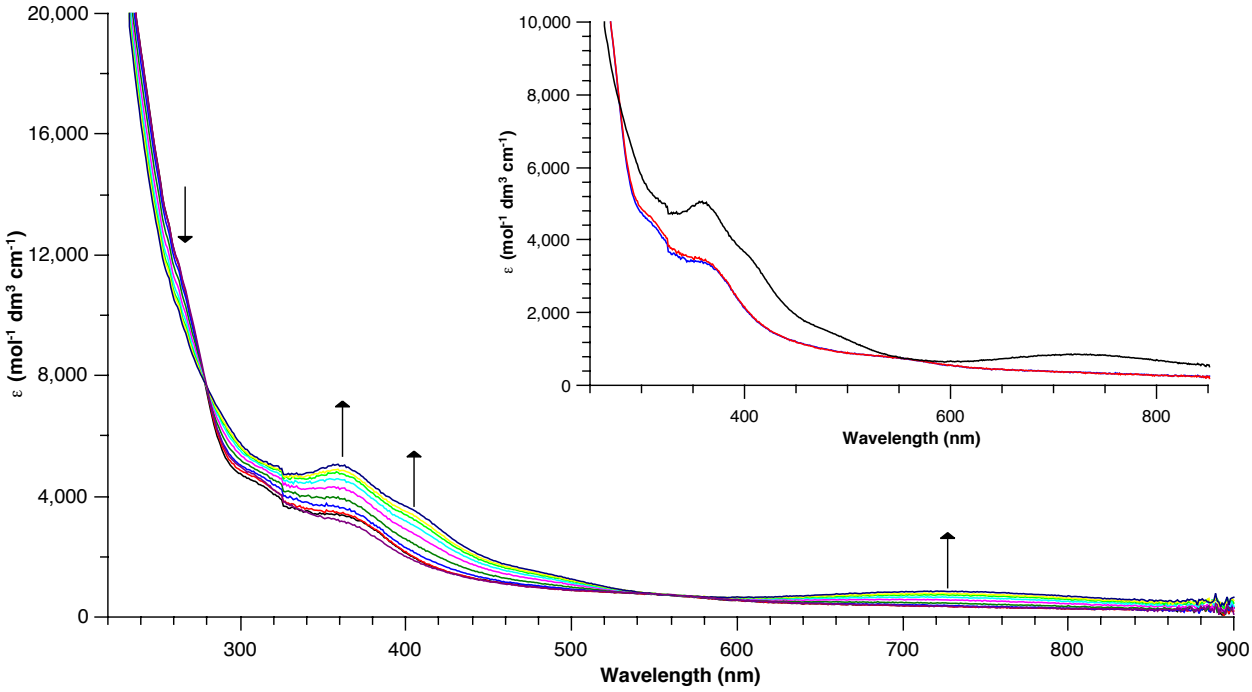


Figure 3.9.2: Spectroelectrochemistry of [Ni(L3)Fe(benzyl-NC)$_4$](PF$_6$)$_2$ redox process at 0.15 V vs Fc+/Fc at -20 ºC in MeCN with 0.2 M [N^{n}Bu$_4$][BF$_4$] as supporting electrolyte over repeat scans from reduced (purple) to oxidised (black), and (inset); reduced (red), oxidised (black) and re-reduced (blue).

Table 3.9.1: Summary of UV/vis spectra of [Ni(L3)Fe(R-NC)$_4$]$^{2+/3+}$ (R = ^{t}Bu and benzyl).

Complex	λ_{max} (nm)	ε (mol^{-1} dm^3 cm^{-1})	Isobestic point (nm)
[Ni(L3)Fe(^{t}BuNC)$_4$]$^{2+}$	260, 307, 356, 560	24000, 8720, 5200, 900	
[Ni(L3)Fe(^{t}BuNC)$_4$]$^{3+}$	260, 356, 400, 560, 731	17960, 12140, 9020, 800, 1976	278, 548, 572
[Ni(L3)Fe(benzyl-NC)$_4$]$^{2+}$	301, 359	4820, 3220	
[Ni(L3)Fe(benzyl-NC)$_4$]$^{3+}$	359, 407, 729	5160, 3500, 940	278

The [Ni(L3)Fe(^{t}BuNC)$_4$]$^{3+/2+}$ and [Ni(L3)Fe(benzyl-NC)$_4$]$^{3+/2+}$ couples exhibit chemically reversible behavior over the timescale of the spectroelectrochemical experiment, indicated by the complete restoration of the original UV/Vis spectrum after complete oxidation and subsequent reduction (Figures 3.9.1 and 3.9.2, inset). The presence of isobestic points at 278, 548 and 572 nm for [Ni(L3)Fe(^{t}BuNC)$_4$]$^{3+/2+}$ and at 278 nm for [Ni(L3)Fe(benzyl-NC)$_4$]$^{3+/2+}$ indicate that the oxidations of [Ni(L3)Fe(R-NC)$_4$]$^{2+}$ to [Ni(L3)Fe(R-NC)$_4$]$^{3+}$ (R = ^{t}Bu and benzyl) proceed without the formation of long-lived detectable intermediates. The emergence

of a low energy transition at 731 nm (ε = 1976 mol^{-1} dm^3 cm^{-1}) for $[Ni(L3)Fe(^tBuNC)_4]^{3+/2+}$ and at 729 nm (ε = 940 mol^{-1} dm^3 cm^{-1}) for $[Ni(L3)Fe(benzyl\text{-}NC)_4]^{3+/2+}$ may be associated with intervalence charge transfer between the Ni and Fe centres that occurs on the oxidation of $[Ni(L3)Fe(R\text{-}NC)_4]^{2+}$. The higher energy bands evident at 350 nm are similar to that observed for other $Ni^{III/II}$ transitions reported previously, for example, $[Ni^{III}(cyclam)Cl_2]Cl$ and $[Ni^{III}(methyl\text{-}cyclam)Cl_2]Cl$ (cyclam = 1,4,8,11-tetraazacyclotetradecane),[34] and $[Ni^{III}(cyclam)(NCCH_3)_2]^{3+}$.[35]

3.9.2 IR Spectroelectrochemistry of $[Ni(L3)Fe(R\text{-}NC)_4](PF_6)_2$ (R = ^{t}Bu) and the IR spectrum of $Ni(L3)Fe(R\text{-}NC)_4](PF_6)_2$ (R = benzyl)

The changes in the IR spectra associated with the $[Ni(L3)Fe(^tBuNC)_4]^{3+/2+}$ process at $E_{½}$ = 0.15 V vs Fc^+/Fc in the isonitrile CN stretching frequency range were investigated by IR spectroscopy. IR spectrum of $[Ni(L3)Fe(^tBuNC)_4]^{2+}$ was recorded in MeCN solution with 0.2 M $[N^nBu_4][BF_4]$ as supporting electrolyte and for $[Ni(L3)Fe(^tBuNC)_4]^{3+}$ following controlled potential electrolysis via the sampling of a 1 mM solution. The changes in the IR spectra associated with the $[Ni(L3)Fe(^tBuNC)_4]^{3+/2+}$ process and the IR spectrum of $[Ni(L3)Fe(benzyl\text{-}NC)_4](PF_6)_2$ are shown in Figures 3.9.3 and 3.9.4 and in Table 3.9.2.

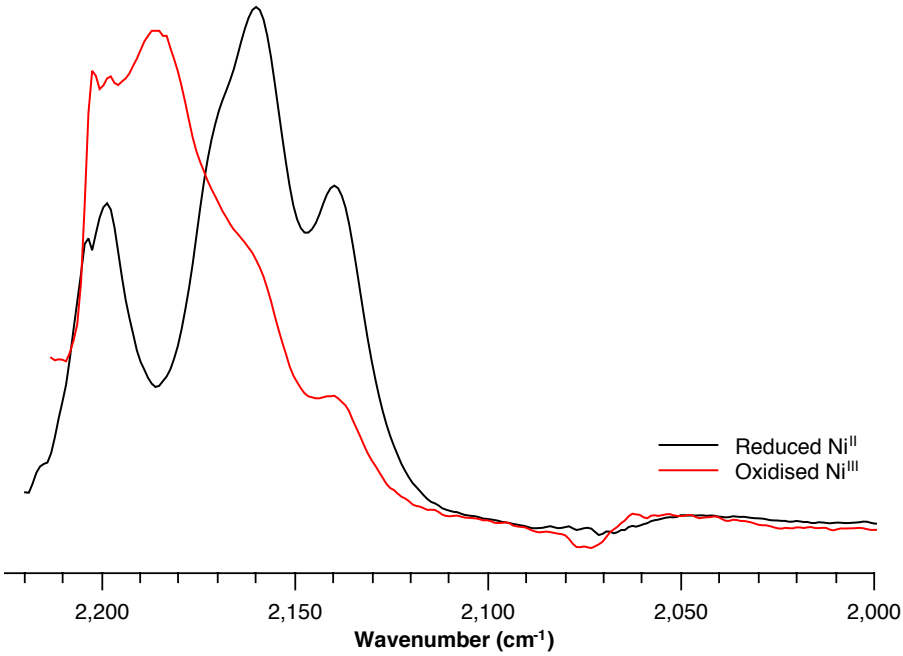


Figure 3.9.3: IR spectra of [Ni(L3)Fe(^{t}BuNC)$_4$](PF$_6$)$_2$ in MeCN before (black) and after (red) oxidation via controlled potential electrolysis.

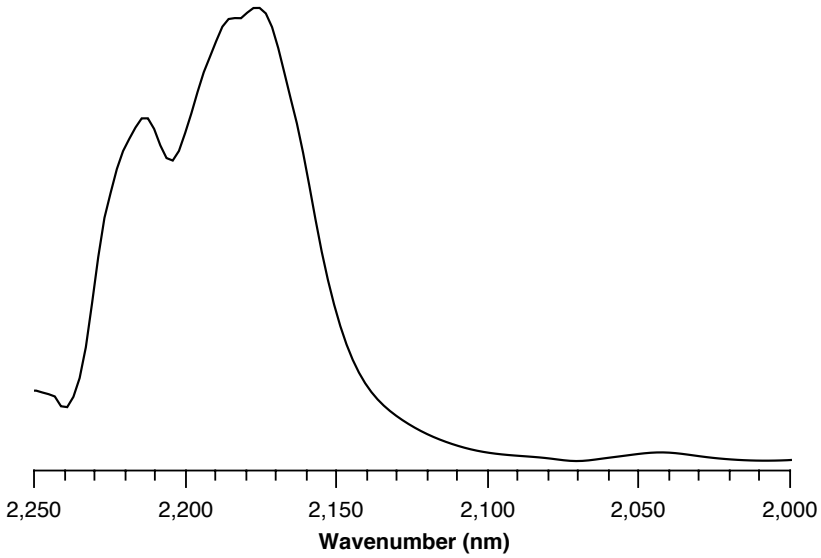


Figure 3.9.4: IR spectrum of [Ni(L3)Fe(benzyl-NC)$_4$](PF$_6$)$_2$ in MeCN.

Table 3.9.2: IR spectra of [Ni(L3)Fe(^{t}BuNC)$_4$]$^{2+}$, [Ni(L3)Fe(^{t}BuNC)$_4$]$^{3+}$ and [Ni(L3)Fe(benzyl-NC)$_4$]$^{2+}$.

Complex	**Wavenumber /cm^{-1}**
[Ni(L3)Fe(^{t}BuNC)$_4$]$^{2+}$	2199, 2170sh, 2160, 2140
[Ni(L3)Fe(^{t}BuNC)$_4$]$^{3+}$	2201, 2186, 2161sh, 2140
[Ni(L3)Fe(benzyl-NC)$_4$]$^{2+}$	2225, 2213, 2196, 2167

The presence of four IR bands in the ν_{CN}(isonitrile) stretching frequency region in the IR spectra of $[Ni(L3)Fe(R\text{-}NC)_4]^{2+}$ (R = ^{t}Bu and benzyl) (black trace) is consistent with local C_{2v} symmetry about the iron centre, found in the solid state structure of $[Ni(L3)[Fe(CN^tBu)_4](PF_6)_2$ (Section 3.7.1), being maintained in MeCN solution. The ν_{CN}(isonitrile) stretching frequencies for $[Ni(L3)Fe(benzyl\text{-}NC)_4]^{2+}$ are *ca.* 27 to 50 cm^{-1} higher in frequency than their counterparts in $[Ni(L3)Fe(^tBuNC)_4]^{2+}$ consistent with less π-backbonding within the $[Ni(L3)Fe(benzyl\text{-}NC)_4]^{2+}$ complex. The range of ν_{CN}(isonitrile) stretching frequencies for $[Ni(L3)Fe(R\text{-}NC)_4]^{2+}$ (R = ^{t}Bu and benzyl) is similar to that found for other complexes incorporating a low-spin $[Fe(CN\text{-}R)]^{2+}$ fragment (*e.g.* $[Fe_2(\mu\text{-}S_2C_3H_6)(^tBuCN)_2(CO)_4H]^+$ and $[Fe(CN\text{-}Me)_6]^{2+}$)[36, 37].

The oxidation of $[Ni(L3)Fe(^tBuNC)_4]^{2+}$ to $[Ni(L3)Fe(^tBuNC)_4]^{3+}$ is accompanied by moderate shifts of the ν_{CN}(isonitrile) stretching frequencies to higher energy consistent with less π-backbonding within $[Ni(L3)Fe(^tBuNC)_4]^{3+}$ as a consequence of less electron density at the Fe centre and with an oxidation process that is largely localized at the Ni centre. The loss of electron density at the Ni centre that accompanies oxidation may be compensated by an increase in donation of electron density from the apical S(3) donor as revealed by DFT calculations that suggest that $[Ni(L3)Fe(^tBuNC)_4]^{3+}$ is associated with a shorter Ni(1)-S(3) distance (see Section 3.12). Overall the IR spectroscopic changes are consistent with the assignment of the $[Ni(L3)Fe(^tBuNC)_4]^{3+/2+}$ process to a formal $Ni^{III/II}Fe^{II}$ redox process.

3.10 EPR spectroscopy of $[Ni(L3)Fe(^tBuNC)_4]^{3+}$

The X-band fluid solution EPR spectrum of electrochemically generated $[Ni(L3)Fe(^tBuNC)_4]^{3+}$ in MeCN solution with 0.2 M $[^nBu_4N][BF_4]$ demonstrates an isotropic *g* value of 2.1177 that indicates a significant spin-orbit coupling interaction of the unpaired

electron with the metal centres (Figure 3.10.1). This supports the hypothesis that the redox couple observed experimentally is centred on the nickel atom as a formal Ni^{III} d^7 system, since a radical-based system centred on the ligand would be expected to show a *g* value much closer to g_e.[38]

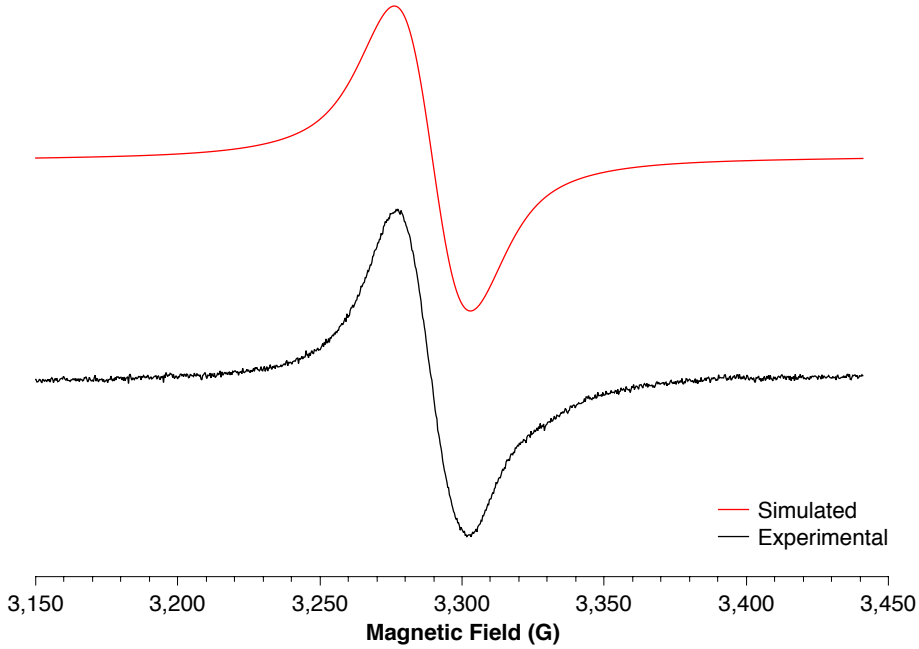


Figure 3.10.1: X-band EPR spectrum of electrochemically generated [Ni(L3)Fe(^{t}BuNC)$_4$]$^{3+}$ in MeCN at 248 K. Black = experimental, red = simulated. Simulation paramaters: g_{iso}, 2.1177; Linewidth, 28 G, Lorentzian/Gaussain distortion, 0.6.

The frozen spectrum (Figure 3.10.2) recorded at 77 K indicates a significant rhombic character (g_{xx}, $g_{yy} > g_{zz} \approx g_e$), not unlike the frozen EPR spectrum of the Ni-C state of the [NiFe] hydrogenase enzyme.[1] However, this spectrum has proven difficult to simulate, and could suggest that a mixture of different EPR-active species are present. Comparison with the electrochemically generated oxidised precursor $[Ni(L3)]^+$ complex indicates that it does not appear to be a loss of the $[Fe(CN^tBu)_4]^{2+}$ fragment, and the UV-Vis spectroelectrochemical measurements appear to rule out the presence of a long-lived intermediate product (timescale *ca*. 2 minutes) upon oxidation of the $[Ni(L3)Fe(^tBuNC)_4]^{2+}$ species. Further investigation of

the $[Ni(L3)Fe(^tBuNC)_4]^{3+}$ complex is required to fully elucidate the electronic structure of this system.

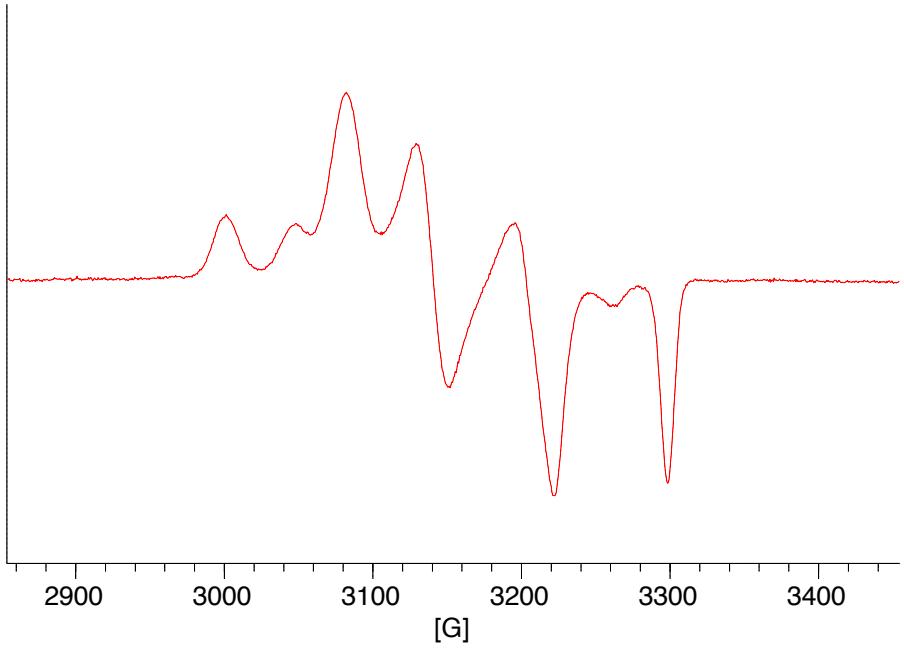


Figure 3.10.2: Frozen solution X-band EPR spectrum of electrochemically generated $[Ni(L3)Fe(^tBuNC)_4]^{3+}$ *in MeCN at 77 K.*

3.11 Electrochemistry of $[Ni(L3)Fe(R\text{-}NC)_4](PF_6)_2$ under hydrogen (R = ^{t}Bu, benzyl)

$[Ni(L3)Fe(R\text{-}NC)_4](PF_6)_2$ (R = ^{t}Bu, benzyl) exhibit chemically reversible oxidation processes that we have assigned to a formal $Ni^{III/II}Fe^{II}$ process. The [NiFe] hydrogenases also possess catalytically relevant states that have been assigned as $Ni^{II}Fe^{II}$ and $Ni^{III}Fe^{II}$, and can operate bidirectionally; *i.e.* as a proton reduction catalyst or as a catalyst for the oxidation of dihydrogen,[39] depending on the physiological needs of the host bacterium and the local chemical conditions. We therefore investigated the potential of $[Ni(L3)Fe(R\text{-}NC)_4](PF_6)_2$ (R = ^{t}Bu, benzyl) to oxidise dihydrogen under electrochemical conditions. A 1 mM $[Ni(L3)Fe(R\text{-}NC)_4](PF_6)_2$ (R = ^{t}Bu, benzyl) solution in MeCN with 0.2 M $[^nBu_4N][BF_4]$ as supporting electrolyte was saturated with dihydrogen gas by bubbling for 2 minutes and then kept under an atmosphere of dihydrogen. The cyclic voltammograms of each $[Ni(L3)Fe(R\text{-}NC)_4](PF_6)_2$ (R

= ^{t}Bu, benzyl) was recorded at 100 mVs^{-1} under these conditions and compared to the same measurements without the presence of dihydrogen. No appreciable current response was measured in the presence of dihydrogen indicating no catalytic activity with respect to the oxidation of dihydrogen on the timescale of the experiment (Figures 3.11.1 and 3.11.2). This could be explained by a sterically hindered coordination sphere around the Ni centre that reduces the potential for binding of the dihydrogen molecule to the Ni centre and necessary for catalysis, or the increased stability of the Ni^{III} state afforded by the coordination of the S(3) thioether making reduction back to Ni^{II} less favourable via the oxidation of dihydrogen.

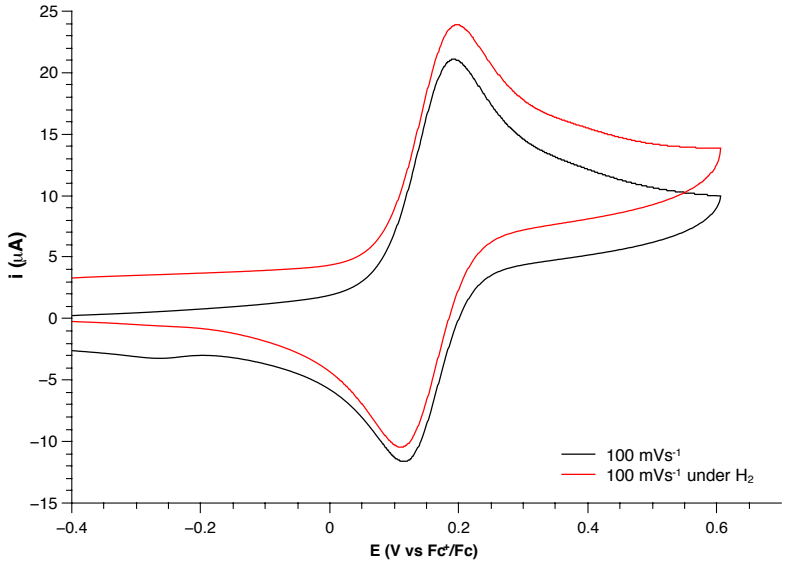


Figure 3.11.1: Cyclic voltammogram of 1 mM [Ni(L3)Fe(^{t}BuNC)$_4$](PF$_6$)$_2$ in MeCN with 0.2 M [N^{n}Bu$_4$][BF$_4$] as supporting electrolyte at 100 mVs^{-1} under no H_2 and in the presence of H_2.

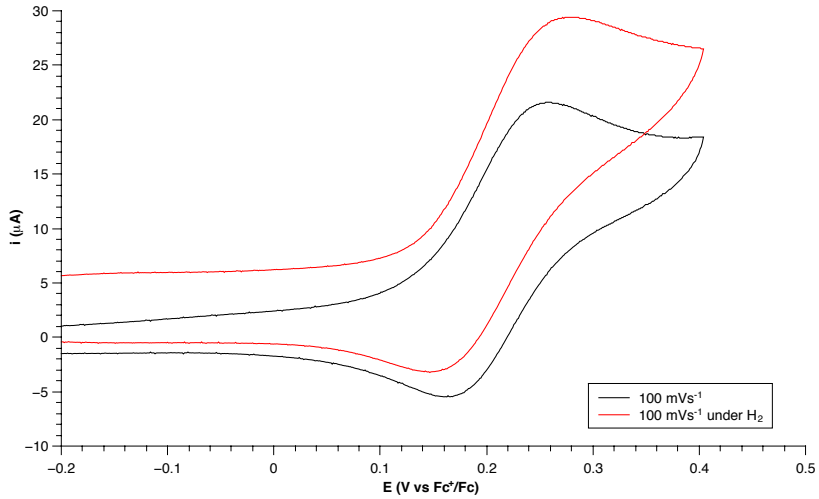


Figure 3.11.2: Cyclic voltammogram of 1 mM [Ni(L3)Fe(benzyl-NC)$_4$](PF$_6$)$_2$ in MeCN with 0.2 M [N^{n}Bu$_4$][BF$_4$] as supporting electrolyte at 100 mVs^{-1} under no H$_2$ and in the presence of H$_2$.

3.12 DFT Calculations

We undertook DFT calculations using models of [Ni(L3)Fe(^{t}BuNC)$_4$]$^{3+/2+}$ and [Ni(L3)]$^{+/0}$ to gain insight into the electronic structures of these centers and to provide a framework within which to interpret the X-ray crystallographic and spectroscopic results.

The X-ray crystallographic structure of [Ni(L3)] (Section 3.4) shows that the Ni centre adopts an approximate square-based pyramidal environment with a N_2S_2 donor set in the equatorial plane and a thioether sulfur donor in the apical position that interacts weakly with the metal center [Ni-S(3) = 2.820(2) Å and sum of the empirical atomic radii = 2.35 Å] (Table 3.4.1). A square-planar geometry is typical of a low-spin Ni^{II} center and results in a diamagnetic complex. However, ^{1}H-NMR spectroscopy suggests that [Ni(L3)] is paramagnetic in solution, presumably due to the co-ordination of the thioether sulfur that results in a high-spin pentacoordinated complex. Therefore we undertook gas-phase DFT calculations on models of [Ni(L3)] in the closed-shell (S = 0) and triplet state (S = 1) configurations to investigate the differences in geometry for these states. Selected metrical parameters for the geometry

optimized structures are presented in Table 3.12.1 and the calculated structures of [Ni(L3)] in the S = 1 and S= 0 states are shown in Figure 3.12.1

Table 3.12.1: Selected bond lengths and angles for [Ni(L3)] in the S = 1 and S= 0 states.

Bond	**Length /Å**	**Atoms**	**Angle /º**	**Atoms**	**Angle /º**
S=1					
Ni(1)-N(1)	2.292	N(1)-Ni(1)-N(2)	81.9	S(1)-Ni(1)-N(2)	135.7
Ni(1)-N(2)	2.154	S(1)-Ni(1)-S(2)	102.0	N(1)-Ni(1)-S(3)	84.2
Ni(1)-S(1)	2.207	N(1)-Ni(1)-S(1)	89.0	S(1)-Ni(1)-S(3)	134.1
Ni(1)-S(2)	2.370	N(2)-Ni(1)-S(2)	86.0		
Ni(1)-S(3)	2.360	N(1)-Ni(1)-S(2)	167.5	$\tau = 0.53$	
S=0					
Ni(1)-N(1)	2.047	N(1)-Ni(1)-N(2)	87.7	S(1)-Ni(1)-N(2)	173.0
Ni(1)-N(2)	2.023	S(1)-Ni(1)-S(2)	92.0	N(1)-Ni(1)-S(3)	81.4
Ni(1)-S(1)	2.205	N(1)-Ni(1)-S(1)	86.7	S(1)-Ni(1)-S(3)	97.9
Ni(1)-S(2)	2.175	N(2)-Ni(1)-S(2)	92.1		
Ni(1)-S(3)	2.880	N1(1)-Ni(1)-S(2)	163.4	$\tau = 0.16$	

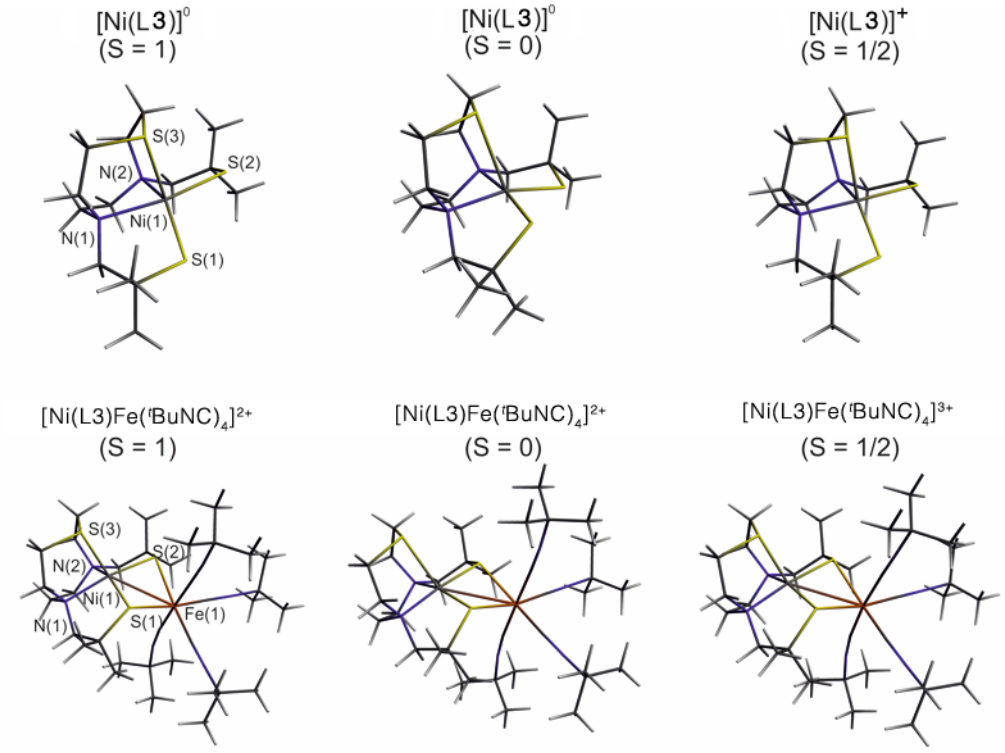


Figure 3.12.1: Gas phase DFT calculated structures of [Ni(L3)] in the S = 0 and S = 1 states, $[Ni(L3)]^+$, $[Ni(L3)Fe(^tBuNC)_4]^{2+}$ in the S = 0 and S = 1 states and $[Ni(L3)Fe(^tBuNC)_4]^{3+}$.

The DFT calculations for [Ni(L3)] (S = 0) reproduce the essential features of the geometry determined by X-ray crystallography; the calculated equatorial Ni-S and Ni-N distances are within *ca.* 0.01 and 0.06 Å of the experimental structure, and the axial Ni-S distances are within *ca.* 0.06 Å of one another. The degree of trigonal distortion from a square pyramidal geometry, as measured by τ, is greater in the calculated structure (τ = 0.16 and 0.04, for the calculated and experimental structures, respectively, Tables 3.4.1 and 3.12.1). In contrast the DFT calculated geometry of [Ni(L3)] (S = 1) is significantly different from those of the experimental and calculated [Ni(L3)] (S = 0) structures. The Ni-S(2) distance is overestimated by *ca.* 0.20 Å in the calculated structure of [Ni(L3)] (S = 1) and features a co-ordinated thioether sulfur donor [Ni-S(3) = 2.360 *vs.* 2.820(2) Å in the experimental structure]. In addition, the calculated geometry for [Ni(L3)] (S = 1) features a significant trigonal distortion, τ = 0.53 (Table 3.13.1). Thus, based on these differences in calculated geometries and their comparisons with the structure derived from X-ray crystallography (Section 3.4), the DFT calculations are consistent with the assignment of a singlet (S = 0) configuration in the solid state structure of [Ni(L3)]. The S = 0 state is 1.4 kcal mol^{-1} lower in energy than the S = 1 structure in the gas phase suggesting that there is only a small energy barrier between the S = 0 and S = 1 states such that the paramagnetic S = 1 state may become preferred in solution.

The gas-phase geometry optimization of $[Ni(L3)]^{+}$ suggests that the oxidation of [Ni(L3)] is accompanied by a shortening of the Ni-S(3) thioether distance [Ni-S(3) = 2.348 Å], a decrease in the S(1)-Ni-N(2) angle [S(1)-Ni-N(2) = 135.8º] and a significant trigonal distortion away from square pyramidal (τ = 0.69, Table 3.12.2, Figure 3.12.1).

Table 3.12.2: Selected bond lengths and angles for $[Ni(L3)]^+$.

Bond	**Length /Å**	**Atoms**	**Angle /º**	**Atoms**	**Angle /º**
Ni(1)-N(1)	2.051	N(1)-Ni(1)-N(2)	87.8	S(1)-Ni(1)-N(2)	135.8
Ni(1)-N(2)	2.083	S(1)-Ni(1)-S(2)	89.0	N(1)-Ni(1)-S(3)	88.5
Ni(1)-S(1)	2.144	N(1)-Ni(1)-S(1)	93.0	S(1)-Ni(1)-S(3)	134.9
Ni(1)-S(2)	2.226	N(2)-Ni(1)-S(2)	89.3		
Ni(1)-S(3)	2.348	N1(1)-Ni(1)-S(2)	177.1	$\tau = 0.69$	

An inspection of the α- and β-spin manifolds from the DFT calculation of $[Ni(L3)]^+$ shows that the β-spin LUMO (61a β, Figure 3.12.2) corresponds to the formally singularly occupied molecular orbital (SOMO) with its α-spin counterpart (60a α) occupied. The β-spin LUMO is predominantly Ni- [45.3% total with Ni $3d_{yz}$ (9.5%), $3d_{x^2-y^2}$ (5.2%) and $3d_{z^2}$ (30.6%)] and S-based [29.3% total S(1) and 11.0% total S(3)]; this formulation mirrors the spin density distribution that shows the unpaired electron spin lies across the Ni, S(1) and S(3) centers (Figure 3.12.2).

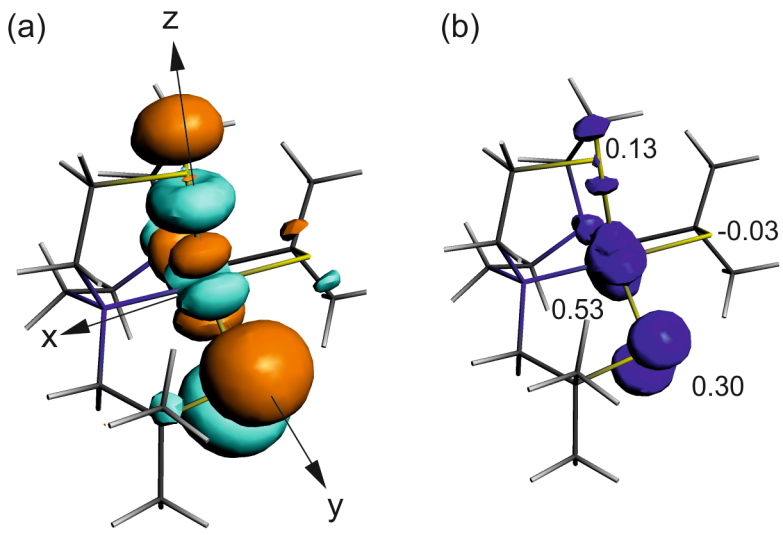


Figure 3.12.2: (a) The DFT calculated β-spin LUMO for $[Ni(L3)]^+$ with an isosurface value of 0.03 e Å^{-3} and (b) the spin density distribution for $[Ni(L3)]^+$ with an isosurface value of 0.01 e Å^{-3}.

Selected metrical parameters for gas-phase, geometry optimized models of $[Ni(L3)Fe(^tBuNC)_4]^{2+}$ in the S = 0 and S = 1 states are shown in Table 3.12.3 and the gas-phase DFT calculated structures of each state are shown in Figure 3.13.1.

Table 3.12.3: Selected bond lengths and angles for $[Ni(L3)Fe(^tBuNC)_4]^{2+}$ (S = 1) and $[Ni(L3)Fe(^tBuNC)_4]^{2+}$ (S = 0).

Bond	**Length /Å**	**Bond Angle**	**Angle /º**	**Bond Angle**	**Angle /º**
S = 1					
Ni(1)-N(1)	2.179	N(1)-Ni(1)-N(2)	84.1	S(1)-Fe(1)-C(2)	168.3
Ni(1)-N(2)	2.153	S(1)-Ni(1)-S(2)	94.2	C(1)-Fe(1)-C(4)	178.2
Ni(1)-S(1)	2.294	S(1)-Ni(1)-N(1)	87.7		
Ni(1)-S(2)	2.313	S(2)-Ni(1)-N(2)	88.6	τ = 0.20	
Ni(1)-S(3)	2.325	S(1)-Ni(1)-N(2)	166.5		
Fe(1)-S(1)	2.468	S(2)-Ni(1)-N(1)	154.6		
Fe(1)-S(2)	2.443	S(1)-Ni(1)-S(3)	113.7		
Fe(1)-C(1)	1.909	N(1)-Ni(1)-S(3)	86.6		
Fe(1)-C(2)	1.866	S(1)-Fe(1)-C(1)	79/7		
Fe(1)-C(3)	1.871	S(2)-Fe(1)-C(1)	81.3		
Fe(1)-C(4)	1.894	S(1)-Fe(1)-C(3)	89.9		
Ni(1)-Fe(1)	3.141	S(2)-Fe(1)-C(2)	90.1		
S = 0					
Ni(1)-N(1)	2.008	N(1)-Ni(1)-N(2)	88.7	S(1)-Fe(1)-C(2)	168.4
Ni(1)-N(2)	2.006	S(1)-Ni(1)-S(2)	88.1	C(1)-Fe(1)-C(4)	179.1
Ni(1)-S(1)	2.193	S(1)-Ni(1)-N(1)	90.2		
Ni(1)-S(2)	2.189	S(2)-Ni(1)-N(2)	91.2	τ = 0.20	
Ni(1)-S(3)	2.721	S(1)-Ni(1)-N(2)	162.8		
Fe(1)-S(1)	2.455	S(2)-Ni(1)-N(1)	174.1		
Fe(1)-S(2)	2.435	S(1)-Ni(1)-S(3)	108.7		
Fe(1)-C(1)	1.907	N(1)-Ni(1)-S(3)	84.7		
Fe(1)-C(2)	1.866	S(1)-Fe(1)-C(1)	81.3		
Fe(1)-C(3)	1.868	S(2)-Fe(1)-C(1)	83.0		
Fe(1)-C(4)	1.896	S(1)-Fe(1)-C(3)	94.1		
Ni(1)-Fe(1)	3.297	S(2)-Fe(1)-C(2)	95.2		

$[Ni(L3)Fe(^tBuNC)_4]^{2+}$ (S = 1) features a Ni center in an approximate square pyramidal environment with the thioether S donor located at the apical position at a distance of Ni(1)-S(3) = 2.325 Å. The DFT optimized structure of $[Ni(L3)Fe(^tBuNC)_4]^{2+}$ (S = 1) underestimates the Ni(1)-S(3) distance in the experimental structure [Ni(1)-S(3) = 2.686(2) Å] by *ca.* 0.29 Å.

In contrast the gas-phase geometry optimization of $[Ni(L3)Fe(^tBuNC)_4]^{2+}$ (S = 0) gives an Ni(1)-S(3) distance that is within *ca.* 0.11 Å of that in the experimental structure. DFT calculations for $[Ni(L3)Fe(^tBuNC)_4]^{2+}$ (S = 1) overestimate the Ni-S(1)/S(2) and Ni-N(1)/N(2) distances by *ca.* 0.10 Å whereas those for the $[Ni(L3)Fe(^tBuNC)_4]^{2+}$ (S = 0) model reproduce these distances to within 0.01 to 0.04 Å. Thus, the calculated structure of $[Ni(L3)Fe(^tBuNC)_4]^{2+}$ (S = 0) approaches that of the experimental structure. It should be noted, however, that the model of $[Ni(L3)Fe(^tBuNC)_4]^{2+}$ (S = 0) overestimates the Ni-S(3) distance as determined by X-ray crystallography by *ca*. 0.11 Å, which may suggest that the experimental structure of $[Ni(L3)Fe(^tBuNC)_4]^{2+}$ represents an intermediate S = 1, 0 spin state that approaches the S = 0 limit. There is no significant trigonal distortion for the $[NiN_2S_3]$ unit in the experimental $[Ni(L3)Fe(^tBuNC)_4]^{2+}$ and calculated $[Ni(L3)Fe(^tBuNC)_4]^{2+}$ (S = 0) and $[Ni(L3)Fe(^tBuNC)_4]^{2+}$ (S = 1) structures; each may be described as possessing a similar distorted square-pyramidal geometry (τ = 0.20). $[Ni(L3)Fe(^tBuNC)_4]^{2+}$ (S = 0) is 2.5 kcal mol^{-1} lower in energy than $[Ni(L3)Fe(^tBuNC)_4]^{2+}$ (S = 1) and the geometry of the $[Fe(^tBuNC)_4]^{2+}$ unit remains essentially invariant between the $[Ni(L3)Fe(^tBuNC)_4]^{2+}$ (S = 0) and $[Ni(L3)Fe(^tBuNC)_4]^{2+}$ (S = 1) structures.

The gas-phase geometry optimized structure of $[Ni(L3)Fe(^tBuNC)_4]^{3+}$ (Table 3.12.4) broadly retains the geometrical features calculated for $[Ni(L3)Fe(^tBuNC)_4]^{2+}$ (S = 1).

Table 3.12.4: Selected bond lengths and angles for $[Ni(L3)[Fe(^tBuNC)_4]^{3+}$.

Bond	**Length /Å**	**Bond Angle**	**Angle /º**	**Bond Angle**	**Angle /º**
Ni(1)-N(1)	2.033	N(1)-Ni(1)-N(2)	88.5	S(1)-Fe(1)-C(2)	168.6
Ni(1)-N(2)	2.035	S(1)-Ni(1)-S(2)	89.7	C(1)-Fe(1)-C(4)	174.1
Ni(1)-S(1)	2.222	S(1)-Ni(1)-N(1)	89.2		
Ni(1)-S(2)	2.220	S(2)-Ni(1)-N(2)	90.2	$\tau = 0.19$	
Ni(1)-S(3)	2.391	S(1)-Ni(1)-N(2)	161.2		
Fe(1)-S(1)	2.428	S(2)-Ni(1)-N(1)	172.6		
Fe(1)-S(2)	2.399	S(1)-Ni(1)-S(3)	107.9		
Fe(1)-C(1)	1.927	N(1)-Ni(1)-S(3)	87.9		
Fe(1)-C(2)	1.887	S(1)-Fe(1)-C(1)	82.4		
Fe(1)-C(3)	1.892	S(2)-Fe(1)-C(1)	83.9		
Fe(1)-C(4)	1.917	S(1)-Fe(1)-C(3)	93.2		
Ni(1)-Fe(1)	3.193	S(2)-Fe(1)-C(2)	94.3		

The Ni center adopts a distorted a square-pyramidal geometry with Ni-S(3) = 2.391 Å and τ = 0.19. The Fe center maintains a distorted octahedral geometry with only small increases (*ca.* 0.2 Å) and decreases (*ca.* 0.04 Å) in the average Fe-C and Fe-S distances, respectively as $[Ni(L3)[Fe(^tBuNC)_4]^{2+}$ (S = 0 or 1) is oxidized to $[Ni(L3)[Fe(^tBuNC)_4]^{3+}$. Thus, the absence of significant structural differences for $[Ni(L3)[Fe(^tBuNC)_4]^{2+}$ and $[Ni(L3)[Fe(^tBuNC)_4]^{3+}$ is consistent with the electrochemical and chemical reversibility observed experimentally for the $[Ni(L3)[Fe(^tBuNC)_4]^{2+/3+}$ redox process.

The calculated IR ν_{CN}(isonitrile) frequencies for $[Ni(L3)[Fe(^tBuNC)_4]^{2+}$ (S = 0), $[Ni(L3)[Fe(^tBuNC)_4]^{2+}$ (S = 1) and $[Ni(L3)[Fe(^tBuNC)_4]^{3+}$ and the experimental data for $[Ni(L3)[Fe(^tBuNC)_4]^{2+}$ and $[Ni(L3)[Fe(^tBuNC)_4]^{3+}$ are shown in Table 3.12.5.

Table 3.12.5: Gas-phase calculated and experimental (in MeCN solution) ν_{CN}(isonitrile) stretching frequencies for $[Ni(L3)[Fe(^tBuNC)_4]^{2+}$ ($Ni^{II}Fe^{II}$) and $[Ni(L3)[Fe(^tBuNC)_4]^{3+}$ ($Ni^{III}Fe^{II}$).

ν_{CN}(isonitrile) /cm^{-1}				
$Ni^{II}Fe^{II}$ S = 0 state Calculated	$Ni^{II}Fe^{II}$ S = 1 state Calculated	$Ni^{II}Fe^{II}$ Experimental	$Ni^{III}Fe^{II}$ S = 1/2 Calculated	$Ni^{III}Fe^{II}$ Experimental
2185	2186	2199	2190	2201
2150	2154	2170sh	2171	2186
2134	2140	2160	2164	2161sh
2112	2105	2140	2128	2140

The gas-phase DFT calculated ν_{CN}(isonitrile) stretching frequencies for $[Ni(L3)[Fe(^tBuNC)_4]^{2+}$ ($Ni^{II}Fe^{II}$) and $[Ni(L3)[Fe(^tBuNC)_4]^{3+}$ ($Ni^{III}Fe^{II}$) typically underestimate the experimentally determined ν_{CN}(isonitrile) stretching frequencies by *ca.* 7 – 28 cm^{-1}. Nevertheless they generally reproduce the slight increase in ν_{CN}(isonitrile) stretching frequencies associated with the oxidation of $[Ni(L3)[Fe(^tBuNC)_4]^{2+}$ to $[Ni(L3)[Fe(^tBuNC)_4]^{3+}$ (Table 3.12.5). The difference between the calculated ν_{CN}(isonitrile) stretching frequencies of $[Ni(L3)[Fe(^tBuNC)_4]^{2+}$ (S = 1) and $[Ni(L3)[Fe(^tBuNC)_4]^{2+}$ (S = 0) is small and a comparison of the calculated and experimental ν_{CN}(isonitrile) stretching frequencies alone cannot unambiguously confirm the spin state of $[Ni(L3)[Fe(^tBuNC)_4]^{2+}$ in solution; ^{1}H-NMR spectroscopy suggests that $[Ni(L3)[Fe(^tBuNC)_4]^{2+}$ is in the triplet (S = 1) state in MeCN solution.

The β-spin LUMO (132a β, Figure 3.12.3) of $[Ni(L3)[Fe(^tBuNC)_4]^{3+}$ corresponds to the formally singularly occupied molecular orbital (SOMO) with its α-spin counterpart (129a α) occupied. The β-spin LUMO possesses Ni [40.9% total with Ni $3d_{z^2}$ (33.9%) and $3d_{yz}$ (7.0%)], S [6.4% total S(1), 3.7% total S(2) and 21.4% total S(3)] and Fe [10.7% total with Fe $3d_{xy}$ (8.8%) and $3d_{yz}$ (1.9%)] character. This composition is in line with the calculated spin density for $[Ni(L3)[Fe(^tBuNC)_4]^{3+}$ (Figure 3.12.3) that lies principally across the Ni(1) and S(3)

centres. Thus, the calculations suggest that the co-ordination of a $[Fe(^tBuCN)_4]^{2+}$ fragment to the $[NiN_2S_3]$ unit substantially decreases the equatorial thiolate S character in the SOMO from 29.3% in $[Ni(L3)]^+$ to 10.1% in $[Ni(L3)[Fe(^tBuNC)_4]^{3+}$.

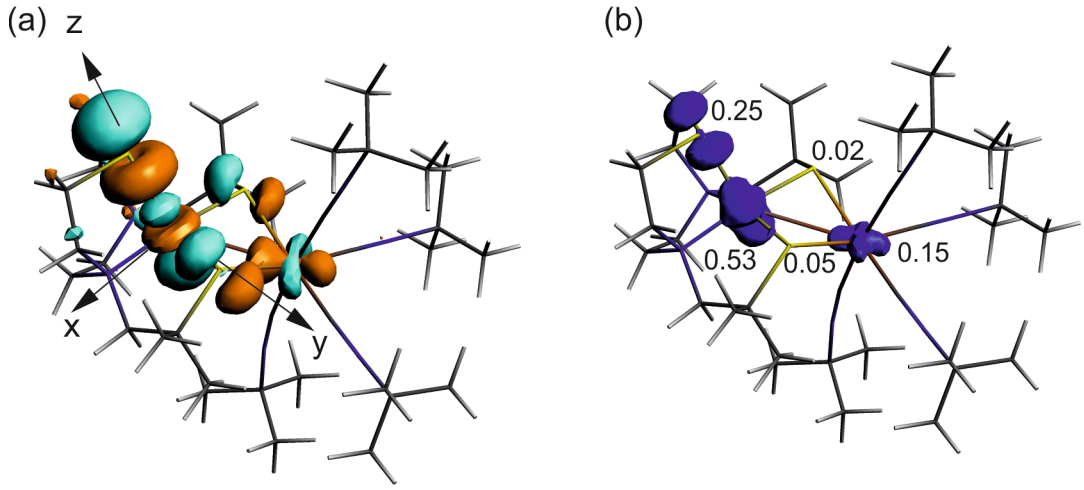


Figure 3.12.3: (a) The DFT calculated β-spin LUMO for $[Ni(L3)[Fe(^tBuNC)_4]^{3+}$ with an isosurface value of 0.03 e Å^{-3} and (b) the spin density distribution for $[Ni(L3)[Fe(^tBuNC)_4]^{3+}$ with an isosurface value of 0.01 e Å^{-3}.

The structure of the Ni site in Ni-C may be described as approximately square-based pyramidal in which the base plane is formed from three CysS donors and the bridging hydride, and the apical position is occupied by the remaining CysS donor.[40] An analysis of the *g*-tensor for the Ni-C state of the [NiFe] hydrogenase from *Desulfovibrio vulgaris* Miyazaki F, supported by DFT calculations, reveals a formal Ni^{III} $3d_{z^2}$ ground state in which there is significant delocalization of spin into the 3*p* orbital the apical Cys549 S-donor together with some delocalization onto the equatorial Cys546 S-donor.[41] In these respects the electronic structure of $[Ni(L3)[Fe(^tBuNC)_4]^{3+}$ shows a close correspondence to that proposed for the Ni-C state of the [NiFe] hydrogenases *i.e.* an essentially Ni^{III} $3d_{z^2}$ ground state with significant delocalization of spin onto the apical S-donor, which in $[Ni(L3)[Fe(^tBuNC)_4]^{3+}$ is derived from the thioether group.

3.13 Conclusions and Future Work

The ability for the [NiFe] hydrogenase enzyme to support the unusual Ni^{III} oxidation state and make use of it as a potent oxidising agent makes it an intriguing target for the synthesis and characterization of small molecule analogues.

We have synthesized and characterized the binuclear [NiFe] compounds $[Ni(L3)Fe(R\text{-}NC)_4](PF_6)_2$ (R = ^{t}Bu, benzyl) analogues of the active sites of the [NiFe] hydrogenases. The X-ray crystallographic structure of $[Ni(L3)Fe(^t BuNC)_4](PF_6)_2$ shows a close correspondence to the [NiFe] centre at the active sites of the [NiFe] hydrogenases.[8, 42] $[Ni(L3)Fe(R\text{-}NC)_4](PF_6)_2$ (R = ^{t}Bu, benzyl) exhibit chemically reversible oxidation processes at $E_{½}$ = 0.15 V vs Fc^+/Fc (R = ^{t}Bu) and $E_{½}$ = 0.21 V vs Fc^+/Fc (R = benzyl). Electrochemical, spectroscopic and DFT studies suggest that the reversible oxidation process is localized about the Ni center and involves a redox active orbital that is essentially Ni $3d_{z^2}$ and S(3)-based, and which shows a close correspondence with the SOMO calculated for the Ni-C state of the [NiFe] hydrogenase from *D. vulgaris* Miyazaki F.[41] The DFT calculations, together with the spectroscopic signatures of $[Ni(L3)Fe(R\text{-}NC)_4]^{3+}$ (R = ^{t}Bu, benzyl), are consistent with an assignment of the $[Ni(L3)Fe(R\text{-}NC)_4]^{3+}$ (R = ^{t}Bu, benzyl) to a formal $Ni^{III}Fe^{II}$ center that mirrors that of the Ni-C state.[40, 41]

The SOMO of $[Ni(L3)]^+$ possesses significantly more equatorial S-character than in $[Ni(L3)Fe(^t BuNC)_4]^{3+}$ (29.3 % *vs.* 10.1%, respectively). Thus, the coordination of a $[Fe(^t BuCN)_4]^{2+}$ fragment to $[Ni(L3)]^+$ in $[Ni(L3)Fe(^t BuNC)_4]^{3+}$ appears to limit thiyl radical contributions derived from the equatorial S donors in the SOMO. This suggests that the coordination of the $[Fe(CO)(CN)_2]$ unit to the $Ni(CysS)_4$ center in the Ni-C state of the [NiFe] hydrogenases may also play a similar role to ensure that the spin density is localized across the

Ni and apical CysS centers. This would represent an alternative strategy for controlling the electronic structures of Ni centers bound by CysS ligands in biology. Thus, it has been proposed that the unusual square planar N_2S_2 co-ordination sphere at the active sites of the Ni-containing superoxide dismutases (NiSODs),[43-45] together with the co-ordination of a N donor derived from His1 at the axial position in the oxidized form, promotes a Ni^{III} center with a formal $3d_{z^2}$ ground state[46, 47], thereby suppressing thiolate-based oxidative chemistry that could result in the formation of sulfonate groups which may inactivate the enzyme. In addition, the co-ordination of the $[Fe(^tBuNC)_4]^{2+}$ fragment to [Ni(L3)] in $[Ni(L3)Fe(^tBuNC)_4]^{3+}$ may suppress significant changes in the geometry of the [Ni(L3)] unit on oxidation as well as modulating the redox potential of the $[Ni(L3)Fe(^tBuNC)_4]^{3+/2+}$ couple. The $[Fe(CO)(CN)_2]$ center may play a similar roles at the active site of the [NiFe] hydrogenases in addition to supporting a bridging hydride species between the Ni and Fe centers in the Ni-C state.[48]

$[Ni(L3)Fe(R\text{-}NC)_4](PF_6)_2$ (R = ^{t}Bu, benzyl) did not exhibit any catalytic activity towards the oxidation of dihydrogen under electrochemical conditions. We note that the potentials of the $[Ni(L3)Fe(R\text{-}NC)_4]^{3+/2+}$ (R = ^{t}Bu, benzyl) couples are *ca.* 0.95 V more positive than those of the [NiFe] hydrogenases (-0.755 to -1.060 V vs Fc^+/Fc)[32, 49] and this could be one of the reasons that $[Ni(L3)Fe(R\text{-}NC)_4](PF_6)_2$, does not demonstrate any catalytic activity with respect to the oxidation of dihydrogen. Alternatively, the saturated coordination sphere around the Ni^{II} and Fe^{II} centres may also inhibit substrate binding. In addition the coordination sphere about the Ni centre in $[Ni(L3)Fe(R\text{-}NC)_4](PF_6)_2$ may stabilize the Ni^{III} state to reduce its effectiveness as an agent for the oxidation of dihydrogen.

Further investigations of $[Ni(L3)Fe(R\text{-}NC)_4](PF_6)_2$ will focus on reactions with hydride in an attempt to synthesize bridged Ni-μ(H)-Fe species and on the preparation of isotopically

enriched ^{61}Ni (I = 3/2) [Ni(L3)Fe(R-NC)$_4$](PF$_6$)$_2$ for more advanced EPR spectroscopic studies on [Ni(L3)Fe(R-NC)$_4$]$^{3+}$ to provide more insights into the electronic structures of these rare examples of [Ni^{III}Fe^{II}] complexes.

3.14 Experimental

Synthesis of diaminoethylsulfide (DAES).

2-aminoethanethiol hydrochloride (5.68 g, 50.0 mmol) and 2-chloroethanamine hydrochloride (5.80 g, 50.0 mmol) in water (35 ml) was cooled to 0 ºC. NaOH (6.0 g) was added to the solution and left to stir overnight. The colourless solution was extracted with $CHCl_3$ (5x 30 ml) and dried over Na_2SO_4. The solvent was removed *in vacuo* to leave a colourless oil. Yield = 57%. ^{1}H NMR (400 MHz, $CDCl_3$) 2.86 (t, J = 6.34 Hz, 4H), 2.60 (t, J = 6.40 Hz, 4H), 1.38 (br. s., 4H), MS (ESI+, *m/z*): 121.08 (M+H).

Synthesis of ditosyl-diaminoethylsulfide (DAES-Ts)

Diaminoethylsulfide (DAES) (2.30 g, 18.81 mmol) in water (35 ml) with NaOH (1.67 g, 41.40 mmol) was cooled to 5 ºC. *P*-toluenesulfonyl-chloride (7.91 g, 41.5 mmol) in Et_2O (100 ml) was added dropwise to this solution over 1 hour. The solution was stirred for 1 hour at 5-10 ºC and was then allowed to warm to room temperature before it was stirred for a further 3 hours. A white precipitate was collected by filtration and washed with water (20 ml), EtOH (20 ml) and Et_2O (20 ml) to yield a white crystalline solid. Yield = 67%. ^{1}H NMR (400 MHz, $CDCl_3$) δ ppm 7.74 (d, J = 8.00 Hz, 4H), 7.30 (d, J = 8.04 Hz, 4H), 3.06 (q, J = 6.48 Hz, 4H), 2.54 (t, J = 6.65 Hz, 4H), 2.42 (s, 6H). MS (ESI+, *m/z*): 429.097 (M+), 451.080 (M+Na).

Synthesis of disodium-ditosyl-diaminoethylsulfide (Na_2DAES-Ts)

Ditosyl-diaminoethylsulfide (9.00 g, 0.021 mol) was added to sodium metal (2.0 g, 0.09 mol) in anhydrous ethanol (100 ml). The resulting solution was heated to reflux at 80 ºC for 2 hours. The white precipitate was collected by filtration and washed with Et_2O (25 ml) and dried *in*

vacuo to yield a free-flowing powdery white solid which was used without further characterisation Yield = 83%.

Synthesis of 4,7-ditosyl-1,4,7-thiadiazonane [N_2S-Ts]

Disodium-ditosyl-diaminoethylsulfide (Na_2DAES-Ts) (9.10 g, 19.26 mmol) in anhydrous DMF (60 ml) was heated at 80 ºC under an inert atmosphere. Ethylene di(*p*-toluenesulfonate) (7.85 g, 21.18 mmol) in anhydrous DMF (70 ml) was added dropwise to this solution over 10 hours. The orange solution was reduced to 15 ml in volume *in vacuo* then decanted into ice water to form a cream precipitate that was extracted with DCM and recrystallised by the addition of methanol to yield a white crystalline solid. Yield = 61%. ^{1}H NMR (400 MHz, $CDCl_3$) δ ppm 7.67 (d, *J* = 8.28 Hz, 4H), 7.33 (d, *J* = 7.91 Hz, 4H), 3.51 (br. s., 4H), 3.38 (s, 4H), 3.04 - 3.22 (m, 4H), 2.44 (s, 6H). MS (ESI+, m/z): 455.112 (M+H), 477.095 (M+Na).

Synthesis of 1,4,7-thiadiazonane dihydrobromide ([N_2S].2HBr)

4,7-Ditosyl-1,4,7-thiadiazonane (1.20 g, 2.64 mmol) in anhydrous THF (60 ml) and anhydrous ethanol (5 ml) was cooled to -78 ºC under argon, and then gaseous ammonia (500 ml) added to the solution via a condenser. Lithium metal (5.5 g, 79 mmol, 30x excess) was added in portions to give a deep blue solution that returned to orange over time. After stirring for 12 hours at room temperature, allowing the ammonia to evaporate, water (10 ml) was added to quench any remaining lithium. 6M HCl (20 ml) and water (10 ml) was added to the resulting white paste, which partially dissolved, and the mixture washed with Et_2O (2x 35 ml) and reduced in volume to 15 ml. 6M KOH (20 ml) was added to the mixture and the solution extracted with $CHCl_3$ and dried over $MgSO_4$. The solvent was removed *in vacuo* to leave an orange oil which was dissolved in a minimum amount of Et_2O/EtOH (2:1). HBr solution (48% w/v) was added to form a cream precipitate, which was collected by filtration and dried *in*

vacuo to yield a white crystalline solid. Yield = 0.519 g, 64%. ^{1}H NMR (400 MHz, D_2O) δ ppm, 3.67 (s, 4H), 3.40 - 3.49 (m, 4H), 3.01 - 3.09 (m, 4H). MS (ESI+, *m/z*, M = $C_6H_{14}N_2S$): 147.093 (M+H).

Synthesis of 1,1'-(1,4,7-thiadiazonane)bis(2-methylpropane-2-thiol) [H_2L3]

1,4,7-Thiadiazonane dihydrobromide (0.520 g, 1.69 mmol) in water (20 ml) was combined with NaOH until the solution reached pH 11 then the solution was extracted with $CHCl_3$ (10x 30 ml) and reduced *in vacuo* to leave a colourless oil. The resulting oil was combined with isobutylene sulfide (3.3 ml, 0.034 mol) in a pressure tube under argon at 70 ºC for 3 hours with continual stirring. Excess isobutylene sulfide was removed *in vacuo* to leave a pale yellow oil that was used without further purification. Yield = 0.48 g, 88 %. ^{1}H NMR (400 MHz, CDl_3) δ ppm 3.32 - 3.36 (m, 2H), 2.39 (s, 4H), 1.60 (s, 12H), 1.53 (s, 2H), 1.46 (s, 1H), 1.43 (d, *J* = 5.02 Hz, 4H), 1.35 - 1.40 (m, 3H), 1.26 (s, 1H), 1.22 (s, 1H). MS (ESI+, m/z): 321.148 (M-H), 323.161 (M+H).

Synthesis of 1,1'-(1,4,7-thiadiazonane)bis(2-methylpropane-2-thiolato) nickel(II), [Ni(L3)]

Solutions of potassium hydroxide (0.137 g, 2.43 mmol) in dry, degassed EtOH (7 ml) and [$L^2N_2S_3H_2$] (0.262 g, 0.81 mmol) in anhydrous EtOH (10 ml) were combined dropwise over 10 minutes. $NiCl_2.6H_2O$ (0.190g, 0.80 mmol) in anhydrous EtOH (20 ml) was added dropwise to the ligand solution to afford an immediate colour change from green to brown. The solution was stirred for 12 hours before the solvent was removed *in vacuo*. The resulting solid was washed with diethyl ether (2x 20 ml) and hot hexane (25 ml) to yield a dark crystalline solid. Yield = 0.26 g, 85%. MS (ESI+, m/z): 378.076 (M+). Anal. Calcd. (%) for [$C_{14}H_{28}N_2S_3Ni$] C, 44.34; H, 7.44; N, 7.39; Found: C, 44.75; H, 7.75; N, 7.02. Crystals suitable for X-ray

diffraction were grown from the vapour diffusion of Et_2O into a solution of the product in MeCN.

Synthesis of [Ni(L3)Fe($CN^tBu)_4$] $(PF_6)_2$

[Ni(L3)] (0.200 g, 0.52 mmol) in MeCN (6 ml) was combined dropwise with a solution of $FeCl_2$ (0.056 g, 0.52 mmol) in MeCN (6 ml) over 10 minutes. The brown solution turned deep red after stirring for 4 hours then tert-butyl isocyanide (0.24 ml, 2.08 mmol) was added dropwise. The mixture was stirred at room temperature for 1 hour. The solvent was removed *in vacuo* to leave a red, solid residue, which was dissolved in MeOH (10 ml) and then NH_4PF_6 (0.2 g, 12.5 mmol) added. The mixture was left to stand for 1 hour to yield a red precipitate, which was collected via filtration and washed with Et_2O (2 ml). Yield = 41 mg, 13 %. The deep red filtrate was left to stand at 5 ºC overnight to yield a second crop of red crystalline solid, isolated via filtration and washed with MeOH (0.5 ml) and Et_2O (2 ml). Yield = 54 mg, 17 %. Crystals suitable for X-ray diffraction studies were grown from a MeOH solution via slow evaporation. MS (ESI+, m/z): 911.2699 (M+ [-PF_6]), 300.0792 (M2+ [-($CN^tBu)_2$] [-$(PF_6)_2$]). Anal. Calcd. (%) for [$C_{34}H_{64}F_{12}FeN_6NiP_2S_3$] C, 38.61; H, 6.10; N, 7.95; Found: C, 39.13; H, 6.05; N, 7.49.

Synthesis of [Ni(L3)Fe(benzyl-NC)$_4$]$(PF_6)_2$

A solution of [Ni(L3)] (0.250 g, 0.659 mmol) in MeCN (7 ml) was combined dropwise with $FeCl_2$ (0.084 g, 0.659 mmol) in MeCN (15 ml) over 10 minutes. The brown solution turned deep red after stirring for 4 hours and then benzyl isocyanide (0.32 ml, 2.64 mmol) was added dropwise and the reaction mixture left to react for 12 hours. The solution was filtered to remove a brown precipitate and the solvent removed *in vacuo* to yield a red/brown residue. The residue was dissolved in MeOH (10 ml), filtered and then NH_4PF_6 (0.4 g, 25 mmol) in MeOH (5 ml)

was added. The mixture was left to stand overnight to yield a dark solid. The product was purified via anaerobic column chromatography on activated alumina (eluent DCM/MeOH 99:1) to yield a brown residue that was dissolved in DCM (2 ml) and the solution added dropwise to an excess of swirling Et_2O (80 ml). The product was recovered via filtration as a fine brown powder. Yield = 39 mg, 5 %. MS (ESI+, m/z): 451.1229 (M+ [-$(PF_6)_2$]). Anal. Calcd. (%) for [$C_{46}H_{56}F_{12}FeN_6NiP_2S_3$] C, 46.29; H, 4.73; N, 7.04; Found: C, 46.70; H, 4.81; N, 6.85.

Attempted synthesis of [Ni(L3)Fe(cyclohexyl-NC)$_4$](PF_6)$_2$

The synthesis of [Ni(L3)Fe(cyclohexyl-NC)$_4$](PF_6)$_2$ was attempted following the procedure employed for the synthesis of [Ni(L3)Fe(benzyl-NC)$_4$](PF_6)$_2$ except with cyclohexyl isocyanide in place of benzyl isocyanide. Mass spectrometry indicated that the crude red solid contained the desired product. Attempts were made to purify the complex by anaerobic column chromatography (eluent: 99:1 DCM/MeOH), however, it was not possible to isolate the complex as a pure solid. MS (ESI+, m/z): 435.1856 (M^{2+} [-$(PF_6)_2$]).

3.15 References

1. J. Riethausen, O. Rudiger, W. Gartner, W. Lubitz and H. S. Shafaat, *ChemBioChem*, 2013, **14**, 1714-1719.
2. H. Tai, K. Nishikawa, S. Inoue, Y. Higuchi and S. Hirota, *J. Phys. Chem. B*, 2015.
3. S. Ogo, *Chem. Commun. (Cambridge, U. K.)*, 2009, 3317-3325.
4. C. Tard and C. J. Pickett, *Chem. Rev. (Washington, DC, U. S.)*, 2009, **109**, 2245-2274.
5. S. Canaguier, V. Artero and M. Fontecave, *Dalton Trans.*, 2008, 315.
6. S. Ogo, K. Ichikawa, T. Kishima, T. Matsumoto, H. Nakai, K. Kusaka and T. Ohhara, *Science*, 2013, **339**, 682-684.
7. S. P. J. Albracht, E. G. Graf and R. K. Thauer, *FEBS Lett.*, 1982, **140**, 311-313.
8. F. Dole, A. Fournel, V. Magro, E. C. Hatchikian, P. Bertrand and B. Guigliarelli, *Biochemistry*, 1997, **36**, 7847-7854.
9. M. Teixeira, I. Moura, A. V. Xavier, B. H. Huynh, D. V. DerVartanian, H. D. Peck, J. LeGall and J. J. Moura, *J. Biol. Chem.*, 1985, **260**, 8942-8950.
10. H. Tai, K. Nishikawa, M. Suzuki, Y. Higuchi and S. Hirota, *Angew. Chemiw Intl. Ed.*, 2014, **53**, 13817-13820.
11. C. Sodipo, University of Nottingham, 2013.
12. C. Perotto, University of Nottingham, 2012.
13. C. A. Grapperhaus, M. Li, A. K. Patra, S. Poturovic, P. M. Kozlowski, M. Z. Zgierski and M. S. Mashuta, *Inorg. Chem.*, 2003, **42**, 4382-4388.
14. C. C. Howard and W. Marckwald, *Berichte der deutschen chemischen Gesellschaft*, 1899, **32**, 2038-2042.
15. R. Mattes, P. Steinhoff and P. Hoffmann, *Z. Naturforsch., B: Chem. Sci.*, 1987, **42b**, 867-873.
16. A. J. Birch, *Pure Appl. Chem.*, 1996, **68**.
17. A. J. Birch, *Journal of the Chemical Society (Resumed)*, 1944, 430-436.
18. P. Sobik, J. Grunenberg, K. Boeroeczky, H. Laatsch, I. Wagner-Doebler and S. Schulz, *J. Org. Chem.*, 2007, **72**, 3776-3782.
19. L. Sacconi, *Pure Appl. Chem.*, 1968, **17**, 95-128.
20. M. G. O'Toole, M. Kreso, P. M. Kozlowski, M. S. Mashuta and C. A. Grapperhaus, *J. Biol. Inorg. Chem.*, 2008, **13**, 1219-1230.
21. N. G. Connelly and W. E. Geiger, *Chem. Rev. (Washington, DC, U. S.)*, 1996, **96**, 877-910.
22. C. U. Perotto, G. Marshall, G. J. Jones, E. Stephen Davies, W. Lewis, J. McMaster and M. Schroder, *Chem. Commun. (Cambridge, U. K.)*, 2015, **51**, 16988-16991.
23. D. Sellmann, S. Funfgelder, G. Pohlmann, F. Knoch and M. Moll, *Inorg. Chem.*, 1990, **29**, 4772-4778.
24. A. Perra, E. S. Davies, J. R. Hyde, Q. Wang, J. McMaster and M. Schroder, *Chem. Commun. (Cambridge, U. K.)*, 2006, 1103-1105.
25. G. Musie, P. J. Farmer, T. Tuntulani, J. H. Reibenspies and M. Y. Darensbourg, *Inorg. Chem.*, 1996, **35**, 2176-2183.
26. C. A. Boyke, T. B. Rauchfuss, S. R. Wilson, M. M. Rohmer and M. Benard, *J. Am. Chem. Soc.*, 2004, **126**, 15151-15160.
27. S. M. Bellows, W. W. Brennessel and P. L. Holland, *Eur. J. Inorg. Chem.*, 2016, **2016**, 3344-3355.
28. S. E. Gibson, H. Ibrahim, C. Pasquier, M. A. Peplow, J. M. Rushton, J. W. Steed and S. Sur, *Chem. Eur. J.*, 2002, **8**, 269-276.
29. A. Volbeda, M. H. Charon, C. Piras, E. C. Hatchikian, M. Frey and J. C. Fontecilla-Camps, *Nature*, 1995, **373**, 580-587.

30. R. S. Nicholson and I. Shain, *Anal. Chem.*, 1964, **36**, 706-723.
31. S. Chandra and R. Kumar, *Spectrochim Acta A Mol Biomol Spectrosc*, 2005, **62**, 518-525.
32. C. Fichtner, C. Laurich, E. Bothe and W. Lubitz, *Biochemistry*, 2006, **45**, 9706-9716.
33. R. S. Nicholson, *Anal. Chem.*, 1966, **38**, 1406-1406.
34. J. Taraszewska, J. Sałdo, J. Michalik and B. Korybut-Daszkiewicz, *Pol. J. Chem.*, 2000, **74**, 813-822.
35. J. Nishigaki, T. Matsumoto and K. Tatsumi, *Inorg. Chem.*, 2012, **51**, 3690-3697.
36. J. L. Nehring and D. M. Heinekey, *Inorg. Chem.*, 2003, **42**, 4288-4292.
37. A. Vogler, *Isonitrile Chemistry*, Academic Press, New York, 1971.
38. P. W. Atkins, T. Overton, J. Rourke, M. Weller and F. A. Armstrong, *Shriver & Atkins' Inorganic Chemistry*, Oxford University Press, Oxford; New York, 2010.
39. T.-W. Chiou and W.-F. Liaw, *C. R. Chim.*, 2008, **11**, 818-833.
40. W. Lubitz, E. Reijerse and M. van Gastel, *Chem Rev*, 2007, **107**, 4331-4365.
41. M. Kampa, W. Lubitz, M. van Gastel and F. Neese, *J. Biol. Inorg. Chem.*, 2012, **17**, 1269-1281.
42. A. Volbeda and J. C. Fontecilla-Camps, *Dalton Trans.*, 2003, 4030-4038.
43. D. P. Barondeau, C. J. Kassmann, C. K. Bruns, J. A. Tainer and E. D. Getzoff, *Biochemistry*, 2004, **43**, 8038-8047.
44. A. T. Fiedler, P. A. Bryngelson, M. J. Maroney and T. C. Brunold, *J. Am. Chem. Soc.*, 2005, **127**, 5449-5462.
45. J. Wuerges, J. W. Lee, Y. I. Yim, H. S. Yim, S. O. Kang and K. Djinovic Carugo, *Proc. Natl. Acad. Sci. U. S. A.*, 2004, **101**, 8569-8574.
46. E. P. Broering, S. Dillon, E. M. Gale, R. A. Steiner, J. Telser, T. C. Brunold and T. C. Harrop, *Inorg. Chem.*, 2015, **54**, 3815-3828.
47. P. A. Stenson, A. Board, A. Marin-Becerra, A. J. Blake, E. S. Davies, C. Wilson, J. McMaster and M. Schroder, *Chem. Eur. J.*, 2008, **14**, 2564-2576.
48. S. Foerster, M. Stein, M. Brecht, H. Ogata, Y. Higuchi and W. Lubitz, *J. Am. Chem. Soc.*, 2003, **125**, 83-93.
49. H. Ogata, W. Lubitz and Y. Higuchi, *Dalton Trans.*, 2009, 7577-7587.

Chapter Four

Substitution of Nickel for Other Metals in [NiFe] Enzyme Analogues

4.1 Introduction and aims

The N,N'-diethyl-3,7-diazononane-1,9-dithiolate $(L1)^{2-}$ ligand has been widely used to coordinate to Ni centres in small molecule analogues of the active site of the [NiFe] hydrogenases.[1-5] However, there are very few examples of other transition metal complexes with this ligand beyond multinuclear complexes containing Mn(L1)[6] or Fe(L1)[7] units (Figure 4.1.1). Complexes of Mn^{II} with $(L1)^{2-}$ are isolated as Mn_2 dimers[6, 7] whereas Fe(L1) supports the formation of a hexanuclear cluster that possesses a stair-like $[Fe_6(\mu_3\text{-}S)_4(\mu_2\text{-}SR)_4]$ core and which exhibits electrochemically irreversible oxidation and reduction processes at $E_{½}$ = +490 and -810 mV *vs* SCE, respectively.[6, 7]

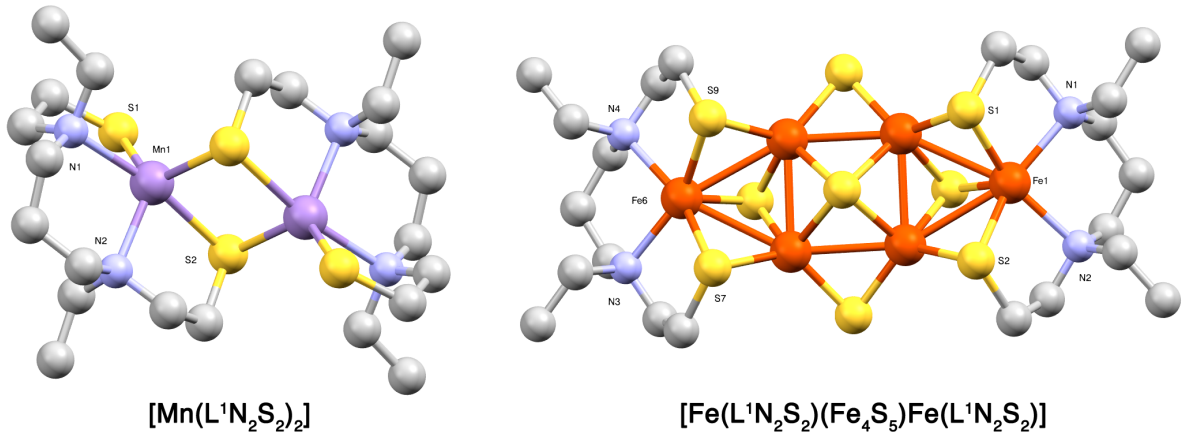
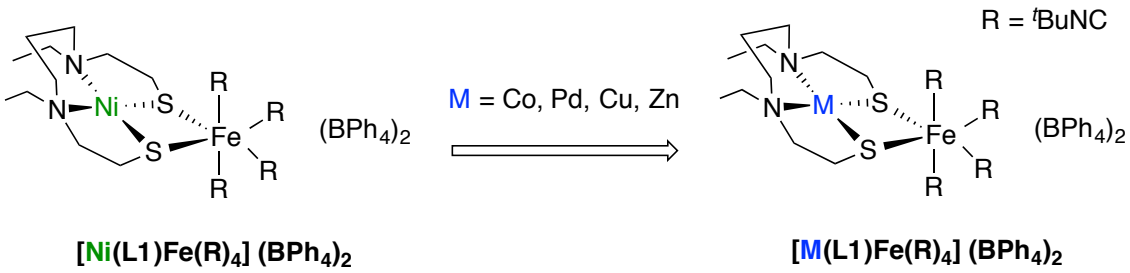


Figure 4.1.1: Examples of multinuclear Fe and Mn complexes featuring the $(L1)^{2-}$ ligand, (solid state structures of complexes referenced in text taken from CCSD).[8]

We have successfully synthesized and characterized $[Ni(L1)Fe(CN^tBu)_4](BPh_4)_2$ (Scheme 3.1) as an analogue of the active site of the [NiFe] hydrogenase and demonstrated that its reduction to $[Ni(L1)Fe(CN^tBu)_4]^+$ generates an effective model for the Ni-L state of the [NiFe] hydrogenase (Chapter 1).[5, 9] However, $[Ni(L1)Fe(CN^tBu)_4](BPh_4)_2$ does not appear to catalyse the uptake or production of dihydrogen. Given the limited investigations of the coordination chemistry of $(L1)^{2-}$ with other transition metals and the limited catalytic activity

of $[Ni(L1)Fe(CN^tBu)_4](BPh_4)_2$ towards dihydrogen production we attempted to synthesize a range of monomeric M(L1) (M = Pd, Co, Zn and Cu) complexes and to investigate their coordination to $[Fe(CN^tBu)_4]^{2+}$ centres (Scheme 4.1.1). The chemistries of the resulting $[M(L1)Fe(CN^tBu)_4]^{2+}$ complexes could then be compared with that of $[Ni(L1)Fe(CN^tBu)_4]^{2+}$.

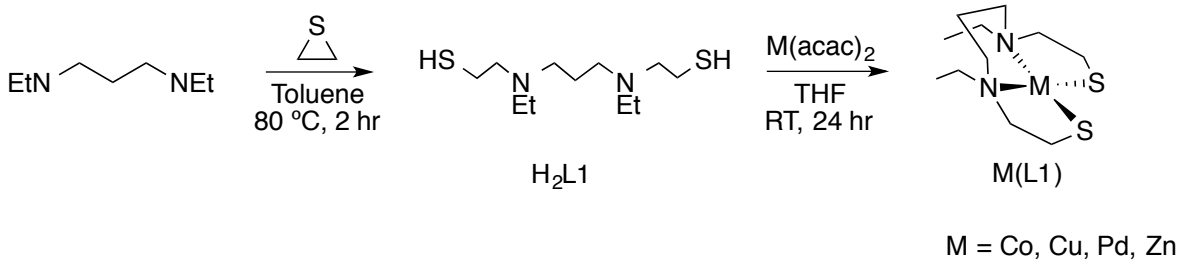


Scheme 4.1.1: Other transition metals in place of Ni in $[M(L1)Fe(CN^tBu)_4](BPh_4)_2$ (M = Pd, Co, Zn and Cu)

4.2 Results and discussion

4.2.1 The syntheses of M(L1) (M = Pd, Co and Zn) and the attempted synthesis of Cu(L1)

We adopted the procedure for the synthesis of [Ni(L1)] (Chapter 1) for the syntheses of M(L1) (M = Pd, Co and Zn) and the attempted synthesis of Cu(L1). (H_2L1) reacts with $M(acac)_2$ (M = Pd, Co and Zn) in THF at room temperature to yield the corresponding [M(L1)] complexes as precipitates (Scheme 4.2.1). The solubilities of $M(acac)_2$ (M = Pd, Co and Zn) in THF are considerably lower than $Ni(acac)_2$; however, these solubilities are sufficient to enable the reaction and the isolation of [M(L1)] without significant changes to the reaction conditions.



Scheme 4.2.1: General Synthesis for M(L1) (M = Co, Cu, Pd, Zn) Complexes.

Pd(L1) was isolated as an air-stable yellow/orange solid that dissolves in MeCN to yield a yellow solution. The formulation of Pd(L1) was confirmed by elemental analysis, mass spectrometry and by ^{1}H and ^{13}C NMR spectroscopies. Co(L1) was isolated as an air-sensitive, dark blue crystalline solid that dissolves in MeCN to generate a deep blue MeCN solution that on exposure to air leads to the formation of a brown solution. The ^{1}H NMR spectrum of Co(L1) in CD_3CN is broad and poorly resolved, which suggests that Co(L1) is paramagnetic. Co(L1) is EPR silent in a fluid MeCN solution in a flat cell at X-band frequency, suggesting the presence of multiple unpaired electrons in Co(L1). The formulation of Co(L1) was supported by ICP-OES, elemental analysis and mass spectrometry. Zn(L1) was isolated as an air stable, pale yellow crystalline solid with a formulation confirmed by mass spectrometry and by ^{1}H and ^{13}C NMR spectroscopies. The reaction between $Cu(acac)_2$ and (H_2L1) in THF is accompanied by the formation of a dark green solution. However, no precipitate formed and mass spectrometry of the reaction mixture identified features consistent with the formation of the disulfide of (L1) suggesting oxidation of the thiol units in (H_2L1) by Cu^{II}.

Crystals of Pd(L1) and Zn(L1), suitable for X-ray diffraction, were obtained by the slow evaporation of solutions of the complexes in THF. Crystals of Co(L1) suitable for X-ray

diffraction studies were grown from dry, degassed CD_3CN solution in a glovebox by slow evaporation.

4.2.2 X-ray crystallographic studies of M(L1) (M = Pd, Co and Zn)

4.2.2.1 The X-ray crystal structure of Pd(L1)

Pd(L1) crystallises in the P-1 space group. The structure of Pd(L1) is shown in Figure 4.2.1 and selected bond lengths and angles are shown in Table 4.2.1.

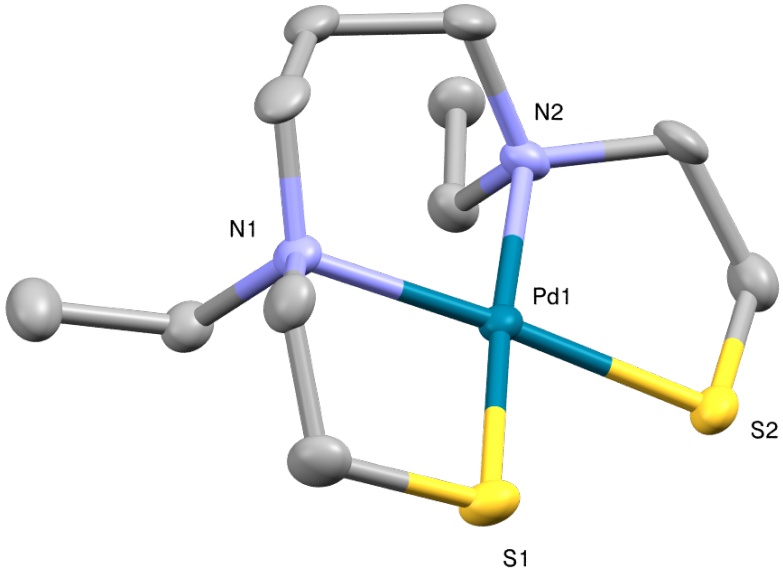


Figure 4.2.1 – The X-ray crystal structure of Pd(L1) with thermal ellipsoids at 50%. The hydrogen atoms are omitted for clarity.

Table 4.2.1 – Selected bond lengths and angles for Pd(L1)

Bond	Length	Bond Angle /Å	Angle /º
Pd(1)-S(1)	2.271(2)	N(1)-Pd(1)-S(2)	175.6(2)
Pd(1)-N(1)	2.147(8)	N(2)-Pd(1)-S(1)	176.0(2)
Pd(1)-S(2)	2.275(3)	N(2)-Pd(1)-S(2)	87.8(2)
Pd(1)-N(2)	2.139(6)	S(1)-Pd(1)-N(1)	87.5(2)
		S(1)-Pd(1)-S(2)	88.18(9)
		N(1)-Pd(1)-N(2)	96.5(3)

The Pd centre in Pd(L1) is four coordinate and is bound by two amine N- and two thiolate S-donors with Pd(1)-S and Pd(1)-N distances that are typical of those found in other Pd^{II} complexes.[10-12] Each Pd(1)-S and Pd(1)-N distance, and N-Pd(1)-S angle are not significantly different from their other counterparts within the structure. The dihedral angle between the planes defined by N(1)-Pd(1)-N(2) and S(1)-Pd(1)-S(2) is 179.60(2) º and this, together with the bond angles about the Pd(1) centre (Table 4.2.1), shows that the geometry in Pd(L1) is essentially square planar. A comparison of the equivalent dihedral angle in Ni(L1) [173.060(1) º], the S(1)-M-S(2) and the N(1)-M-N(2) angles [88.18(9)º and 96.5(3) º for M = Pd, and 84.20(2) º and 98.00(6) º for M = Ni[13]] show that Pd(L1) possesses a more regular square planar geometry than that of Ni(L1).

4.2.2.2 The X-ray crystal structure of Co(L1)

Co(L1) crystallises in the P-1 space group. The structure of Co(L1) is shown in Figure 4.2.2 and selected bond lengths and angles are shown in Table 4.2.2.

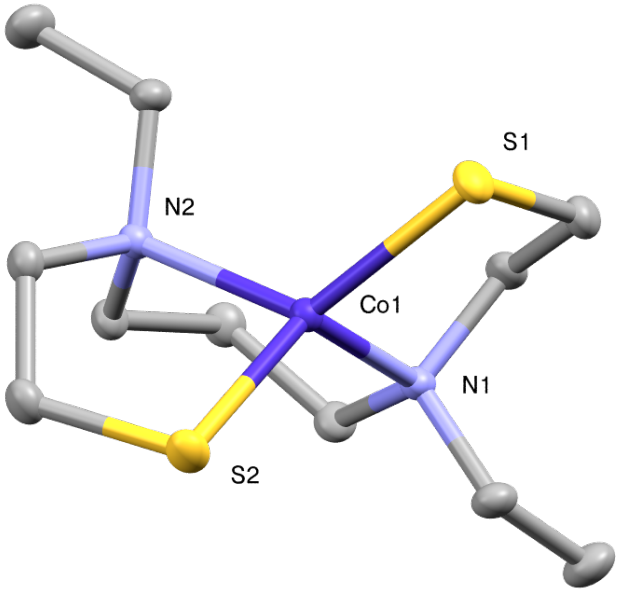


Figure 4.2.2: The X-ray crystal structure of Co(L1) with thermal ellipsoids at 50%. Hydrogen atoms omitted for clarity.

Table 4.2.2 – Selected bond lengths and angles for Co(L1)

Bond	**Length / Å**	**Bond Angle**	**Angle /º**
Co(1)-S(1)	2.2520(5)	S(1)-Co(1)-S(2)	126.09(2)
Co(1)-N(1)	2.2451(5)	N(1)-Co(1)-N(2)	102.69(6)
Co(1)-S(2)	2.085(1)	S(1)-Co(1)-N(1)	91.33(4)
Co(1)-N(2)	2.090(2)	S(2)-Co(1)-N(2)	92.09(4)
		S(1)-Co(1)-N(2)	122.37(4)
		S(2)-Co(1)-N(1)	122.51(4)

Co(L1) is four coordinate and the dihedral angle between the planes defined N(1)-Co(1)-N(2) and S(1)-Co(1)-S(2) (68.664(6) º) shows that Co($L^1N_2S_2$) adopts a distorted tetrahedral geometry in contrast to M($L^1N_2S_2$) (M = Pd, Ni), which adopt essentially square planar geometries. A distorted tetrahedral coordination sphere in Co(L1) potentially consistent with the magnetic properties of this complex in solution. Thus, Co(L1) exhibits a broad ^{1}H-NMR spectrum in CD_3CN, and is EPR silent at room temperature at X-band frequencies, consistent with a d^7 metal centre with an S = 3/2 ground state. The Co-N and Co-S distances are similar to those of other Co^{II} complexes in a distorted tetrahedral coordination geometry.[14-16]

4.2.2.3 The X-ray crystal structure of Zn(L1)

Zn(L1) crystallises in the C2/c space group. The structure of Zn(L1) is shown in Figure 4.2.3 and selected bond lengths and angles are shown in Table 4.2.3.

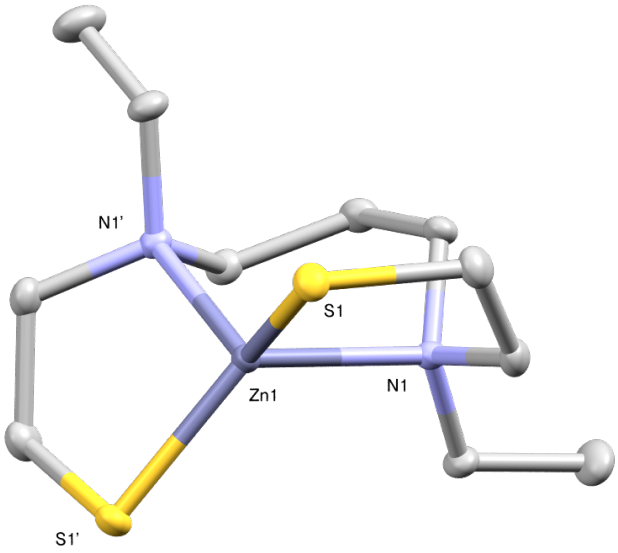


Figure 4.2.3 – The X-ray crystal structure of Zn(L1) with thermal ellipsoids at 50%. Hydrogen atoms omitted for clarity.

Table 4.2.3 – Selected bond lengths and angles for Zn(L1)

Bond	**Length**	**Bond Angle /Å**	**Angle /º**
Zn(1)-N(1)	2.1310(10)	S(1)-Zn(1)-S(1')	126.75(2)
Zn(1)-S(1)	2.2529(3)	S(1)-Zn(1)-N(1)	93.12(3)
		N(1)-Zn(1)-N(1')	98.24(6)
		N(1)-Zn(1)-S(1')	122.16(3)

Zn(L1) is four coordinate and the dihedral angle between the planes defined N(1)-Zn(1)-N(2) and S(1)-Zn(1)-S(2) (69.30(4) º) shows that Zn(L1) adopts a distorted tetrahedral geometry that is consistent with a d^{10} Zn^{II} metal centre. The Zn-N and Zn-S distances are comparable to those found for other $Zn(N_2X_2)$ complexes (X = S, O);[17-19] the Zn-N distances [2.1310(10) Å] are longer than the Co-N distances [2.085(1)-2.090(2) Å] in Co(L1) while the Zn-S distances [2.2529(3) Å] are comparable to the Co-S distances in Co(L1) [2.2520(5) Å].

4.2.2.4 Conclusions from the X-ray crystal structures of M(L1) (M = Pd, Co, Zn)

The X-ray crystal structures of M(L1) (M = Pd, Co, Zn), together with that for Ni($L^1N_2S_2$), demonstrate that $(L1)^{2-}$ forms four-coordinate complexes with 3*d* and 4*d* transition metal centres. The geometries range from essentially square planar M(L1) (M = Pd, Ni; dihedral angle = 1.68(18) º[13] and 6.94(1) º, respectively) to distorted tetrahedral M(L1) (M = Co, Zn; dihedral angle = 68.664(6) º and 69.30(4) º, respectively). In this respect $(L1)^{2-}$ shows a degree of flexibility in its mode of coordination that may be important for the incorporation of M(L1) units in bimetallic complexes and for changes in geometry that may accompany any redox processes. The S-S distance is also variable, and is markedly shorter for the square planar configuration than the distorted tetrahedral geometry by ca. 0.8 to 1.1 Å. The S-S distances for M(L1) (M = Co, Zn; 4.0086(3) Å, 4.0263(7) Å, respectively) are almost the same, while the M(L1) (M = Ni, Pd; 2.9151(9) Å,[13] 3.210(3) Å, respectively) show a greater variation, which could be explained by the larger Pd^{2+} cation. The smaller S-S distance exhibited by the square planar M(L1) complexes could indicate one of the reasons that complexation to an iron fragment and subsequent formation of the M-(S_2)-Fe moiety appears to be more facile for this initial geometry. Upon formation of these M-(S_2)-Fe systems, the S-S distance contracts by a small degree in comparison to the parent M(L1) complex (M = Ni, Pd). For M(L1) and [M(L1)Fe(CN^tBu)$_4$](BPh_4)$_2$, these values are 2.9151(9) Å vs 2.8810(5) Å (M = Ni) and 3.210(3) Å vs 3.066(5) Å (M = Pd) (Section 4.4), reflecting a more significant contraction for the [PdFe] system of ca. 0.2 Å compared to the much smaller difference for the [NiFe] system. The S-S distance of Co(L1) (4.0086(3) Å) compared to [Co(L1)(CN^tBu)Fe(CNtBu)$_4$](BPh_4)$_2$ (3.071(11) Å) (Section 4.8), however, is a change of almost 1 Å, reflecting a significant change between the parent complex and that of the [CoFe] compund. It is difficult to draw any significant conclusions from this result in comparison with the square-planar parent complexes due to the coordination of the additional isocyanide

ligand at the cobalt centre, however, it is clear that the addition of the iron centre to the coordination sphere acts to reduce the S…S distance. In the $[Co(L1)(CN^tBu)Fe(CNtBu)_4](BPh_4)_2$ complex, the additional isocyanide ligand acts to form the base of a square-based pyramidal system with the four basal atoms (C(1), N(1), S(1) and S(2)) in a nearly square planar geometry, with the other nitrogen atom (N(2)) occupying the axial position. This coordination sphere could explain the significant change in S…S distance, as it is much more similar to the S…S geometry in the square planar systems (M = Ni, Pd). The S…S distances in these [MFe] complexes (M = Ni, Pd, Co) are within 0.12 Å of each other.

4.2.3 Electrochemical studies of M(L1) (M = Pd, Co and Zn)

4.2.3.1 Electrochemistry of Pd(L1)

The cyclic voltammgram of a 1 mM solution of Pd(L1) in MeCN with $[N^nBu_4][BF_4]$ (0.2 M) as supporting electrolyte (Figure 4.2.1) possesses an irreversible reduction process at -2.54 V vs Fc^+/Fc. This behaviour is similar to that for Ni(L1), which also demonstrates a non-reversible reduction process at -2.35 V vs Fc^+/Fc in MeCN solution.[20]

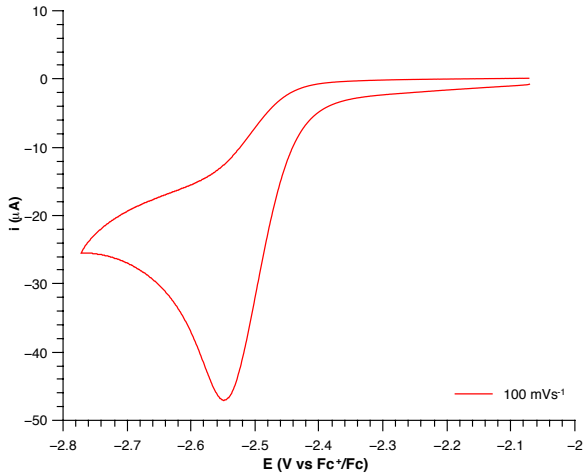


Figure 4.2.1: Cyclic voltammogram of 1 mM Pd(L1) in MeCN with 0.2 M $[N^nBu_4][BF_4]$ as supporting electrolyte at 100 mVs^{-1}

4.2.3.2 Electrochemistry of Co(L1)

The cyclic voltammogram of Co(L1) in MeCN solution with $[N^nBu_4][BF_4]$ (0.2 M) as supporting electrolyte is shown in Figure 4.2.2. Co(L1) possesses an oxidation process at -0.2 V vs Fc^+/Fc that is associated with a corresponding reduction process at -0.8 V vs Fc+/Fc. This process is not electrochemically reversible and maybe associated with a complex ECE-type process.[21] Unlike Ni(L1)[20] and Pd(L1), Co(L1) does not appear to possess a non-reversible reduction process at around -2.3 to -2.5 V vs Fc^+/Fc in MeCN. However, we note that these potentials are close to the edge of the MeCN solvent window,[22] and it may be that the equivalent reduction process for Co(L1) lies at more negative potentials than can be accessed in MeCN as a solvent.

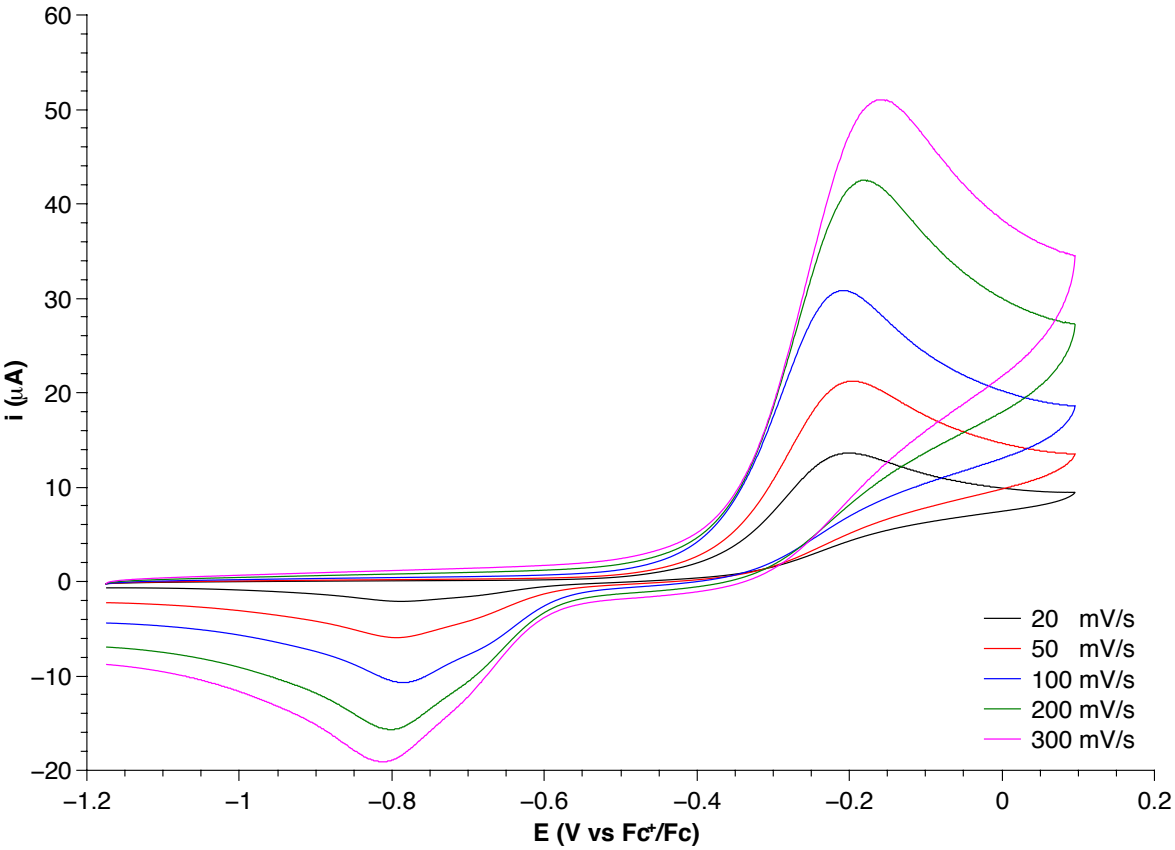


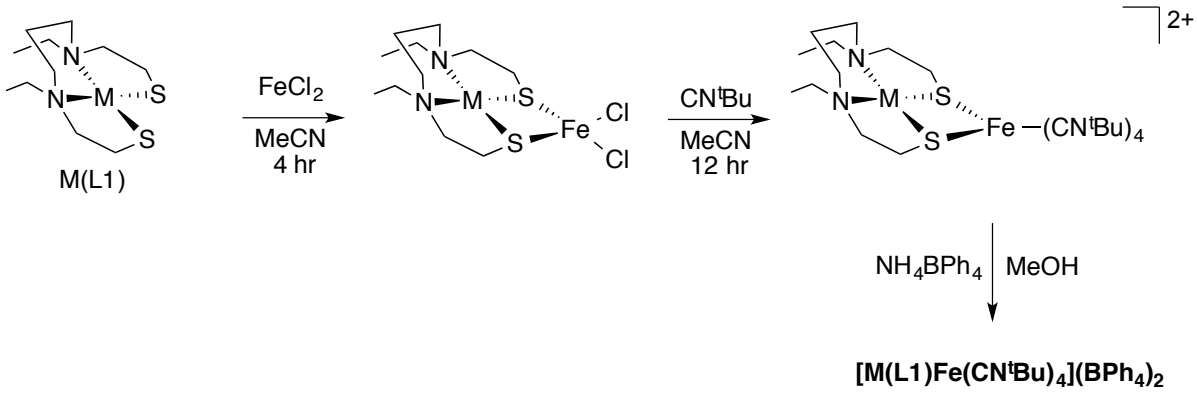
Figure 4.2.2: Cyclic voltammogram of 1 mM Co(L1) in MeCN with 0.2 M $[N^nBu_4][BF_4]$ as supporting electrolyte between 20-300 mVs^{-1}

4.2.3.3 Electrochemistry of Zn(L1)

The cyclic voltammogram of Zn(L1) in MeCN solution with $[N^nBu_4][BF_4]$ (0.2 M) as supporting electrolyte does not possess any redox processes within the solvent window, which is not unexpected for a d^{10} complex.

4.3 The attempted syntheses of $[M(L1)Fe(CN^tBu)_4](BPh_4)_2$ (M = Pd, Co and Zn)

The syntheses of $[M(L1)Fe(CN^tBu)_4](BPh_4)_2$ from $M(L^1N_2S_2)$ (M = Pd, Co and Zn) were attempted using the same conditions used for the synthesis of $[Ni(L1)Fe(CN^tBu)_4](BPh_4)_2$ from $Ni(L^1N_2S_2)$ (Chapter 2). This synthetic scheme is shown in Scheme 4.3.



Scheme 4.3: The synthetic scheme for $[M(L1)Fe(CN^tBu)_4](BPh_4)_2$ from $M(L^1N_2S_2)$ (M = Pd, Co and Zn).

Pd(L1) reacts readily with $FeCl_2$ in MeCN solution; the solution turns from yellow to deep orange almost immediately and then slowly to a paler orange/yellow colour over 4 hours. The dropwise addition of ^{t}BuNC yields a yellow/orange solution after stirring for 12 hours. The removal of the solvent *in vacuo* and a subsequent precipitation from MeOH solution on the addition of $NaBPh_4$ yields $[Pd(L1)Fe(CN^tBu)_4](BPh_4)_2$ as a yellow solid. The formulation of the complex was confirmed by accurate mass spectrometry and by ^{1}H- and ^{13}C-NMR spectroscopies.

Co(L1) reacts with $FeCl_2$ in MeCN, with the solution turning from dark blue to green over 4 hours, and then to dark brown on addition of ^tBuNC after 12 hours. The removal of the solvent *in vacuo* and the subsequent addition of $NaBPh_4$ to a MeOH solution yields a brown intractable solid. Despite a number of attempts under varying conditions, and attempts to purify the isolated brown solid via chromatography, it was not possible to isolate pure material. However, mass spectrometry suggested that $[Co(L1)Fe(CN^tBu)_4]^{2+}$ was present in the dark green filtrate following the precipitation of the brown solid (Figure 4.3.1). Thus, the filtrate was left to stand at 5ºC under argon in an attempt to encourage precipitation. Dark orange crystals were isolated after a few days, washed with small amounts of MeOH and pentane, and analysed by X-ray crystallography and mass spectrometry, and were determined to be $[Co(L1)(CN^tBu)Fe(CN^tBu)_4](BPh_4)_2$. This complex differs from the intended product by the coordination of an additional isocyanide ligand at the Co centre.

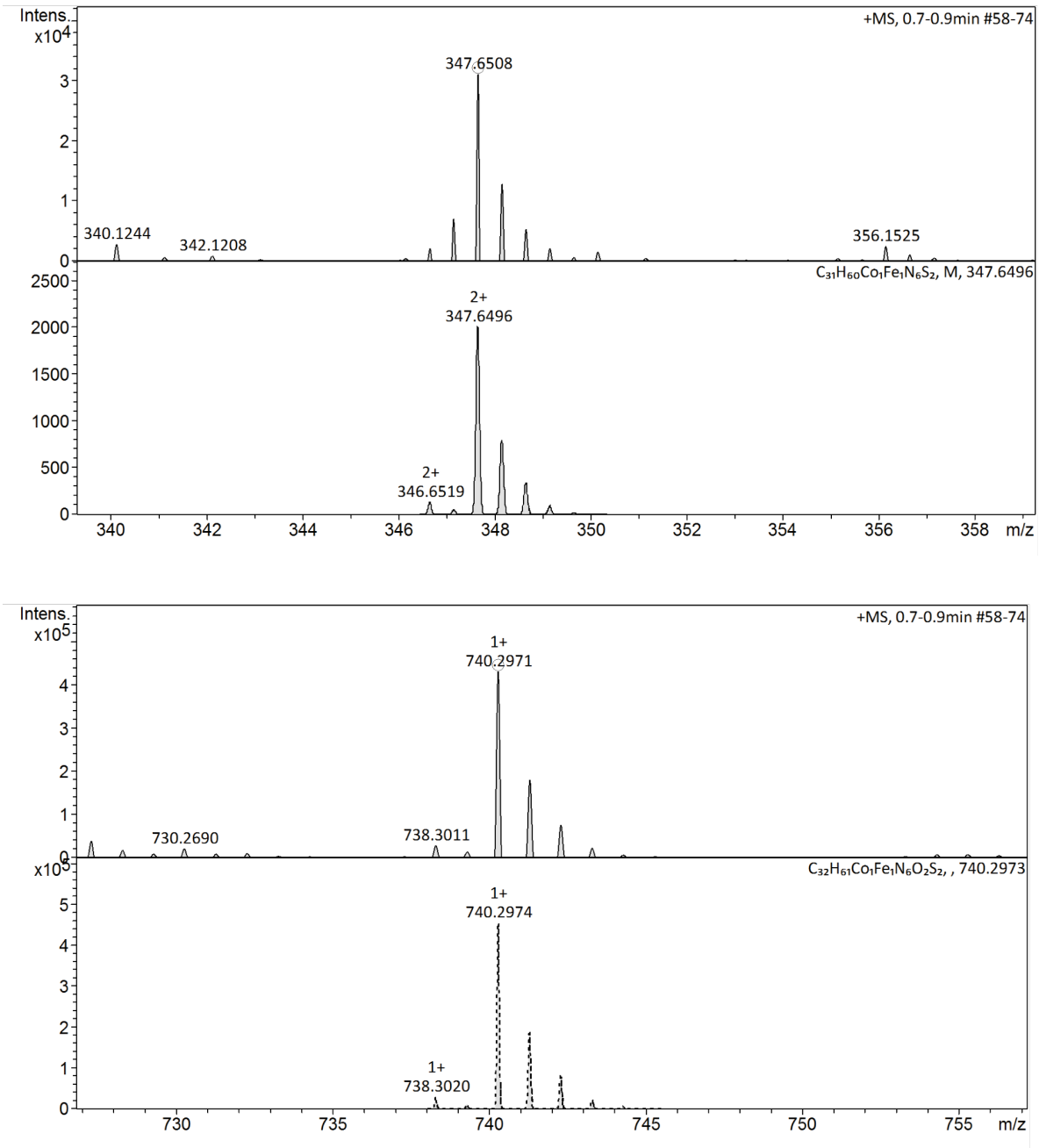


Figure 4.3.1: ESI-MS+ of $[Co(L1)Fe(CN^tBu)_4]^{2+}$ and predicted isotope pattern at m/z 347.6496 (top) and the formate adduct $[Co(L1)Fe(CN^tBu)_4](CO_2H)^+$ at 740.2971 (bottom) recorded during attempted $[Co(L1)Fe(CN^tBu)_4](BPh_4)_2$ synthesis.

In spite of several attempts under a number of conditions, Zn(L1) does not appear to react with $FeCl_2$ in solution. Zn(L1) possesses the greatest tetrahedral distortion across the Zn(L1) (M = Ni, Pd, Co and Zn) series of complexes. Thus, the distance between the two thiolate S-atoms [S….S = 4.0263(7) Å in Zn(L1)] may be too great to promote the formation of the thiolate bridged Zn-Fe structure in $[Zn(L1)Fe(CN^tBu)_4]^{2+}$.

4.4 X-ray crystallography of $[Pd(L1)Fe(CN^tBu)_4](BPh_4)_2$

Crystals suitable for X-ray diffraction studies were grown from MeOH at 5ºC over approximately 72 hours. $[Pd(L1)Fe(CN^tBu)_4](BPh_4)_2$ crystallises in the P-1 space group and the structure of the $[Pd(L1)Fe(CN^tBu)_4]^{2+}$ cation is shown in Figure 4.4.1 with selected bond lengths and angles shown in Table 4.4.1.

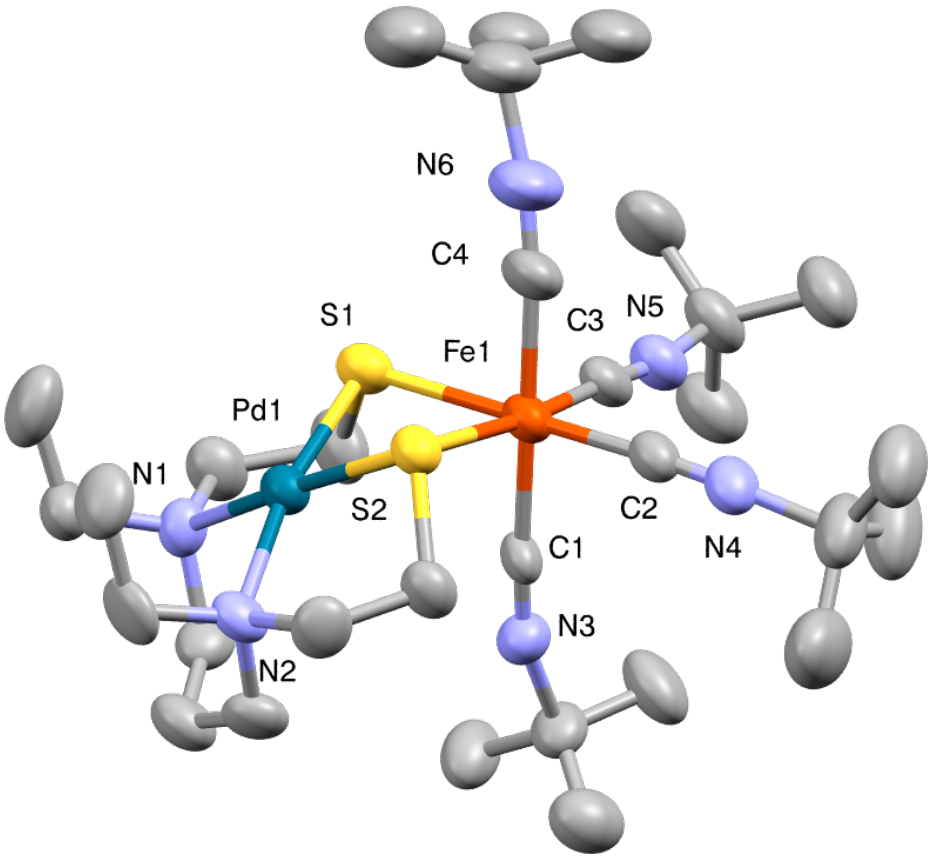


Figure 4.4.1 – The X-ray crystal structure of the $[Pd(L1)Fe(CN^tBu)_4]^{2+}$ cation in $[Pd(L1)Fe(CN^tBu)_4](BPh_4)_2$ with thermal ellipsoids at 50%. Hydrogen atoms and $(BPh_4)^-$ anions omitted for clarity.

Table 4.4.1 – Selected bond lengths and angles for $[Pd(L1)Fe(CN^tBu)_4](BPh_4)_2$

Bond	**Length /Å**	**Bonds**	**Angle /º**	**Bonds**	**Angle /º**
Pd(1)-Fe(1)	3.189(3)	N(1)-Pd(1)-S(1)	87.9(3)	Pd(1)-S(1)-Fe(1)	87.3(1)
Pd(1)-N(1)	2.12(1)	N(2)-Pd(1)-S(2)	88.5(3)	S(1)-Fe(1)-C(4)	84.4(6)
Pd(1)-N(2)	2.11(1)	N(1)-Pd(1)-N(2)	97.0(4)	S(2)-Fe(1)-S(1)	81.8(1)
Pd(1)-S(1)	2.259(4)	S(1)-Pd(1)-S(2)	85.4(1)	S(2)-Fe(1)-C(1)	95.9(4)
Pd(1)-S(2)	2.261(3)	N(1)-Pd(1)-S(2)	170.5(3)	C(1)-Fe(1)-C(2)	88.2(6)
Fe(1)-S(1)	2.359(4)	S(1)-Pd(1)-N(2)	169.0(3)	C(1)-Fe(1)-C(3)	86.9(6)
Fe(1)-S(2)	2.322(4)			C(1)-Fe(1)-C(4)	175.2(7)
Fe(1)-C(1)	1.89(1)	Pd-Fe Torsion	136.68(18)		
Fe(1)-C(2)	1.88(2)	C(1)-N(3)-C(20)	161(1)		
Fe(1)-C(3)	1.87(2)				
Fe(1)-C(4)	1.89(1)				

The solid state structure of $[Pd(L1)Fe(CN^tBu)_4](BPh_4)_2$ is similar to that of $[Ni(L1)Fe(CN^tBu)_4](BPh_4)_2$ (Chapter 2). The Pd(L1) centre possesses a distorted square planar geometry; the dihedral angle between the planes defined by Pd(1), N(1), N(2) and Pd(1), S(1), S(2) = 168.0(9) º and 179.96(2) º, for $[Pd(L1)Fe(CN^tBu)_4](BPh_4)_2$ and Pd(L1), respectively. Similarly to Ni(L1) and $[Ni(L1)Fe(CN^tBu)_4]^{2+}$,[5, 13] the Pd(L1) unit binds to a pseudo-octahedral Fe^{II} centre via its two thiolate donors and the coordination sphere about the Fe^{II} centre is completed by the coordination of four ^{t}BuNC ligands. The Pd(L1) unit is more distorted from square planar compared to the parent complex (Pd(L1)); [169.0(3)-170.5(3)º] compared to [175.6(2)-176.0(2)º] for the S(1)-M-N(2) and S(2)-M-N(1) angles in each complex respectively which could be due to steric demands and crystal packing effects due to the larger Pd^{II} ion. The [M-Fe] distance is similar between [NiFe] and [PdFe] at 3.1683(3) Å and 3.189(3) Å respectively, while the dihedral angle (defined as the angle between the S(1)-M(1)-S(2) and S(1)-Fe(1)-S(2) planes (M = Ni, Pd) is slightly greater for the Pd system (136.68(18) º) compared to the Ni system (135.48(2) º). Taken together, it demonstrates that $[M(L1)Fe(CN^tBu)_4]^{2+}$ (M = Ni, Pd) are very similar in the solid state with

the exchange of the Ni centre for the larger Pd cation not affecting the geometry of the overall complex significantly.

The Pd-(S_2)-Fe motif approximates the core structure of the active site of the Ni-SI state of [NiFe] hydrogenase from *Desulfovibrio gigas*, although the Pd-Fe distance [3.189(3) Å] is significantly longer than the Ni-Fe distance found in the Ni-SI state of the enzyme [2.9 Å].[23]

The equatorial isocyanide ligands [defined by atoms C(2) and C(3)] bind to the Fe centre in an essentially linear mode in contrast to the two axial ligands [defined by atoms C(1) and C(4)] that exhibit a significant bend between the tertiary C atom of the ^{t}Bu group and the CN unit [C(1)-N(3)-C(20) = 161(1)º and C(4)-N(6)-C(28) = 170(1)º]. For the ^{t}BuNC ligand, defined by C(1), this angle may be explained by steric crowding of the bulky ^{t}Bu group against the axial face of the Pd centre, which is positioned towards this ligand due to the butterfly nature of the Pd-(S_2)-Fe core (dihedral angle between the planes defined by Pd(1)-S(1)-S(2) and Fe(1)-S(1)-S(2) = 136.68(18) º). As for [Ni(L1)Fe(CN^tBu)$_4$](BPh_4)$_2$ which has a similar butterfly torsion defined by the planes Ni(1)-S(1)-S(2) and Fe(1)-S(1)-S(2) of 135.48(2) º,[5] the effect of this crowding results in a breaking of the magnetic equivalence that would normally be expected for these terminal functional groups, in this case as three distinct singlets integrating to 9, and 18 and 9 protons corresponding to the face-crowded, more deshielded ^{t}Bu group at a higher chemical shift (1.71 ppm) and the other ^{t}Bu groups at a lower chemical shifts (1.49 and 1.53 ppm). [Ni(L1)Fe(CN^tBu)$_4$](BPh_4)$_2$ possesses two singlets in this region at 1.81 and 1.49 ppm, that integrate to 9 and 27 protons corresponding to the face-crowded ^{t}Bu group and the other three ^{t}Bu groups, respectively. The separation of ^{t}Bu resonances in [Pd(L1)Fe(CN^tBu)$_4$](BPh_4)$_2$, which gives rise to a 9-16-9 integration

pattern, suggests that the axial ^{t}Bu group defined by C(4) is also more deshielded relative to the ^{t}Bu groups in the equatorial positions.

4.5 Infrared spectroscopy of $[Pd(L1)Fe(CN^{t}Bu)_4](BPh_4)_2$

The infrared spectrum of $[Pd(L1)Fe(CN^{t}Bu)_4](BPh_4)_2$ recorded in MeCN is shown in Figure 4.5.1 and the frequencies of the absorption bands associated with the C≡N bonds of the isocyanide ligands are shown in Table 4.5.1. $[Pd(L1)Fe(CN^{t}Bu)_4](BPh_4)_2$ exhibits a similar IR spectrum in MeCN to $[Ni(L1)Fe(CN^{t}Bu)_4](BPh_4)_2$ (Table 4.5.1), which possesses four peaks between 2148 to 2205 cm^{-1} corresponding to the vibrational modes of the isocyanide ligands consistent with a local C_{2v} symmetry around the Fe^{II} centre.

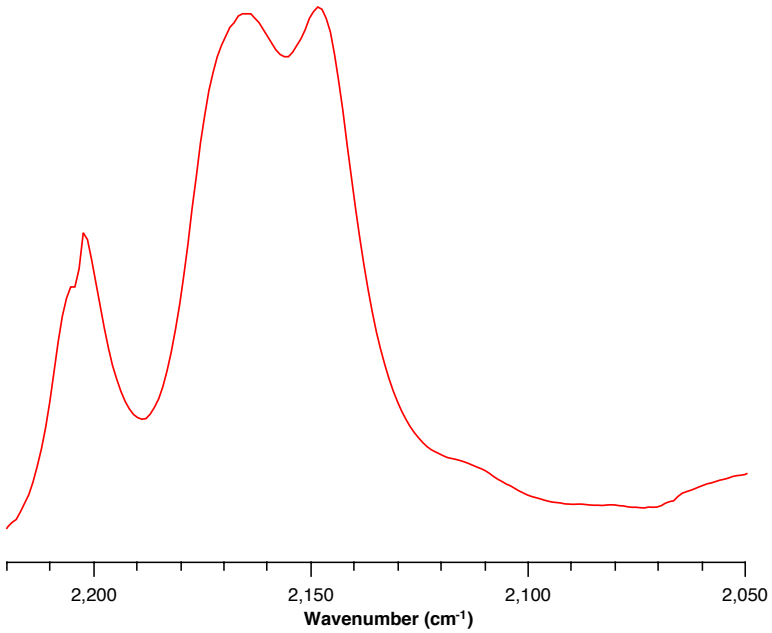


Figure 4.5.1: IR spectrum of terminal C≡N bands of $[Pd(L1)Fe(CN^{t}Bu)_4](BPh_4)_2$ in MeCN solution at 298 K.

Table 4.5.1: IR spectra of $[M(L1)Fe(CN^{t}Bu)_4](BPh_4)_2$ (M = Pd, Ni)[5]

Complex	**Wavenumber /cm^{-1}**
$[Pd(L1)Fe(CN^{t}Bu)_4](BPh_4)_2$	2205(sh), 2202, 2165, 2148
$[Ni(L1)Fe(CN^{t}Bu)_4](BPh_4)_2$	2200, 2170, 2161, 2144

Each C≡N stretching frequency in $[Pd(L1)Fe(CN^tBu)_4](BPh_4)_2$ is shifted to higher energy compared to those of $[Ni(L1)Fe(CN^tBu)_4](BPh_4)_2$ (Table 4.5.1). This is commensurate with the increase in effective nuclear charge of the Pd^{II} centre relative to that of Ni^{II} [24] that results in a lower electron density around the Fe^{II} centre and consequent reduction in the π back-donation into the π* orbitals of the isocyanide ligands.

4.6 Electrochemical studies of $[Pd(L1)Fe(CN^tBu)_4](BPh_4)_2$

The cyclic voltammogram of $[Pd(L1)Fe(CN^tBu)_4](BPh_4)_2$ in MeCN solution with $[N^nBu_4][BF_4]$ (0.2 M) as supporting electrolyte exhibits possesses a number of overlapping irreversible reduction processes between -1.2 to -1.6 V vs Fc^+/Fc at 100 mVs^{-1} (Figure 4.6.1) that show no associated oxidation processes even at higher scan rates (up to 300 mVs^{-1}).

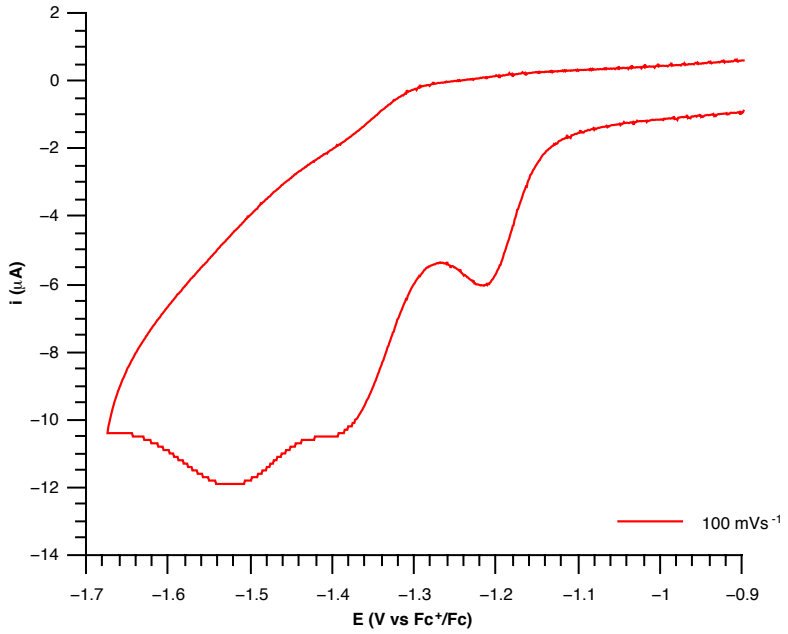


Figure 4.6.1: Cyclic voltammogram of 1 mM $[Pd(L1)Fe(CN^tBu)_4](BPh_4)_2$ in MeCN with 0.2 M $[N^nBu_4][BF_4]$ as supporting electrolyte at 100 mVs^{-1} scan rate.

In contrast, $[Ni(L1)Fe(CN^tBu)_4](BPh_4)_2$ possesses a reversible reduction process at -1.39 V *vs* Fc^+/Fc that has been assigned to a formal $Ni^{II/I}$ couple that is localized on the $Ni(N_2S_2)$ unit

(Figure 4.6.2).[5] Thus, in spite of a similar coordination sphere and coordination geometry, $[Pd(L1)Fe(CN^tBu)_4](BPh_4)_2$ does not appear to support a reversible $Pd^{II/I}$ couple. This could be explained by the more diffuse d orbitals of the Pd (I) ion compared to that of the Ni (I) and by poorer orbital overlap with the ligand orbitals of the thiolate donors. In the Ni^I system, the metal centre adopts a d^9 configuration with the unpaired electron residing in a d orbital in the equatorial plane with significant contribution from the orbitals of the two sulfur atoms;[5] this configuration may be unfavourable for the larger Pd^I centre resulting in decomposition of the electrochemically generated species on the timescale of the cyclic voltammetry experiment.

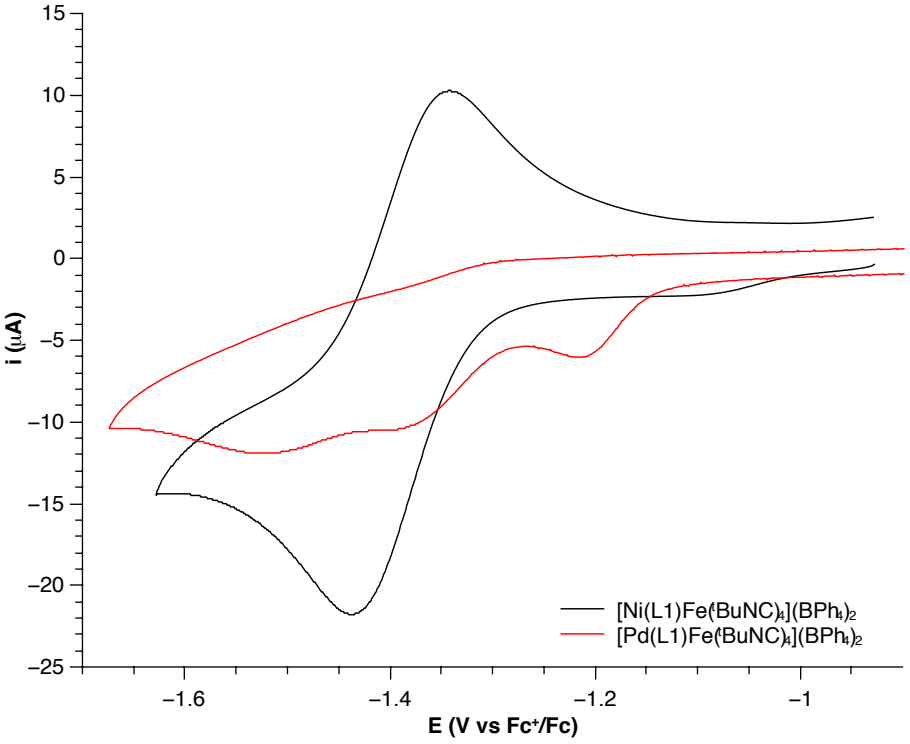


Figure 4.6.2: Cyclic voltammogram comparison of 1 mM $[M(L1)Fe(CN^tBu)_4](BPh_4)_2$ (M = Ni, Pd) in MeCN with 0.2 M $[N^nBu_4][BF_4]$ as supporting electrolyte at 100 mVs^{-1} scan rate.

4.7 DFT Calculations of $[Pd(L1)Fe(CN^tBu)_4]^{2+}$

DFT calculations were performed on a model of $[Pd(L1)Fe(CN^tBu)_4]^{2+}$, derived from the X-ray crystal structure of $[Pd(L1)Fe(CN^tBu)_4](BPh_4)_2$ (Section 4.4). Geometry optimizations were undertaken in the gas phase and the energy minimum was confirmed by frequency

calculations. The geometry optimized structure is shown in Figure 4.7.1 and selected bond distances and angles for the calculated and experimental geometries are shown in Table 4.7.1.

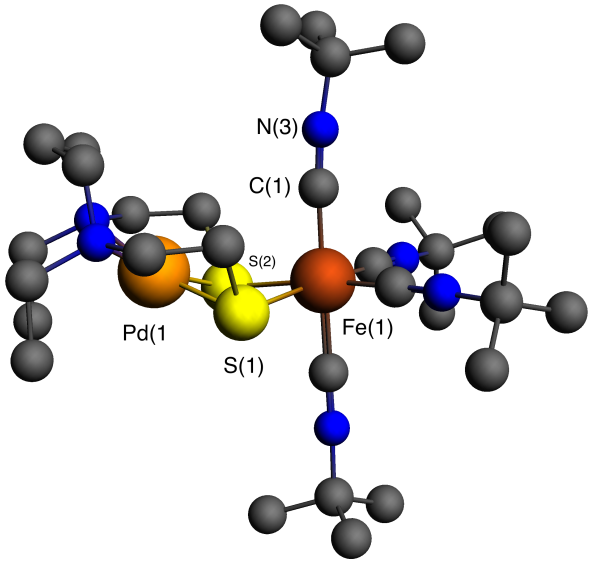


Figure 4.7.1: gas-phase geometry optimised structure of $[Pd(L1)Fe(CN^tBu)_4]^{2+}$ *based on starting geometry from the solid state structure of the complex.*

Table 4.7.1: Selected bond lengths and angles of XRD structure and DFT geometry optimised structure of $[Pd(L1)Fe(CN^tBu)_4]^{2+}$

Bond	**Length (XRD) /Å**	**Length (DFT) /Å**
Pd(1)-Fe(1)	3.189(3)	3.430
Pd(1)-N(1)	2.12(1)	2.204
Pd(1)-N(2)	2.11(1)	2.206
Pd(1)-S(1)	2.259(4)	2.323
Pd(1)-S(2)	2.261(3)	2.321
Fe(1)-S(1)	2.359(4)	2.421
Fe(1)-S(2)	2.322(4)	2.420
Atoms	**Angle (XRD) /º**	**Angle (DFT) /º**
Pd-S-S-Fe	136.68(18)	148.94
C(1)-N(3)-C(5)	161(1)	173.39

A comparison of the calculated and experimental geometries show that Pd-S, Pd-N, Fe-S, Fe-C are reproduced to within 0.06 to 0.08 Å. The Pd-Fe distance is reproduced to within 0.2 Å. The DFT calculations also reproduce the trend in the C-N-C bond angles, albeit with a slight relaxation towards more linear (161(1) º vs 173.39 º) for the face-crowded axial ligand. The

slightly longer Pd-Fe distance (*ca*. 0.2 Å) correlates with the slightly increased Pd-S-S-Fe torsion, suggesting that crystal packing effects do affect the geometry of the system in the solid state and this dihedral angle relaxes slightly in the gas phase calculation (*ca*. 8 º more obtuse).

Thus, the DFT calculations reproduce the principal features of the experimental structure of $[Pd(L1)Fe(CN^tBu)_4]^{2+}$ which suggests that the DFT calculations can provide a qualitative description of the electronic structure of $[Pd(L1)Fe(CN^tBu)_4]^{2+}$.

A comparison of the experimental and unscaled gas-phase calculated IR spectra of $[Pd(L1)Fe(CN^tBu)_4]^{2+}$ is shown in Figure 4.7.2. The calculated spectrum posseses four IR bands in the C≡N stretching region that are shifted by an average of 12 cm^{-1} to lower energy relative to those in the experimental spectrum. This difference may be a consequence of the DFT calculations being undertaken in the gas phase rather than in solution and/or the neglect of anharmonic effects in calculations based on a harmonic approximation.[25, 26]

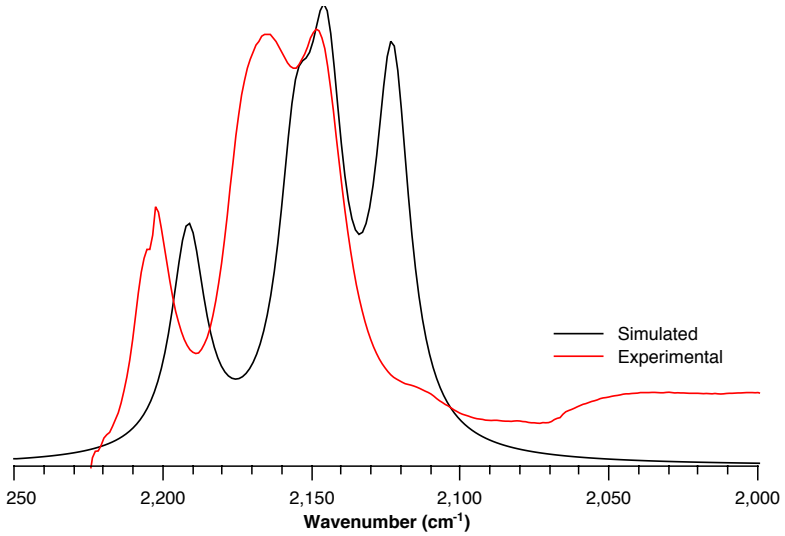


Figure 4.7.2: The experimental and DFT gas-phase calculated IR spectra of $[Pd(L1)Fe(CN^tBu)_4](BPh_4)_2$ *in MeCN (experimental) and* $[Pd(L1)Fe(CN^tBu)_4]^{2+}$.

The redox-active LUMO in $[Pd(L1)Fe(CN^tBu)_4]^{2+}$ is localized on the $Pd(N_2S_2)$ centre with a composition of 33.2% Pd, 40.2% S, and 15.1% N (Figure 4.7.3) with essentially no contributions from the $[Fe(CN^tBu)_4]^{2+}$ fragment. The SOMO in the reduced $[Pd(L1)Fe(CN^tBu)_4]^{+}$ species, derived from gas-phase geometry optimizations, possesses 43.8 % Pd, 29.9 % S and 13.8% N (Figure 4.7.4) character. In contrast the composition of the SOMO calculated for $[Ni(L1)Fe(CN^tBu)_4]^{+}$ possesses 60.8% Ni and 31% from the S and N atoms combined.[5] Thus, these calculations suggest that the reduction of $[Pd(L1)Fe(CN^tBu)_4]^{2+}$ to $[Pd(L1)Fe(CN^tBu)_4]^{+}$ is likely to be localized on the $Pd(N_2S_2)$ unit, however, in contrast to $[Ni(L1)Fe(CN^tBu)_4]^{2+/+}$ this reduction process is likely to be more ligand- than metal-based. Consequently, the reduction of $[Pd(L1)Fe(CN^tBu)_4]^{2+}$ to $[Pd(L1)Fe(CN^tBu)_4]^{+}$ may result in a species with considerable ligand-radical character. This ligand-radical may react with other species in solution such that the reduction of $[Pd(L1)Fe(CN^tBu)_4]^{2+}$ becomes irreversible and is accompanied by the generation of other redox active species.

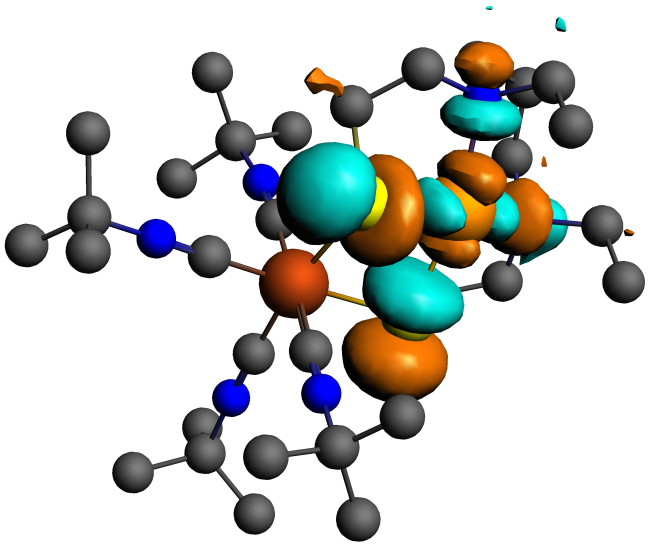


Figure 4.7.3: Kohn-Sham LUMO of $[Pd(L1)Fe(CN^tBu)_4]^{2+}$ plotted with an isosurface value of 0.03 eÅ^{-3} demonstrating localisation of the molecular orbital at the $Pd(N_2S_2)$ centre.

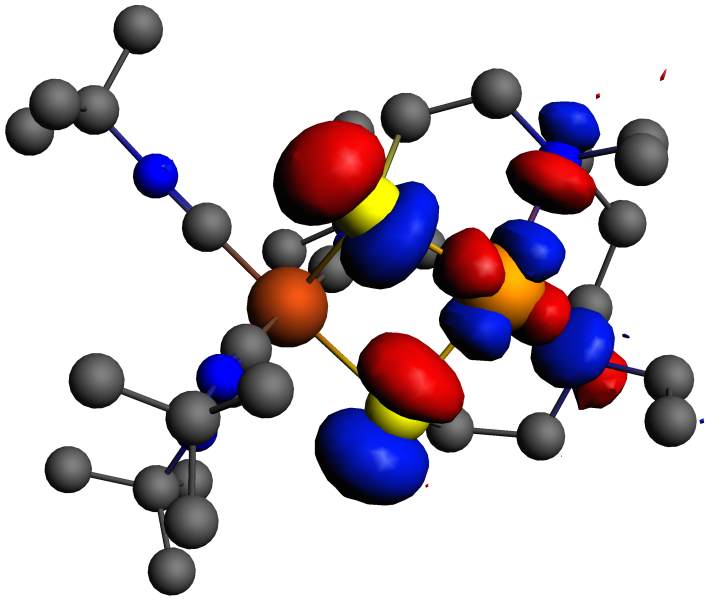


Figure 4.7.4: Kohn-Sham SOMO of [Pd(L1)Fe(CN^{t}Bu)$_4$]$^+$ derived from a gas-phase spin restricted DFT calculation, plotted with an isosurface value of 0.03 eÅ^{-3}.

4.8 X-ray crystallography of [Co(L1)(CN^{t}Bu)Fe(CN^{t}Bu)$_4$](BPh$_4$)$_2$

[Co(L1)(CN^{t}Bu)Fe(CN^{t}Bu)$_4$](BPh$_4$)$_2$ crystallises in the P2$_1$/c space group and the structure of the [Co(L1)(CN^{t}Bu)Fe(CN^{t}Bu)$_4$]$^{2+}$ cation is shown in Figure 4.8.1 with selected bond lengths and angles shown in Table 4.8.1.

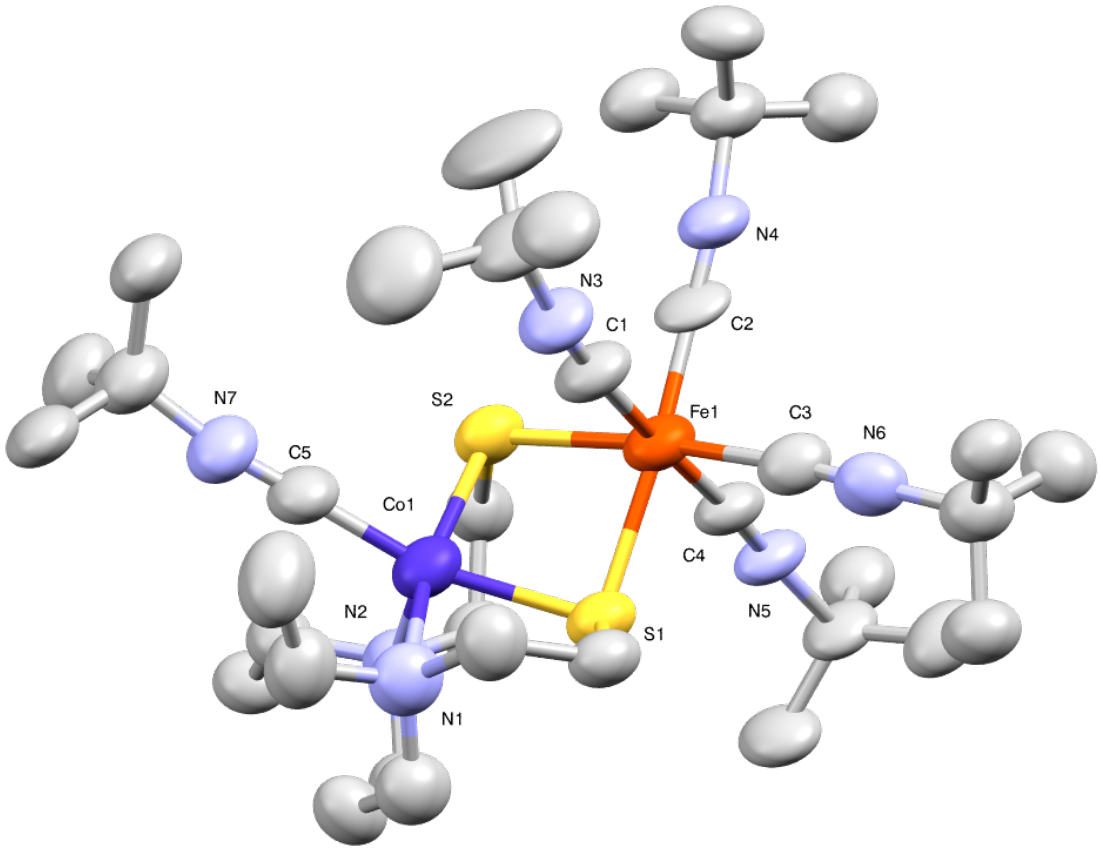


Figure 4.8.1: The X-ray crystal structure of $[Co(L1)(CN^tBu)Fe(CN^tBu)_4]^{2+}$ *in* $[Co(L1)(CN^tBu)Fe(CN^tBu)_4](BPh_4)_2$ *with thermal ellipsoids at 25%. Hydrogen atoms and* BPh_4 *anions removed for clarity. The cobalt-coordnating isocyanide group (C5)-(N7) is visible on the left.*

Table 4.8.1: Selected bond lengths and angles for $[Co(L1)(CN^tBu)Fe(CN^tBu)_4](BPh_4)_2$

Bond	**Length /Å**	**Bonds**	**Angle /º**	**Bonds**	**Angle /º**
Co(1)-Fe(1)	3.28(1)	N(1)-Co(1)-N(2)	103(1)	S(1)-Fe(1)-C(1)	97.5(9)
Co(1)-N(1)	2.08(2)	S(1)-Co(1)-S(2)	85.4(3)	C(1)-Fe(1)-C(4)	178(1)
Co(1)-N(2)	2.11(2)	N(1)-Co(1)-S(1)	83.2(8)	C(1)-Fe(1)-C(2)	89(1)
Co(1)-S(1)	2.25(1)	N(2)-Co(1)-S(1)	94.1(7)	C(1)-Fe(1)-C(3)	92(1)
Co(1)-S(2)	2.28(1)	S(1)-Co(1)-C(5)	166(1)	S(2)-Fe(1)-C(4)	95.2(8)
Co(1)-C(5)	1.77(4)	N(1)-Co(1)-C(5)	103(1)	C(4)-Fe(1)-C(3)	86(1)
Fe(1)-S(1)	2.352(9)	S(2)-Co(1)-C(5)	86(1)	S(1)-Fe(1)-C(3)	91.6(9)
Fe(1)-S(2)	2.34(1)	N(2)-Co(1)-C(5)	97(1)		
Fe(1)-C(1)	1.90(2)	N(1)-Co(1)-S(2)	165.3(8)	**Torsion**	**Angle /º**
Fe(1)-C(2)	1.87(2)	Co(1)-S(1)-Fe(1)	90.7(3)	Co(1)-S(1)-S(2)-Fe(1)	144.9(2)
Fe(1)-C(3)	1.95(4)				
Fe(1)-C(4)	1.88(2)				

$[Co(L1)(CN^tBu)Fe(CN^tBu)_4]^{2+}$ contains a five-coordinate Co centre in an approximate square pyramidal geometry ($\tau = 0.016$).[27] One $(L1)^{2-}$ ligand and an additional ^{t}BuNC donor bind the Co centre. Atoms N(1), S(1) and S(2) of the $L^1N_2S_2^{2-}$ ligand together with C(5) of the ^{t}BuNC ligand constitute the approximate equatorial plane about the Co centre. The $[Co(L1)(CN^tBu)]$ unit binds to a pseudo-octahedral Fe^{II} centre via its two thiolate donors to give a butterfly shaped Co-(S_2)-Fe core. The coordination sphere about the Fe^{II} centre is completed by the coordination of four ^{t}BuNC ligands.

The dihedral angle between the Co and Fe atoms [144.9(2) º] (defined as the angle between the S(1)-Co(1)-S(2) and S(1)-Fe(1)-S(2) planes) and the intraatomic distance between them [3.28(1) Å] are also increased relative to the analogous [MFe] complexes (M = Ni, Pd), possibly due to the increased steric bulk of this geometry relative to that seen in the [NiFe] and [PdFe] systems.

The Fe centre retains the pseudo-octahedral geometry seen in the [NiFe] and [PdFe] complexes, with very similar Fe-C bond lengths (between 1.87(2) and 1.96(3) Å) and angles to the isocyanide ligands. The Fe-S distances (2.352(9) to 2.34(1) º) are comparable to that observed in the [NiFe] and [PdFe] complexes.

In contrast to $[M(L1)Fe(CN^tBu)_4]^{2+}$ (M = Ni,[5] Pd), the $[Co(L1)(CN^tBu)Fe(CN^tBu)_4]^{2+}$ system binds an additional ^{t}BuNC ligand at the Co centre.

4.9 Electrochemical studies of $[Co(L1)(CN^tBu)Fe(CN^tBu)_4](BPh_4)_2$

The cyclic voltammograms of $[Co(L1)(CN^tBu)Fe(CN^tBu)_4](BPh_4)_2$ recorded in MeCN solution with $[N^nBu_4][BF_4]$ (0.2 M) as supporting electrolyte are shown in Figure 4.9.1. $[Co(L1)(CN^tBu)Fe(CN^tBu)_4](BPh_4)_2$ possesses two reduction process at -1.53 V and -1.30 V

vs Fc^+/Fc that are associated with an oxidation process at -1.07 V vs Fc^+/Fc (Figure 3.13), consistent with a potential ECE-type process. There is no evidence of the reduction and oxidation processes at ca. -0.8 V and ca. -0.2 V *vs* Fc^+/Fc for the parent Co(L1) complex in the cyclic voltammograms of $[Co(L1)(CN^tBu)Fe(CN^tBu)_4](BPh_4)_2$. We did not investigate the nature of the reduction products further given the irreversible nature of the redox processes of $[Co(L1)(CN^tBu)Fe(CN^tBu)_4](BPh_4)_2$.

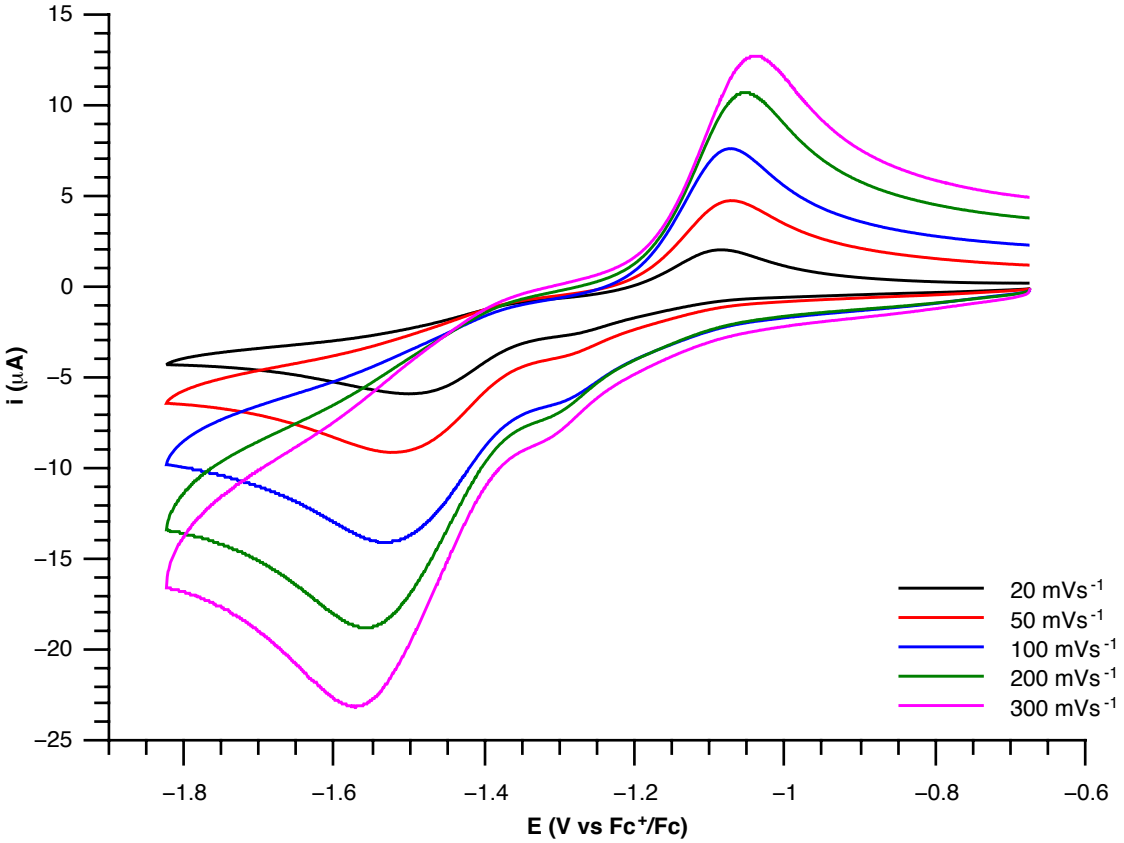


Figure 4.9.1: Cyclic voltammograms of 1 mM $[Co(L1)(CN^tBu)Fe(CN^tBu)_4](BPh_4)_2$ in MeCN solution with 0.2 M $[N^nBu_4][BF_4]$ as supporting electrolyte between 20-300 mVs^{-1}.

4.10 DFT Calculations of $[Co(L1)(CN^tBu)Fe(CN^tBu)_4]^{2+}$

Unrestricted DFT calculations were performed on a model of $[Co(L1)(CN^tBu)Fe(CN^tBu)_4]^{2+}$, derived from the X-ray crystal structure of $[Co(L1)(CN^tBu)Fe(CN^tBu)_4](BPh_4)_2$ (Section 4.8). Geometry optimizations were undertaken in the gas phase and the energy minimum was

confirmed by frequency calculations. The resulting HOMO of the complex (Figure 4.10.1) displayed even greater ligand character than previously studied systems, in fact with only 24.58% contribution from the Co centre in total (18.99% d_{z2}, 6.88% d_{x2-y2}), the HOMO is dominated by ligand contributions with almost 50% residing on the sulfur atoms alone. Despite the coordination of the additional isocyanide ligand at the metal centre in this system, it appears to have very little contribution (<4%) to the HOMO and almost all of that confined to the s orbital of the terminal carbon. There is no evidence here of back donation into the π* orbital here despite the direct ligation to the metal which might be expected for such an electron rich system bound to a relatively potent electron density sink.[28] The LUMO of $[Co(L1)(CN^tBu)Fe(CN^tBu)_4]^{2+}$ (Figure 4.10.2) is strongly centred on the Co centre (30.33 % Co d_{xy}, 28.11 % Co d_{xz}, 27.5 % Co d_{yz}, 2.6 % S_p, 1% N_p), in comparison to the analogous $[Ni(L1)(CN^tBu)Fe(CN^tBu)_4]^{2+}$ system which demonstrates significantly more ligand character in the LUMO (44 % Ni d_{xy}, 32 % S_p), with very little contribution from the extra coordinated isocyanide ligand at the Co centre.

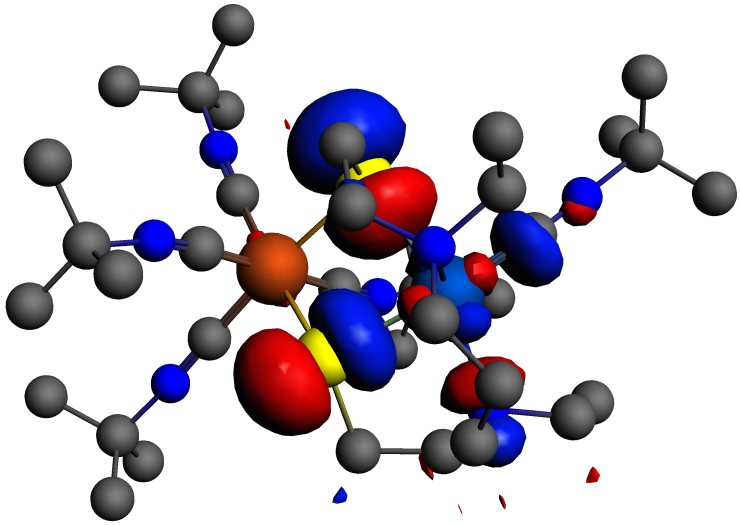


Figure 4.10.1: Kohn-Sham HOMO of $[[Co(^tBuNC)(L1)]Fe(^tBuNC)_4]^{2+}$ unrestricted calculation, plotted with an isosurface value of 0.03 eÅ^{-3}.

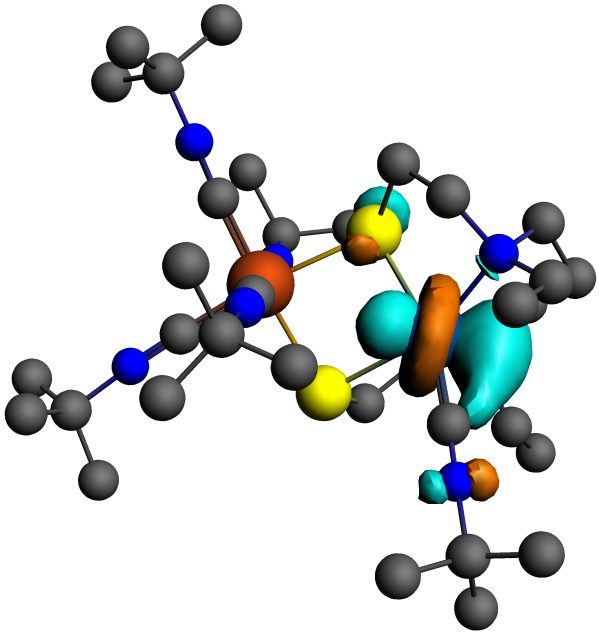


Figure 4.10.2: Kohn-Sham LUMO of [[Co(^{t}BuNC)(L1)]Fe(^{t}BuNC)$_4$]$^+$ unrestricted calculation, plotted with an isosurface value of 0.03 eÅ^{-3}.

4.11 Conclusions

We have used the N,N'-diethyl-3,7-diazononane-1,9-dithiolate $(L1)^{2-}$ ligand to synthesise M(L1) (M = Pd, Co, Zn). Attempts to react (H_2L1) with Cu(acac)$_2$ in THF led to the formation of disulfides. M(L1) (M = Pd, Co, Zn) have been characterized by X-ray crystallography that shows that the metal centre in each complex is four coordinate in the solid state and shows that the $(L1)^{2-}$ ligand can accommodate a range of geometries that may be described as ranging from distorted square planar to distorted tetrahedral, with dihedral angles ranging from 1.68(18) º to 69.30(4) º from most square planar to most distorted tetrahedral. The S…S distance also varied, from ca. 4 Å in the distorted tetrahedral geometry to between ca. 2.9 and 3.2 Å in the square planar arrangement. M(L1) (M = Pd, Co) were investigated by electrochemistry and both complexes exhibit irreversible redox processes between E = -1.2 V and -1.5 V *vs* Fc^+/Fc.

We investigated the coordination of M(L1) (M = Pd, Co, Zn) to a $[Fe(CN^tBu)_4]^{2+}$ fragment and isolated $[Pd(L1)Fe(CN^tBu)_4](BPh_4)_2$ and $[Co(L1)(CN^tBu)Fe(CN^tBu)_4](BPh_4)_2$. X-ray crystallography shows that $[Pd(L1)Fe(CN^tBu)_4](BPh_4)_2$ possesses a similar structure to $[Ni(L1)Fe(CN^tBu)_4](BPh_4)_2$ (Chapter 2). Notable differences between the structures include a greater Pd···Fe distance in $[Pd(L1)Fe(CN^tBu)_4](BPh_4)_2$ [3.189(2) Å] when compared to the Ni···Fe distance in $[Ni(L1)Fe(CN^tBu)_4](BPh_4)_2$ [3.1682(3) Å] and a smaller dihedral angle between the planes defined by N(1)-M(1)-N(1) and S(1)-M(1)-S(2) for M = Pd (dihedral angle = 168.0(9) º and 169.81(5) º for M = Pd and Ni, respectively).

The electrochemical behaviours of $[Pd(L1)Fe(CN^tBu)_4](BPh_4)_2$ and $[Ni(L1)Fe(CN^tBu)_4](BPh_4)_2$ are markedly different. $[Ni(L1)Fe(CN^tBu)_4](BPh_4)_2$ exhibits a reversible redox process at -1.39 V vs Fc^+/Fc that has been assigned to a formal $Ni^{II/I}$ couple[5] whereas $[Pd(L1)Fe(CN^tBu)_4](BPh_4)_2$ posesses multiple irreversible reduction processes in the range of -1.2 to -1.5 V *vs* Fc^+/Fc. While the Pd^I oxidation state is not uncommon, complexes featuring Pd in this state tend to be dimeric, featuring Pd-Pd bonds, and frequently employ high-field ligands;[29] monomeric Pd^I complexes are much less common.[30] In addition, DFT calculations on models of $[Pd(L1)Fe(CN^tBu)_4]^{2+}$ and $[Pd(L1)Fe(CN^tBu)_4]^+$ suggest that the reduction of $[Pd(L1)Fe(CN^tBu)_4]^{2+}$ to $[Pd(L1)Fe(CN^tBu)_4]^+$ is associated with the development of ligand-based radical character across the $Pd(N_2S_2)$ unit that may also result in the irreversibility of the reduction processes.

X-ray crystallography reveals that $[Co(L1)(CN^tBu)Fe(CN^tBu)_4](BPh_4)_2$ possesses a five-coordinate Co centre in an approximate square pyramidal geometry in which an additional ^{t}BuNC ligand binds to the Co centre. Interestingly, the square-based pyramidal geometry adopted is similar to the geometry at the nickel centre of the [NiFe] hydrogenase enzyme

active site itself during active states, for example, Ni-C, where the nickel (III) centre is also formally d^7 and five coordinate, binding the four cystinyl residues and the bridging hydride species, although the Ni-Fe distance here is markedly shorter (ca. 2.5 Å) than $[Co(L1)(CN^tBu)Fe(CN^tBu)_4]^{2+}$ (3.28(1) Å).[31, 32] Electrochemical experiments show that $[Co(L1)(CN^tBu)Fe(CN^tBu)_4](BPh_4)_2$ possesses irreversible reduction processes. This irreversibility may be associated with the loss of ^{t}BuNC ligand coordinated to the Co centre on reduction and subsequent decomposition of an unstable intermediate more rapidly than the timescale of the electrochemistry experiment.

Our structural, electrochemical and theoretical characterizations of $[Pd(L1)Fe(CN^tBu)_4](BPh_4)_2$ and $[Co(L1)(CN^tBu)Fe(CN^tBu)_4](BPh_4)_2$ reinforce the consensus view that the Fe^{II} centre present in these complexes and at the active site of the [NiFe] hydrogenases modulates the electrochemical behaviour of these centres rather than being the formal redox active species. Our results suggest that the incorporation of a formal Ni^{II} centre facilitates the electrochemical and chemically reversibile redox behavior of $[Ni(L1)Fe(CN^tBu)_4](BPh_4)_2$ that reproduces the formal $Ni^{II/I}$ oxidation states associated with the Ni-SI and Ni-L states of the [NiFe] hydrogenases that may have key roles in the catalytic cycle of this enzyme.[23, 33-35]

4.12 Experimental

Synthesis of N,N'-diethyl-3,7-diazanonane-1,9-dithiolatopalladium(II) [Pd(L1)]

(H_2L1) (0.20 g, 0.66 mmol) was added dropwise to $Pd(acac)_2$ (0.164 g, 0.66 mmol) in dry THF (40 ml) with stirring. The solution changed from yellow to orange over 15 minutes and the mixture was stirred for a further 15 minutes. The solution was left to stand overnight to precipitate a yellow crystalline solid, which was recovered by filtration and dried under a flow of argon. Yield = 29.4 mg, 13 %. MS (ESI+, m/z): 355.0489 (M+H), 377.0308 (M+Na). Anal. Calcd. (%) for [$C_{11}H_{24}N_2S_2Pd$]: C, 37.23; H, 6.82; N, 7.89; Found: C, 35.23; H, 6.54; N, 7.27. ^{1}H NMR (400 MHz, CD_3CN) δ ppm 0.91 (t, 6H), 1.71 (m, 1H), 2.03 (m, 3H), 2.61 (m, 6H), 2.91 (m, 1H), 2.94 (m, 1H), 3.18 (m, 4H), 3.33 (m, 2H). ^{13}C NMR (100 MHz, CD_3CN) δ ppm 64.5 (CH2), 56.0 (CH2), 45.0 (CH2), 23.6 (CH2), 23.6 (CH2), 4.60 (CH3).

Synthesis of N,N'-diethyl-3,7-diazanonane-1,9-dithiolatocobalt(II) [Co(L1)]

(H_2L1) (4.75 g, 18.7 mmol) was added to a solution of $Co(acac)_2$ (5.03 g, 19.6 mmol) in THF (120 ml) at room temperature. The solution changed colour from ruby to purple immediately, and the mixture was stirred for 12 hours and filtered to recover a deep blue crystalline solid that was washed with THF (1x 10 ml) and dried *in vacuo*. Yield = 2.98 g, 52 %. MS (ESI+, m/z): 308.0790 (M+H), 330.0606 (M+Na). Anal. Calcd. (%) for [$C_{11}H_{24}N_2S_2Co$]: Co, 19.17; C, 42.98; H, 7.87; N, 9.11; Found: Co, 20.80; C, 43.07; H, 7.98; N, 9.11.

Synthesis of N,N'-diethyl-3,7-diazanonane-1,9-dithiolzinc(II) [Zn(L1)]

(H_2L1) (0.25 g, 1.0 mmol) was added dropwise to $Zn(acac)_2$ (0.22 g, 1.0 mmol) in dry THF (40 ml) with stirring over 15 minutes. The colourless solution was stirred for a further 15 minutes and the mixture was left to stand overnight to precipitate very pale yellow crystals, which were recovered by filtration and dried under a flow of argon. Yield = 79 mg, 25%. MS

(ESI+, m/z): 313.0755 (M+H), 335.0568 (M+Na). 79 mg (25.2 %). ^{1}H NMR (400 MHz, CD_3CN) δ ppm 1.25 (t, J=7.2 Hz, 6H), 2.71 - 2.79 (m, 8H), 2.82 (dd, J=10.7, 5.2 Hz, 4H), 2.87 - 2.94 (m, 2H), 2.94 - 3.11 (m, 4H). ^{13}C NMR (101 MHz, CD_3CN) d ppm 64.52 (CH_2), 55.95 (CH_2), 44.88 (CH_2), 23.56 (CH_2), 4.59 (CH_3).

Attempted synthesis of N,N'-diethyl-3,7-diazanonane-1,9-dithiolcopper(II) [Cu(L1)]

(H_2L1) (4.89 g, 19.5 mmol) was added dropwise to $Cu(acac)_2$ (5.10 g, 19.0 mmol) in dry THF (100 ml) with stirring over 15 minutes. The blue solution turned darker blue/green upon addition of the thiol, and was left to stir overnight, however no precipitate was evident after 24 hours. Mass spectrometry analysis indicated no presence of the desired product, but showed some evidence of disulfide formation in the ligand. MS (ESI+, m/z): 249.1458 [$C_{11}H_{24}N_2S_2$] (M+H),

Synthesis of [Pd(L1)Fe(CN^{t}Bu)$_4$](BPh$_4$)$_2$

A solution of Pd(L1) (0.05 g, 0.141 mmol) in MeCN (5 mL) was added dropwise to $FeCl_2$ (0.018 g, 0.141 mmol) in MeCN (5 ml) to afford an immediate colour change from yellow to dark orange. The mixture was stirred for 4 hours. *tert*-Butyl isocyanide (0.07 ml, 0.563 mmol) was added and the mixture was left to stir for 12 hours. The mixture was filtered and the solvent removed *in vacuo*. The solid residue was taken up in MeOH (15 ml) and $NaBPh_4$ (0.205 g, 0.6 mmol) added to precipitate a yellow solid, which was then washed with MeOH (2x 2 ml) then triturated with MeCN (15 ml) to remove an insoluble orange impurity. The product was isolated as a yellow solid by the addition of Et_2O (80 ml), filtered and dried *in vacuo*. Crystals suitable for X-ray diffraction studies were grown from MeOH solution. Yield = 11 mg (5.6 %). MS (ESI+, m/z): 371.1369 (M2+ +H –[2BPh_4]). ^{1}H NMR (400 MHz, CD_3CN) δ ppm 1.35 (t, J=7.1 Hz, 6H), 1.49 (s, 18H), 1.53 (br. s., 9H), 1.71 (s, 9H), 2.35 -

2.49 (m, 2H), 2.63 (d, J=3.5 Hz, 6H), 2.85 (td, J=13.5, 3.4 Hz, 4H), 2.96 - 3.10 (m, 6H), 6.79 - 6.89 (m, 8H), 7.00 (t, J=7.4 Hz, 16H), 7.27 (br. s., 16H). ^{13}C NMR (101 MHz, CD_3CN) δ ppm 145.71 (C), 135.74 (C), 128.35 (C), 125.62 (CH), 124.33 (CH), 121.80 (CH), 62.56 (CH_2), 55.87 (CH_2), 43.93 (CH_2), 31.36 (CH_2) 29.70 (CH_3), 25.93 (CH_2), 11.26 (CH_3).

Synthesis of [Co(L1)(CN^{t}Bu)Fe(CN^{t}Bu)$_4$](BPh$_4$)$_2$

A solution of Co(L1) (0.2 g, 6.5 mmol) in MeCN was added dropwise to $FeCl_2$ (82 mg, 6.6 mmol) in MeCN and stirred for 4 hours. To this was added *tert*-Butyl isocyanide (3.25 ml, 26.0 mmol), affording an immediate colour change to brown. The solution was stirred for 12 hours, filtered and the solvent removed *in vacuo*. The solid residue was taken up in MeOH (5 ml), then $NaBPh_4$ (4.45 g, 13.0 mmol) in MeOH (15 ml) was carefully added. A dark orange/brown crystalline solid was isolated after 3 days via filtration, washed with MeOH (2 ml) and pentane (3x 2 ml). Yield = 88 mg (16 %). MS (ESI+, m/z): 347.6508 (M2+ [-2BPh_4, -CNC_4H_9]). Anal. Calcd. (%) for [$C_{84}H_{109}B_2CoFeN_7S_2$]: C, 71.18; H, 7.75; N, 6.92; Found: C, 70.15; H, 6.85; N, 6.81.

Attempted synthesis of [Zn(L1)Fe(CN^{t}Bu)$_4$](BPh$_4$)$_2$

A solution of Zn(L1) (0.05 g, 0.159 mmol) in MeCN (5 ml) was added dropwise to $FeCl_2$ (0.02 g, 0.159 mmol) in MeCN (5 ml) and the mixture was stirred for 4 hours. *tert*-Butyl isocyanide (0.08 ml, 0.64 mmol) was added and the mixture was left to stir for a further 12 hours. Mass spectrometric analysis indicated no presence of the desired product with the only significant peaks being the starting material and the formation of the Fe(NC^{t}Bu)$_5$Cl by-product. The solvent was removed *in vacuo* and the solid residue taken up in MeOH (10 ml) and solid $NaBPh_4$ (0.22 g, 0.65 mmol) added to encourage precipitation, however, no product was isolated.

4.13 References

1. S. Ogo, K. Ichikawa, T. Kishima, T. Matsumoto, H. Nakai, K. Kusaka and T. Ohhara, *Science*, 2013, **339**, 682-684.
2. J. A. Denny and M. Y. Darensbourg, *Chem. Rev. (Washington, DC, U. S.)*, 2015, **115**, 5248-5273.
3. M. V. Rampersad, S. P. Jeffery, M. L. Golden, J. Lee, J. H. Reibenspies, D. J. Darensbourg and M. Y. Darensbourg, *J. Am. Chem. Soc.*, 2005, **127**, 17323-17334.
4. F. Osterloh, W. Saak and S. Pohl, *J. Am. Chem. Soc.*, 1997, **119**, 5648-5656.
5. C. U. Perotto, G. Marshall, G. J. Jones, E. Stephen Davies, W. Lewis, J. McMaster and M. Schroder, *Chem. Commun. (Cambridge, U. K.)*, 2015, **51**, 16988-16991.
6. J. Schneider, B. Schnautz, R. Hauptmann and G. Henkel, *Acta Crystallogr. C*, 1999, **55**, 489.
7. F. Osterloh, W. Saak, S. Pohl, M. Kroeckel, C. Meier and A. X. Trautwein, *Inorg. Chem.*, 1998, **37**.
8. C. R. Groom, I. J. Bruno, M. P. Lightfoot and S. C. Ward, *Acta Crystallogr. B*, 2016, **72**, 171-179.
9. H. Tai, K. Nishikawa, S. Inoue, Y. Higuchi and S. Hirota, *J. Phys. Chem. B*, 2015.
10. I. M. Atkinson, J. D. Chartres, A. M. Groth, L. F. Lindoy, M. P. Lowe, G. V. Meehan, B. W. Skelton and A. H. White, *Dalton Trans.*, 2001, 2801-2806.
11. T. Głowiak and T. Ciszewska, *Acta Crystallogr. B*, 1982, **38**, 1735-1737.
12. D. Herebian, E. Bothe, E. Bill, T. Weyhermüller and K. Wieghardt, *J. Am. Chem. Soc.*, 2001, **123**, 10012-10023.
13. J. Schneider, R. Hauptmann, F. Osterloh and G. Henkel, *Acta Crystallogr. C*, 1999, **55**, 328-330.
14. S. Petriček, *Croat. Chem. Acta*, 2011, 515-520.
15. D. M. Jenkins, A. J. Di Bilio, M. J. Allen, T. A. Betley and J. C. Peters, *J. Am. Chem. Soc.*, 2002, **124**, 15336-15350.
16. M. Cibian, S. Langis-Barsetti, F. G. De Mendonça, S. Touaibia, S. Derossi, D. Spasyuk and G. S. Hanan, *Eur. J. Inorg. Chem.*, 2015, **2015**, 73-82.
17. A. W. Kleij, *Dalton Trans.*, 2009, 4635-4639.
18. G. A. Morris, H. Zhou, C. L. Stern and S. T. Nguyen, *Inorg. Chem.*, 2001, **40**, 3222-3227.
19. M. M. Ibrahim and A. Mosa, *Arabian J. Chem.*, 2014, **7**, 672-679.
20. C. Perotto, University of Nottingham, 2012.
21. R. S. Nicholson and I. Shain, *Anal. Chem.*, 1964, **36**, 706-723.
22. M. C. Buzzeo, C. Hardacre and R. G. Compton, *ChemPhysChem*, 2006, **7**, 176-180.
23. A. Volbeda, E. Garcin, C. Piras, A. L. de Lacey, V. M. Fernandez, E. C. Hatchikian, M. Frey and J. C. Fontecilla-Camps, *J. Am. Chem. Soc.*, 1996, **118**, 12989-12996.
24. E. Clementi, D. L. Raimondi and W. P. Reinhardt, *J. Chem. Phys.*, 1967, **47**, 1300-1307.
25. L. Fan and T. Ziegler, *J. Phys. Chem.*, 1992, **96**, 6937-6941.
26. M. L. Laury, M. J. Carlson and A. K. Wilson, *J. Comput. Chem.*, 2012, **33**, 2380-2387.
27. A. W. Addison, T. N. Rao, J. Reedijk, J. van Rijn and G. C. Verschoor, *J. Chem. Soc., Dalton Trans.*, 1984, 1349-1356.
28. P. W. Atkins, T. Overton, J. Rourke, M. Weller and F. A. Armstrong, *Shriver & Atkins' Inorganic Chemistry*, Oxford University Press, Oxford; New York, 2010.
29. T. Tanase, T. Fukushima, T. Nomura, Y. Yamamoto and K. Kobayashi, *Inorg. Chem.*, 1994, **33**, 32-39.

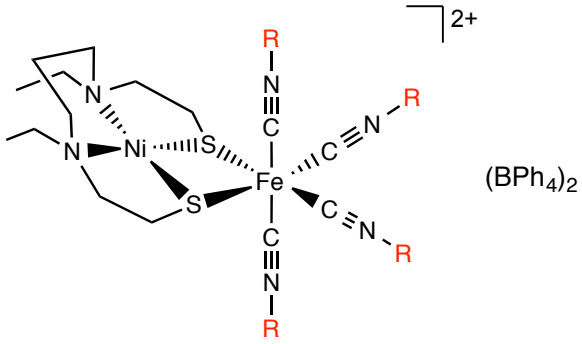
30. N. T. Oleg and G. B. Lev, *Russ. Chem. Rev.*, 1983, **52**, 117.
31. T.-W. Chiou and W.-F. Liaw, *C. R. Chim.*, 2008, **11**, 818-833.
32. S. Foerster, M. Stein, M. Brecht, H. Ogata, Y. Higuchi and W. Lubitz, *J. Am. Chem. Soc.*, 2003, **125**, 83-93.
33. F. Dole, A. Fournel, V. Magro, E. C. Hatchikian, P. Bertrand and B. Guigliarelli, *Biochemistry*, 1997, **36**, 7847-7854.
34. M. Teixeira, I. Moura, A. V. Xavier, B. H. Huynh, D. V. DerVartanian, H. D. Peck, J. LeGall and J. J. Moura, *J. Biol. Chem.*, 1985, **260**, 8942-8950.
35. R. Hidalgo, P. A. Ash, A. J. Healy and K. A. Vincent, *Angew. Chemiw Intl. Ed.*, 2015, **54**, 7110-7113.

Chapter Five

Conclusions

5.1 Conclusions

A range of novel [NiFe] complexes of the form $[Ni(L1)Fe(R)_4](BPh_4)_2$ (R = various isocyanides) have been synthesised that possess a reversible $Ni^{II/I}$ reduction process at –1.18 to –1.40 V vs Fc^+/Fc based around a four-coordinate $[Ni(N_2S_2)]$ core (Figure 5.1.1). The majority of these complexes have been characterised structurally through X-ray diffraction, electrochemical, EPR, IR and UV/vis spectroscopy experiments and we demonstrate that they possess a Ni-(S_2)-Fe moiety and a pseudooctahedral Fe^{II} centre; key structural features that draw inspiration from the Ni-SI form of the [NiFe] hydrogenases. [1, 2]



$[Ni(L1)Fe(CN\text{-}R)_4](BPh_4)_2$

R = ^{t}Bu, ^{i}Pr, ^{n}Bu, benzyl, cyclohexyl, PhOMe, PhF

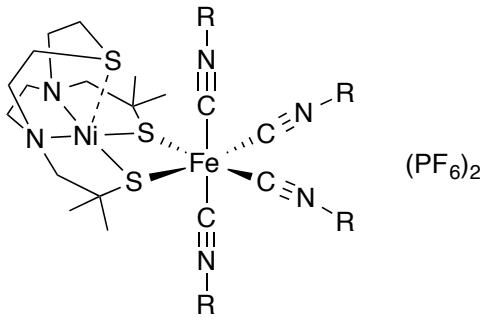
Figure 5.1.1: General structure of the [NiFe] complexes synthesised in Chapter Two.

The reduction of these $[Ni(L1)Fe(L)_4]^{2+}$ complexes to $[Ni(L1)Fe(L)_4]^+$ is associated with a structural rearrangement of one of the isocyanide ligands to a bridging mode between the Ni and Fe centres, and that this reduction is localised on the $[Ni(N_2S_2)]$ unit, giving rise to a formal $[Ni^IFe^{II}]$ system that is a compelling model for that of the Ni-L state of the [NiFe] hydrogenase enzyme.[3] We have extended the range of synthetic analogues that model this $[Ni^IFe^{II}]$ configuration and have demonstrated that these systems are potential electrocatalysts for proton

reduction and that the reduction potential of the $Ni^{II/I}$ process can be tuned through the variation of the functional group of the Fe-bound isocyanides through charge transfer.

Substitution of other transition metals in place of Ni in $[Ni(L1)Fe(^tBuNC)_4]^{2+}$ was performed and $[Pd(L1_3)Fe(^tBuNC)_4](BPh_4)_2$ and $[Co(L1)(^tBuNC)Fe(^tBuNC)_4](BPh_4)_2$ were isolated which have been characterised via X-ray crystallography. $[Pd(L1)Fe(^tBuNC)_4](BPh_4)_2$ bears a striking structural similarity to $[Ni(L1)Fe(^tBuNC)_4](BPh_4)_2$, however, the electrochemical behaviour is markedly different. $[Co(L1)(^tBuNC)Fe(^tBuNC)_4](BPh_4)_2$ binds an additional isocyanide ligand at the Co centre, yielding a pentacoordinate system. These complexes serve to demonstrate the key role that Ni offers in these [NiFe] hydrogenase analogues. En route to synthesising these [MFe] systems, we have expanded the range of [M(L1)] compounds known (M = Pd, Co, Zn) and shown that the N,N'-diethyl-3,7-diazononane-1,9-dithiolate $(L1)^{2-}$ ligand possesses considerable structural flexibility as a tetradentate ligand, demonstrating square-planar and distorted tetrahedral geometries with dihedral angles ranging from 1.68(18) º to 69.30(4) º from most square planar to most distorted tetrahedral.

We have synthesized and characterized the binuclear [NiFe] compounds $[Ni(L3)Fe(R\text{-}NC)_4](PF_6)_2$ (R = ^{t}Bu, benzyl) analogues of the active sites of the [NiFe] hydrogenases. The X-ray crystallographic structure of $[Ni(L3)Fe(^tBuNC)_4](PF_6)_2$ shows a close correspondence to the [NiFe] centre at the active sites of the [NiFe] hydrogenases (Figure 5.1.2).[4]



$[Ni(L3)Fe(CN\text{-}R)_4](PF_6)_2$

Figure 5.1.2: General structure of the $[Ni(L3)Fe(R\text{-}NC)_4](PF_6)_2$ complexes (R = ^{t}Bu, benzyl) synthesised in Chapter Three.

$[Ni(L3)Fe(R\text{-}NC)_4](PF_6)_2$ (R = ^{t}Bu, benzyl) exhibit chemically reversible oxidation processes at $E_{½}$ = 0.15 V vs Fc^+/Fc (R = ^{t}Bu) and $E_{½}$ = 0.21 V vs Fc^+/Fc (R = benzyl). Electrochemical, spectroscopic and DFT studies suggest that the reversible oxidation process is localized about the Ni center and involves a redox active orbital that is essentially Ni $3d_{z^2}$ and S(3)-based, and which shows a close correspondence with the SOMO calculated for the Ni-C state of the [NiFe] hydrogenase from *D. vulgaris* Miyazaki F.[5] The DFT calculations, together with the spectroscopic signatures of $[Ni(L3)Fe(R\text{-}NC)_4]^{3+}$ (R = ^{t}Bu, benzyl), is consistent with an assignment of the $[Ni(L3)Fe(R\text{-}NC)_4]^{3+}$ (R = ^{t}Bu, benzyl) to a formal $[Ni^{III}Fe^{II}]$ center that mirrors that of the Ni-C state.[5, 6] The range of synthetic analogues of these $[Ni^{III}Fe^{II}]$ systems has been expanded and it has been shown that moderation of the $Ni^{III/II}$ reduction potential is possible through the selection of the ligand at the Fe^{II} centre. Through the use of a pendant thioether at the pentacoordinate Ni^{III} centre, $[Ni(L3)Fe(R\text{-}NC)_4]^{3+}$ offers a compelling model of the Ni-C state of the [NiFe] hydrogenase enzyme.[7-9]

The structural, electrochemical and theoretical characterizations of $[Pd(L1)Fe(CN^tBu)_4](BPh_4)_2$ and $[Co(L1)(CN^tBu)Fe(CN^tBu)_4](BPh_4)_2$ reinforce the consensus view that the Fe^{II} centre present in these complexes and at the active site of the [NiFe]

hydrogenases modulates of the electrochemical behaviour of these centres rather than being the formal redox active species. These results suggest that the incorporation of a formal Ni^{II} centre facilitates the electrochemical and chemically reversibile redox behavior of $[Ni(L1)Fe(CN^tBu)_4](BPh_4)_2$ that reproduces the formal $Ni^{II/I}$ oxidation states associated with the Ni-SI and Ni-L states of the [NiFe] hydrogenases that may have key roles in the catalytic cycle of this enzyme.[1, 10-12]

5.2 References

1. A. Volbeda, E. Garcin, C. Piras, A. L. de Lacey, V. M. Fernandez, E. C. Hatchikian, M. Frey and J. C. Fontecilla-Camps, *J. Am. Chem. Soc.*, 1996, **118**, 12989-12996.
2. A. Volbeda, M. H. Charon, C. Piras, E. C. Hatchikian, M. Frey and J. C. Fontecilla-Camps, *Nature*, 1995, **373**, 580-587.
3. C. U. Perotto, G. Marshall, G. J. Jones, E. Stephen Davies, W. Lewis, J. McMaster and M. Schroder, *Chem. Commun. (Cambridge, U. K.)*, 2015, **51**, 16988-16991.
4. A. Volbeda and J. C. Fontecilla-Camps, *Dalton Trans.*, 2003, 4030-4038.
5. M. Kampa, W. Lubitz, M. van Gastel and F. Neese, *J. Biol. Inorg. Chem.*, 2012, **17**, 1269-1281.
6. W. Lubitz, E. Reijerse and M. van Gastel, *Chem. Rev. (Washington, DC, U. S.)*, 2007, **107**, 4331-4365.
7. T. R. Simmons, G. Berggren, M. Bacchi, M. Fontecave and V. Artero, *Coord. Chem. Rev.*, 2014, **270-271**, 127-150.
8. A. Abou-Hamdan, P. Ceccaldi, H. Lebrette, O. Gutierrez-Sanz, P. Richaud, L. Cournac, B. Guigliarelli, A. L. De Lacey, C. Leger, A. Volbeda, B. Burlat and S. Dementin, *J. Biol. Chem.*, 2015, **290**, 8550-8558.
9. H. Ogata, W. Lubitz and Y. Higuchi, *Dalton Trans.*, 2009, 7577-7587.
10. F. Dole, A. Fournel, V. Magro, E. C. Hatchikian, P. Bertrand and B. Guigliarelli, *Biochemistry*, 1997, **36**, 7847-7854.
11. M. Teixeira, I. Moura, A. V. Xavier, B. H. Huynh, D. V. DerVartanian, H. D. Peck, J. LeGall and J. J. Moura, *J. Biol. Chem.*, 1985, **260**, 8942-8950.
12. R. Hidalgo, P. A. Ash, A. J. Healy and K. A. Vincent, *Angew. Chemiw Intl. Ed.*, 2015, **54**, 7110-7113.

Appendices

Appendix 1: General Experimental Procedures and Physical Measurements

Appendix 2: X-Ray Crystallographic Experimental Details and Structure Solution

Appendix 3: Computational Methods

Appendix 4: Crystallography Tables

Appendix 1: General Experimental Procedures and Physical Measurements

All preparations were carried out under inert atmosphere (N_2 or Ar as high-purity gasses from BOC Gasses) using standard Schlenk techniques unless otherwise indicated. Reagents purchased from suppliers were used as received. Anhydrous DCM, MeOH and EtOH were purchased from suppliers and used as supplied and stored over molecular sieves. Anhydrous THF was dried by passage through activated alumina towers. FTIR spectra were recorded using a Thermo Scientific Nicolet Avatar 320 FT-IR, a Perkin-Elmer 1600 Series FTIR spectrometer or a Bruker Alpha series spectrometer with a CaF_2 solution cell accessory. ^{1}H and ^{13}C NMR data were recorded on either a Bruker AV(III)400 or Bruker DPX 400 NMR spectrometer at 298 K. Cyclic voltammetry was carried out using an Autolab PGSTAT 30 or Autolab PGSTAT 20 potentiostat in a single compartment cell with a three electrode system comprising a glassy carbon working electrode, saturated $Ag/AgCl_2$ reference electrode and platinum wire counter electrode. Experiments were carried out at 293 K in MeCN containing 1 mM of test sample and 0.2 M $[N^nBu_4][BF_4]$ as supporting electrolyte unless otherwise specified. Cyclic voltammograms were recorded at varying scan rates from 20 to 300 mVs^{-1} and the potentials of these measurements were referenced to the Fc^+/Fc redox couple[1, 2]. Catalytic cyclic voltammetry experiments were carried out by the addition of a 0.5 M solution of TFA in MeCN in a sealed single compartment cell under argon[3]. Spectroelectrochemical controlled potential electrolysis measurements were carried out *in situ* using a quartz reactor cuvette comprising a glassy carbon working electrode, saturated $Ag/AgCl_2$ reference electrode and platinum/iridium alloy mesh counter electrode in a Perkin-Elmer Lambda 16 UV-Vis spectrometer at 248 K. EPR spectrometry was carried out in in fluid solution in a flat quartz cell or as a frozen solution in a standard quartz EPR tube on a Bruker EMX spectrometer with an X-band microwave bridge using WinEPR software.[4] EPR simulations were carried out using the Simfonia software tool.[5]

Appendix 2: X-Ray Crystallographic Experimental Details and Structure Solution

Crystals were examined variously on an Agilent Technologies SuperNova Atlas CCD diffractometer, an Agilent Technologies GV1000 Titan S2 CCD diffractometer, or an Agilent Technologies XtalLAB PRO MM007, PILATUS3 R 200K solid state diffractometer using mirror-monochromated Cu Kα radiation (λ = 1.5418 Å). Software used was CrysAlisPro (control and integration)[6], and SHELXT[7], SHELXL[8], OLEX2[9] and Mercury[10] for structure solution and refinement and for molecular graphics, with additional molecular graphics generated using PovRay[11].

Appendix 3: Computational Methods

DFT calculations were carried out using the ADF software suite[12] with the BP86 functional with a Slater-optimised TZP basis set.[13] Starting geometry was taken from the crystal structures of all complexes studied and subject to geometry optimisation and vibrational analysis to generate molecular orbital information and IR spectra.[14] Since it was not possible to grow crystals of the reduced or oxidised forms of these complexes, charges were assigned *in silico* to the XRD structure, followed by a geometry optimisation to simulate changes in oxidation state of the system. Molecular orbital graphics were plotted using a isosurface value of 0.03 $eÅ^{-3}$.

Appendix 4: Crystallography Tables

Structures in Chapter 2

Complex	**$[Ni(L1)_2]Ni(BPh_4)_2$**	**$[Ni(L2)_2]Ni(PF_6)_2$**
Crystal data		
Chemical formula	$C_{22}H_{48}N_4Ni_3S_4 \cdot 2(C_{24}H_{20}B)$	$C_{10}H_{22}N_2Ni_{1.5}S_2 \cdot F_6P$
M_r	1311.43	934.90
Crystal system, space group	Triclinic, $P\bar{1}$	Monoclinic, $P2_1/n$
Temperature (K)	120	120
a, b, c (Å)	10.3613 (5), 11.9245 (5), 14.1501 (7)	7.2899 (2), 12.6662 (3), 18.1691 (6)
α, β, γ (°), β (°) (col 2)	65.752 (5), 80.584 (4), 80.502 (4)	90.823 (3)
V (Å^3)	1563.24 (14)	1677.49 (9)
Z	1	4
Radiation type	Cu $K\alpha$	Cu $K\alpha$
μ (mm^{-1})	2.64	12.02
Crystal size (mm)	0.19 × 0.15 × 0.05	0.14 × 0.03 × 0.01
Data collection		
Diffractometer	GV1000, Titan S2	GV1000, Atlas
Absorption correction	Gaussian *CrysAlis PRO*, Agilent Technologies Version 1.171.37.35 (release 13-08-2014 CrysAlis171 .NET)(compiled Aug 13 2014,18:06:01)Numerical absorption correction based on gaussian integration over a multifaceted crystal model. Empirical absorption correction using spherical harmonics, implemented in SCALE3 ABSPACK scaling algorithm.	Gaussian *CrysAlis PRO*, Agilent Technologies, Version 1.171.37.35 (release 13-08-2014 CrysAlis171 .NET) (compiled Aug 13 2014,18:06:01) Numerical absorption correction based on gaussian integration over a multifaceted crystal model. Empirical absorption correction using spherical harmonics, implemented in SCALE3 ABSPACK scaling algorithm.
Tmin, Tmax	0.665, 0.853	0.393, 0.858
No. of measured, independent and observed [$I > 2\sigma(I)$] reflections	11127, 6051, 5581	4200, 2630, 2312
R_{int}	0.029	0.023
(sin θ/λ)max (Å^{-1})	0.621	0.624
Refinement		
$R[F2 > 2\sigma(F2)]$, $wR(F2)$, S	0.033, 0.091, 1.04	0.032, 0.082, 1.07
No. of reflections	6051	2630
No. of parameters	378	207
H-atom treatment	H-atom parameters constrained	H-atom parameters constrained
Δρmax, Δρmin (e Å^{-3})	0.48, -0.39	0.43, −0.42

Complex	**[Ni(L1)Fe(^{t}BuCN)$_4$](BPh$_4$)$_2$**	**[Ni(L1)Fe(^{i}PrCN)$_4$](BPh$_4$)$_2$**
Crystal data		
Chemical formula	$C_{31}H_{60}FeN_6NiS_2 \cdot 2(C_{24}H_{20}B)$	$C_{27}H_{52}FeN_6NiS_2 \cdot 2(C_{24}H_{20}B)$
M_r	1333.94	1277.84
Crystal system, space group	Triclinic, $P\bar{1}$	Triclinic, $P\bar{1}$
Temperature (K)	120	120
a, b, c (Å)	14.0905 (5), 15.6386 (5), 18.0502 (5)	12.4196 (4), 14.9984 (6), 21.2945 (9)
α, β, γ (°)	82.482 (2), 80.363 (3), 69.780 (3)	100.317 (4), 101.040 (3), 109.184 (3)
V (Å^3)	3668.2 (2)	3549.4 (3)
Z	2	2
Radiation type	Cu $K\alpha$	Cu $K\alpha$
μ (mm^{-1})	2.78	2.85
Crystal size (mm)	0.18 × 0.16 × 0.09	0.45 × 0.13 × 0.03
Data collection		
Diffractometer	SuperNova, Dual, Cu at zero, Atlas	GV1000, Atlas S2
Absorption correction	Gaussian *CrysAlis PRO*, Agilent Technologies, Version 1.171.37.35 (release 13-08-2014 CrysAlis171 .NET) (compiled Aug 13 2014,18:06:01) Numerical absorption correction based on gaussian integration over a multifaceted crystal model Empirical absorption correction using spherical harmonics, implemented in SCALE3 ABSPACK scaling algorithm.	Gaussian *CrysAlis PRO*, Agilent Technologies, Version 1.171.37.35 (release 13-08-2014 CrysAlis171 .NET) (compiled Aug 13 2014,18:06:01) Numerical absorption correction based on gaussian integration over a multifaceted crystal model Empirical absorption correction using spherical harmonics, implemented in SCALE3 ABSPACK scaling algorithm.
Tmin, Tmax	0.713, 0.849	0.531, 0.917
No. of measured, independent and observed [$I > 2\sigma(I)$] reflections	28140, 14503, 13491	38314, 13989, 10526
R_{int}	0.030	0.097
(sin θ/λ)max (Å^{-1})	0.624	0.623
Refinement		
$R[F2 > 2\sigma(F2)]$, $wR(F2)$, S	0.036, 0.095, 1.02	0.075, 0.216, 1.03
No. of reflections	14503	13989
No. of parameters	883	814
No of restraints	2054	
H-atom treatment	H-atom parameters constrained	H-atom parameters constrained
Δρmax, Δρmin (e Å^{-3})	0.52, -0.38	1.29, -1.08

Complex	**[Ni(L1)(benzyl-NC)$_4$](BPh$_4$)$_2$**	**[Ni(L1)(cyclohexyl-NC)$_4$](BPh$_4$)$_2$**
Crystal data		
Chemical formula	$C_{43}H_{52}FeN_6NiS_2 \cdot 2(C_{24}H_{20}B)$	$1(C_{39}H_{68}FeN_6NiS_2) \cdot 2(C_{24}H_{20}B)$
M_r	1470.00	1437.85
Crystal system, space group	Monoclinic, $P2_1/n$	Monoclinic, $P2_1/c$
Temperature (K)	120	120
a, b, c (Å)	11.3734 (3), 41.1593 (8), 16.8327 (3)	22.0040 (19), 15.1438 (8), 47.245 (2)
β (°)	99.001 (2)	97.764 (5)
V (Å^3)	7782.7 (3)	15599.1 (17)
Z	4	8
Radiation type	Cu $K\alpha$	Cu $K\alpha$
μ (mm^{-1})	2.68	2.65
Crystal size (mm)	0.57 × 0.18 × 0.14	0.19 × 0.05 × 0.03
Data collection		
Diffractometer	SuperNova, Titan S2	XtalLAB PRO *MM007*, PILATUS3 R 200K
Absorption correction	Gaussian *CrysAlis PRO*, Agilent Technologies, Version 1.171.37.35 (release 13-08-2014 CrysAlis171 .NET) (compiled Aug 13 2014,18:06:01) Numerical absorption correction based on gaussian integration over a multifaceted crystal model. Empirical absorption correction using spherical harmonics, implemented in SCALE3 ABSPACK scaling algorithm.	Gaussian *CrysAlis PRO* 1.171.38.41n (Rigaku Oxford Diffraction, 2015) Numerical absorption correction based on gaussian integration over a multifaceted crystal model Empirical absorption correction using spherical harmonics, implemented in SCALE3 ABSPACK scaling algorithm.
T_{min}, T_{max}	0.446, 0.755	0.996, 0.999
No. of measured, independent and observed [$I > 2\sigma(I)$] reflections	35308, 15313, 13375	129585, 32386, 10553
R_{int}	0.045	0.266
$(\sin \theta/\lambda)_{max}$ (Å^{-1})	0.623	0.648
Refinement		
$R[F^2 > 2\sigma(F^2)]$, $wR(F^2)$, S	0.068, 0.175, 1.07	0.123, 0.397, 0.96
No. of reflections	15313	32386
No. of parameters	930	1788
No. of restraints	-	298
H-atom treatment	H-atom parameters constrained	H-atom parameters constrained
Weighting	$w = 1/[\sigma^2(F_o^2) + (0.0678P)^2 + 16.210P]$ where $P = (F_o^2 + 2F_c^2)/3$	
Δρmax, Δρmin (e Å^{-3})	1.17, -0.45	0.51, -0.72

Complex	**$[Ni(L1)(PhOMe\text{-}NC)_4](BPh_4)_2$**	**$[Ni(L1)(PhF\text{-}NC)_4](BPh_4)_2$**
Crystal Data		
Chemical formula	$C_{43}H_{52}FeN_6NiO_4S_2 \cdot 2(C_{24}H_{20}B) \cdot 0.5(CH_4O) \cdot 0.5(CH_3NO_2)$	$C_{39}H_{40}F_4FeN_6NiS_2 \cdot 2(C_{24}H_{20}B) \cdot C_2H_3N$
M_r	1580.54	1526.92
Crystal system, space group	Triclinic, $P\bar{1}$	Monoclinic, $P2_1/c$
Temperature (K)	120	120
a, b, c (Å)	10.36269 (16), 15.8265 (3), 25.8257 (4)	25.4837 (4), 12.44411 (16), 26.5682 (4)
α, β, γ (°), β (°) (col 2)	77.3646 (15), 87.6475 (13), 82.6463 (14)	114.5143 (19)
V (Å^3)	4098.60 (12)	7665.9 (2)
Z	2	4
Radiation type	Cu $K\alpha$	Cu $K\alpha$
μ (mm^{-1})	2.63	2.82
Crystal size (mm)	0.38 × 0.26 × 0.08	0.49 × 0.30 × 0.29
Data collection		
Diffractometer	SuperNova, Titan S2	SuperNova, Atlas
Absorption correction	Gaussian *CrysAlis PRO* 1.171.38.43 (Rigaku Oxford Diffraction, 2015) Numerical absorption correction based on gaussian integration over a multifaceted crystal model Empirical absorption correction using spherical harmonics, implemented in SCALE3 ABSPACK scaling algorithm.	Gaussian *CrysAlis PRO* 1.171.38.41 (Rigaku Oxford Diffraction, 2015) Numerical absorption correction based on gaussian integration over a multifaceted crystal model Empirical absorption correction using spherical harmonics, implemented in SCALE3 ABSPACK scaling algorithm.
T_{min}, T_{max}	0.520, 0.822	0.421, 0.586
No. of measured, independent and observed [$I > 2\sigma(I)$] reflections	91025, 16448, 16065	32355, 15009, 13519
R_{int}	0.042	0.021
$(\sin\theta/\lambda)_{max}$ (Å^{-1})	0.625	0.622
Refinement		
$R[F^2 > 2\sigma(F^2)]$, $wR(F^2)$, S	0.046, 0.130, 1.05	0.066, 0.179, 1.05
No. of reflections	16448	15009
No. of parameters	1055	1077
No. of restraints	19	165
H-atom treatment	H-atom parameters constrained	H-atom parameters constrained
Weighting		$w = 1/[\sigma^2(F_o^2) + (0.0862P)^2 + 12.3084P]$ where $P = (F_o^2 + 2F_c^2)/3$
Δρmax, Δρmin (e Å^{-3})	2.08, -0.59	1.41, -1.16

Structures in Chapter 3

Complex	**Ni(L3)**	**Ni(L3)Fe(^{t}BuCN)4(PF_6)$_2$**
Crystal data		
Chemical formula	$C_{14}H_{28}N_2NiS_3$	$C_{34}H_{64}FeN_6NiS_3 \cdot 2(F_6P)$
M_r	379.27	1057.59
Crystal system, space group	Monoclinic, $P2_1/n$	Monoclinic, $P2_1/c$
Temperature (K)	120	120
a, b, c (Å)	7.5524 (5), 11.9385 (8), 18.7034 (11)	11.4929 (2), 14.0431 (3), 33.6282 (14)
β (°)	93.364 (6)	95.822 (3)
V (Å^3)	1683.48 (19)	5399.5 (3)
Z	4	4
Radiation type	Cu $K\alpha$	Cu $K\alpha$
μ (mm^{-1})	5.06	4.86
Crystal size (mm)	0.7 × 0.14 × 0.1	0.32 × 0.06 × 0.02
Data collection		
Diffractometer	SuperNova-Duo, Atlas	XtalLAB PRO *MM007*, PILATUS3 R 200K
Absorption correction	Multi-scan *CrysAlis PRO*, Agilent Technologies, Version 1.171.37.34 (release 22-05-2014 CrysAlis171 .NET) (compiled May 22 2014,16:03:01) Empirical absorption correction using spherical harmonics, implemented in SCALE3 ABSPACK scaling algorithm.	Gaussian *CrysAlis PRO* 1.171.38.43 (Rigaku Oxford Diffraction, 2015) Numerical absorption correction based on gaussian integration over a multifaceted crystal model Empirical absorption correction using spherical harmonics, implemented in SCALE3 ABSPACK scaling algorithm.
T_{min}, T_{max}	0.844, 1.000	0.483, 0.930
No. of measured, independent and observed [$I > 2\sigma(I)$] reflections	6608, 3349, 2845	136961, 11279, 7536
R_{int}	0.043	0.206
(sin θ/λ)$_{max}$ (Å^{-1})	0.625	0.633
Refinement		
$R[F^2 > 2\sigma(F^2)]$, $wR(F^2)$, S	0.073, 0.205, 1.12	0.224, 0.587, 2.33
No. of reflections	3349	11279
No. of parameters	185	584
No. of restraints	-	765
H-atom treatment	H-atom parameters constrained	H-atom parameters constrained
Δρmax, Δρmin (e Å^{-3})	1.31, -0.47	1.37, -1.54

Structures in Chapter 4

Complex	**Co(L1)**	**[Co(L1)Fe(^{t}BuCN)$_4$](BPh$_4$)$_2$**
Crystal data		
Chemical formula	$C_{11}H_{24}CoN_2S_2$	$C_{36}H_{69}CoFeN_7S_2 \cdot 2(C_{24}H_{20}B)$
M_r	307.37	1417.30
Crystal system, space group	Triclinic, $P\bar{1}$	Monoclinic, $P2_1/c$
Temperature (K)	120	120
a, b, c (Å)	7.6880 (6), 8.1889 (5), 11.3134 (9)	18.505 (14), 20.2304 (18), 34.59 (3)
α, β, γ (°), β (°) (col 2)	79.235 (6), 87.963 (7), 87.071 (6)	141.32 (15)
V (Å^3)	698.56 (9)	8094 (19)
Z	2	4
Radiation type	Cu $K\alpha$	Cu $K\alpha$
μ (mm^{-1})	12.22	3.87
Crystal size (mm)	0.10 × 0.08 × 0.01	0.11 × 0.05 × 0.05
Data collection		
Diffractometer	SuperNova, Atlas	XtaLAB Pro: Kappa single
Absorption correction	Gaussian *CrysAlis PRO* 1.171.38.43 (Rigaku Oxford Diffraction, 2015) Numerical absorption correction based on gaussian integration over a multifaceted crystal model Empirical absorption correction using spherical harmonics, implemented in SCALE3 ABSPACK scaling algorithm.	Gaussian *CrysAlis PRO* 1.171.38.43 (Rigaku Oxford Diffraction, 2015) Numerical absorption correction based on gaussian integration over a multifaceted crystal model Empirical absorption correction using spherical harmonics, implemented in SCALE3 ABSPACK scaling algorithm.
T_{min}, T_{max}	0.436, 0.853	0.788, 0.869
No. of measured, independent and observed [$I > 2\sigma(I)$] reflections	5062, 2709, 2598	51590, 14479, 2784
R_{int}	0.028	0.434
$(\sin\theta/\lambda)_{max}$ (Å^{-1})	0.623	0.598
Refinement		
$R[F^2 > 2\sigma(F^2)]$, $wR(F^2)$, S	0.027, 0.070, 1.04	0.192, 0.555, 1.12
No. of reflections	2709	14479
No. of parameters	147	891
No. of restraints	0	2032
H-atom treatment	H-atom parameters constrained	H-atom parameters constrained
Δρmax, Δρmin (e Å^{-3})	0.31, -0.31	0.59, -1.00

Complex	**Pd(L1)**	**$[Pd(L1)Fe(^tBuCN)_4](BPh_4)_2$**
Crystal data		
Chemical formula	$C_{11}H_{24}N_2PdS_2$	$C_{31}H_{60}FeN_6PdS_2 \cdot 2(C_{24}H_{20}B)$
M_r	354.84	1381.63
Crystal system, space group	Triclinic, $P\bar{1}$	Triclinic, $P\bar{1}$
Temperature (K)	120	120
a, *b*, *c* (Å)	9.4238 (2), 12.5682 (3), 12.8062 (2)	14.1753 (8), 15.6384 (9), 18.1542 (9)
α, β, γ (°)	90.2442 (19), 109.8800 (18), 93.8536 (19)	82.635 (4), 80.664 (4), 69.579 (5)
V (Å^3)	1422.55 (6)	3710.4 (4)
Z	4	2
Radiation type	Cu *K*a	Cu *K*α
μ (mm^{-1})	13.07	4.39
Crystal size (mm)	0.20 × 0.09 × 0.03	0.19 × 0.05 × 0.05
Data collection		
Diffractometer	SuperNova, Atlas	SuperNova, Dual, Cu at zero, Atlas
Absorption correction	Gaussian *CrysAlis PRO* 1.171.38.43 (Rigaku Oxford Diffraction, 2015) Numerical absorption correction based on gaussian integration over a multifaceted crystal model. Empirical absorption correction using spherical harmonics, implemented in SCALE3 ABSPACK scaling algorithm.	CrysAlisPro 1.171.38.43 (Rigaku Oxford Diffraction, 2015) Numerical absorption correction based on gaussian integration over a multifaceted crystal model. Empirical absorption correction using spherical harmonics, implemented in SCALE3 ABSPACK scaling algorithm.
T_{min}, T_{max}	0.263, 0.741	
No. of measured, independent and observed [$I > 2\sigma(I)$] reflections	33241, 5688, 5554	89917, 13114, 7622
R_{int}	0.045	0.245
$(\sin\theta/\lambda)_{max}$ (Å^{-1})	0.623	0.595
Refinement		
$R[F^2 > 2\sigma(F^2)]$, $wR(F^2)$, *S*	0.064, 0.170, 1.17	0.152, 0.437, 1.37
No. of reflections	5688	13114
No. of parameters	293	863
No of restraints	-	207
H-atom treatment	H-atom parameters constrained	H-atom parameters constrained
Weighting	$w = 1/[\sigma2(Fo2) + (0.047P)2 + 30.6437P]$ where $P = (Fo2 + 2Fc2)/3$	
Δρmax, Δρmin (e Å^{-3})	6.23, -1.10	2.69, -1.32

Complex	**Zn(L1)**
Crystal data	
Chemical formula	$C_{11}H_{24}N_2S_2Zn$
M_r	313.81
Crystal system, space group	Monoclinic, *C*2/*c*
Temperature (K)	120
a, *b*, *c* (Å)	11.4032 (3), 11.1281 (2), 10.8585 (3)
β (°)	95.249 (2)
V (Å^3)	1372.12 (6)
Z	4
Radiation type	Cu *K*α
μ (mm^{-1})	5.13
Crystal size (mm)	0.13 × 0.10 × 0.06
Data Collection	
Diffractometer	SuperNova, Atlas
Absorption correction	Gaussian *CrysAlis PRO* 1.171.38.43 (Rigaku Oxford Diffraction, 2015) Numerical absorption correction based on gaussian integration over a multifaceted crystal model Empirical absorption correction using spherical harmonics, implemented in SCALE3 ABSPACK scaling algorithm.
T_{min}, T_{max}	0.624, 0.769
No. of measured, independent and observed [$I > 2\sigma(I)$] reflections	8053, 1370, 1355
R_{int}	0.018
$(\sin \theta/\lambda)_{max}$ (Å^{-1})	0.622
Refinement	
$R[F^2 > 2\sigma(F^2)]$, $wR(F^2)$, S	0.016, 0.041, 1.08
No. of reflections	1370
No. of parameters	75
H-atom treatment	H-atom parameters constrained
Δρmax, Δρmin (e Å^{-3})	0.29, -0.19

Appendicies References

1. R. R. Gagne, C. A. Koval and G. C. Lisensky, *Inorg. Chem.*, 1980, **19**, 2854-2855.
2. I. Noviandri, K. N. Brown, D. S. Fleming, P. T. Gulyas, P. A. Lay, A. F. Masters and L. Phillips, *J. Phys. Chem. B*, 1999, **103**, 6713-6722.
3. A. Perra, E. S. Davies, J. R. Hyde, Q. Wang, J. McMaster and M. Schroder, *Chem. Commun. (Cambridge, U. K.)*, 2006, 1103-1105.
4. Bruker Instruments Inc, *CW-EPR Acquisition & Processing for the EMX*, (1995), Billerica, MA, USA.
5. R. T. Weber, *WIN-EPR Simfonia*, (1995) Bruker Instruments Inc., Billerica, MA, USA.
6. *CrysAlisPRO*, Oxford Diffraction/Agilent Technologies UK Ltd, Yarnton, England.
7. G. Sheldrick, *Acta Crystallogr. A*, 2015, **71**, 3-8.
8. G. Sheldrick, *Acta Crystallogr. C*, 2015, **71**, 3-8.
9. O. V. Dolomanov, L. J. Bourhis, R. J. Gildea, J. A. K. Howard and H. Puschmann, *J. Appl. Crystallogr.*, 2009, **42**, 339-341.
10. C. F. Macrae, P. R. Edgington, P. McCabe, E. Pidcock, G. P. Shields, R. Taylor, M. Towler and J. van de Streek, *J. Appl. Crystallogr.*, 2008, **41**, 466-470.
11. *Persistence of Vision (TM) Raytracer*, (2004) Persistence of Vision Pty. Ltd., Williamstown, Victoria, Australia.
12. G. te Velde, F. M. Bickelhaupt, E. J. Baerends, C. Fonseca Guerra, S. J. A. van Gisbergen, J. G. Snijders and T. Ziegler, *J. Comput. Chem.*, 2001, **22**, 931-967.
13. E. Van Lenthe and E. J. Baerends, *J. Comput. Chem.*, 2003, **24**, 1142-1156.
14. L. Fan and T. Ziegler, *J. Phys. Chem.*, 1992, **96**, 6937-6941.